FLOW AND HEAT TRANSFER CHARACTERISTICS OF AN IMPINGING JET WITH CROSSFLOW

BRIAN CHEE YUEN, CHEONG

A thesis submitted in partial fulfilment of the
requirements of The Nottingham Trent University
for the degree of Doctor of Philosophy.

This research programme was carried out in the
Department of Mechanical and Manufacturing Engineering,
Faculty of Computing and Technology,
The Nottingham Trent University,
Burton Street, Nottingham NG1 4BU, UK.
Part of the data reduction and analysis was carried out in
Osney Laboratory, Department of Engineering Science,
University of Oxford,
Parks Road, Oxford OX1 3PJ, UK.

September 2002

TABLE OF CONTENTS

FLOW AND HEAT TRANSFER CHARACTERISTICS OF AN IMPINGING JET WITH CROSSFLOW

by

Brian Chee Yuen, Cheong

ABSTRACT

A detailed study of confined single impinging jets with, and without, crossflow has been undertaken to determine the effects of near wall velocity, turbulence, temperature and fluctuating temperature on surface heat transfer. The turbulent incompressible jet discharged from a contoured nozzle of 100 mm diameter with uniform exit velocity and temperature profiles at Reynolds numbers of 20 000 and 40 000, and was subjected to an ambient crossflow at jet-to-crossflow velocity ratios (U_j/U_c) of 2, 3, 4 and 5. Non-dimensional nozzle-to-plate spacings (z/d) of 1.5 and 3 were considered and represent typical distances used in industrial cooling systems involving multiple impinging jets with crossflow.

New detailed experimental hydrodynamic and thermal flow field data have been obtained using the techniques of hot-wire anemometry and cold-wire thermometry. Smoke-flow visualisation has been employed to provide a qualitative insight into the nature of the complex flow field and to substantiate quantitative results. Full surface heat transfer coefficients and effectiveness have been determined using a heater mesh transient technique with double liquid crystals as the thermal indicator.

It has been demonstrated that surface heat transfer beneath a confined single impinging jet in crossflow varies sensitively with the near wall hydrodynamic and thermal characteristics. The impinging jets (with, and without, crossflow) at z/d = 1.5 consistently yield greater magnitude and uniformity of surface heat transfer (compared to those at z/d = 3). For z/d = 1.5, the maximum average heat transfer with fine uniformity is achieved with a moderate strength crossflow ($U_j/U_c = 5$ for Re = 40 000), through which turbulence is induced appreciably with a negligible loss in the momentum of the jet. Heat transfer falls substantially when the strength of crossflow becomes comparable to that of the impinging jet ($U_j/U_c = 2$). For z/d = 3, optimum heat transfer condition exists when the impinging jet and the crossflow act with near equal intensity ($U_j/U_c = 4$ for Re = 40 000). A stronger crossflow would lead to a radical deterioration of the heat transfer performance. It was also revealed that jet deflection by the crossflow increases significantly at higher nozzle-to-plate spacing (z/d = 3) and Reynolds number (40 000).

Experimental near wall flow fields beneath a semi-confined axisymmetric impinging jets at z/d = 2 and 6.5 were compared with predictions from theoretical solutions. For z/d = 2, velocity profiles in the inviscid region of the flow can be predicted accurately using stagnation three-dimensional flow model. Prediction of boundary layer profiles using viscous flow model for an axisymmetric case is also reasonable provided that the flow remains laminar and dominated by the radial wall jet. For z/d = 6.5, the flow field is essentially turbulent and predictions using both the models are inappropriate.

ACKNOWLEDGEMENTS

Throughout the course of my research work I have received a tremendous amount of support from colleagues at The Nottingham Trent University and University of Oxford, for which I am extremely thankful. I would like to express my sincere gratitude to my Director of Studies, Dr Shirley Ashforth-Frost, for her constant support, guidance and trust. I am also indebted to my supervisor, Dr Peter Ireland, whose advice, enthusiasm and encouragement have always inspired me to strive towards the completion of this project. Sincere thank is due to my industrial advisor, Dr Chris Whitney, for his consultation and interest shown in my work.

I would like to extend a special thankyou to Dr David Gillespie for his detailed technical guidance and discussions. I am also grateful to Prof Dick Gentle for his helps and guardian, Mrs Doreen Corlett for maintaining the jet impingement and liquid crystal data bases and Mr J. P. Ling for helping in the processing of the heat transfer data.

Special thanks are due to the laboratory and technical staff; Rob Potter, Keith Adams, Phil Breedon, Judith Keepling, Jezz Keeling, Ralph James, John Grimes, Tim Randall, Gary Griffiths, Kerry Truman and Patrick Timm for their assistance in manufacturing the experimental facility.

I would like to thank my fellow researchers; Dr Mark Wakelam, Dr Y. W. Tan, Dr Uwe Rüdel, Mr Matthew Dalton, Mr Aravin Arumugam, Mr Lorenzo Brignone, Mr Karim Khene and Ms Narimam Amin for their friendship, advice and encouragement.

My greatest thanks go to my family, particularly my brother Chee Leong and sister Lee Cheng, for always supporting and having faith in me. This work forms a tribute to my late mum, and a dedication to all the kids in my family. Finally, I would like to thank everyone at NCCC, especially my girlfriend Zoe Wong and Dr Lam Wah Cheung, for taking active interest in my education and aspirations. May God's name be glorified.

I would like to acknowledge the Nottingham Trent University and the Engineering and Physical Science Research Council (EPSRC) (grant AF/97/0568 to Dr S Ashforth-Frost) for providing financial support towards this work.

LIST OF PUBLICATIONS

- Ashforth-Frost, S., Cheong, B.C.Y. and Ireland, P.T., 2001. Near wall flow characteristics beneath a turbulent impinging jet. Proc. 5th World Conf. on Exp. Heat Transfer, Fluid Mechanics, and Thermodynamics, Thessaloniki, 24 - 28 Sept., Vol. (2), 987 - 992.

- Cheong, B.C.Y., Ashforth-Frost, S. and Ireland, P. T., 2003. A comparison between experimental and predicted flow profiles beneath a semi-confined axisymmetric impinging jet. Submitted to: ASME/IGTI Turbo Expo, Atlanta, Georgia, USA, June 16 – 19.

LIST OF FIGURES

Figure:

LIST OF APPENDICES

NOMENCLATURE

a	Constant.
A	Area (m^2); Constant.
A_{mesh}	Area of heater mesh (m^2).
B	Constant.
c	Local free jet half-radius; Specific heat of test model (J/KgK).
c_n	Nozzle centre-to-centre spacing (m).
c_p	Specific heat at constant pressure (J/kgK).
c_w	Specific heat capacity of wire (J/kgK).
C	Constant.
d	Nozzle diameter (m); Wire diameter (m).
d_c	Calorimeter diameter (m).
e	Fluctuating anemometer voltage (V).
e_1- e_2	Error voltage (V).
e_w	Fluctuating wire voltage (V).
E	Voltage (V).
$E_{0.6}$	Voltage drop for U = 0.6 m/s at reference temperature (V).
E_C	Corrected voltage (V).
E_{in}	Input energy (J).
h	Heat transfer coefficient (W/m^2k).
H	Heat (J).
H_0	Heat flux transferred to fluid (W/m^2).
i	Current (A).
I	Current (A).
k	Thermal conductivity (W/mK).
K	Amplifier gain.
l	Nozzle length (m); length of heat transfer region downstream from the nozzle exit plane; Active wire length (m); Temperature loading factor.
m_w	Mass of wire (Kg).
$\dot{m}$	Mass-flow rate (Kg/s).

$\dot{m}_c$	Crossflow mass-flow rate (kg/s).
$\dot{m}_j$	Jet mass-flow rate (kg/s).
M	Jet-to-crossflow mass velocity ratio, $[(\rho U)_j/(\rho U)_c]$.
M^*	Crossflow-to-jet mass flow rate ratio, $[\dot{m}_c / \dot{m}_j]$.
n	Constant.
N	Constant.
Nu	Nusselt number, [hd/k].
$\overline{Nu}$	Average Nusselt number, [hd/k].
p	Pressure (N/m^2).
Pr	Prandtl number, $[c_p\mu/k]$.
q	Heat flux (W/m^2).
Q	Input power (W).
r	Radial distance from the stagnation point (m), radial component.
R	Averaging area radius (m).
R_0	Reference resistance (Ω).
R_{20}	Resistance at 20°C (Ω).
Re	Reynolds number, $[\rho Ud/\mu]$.
Re_{es}	Equivalent slot width Reynolds number, $[2\rho UB/\mu]$.
R_f	Wire resistance at fluid temperature (Ω).
R_w	Wire resistance (Ω).
ΔR_w	Resistance change (Ω).
Sc	Schmidt number, $[\mu/\rho D_v]$.
Sh	Sherwood number, $[k_c d/D_v]$.
$\overline{St}$	Average Stanton number, $[h/\rho c_p V]$.
S_u	Velocity sensitivity of hot-wire.
$S_{u,cc}$	Velocity sensitivity of cold-wire.
S_θ	Temperature sensitivity of hot-wire.
$S_{\theta,cc}$	Temperature sensitivity of cold-wire.
t	Time (s).

t_1	Time from initialisation to colour change for first crystal (s).
t_2	Time from initialisation to colour change for second crystal (s).
t_i	Instantaneous temperature fluctuation (°C).
t'	RMS temperature Fluctuation (°C).
T	Mean Temperature (°C); Temperature (°C).
T_0	Initial surface temperature (°C); Reference temperature (°C).
T_1	Event temperature of first crystal (°C).
T_2	Event temperature of second crystal (°C).
T_∞	Temperature far from the impingement surface (°C).
T_a	Ambient temperature (°C).
T_{aw}	Adiabatic wall temperature (°C).
T_c	Crossflow temperature (°C).
T_{CL}	Jet exit centreline temperature (°C).
T_{down}	Temperature downstream of heater mesh (°C).
T_f	Fluid temperature (°C).
T_i	Instantaneous temperature (°C).
T_{in}	Channel inlet temperature (°C).
T_j	Jet Temperature (°C).
T_m	Mixed mean temperature (°C).
T_{mesh}	Temperature of heater mesh (°C).
T_{ref}	Reference temperature (°C).
T_s	Surface temperature (°C).
Tu	Turbulent intensity based on main velocity component (%).
T_{up}	Temperature upstream of heater mesh (°C).
T_w	Wall temperature (°C); Temperature of wire (°C).
ΔT_f	Change in fluid temperature (°C).
u	Axial component velocity (m/s).
u_i	Instantaneous velocity fluctuation (m/s).
u'	RMS axial velocity fluctuation (m/s).

U	Mean axial velocity (m/s); Velocity (m/s).
U_{12}	Amplifier input voltage (V).
U_c	Mean crossflow velocity (m/s).
U_{CL}	Mean jet exit centreline velocity (m/s).
U_f	Amplifier output voltage (V).
U_i	Instantaneous velocity (m/s).
U_j	Mean jet exit velocity (m/s).
U_{mesh}	Air velocity through heater mesh (m/s).
v	Radial component velocity (m/s).
v'	RMS radial velocity fluctuation (m/s).
v_m'	RMS mean velocity fluctuation (m/s).
V	Mean radial velocity (m/s); Voltage (V); Volume (m^3).
V_m	Mean velocity (m/s).
V_∞	Velocity far from the impingement surface (m/s).
W	Thermal energy storage (J).
x	Spanwise distance from the jet centre (m); Thickness of test plate (m); Streamwise coordinate.
y	Vertical distance from the impingement plate surface (m).
z	Nozzle-to-plate spacing (m).

Greek Symbols

α	Thermal diffusivity (m^2/s); Temperature coefficient of resistance.
α_0	Reference temperature coefficient of resistance.
α_{20}	Temperature coefficient of resistance at 20°C.
Θ	Dimensionless adiabatic wall temperature (jet effectiveness), $[(T_{aw}-T_c)/(T_j-T_c)]$.
ρ	Density, (Kg/m^3).
σ	Standard deviation.
δ	Boundary layer thickness (m).
ν	Kinematic viscosity, (m^2/s).

τ	Time constant (s).
τ_t	Offset time from mesh heater to the target surface (s).
∞	Infinity.
η	Mesh convective efficiency.
λ_0	Thermal conductivity of fluid (W/mK)
θ	Temperature (°C).
θ_1	Non-dimensional temperature of the first crystal.
θ_2	Non-dimensional temperature of the second crystal.

CHAPTER 1
INTRODUCTION

This chapter discusses the application and development of impinging jets for heat transfer processes in various industries. The purpose and scope of the current research together with the specific aims and objectives are discussed in detail. The rationale behind the choice of impingement geometry and fluid flow parameters is provided. Finally, a summary of the thesis structure is included.

1.1 Background and Statement of the problem

Over the years, jet impingement has emerged as one of the most prominent methods for controlled cooling, heating and drying of a target surface due to its excellent heat and mass transport characteristics. It is used widely and diversely throughout engineering and manufacturing industries to enhance engine performance, product quality, production capacity and provide energy savings. Typical applications of jet impingement technology include cooling of turbine blades, combustion cans and electronic components, heating of coated surfaces, de-icing of aircraft wings, drying of foods and papers, tempering of glass and annealing of metals. In order to obtain high average jet impingement heat and mass transfer over large areas, fine control and management of convective rates through optimisation of the impingement geometry and flow parameters are necessary. This requires the establishment of a detailed understanding of the fluid flow and heat transfer characteristics of impinging jets.

The heat transfer process of impinging jets is strongly influenced by near wall hydrodynamic characteristics. The importance of the inherent near wall turbulence of impinging jets on surface heat transfer, as revealed by Gardon and Akfirat (1965), has been experimentally confirmed, Cooper et al. (1993) and Ashforth-Frost (1994). There also exists an interaction of hydrodynamic and thermal boundary layer that affects localised heat transfer in the stagnation and wall jet regions, Viskanta (1993).

The complex phenomena of Jet Impingement Heat Transfer (JIHT) require in-depth investigations to correlate hydrodynamic and thermal characteristics. However, the collection of experimental data has often been restricted to hydrodynamic characteristic of single impinging jets. Even though most impinging jets exist in the form of jet arrays with a discharge of crossflow fluid, the inherent complex flow and heat transfer phenomena of array impinging jets are still not sufficiently understood. Literature pertaining to single impinging jets with a discharge crossflow, is particularly scarce. Specifically, little is known about the prominent behaviour of crossflow discharge that affects the magnitude and uniformity of the local convective heat transfer coefficient. Performance optimisations of array impinging jets are often conducted through trial-and-error approach. A major breakthrough in jet impingement technology seems unlikely without establishing fundamental knowledge on the interaction of single impinging jets with upstream crossflow.

An increased physical understanding, particularly on the resultant streamwise horseshoe vortex (shown in Figure 1.1), is essential for optimisation of cooling geometries. With the recent remarkable advancement of thermal measurement techniques, e.g. Ireland et al. (1999), fluid flow and heat transfer characteristics of impinging jets can now be correlated more easily and accurately. Information of this kind is invaluable for thermal engineers constantly seeking superior performance and efficiency of heat exchange geometries.

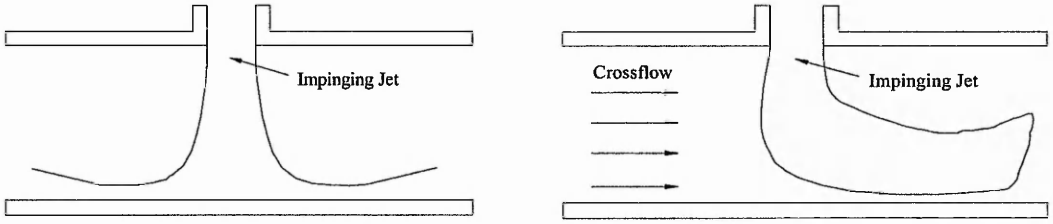

Single Jet without Crossflow Single Jet with Crossflow

Figure 1.1: Single impinging jet with and without crossflow.

The aim of the current work was to investigate the effects of near wall mean velocity, turbulence and temperature characteristics on surface heat transfer beneath a single impinging jet with, and without, crossflow. The hydrodynamic and thermal characteristics of the streamwise horseshoe vortex have been correlated for a range of impingement geometries and flow parameters. The research focused on impinging jets at low nozzle-to-plate spacings ($z/d \leq 4$) due to their proven higher heat transfer efficiencies. The experiments simulated engine representative geometries, primarily those for turbine guide vane cooling, to facilitate the design process of jet impingement devices.

To accomplish the experimental research programme a purpose-built jet impingement facility, with associated instrumentation and data acquisition and analysis systems, was developed. Flow visualisation of impinging jets was performed prior to quantitative measurements to aid the selection of flow parameters, and subsequent interpretation and corroboration of experimental data.

1.2 Aims and Objectives

1.2.1 Specific Aims

1. To seek an understanding of the effect of near wall mean velocity, turbulence and temperature characteristics on surface heat transfer due to a **single impinging jet with, and without, crossflow**.

2. To propose, based on experimental evidence, an optimum arrangement for jet impingement heat transfer involving crossflow.

1.2.2 Objectives

1. Design, build, commission and validate an experimental wind-tunnel facility, which incorporates an existing rig for single jet impingement, for the study of confined single impinging jets with, and without, crossflow. The rig must enable

hot-wire anemometry (HWA) and cold-wire thermometry (CWT) measurements to be made throughout the flow field. It should also provide the means to determine surface temperature and heat transfer distributions using liquid crystal thermography and an image processing system.

2. Develop system and software for the control of instrumentation and the acquisition of experimental data, supported with stringent uncertainty analysis conducted during the experimental design phase.

3. Establish a range of experimental jet impingement geometries and flow regimes to be investigated, based on industrial applications, existing literature, preliminary measurements and smoke flow visualisations.

4. Undertake near wall velocity, turbulence and temperature measurements for single impinging jets with, and without, crossflow. Correlate the fluid flow and heat transfer characteristics of impinging jets for the range of geometries and flow parameters under consideration.

5. Analyse and validate experimental results with comparison to theoretical models.

6. Further develop an application of liquid crystals for thermal field investigation across the streamwise horseshoe vortex.

7. Propose an improved arrangement for heat transfer augmentation due to impinging jets with crossflow.

1.2.3 Rationale

The experimental parameters considered during the current investigation are listed in Table 1.1. A large-scale jet facility with a nozzle outlet diameter of 100 mm has been developed specifically to enable high-resolution boundary layer measurements to be made

for single impinging jets with, and without, crossflow. Reynolds numbers of 20 000 and 40 000 were selected to further on-going research undertaken within the School as they represent typical magnitudes of industrial cooling using impinging jets. The configuration also provides experimental data that are highly sought after for development and validation of numerical turbulence models. The Reynolds numbers were sufficiently large to produce turbulent flow regimes with the formations of characteristic secondary maxima in heat transfer. Therefore, the experimental data were deemed suitable for comparison with numerical results.

Parameter	Range
Jet type	100 mm diameter contoured nozzle
Re	20 000 and 40 000
z/d	1.5 and 3
r/d	0 to 5.5
y/d	0.01 to 0.6
Jet-to-crossflow ratio	1, 2, 3, 4,5 and no crossflow

Table 1.1. Experimental parameters.

The single impinging jet was confined by a perpendicular solid target plate. Two non-dimensional nozzle-to-plate spacings, namely z/d = 1.5 and 3, were considered. An additional upper confinement plate was placed flush with the nozzle outlet plane and parallel with the target plate. These represent some of the low separation distances most commonly found in the array jet configurations; e.g. cooling of turbine guide vanes. Furthermore, two parallel side walls were positioned at x/d = ±4 from the jet axis in order to facilitate the definitions of boundary conditions from a numerical viewpoint. A crossflow was imposed from the inlet end so that the jet was restricted to discharge through the outlet end, thus simulating a complete or maximum crossflow phenomenon as described by Obot and Trabold (1987).

1.3 Thesis Outline

This Chapter has outlined the role of jet impingement technology in the context of modern industrial applications and provided background to the field together with a statement of the problem that has inspired the current research activity. The aims and objectives of the research programme have also been outlined and discussed.

A review of the relevant works of literature is provided in Chapter 2. The review focuses on turbulent impinging jets with, and without, crossflow. It begins with a general description of the geometric arrangement and the flow regions under consideration. The effects of geometric arrangement, confinement, turbulence and jet-to-crossflow velocity ratio on heat transfer, particularly in the stagnation and the wall jet regions are emphasised. Existing empirical correlations for the Nusselt number are given for both laminar and turbulent impinging jets, with and without crossflow. Flow visualisation studies of impinging jets are also documented and summarised. The Chapter concludes with a review of theoretical models directed towards the flow prediction for axisymmetric impinging jets.

Chapter 3 describes the experimental arrangements and the calibration and measurement procedures used for liquid crystal thermography, hot-wire anemometry, cold-wire thermometry and smoke-flow visualisation. Particular attention is given to the selection and development of the experimental facilities and techniques. Validations of the jet impingement rig and computer controlled data acquisition and processing system are also presented.

A comparison between the measured flow field beneath axisymmetric impinging jets and theoretical solutions is provided in Chapter 4. It serves to validate the near wall flow field obtained experimentally and to identify regions of flow transition from laminar to turbulent.

Chapter 5 documents results from smoke flow visualisation for single impinging jet with, and without, crossflow. A detailed discussion on the developing flow regimes is included to facilitate understanding of the hydrodynamic and heat transfer characteristics of impinging jets in the following Chapters.

Experimental near wall results of single impinging jets with, and without, crossflow are presented and discussed in Chapter 6. Detailed hydrodynamic and thermal data are obtained for a wide range of jet parameters. Specifically, velocity, turbulence, temperature and fluctuating temperature characteristics are analysed and interpreted to establish a solid understanding of the near wall phenomena.

In Chapter 7, full surface heat transfer distributions are presented and related directly to the near wall hydrodynamic and thermal characteristics for improved understanding of jet impingement heat transfer. A brief summary of the main findings drawn from the experimental investigation is provided towards the end of the Chapter.

Finally, the conclusions drawn from this research programme are presented in Chapter 8. Optimum arrangements for impingement heat transfer involving crossflow are proposed herein. The practical significance of the study and recommendation for further work are also discussed.

CHAPTER 2
LITERATURE REVIEW

This Chapter provides a literature review on single impinging turbulent jets with, and without, crossflow. Both confined and unconfined jets discharging with either a uniform, or a fully developed, velocity profile have been considered due to the great attention received from an experimental viewpoint. Limited literature pertaining to laminar jet impingement has also been included, where relevant, particularly for comparison of heat transfer correlations and flow patterns within the stagnation region.

2.1 Description of the Flow Field

To aid subsequent presentation and discussion of experimental results, the physical geometry and flow structures under consideration are described. Figure 2.1 and 2.2 show the respective schematic diagrams of the geometric arrangements and flow fields of orthogonal single impinging confined jets with, and without, crossflow. For the latter arrangement it is common to regard the impinging jet as the primary flow and the crossflow as the secondary flow. Even though some fundamental differences exist between single impinging jets with, and without, crossflow, the flow structures are generally divided into three characteristic regions; the free jet region, the stagnation region and the wall jet region.

2.1.1 Free Jet Region

In the free jet region, the shear-driven interaction of the exiting jet and the ambient fluid produces entrainment of mass, momentum and energy. These lead to the development of a radial velocity profile, expansion of jet width, increased mass flow rate and change of jet temperature as it travels downstream. The free jet region can be further subdivided into three zones; the potential core zone, the developing zone and the fully developed zone, Viskanta (1993).

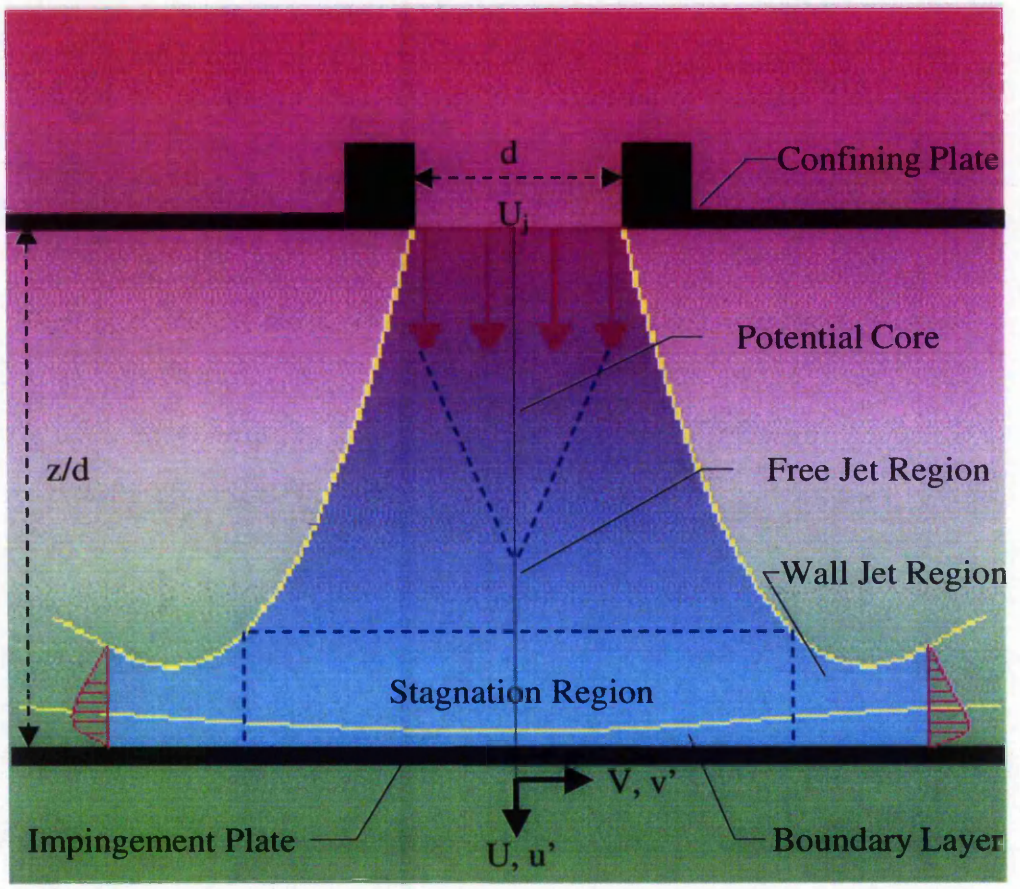

Figure 2.1: Schematic diagram of the flow field of single impinging jet without crossflow.

In the potential core zone the jet centreline velocity and the fluid properties remain constant and can be considered equal to the nozzle exit conditions. The shear interaction in the mixing region surrounding the potential core, however, generates turbulence that diffuses radially with downstream distance and eventually penetrates into the jet axis. The length of the potential core is primarily dependent on the initial velocity profile, the turbulence intensity and the degree of jet confinement. A common definition of the end of potential core is the point at which the centreline velocity $U_{CL} = 0.95U_j$, where U_j is the nozzle exit velocity, Jambunathan et al. (1992). The potential core length for axisymmetric round jets usually extends to about 6 to 7 diameters from the nozzle exit, e.g. Gauntner et al. (1970) and Livingood and Hrycak (1973).

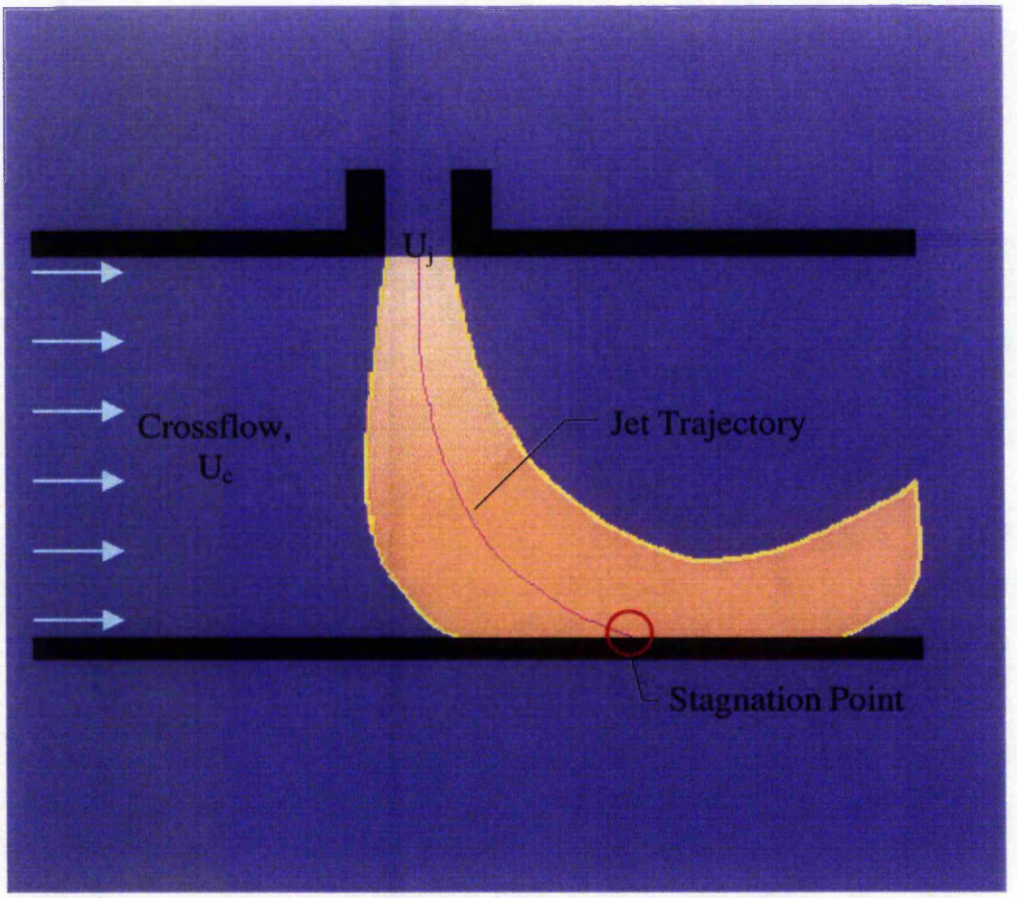

Figure 2.2: Schematic diagram of the flow field of single impinging jet with crossflow.

In the presence of a crossflow, the potential core is deflected downstream from the centre axis. The extent of the deflection is accentuated at larger nozzle-to-plate spacing and lower jet-to-crossflow velocity ratio, U_j/U_c, Sparrow et al. (1975). The velocity trajectory is often taken as the locus of the maximum velocity in the plane of symmetry, e.g. Kamotani (1974). The driving upstream crossflow also results in greater entrainment of fluid and large pressure differences across the jet, particularly at low nozzle-to-plate spacings ($z/d \leq 4$).

Beneath the potential core is the developing zone in which the jet axial velocity and the jet half-width (where $U = U_j/2$) decay linearly with downstream distances,

Schlichting (1968), and further generation of turbulence and entrainment of fluid occur. At greater axial distances from the nozzle exit the jet becomes fully developed and spreads linearly with a regular bell shape, which can best be described by a Gaussian distribution, Reichardt (1942).

2.1.2 Stagnation Region

When the impinging jet reaches the stagnation region, the axial velocity decreases rapidly with a corresponding rise in the static pressure. The thickness of the impingement region boundary layer is approximately constant, Martin (1977), having a radius of about 1.1d from the plate surface, Schrader (1961). The boundary layer thickness of a laminar flow can be predicted using the exact solution for stagnation in three-dimensional flow (Homann model), Popiel and Trass (1991). A significant favourable pressure gradient on the surface helps to stabilise the boundary layer flow and thus delay the transition to turbulent flow, Gardon and Akfirat (1965). The lateral limit of the stagnation region is taken as the location where the pressure gradient reaches zero, Polat (1993), which is approximately 1.4d from the jet axis for small nozzle-to-plate spacings $z/d \leq 5.5$. For a jet with crossflow the point of impingement is swept downstream. Hence, the characteristic of the stagnation region is strongly dependent on nozzle-to-plate spacing and jet-to-crossflow velocity ratio.

2.1.3 Wall Jet Region

Upon impingement in the stagnation region the bulk fluid deflects and accelerates radially outwards to develop into a wall jet along the target plate. The velocity profile in the immediate vicinity of the wall is typical of boundary layer flow, whilst the outer region exhibits features of a free turbulent jet, Polat (1993).

The wall jet shows superior heat transfer characteristics to parallel flow due to the higher turbulence level generated through flow transition and the convection of large-scale turbulence structures and vortices from the edge of the impinging jet. The wall jet

becomes extremely complex when an upstream crossflow is imposed. It is only when the primary impinging jet flow is dominating that a typical characteristic wall jet will form in the presence of crossflow.

2.2 Existing Literature

An extensive amount of research has been conducted which addresses the complex fluid flow and heat transfer phenomena of impinging jets. Button and Wilcock (1978), Button and Jambunathan (1989), Jambunathan and Button (1994) and Chan et al. (1999a and 1999b) provide comprehensive bibliographies of earlier works. Literature reviews of single and multiple turbulent impinging jets have also been published on a regular basis. For instance, Livingood and Hrycak (1973) summarised experimental heat transfer results obtained by Metzger (1962), Gardon and Akfirat (1965, 1966) and Cadek (1968). A subsequent review of single and arrays of slot jets as well as circular jets, which also includes analytical studies and correlation of Nusselt number, is detailed in Hrycak (1981). Downs and James (1987) focused primarily on circular jets and the effects of a wide range of experimental parameters. The configurations and parameters being investigated were tabulated, together with empirical correlations for heat transfer derived both experimentally and theorectically.

In another review of heat transfer data for single circular impinging jets, Jambunathan et al. (1992) derived a simple correlation which did not account for the significant effects of nozzle geometry, confinement, and the generation of turbulence upstream of the jet nozzle. A thorough review of heat transfer to impinging isothermal air and flame jets is provided by Viskanta (1993). The survey covered single and multiple turbulent round and slot jets and the effects of a wide range of parameters on the heat transfer process, including; turbulence, entrainment, geometric effects, jet outlet conditions, angle of attack and other external factors.

Literature pertaining to impinging jet with crossflow is relatively scarce due to its highly sophisticated nature. Sparrow et al. (1975) and Goldstein and Behbahani (1982)

investigated a small range of parametric effects of circular jets with, and without, crossflow on surface heat transfer. Longitudinal and transverse distributions of velocity and temperature for confined single turbulent jet impingement with crossflow was obtained by Kamotani (1974) and Catalano (1989a and 1989b), who compared numerical results with experimental data. A similar comparison for single and twin turbulent impinging jets, with a high jet-to-crossflow ratio (i.e. 30), is also found in Barata et al. (1991). The thermal mixing characteristics of a heated jet with crossflow are experimentally clarified by Andreopoulos (1983) and Nishiyama et al. (1990). Heat transfer characteristics for two-dimensional arrays of impinging jets with crossflow are provided by Metzger et al. (1979), Florschuetz (1981), and Huber and Viskanta (1994).

2.3 Heat Transfer Characteristics of Impinging Jets

2.3.1 Laminar Jet Impingement Heat Transfer

An impinging jet is considered laminar up to a Reynolds number of 1000, Vickers (1959) and McNaughton and Sinclair (1966). Most of the existing heat transfer data of laminar impinging jets have been obtained from either numerical or theoretical investigations. Heat transfer at the stagnation point of an impinging air jet is usually expressed in the form of:

$$Nu = C\,\mathrm{Re}^{n} \tag{2.1}$$

where the exponent, n, varies from as low as 0.23 to 0.67, depending on whether the jet exit velocity profile is uniform or parabolic, Polat et al. (1989). A theoretical solution for stagnation heat transfer, based on laminar boundary layer, was given by Silbukin (1952). It was demonstrated that the Nusselt number was a function of Reynolds number raised to the power 0.5. The stagnation heat transfer coefficient calculated by the laminar stagnation theory for a three-dimensional axisymmetric (circular) impinging jet, i.e. Schlichting (1968) can be expressed as:

$$Nu = 0.76\,\mathrm{Pr}^{0.4}\,\mathrm{Re}^{0.5} \tag{2.2}$$

The Nusselt number dependence of $Re^{0.5}$ was also derived by Sparrow and Lee (1975), who used a solution for the inviscid flow field as a boundary condition to resolve the viscous flow along the impingement surface, beneath a slot jet.

Saad et al. (1977) solved the full Navier-Stokes equations, using the finite-difference technique, to determine the heat transfer characteristics of a laminar round jet impinging orthogonally onto a flat surface for $1.5 \leq z/d \leq 12$ and $950 \leq Re \leq 1960$. It was concluded that the stagnation heat transfer, expressed in the terms of Nusselt number, was proportional to $Re^{0.5}$ for a uniform exit velocity profile. For the case of a parabolic jet exit velocity profile, the Nusselt number was found to be dependent on $Re^{0.36}$. The numerical results also showed that the heat transfer over the entire impingement plate was significantly higher for a fully developed parabolic impinging jet compared to that for a uniform jet. The experimental mass transfer results obtained by Scholts and Trass (1970) for a circular air jet with a parabolic exit velocity profile in the range $500 \leq Re \leq 1960$ did not deliver the 0.36 power dependent as described by Saad et al. (1977). Instead, the stagnation mass transfer was also shown to be a function of $Re^{0.5}$, corroborating with Silbukin's laminar boundary layer theory.

The substantial effect of jet exit velocity profile on the magnitude and the radial location of the maximum friction factor were confirmed by Jambunathan et al. (1989) through a parametric study using the semi-confined configurations. The stagnation point heat transfer obtained by Popiel et al. (1980) for nozzle-to-plate spacings of $2 \leq z/d \leq 20$ and Reynolds numbers of $1050 \leq Re \leq 1860$ suggests that Silbulkin's laminar boundary layer theory is valid up to $z/d \leq 5$. Once the jet is fully developed (at $z/d \geq 8$), the convective heat transfer is considerably augmented by the presence of strong free jet turbulence.

2.3.2 Turbulent Jet Impingement Heat Transfer

An impinging jet starts to become turbulent when the discharge Reynolds number exceeds 1000. Turbulent impinging jets play a more important role in industry due to their ability to yield higher convective heat transfer rates. According to Chamberlain (1966) and Yokobori (1979) (see Ashforth-Frost, 1994 and Ball, 1998), two different modes of heat transfer exist, depending on the nozzle-to-plate spacing. When the impingement surface lies within the potential core of the jet, the axial velocity is constant such that variations in heat transfer rate are caused by fine scale turbulent fluctuations. The stagnation flow is predominantly of laminar nature and the surface heat transfer can simply be expressed by Silbukin's (1952) laminar boundary layer theory. In the region beyond the apex of the potential core variations in both the turbulence and velocity affect the magnitude of heat transfer.

A detailed study of the influence of turbulence on circular jets was provided by Kataoka (1990). It was suggested that heat transfer is greatly affected by large-scale eddy structures, and the enhancement of stagnation heat transfer is mainly attributed to the turbulent surface renewal by large-scale eddies. Experimental results show that maximum stagnation point heat transfer occurs when the impingement plate is located at, or just beyond the apex of the potential core, where the turbulence peaks, Schlunder and Gnielinski (1967). This corresponds to nozzle-to-plate spacings in the range of 6 to 7 for circular jets, Livingood and Hrycak (1973). At further separation distance the increase in turbulence no longer compensates for the drastic fall in jet velocity, hence resulting in an overall decrease in heat transfer coefficients, Gardon and Akfirat (1965).

The presence of an upstream crossflow is known to produce varying impingement heat transfer characteristics, depending on the jet configurations and flow parameters. Sparrow et al. (1975) investigated impingement heat transfer for a turbulent impinging jet with crossflow for $3 \leq z/d \leq 12$ and jet-to-crossflow mass velocity ratio, $M = (\rho U)_j / (\rho U)_c$, of 4 to 12. For larger jet-to-crossflow mass velocity ratios, the maximum heat transfer coefficient was attained in the range of $5 \leq z/d \leq 6$. Whereas for a

smaller jet-to-crossflow mass velocity ratio (i.e. 4), the maximum heat transfer coefficient was obtained at a substantially smaller nozzle-to-plate spacing owing to the effect of jet deflection by the crossflow fluid. Crossflow diminishes the peak in heat transfer coefficient at large nozzle-to-plate spacing but can augment the peak in heat transfer coefficient at low nozzle-to-plate spacing, Goldstein and Behbahani (1982). Interaction with the crossflow reduces the impinging fluid velocity, promotes mixing of streams and incites the generation of secondary vortices. At low nozzle-to-plate spacings ($z/d \leq 4$), the increase in turbulence intensity (due to the mixing with crossflow) and the higher mainstream velocity may lead to enhanced average heat transfer.

In array jet configurations, the average surface heat transfer is highest when obtained with minimum crossflow, while intermediate and complete crossflow cause varying degree of degradation, Obot and Trabold (1987). It is generally found that crossflow spent fluid lowers average heat transfer coefficients as it collides and sweeps away the adjacent impinging jet, resulting in delayed and ineffectual impingement. Crossflow destroys the symmetry about the nozzle exit with a usual resulting increase in the downstream heat transfer and decrease in upstream heat transfer, Metzger and Korstad (1972). However, an increase in the overall impingement heat transfer was seen for $z/d <$ 2 due to the significant addition of convective fluid, Andrews and Hussein (1986). For practical interest, it is desirable to always ensure that the primary impinging jets are dominating the near wall flow field, Florschuetz et al. (1984). However, Whidden et al. (1992) postulated that the highest average heat transfer occurs when impinging jets and the crossflow influences act with near equal intensity. Hrycak (1981) commended that small nozzle-to plate spacings appear to result in higher heat transfer for array jets.

2.3.3 Heat Transfer Correlations

A comparison between theoretical and experimental heat transfer results for a laminar free impinging jet was provided by Donaldson et al. (1971). At the stagnation point, the heat transfer coefficient can be expressed as:

$$Nu = (0.5c\,\mathrm{Pr})^{0.5}\,\mathrm{Re}^{0.5} \tag{2.3}$$

where the local free jet half-radius, c, was taken as 1.13 for fully developed jets. The comparison also revealed that turbulent heat transfer rate is 1.4 to 2.2 times higher than the laminar rate. As the nozzle-to-plate spacing increases and the generation of turbulence in the mixing layer becomes more intense, the heat transfer coefficients match more closely. In addition, the influence of Reynolds number on the heat transfer ratio appeared to be small. Hence, the exponent of Reynolds number for the turbulent jet did not depart much from the 0.5 power determined for laminar flow. According to Gardon and Akfirat (1965), a large part of heat transfer data for single impinging jet could even be correlated very effectively without any separate parameter to characterise turbulence.

Hoogendoorn (1977) correlated turbulence, measured from the free jet at axial displacements equivalent to the nozzle-to-plate spacings, to stagnation heat transfer for $1 \leq z/d \leq 10$ and $\mathrm{Pr} = 0.7$ in the form:

$$\frac{Nu}{\mathrm{Re}^{0.5}} = 0.65 + 2.03\left(\frac{Tu\,\mathrm{Re}^{0.5}}{100}\right) - 2.46\left(\frac{Tu\,\mathrm{Re}^{0.5}}{100}\right)^2 \tag{2.4}$$

The correlation showed increased weight given to the exponent of Reynolds number (i.e. 0.5) as turbulence grows. The increase in turbulence, especially at large nozzle-to-plate spacings ($z/d \geq 7$), was also accounted for in the mass (heat) transfer correlations proposed by Popiel and Boguslawski (1986). The expressions for a contoured nozzle and sharp-edged orifice were given by:

$$Sh = (0.508 + 0.051z/d)\,\mathrm{Re}^{0.5}\,Sc^{0.4} \tag{2.5}$$

$$Sh = (0.7 + 0.086z/d)\,\mathrm{Re}^{0.5}\,Sc^{0.4} \tag{2.6}$$

which applied in the range $1.2 \leq z/d \leq 5.5$ and $1.2 \leq z/d \leq 4$ respectively and was valid for $6000 \leq \mathrm{Re} \leq 44\,000$. At larger nozzle-to-plate spacings ($z/d \geq 7$), turbulence generated in the mixing layer penetrated into the jet axis, giving correlations of:

$$Sh = 0.461\,\mathrm{Re}^{0.75}(z/d)^{-0.87}\,Sc^{0.4} \tag{2.7}$$

$$Sh = 0.551\,\mathrm{Re}^{0.75}(z/d)^{-0.87}\,Sc^{0.4} \tag{2.8}$$

for the contoured nozzle and sharp-edged orifice respectively. Gillespie et al. (1996), however, found that the stagnation heat transfer for impinging jets with both radiused entry and sharped-edged hole profiles was directly proportional to $\mathrm{Re}^{0.5}$. Hrycak (1983) measured stagnation heat transfer beneath an impinging jet discharging with a uniform velocity profile ($14\,000 \leq \mathrm{Re} \leq 67\,000$) which was expressed for $z/d \leq 7$ by:

$$Nu = 1.41\,\mathrm{Re}^{0.5}\,\mathrm{Pr}^{0.4}(z/d)^{0.16}(d/d_c)^{0.28} \tag{2.9}$$

and for the region beyond the potential core ($z/d \geq 7$) by:

$$Nu = 3.92\,\mathrm{Re}^{0.5}\,\mathrm{Pr}^{0.4}(z/d)^{-0.4}(d/d_c)^{0.39} \tag{2.10}$$

Empirical correlations have been developed to enable calculation of local heat transfer distributions. Smirnov et al. (1961) suggested a correlation for $0.5 \leq z/d \leq 10$, $1600 \leq \mathrm{Re} \leq 50\,000$ and $0.7 \leq z/d \leq 10$ of the form:

$$Nu = f(d, \mathrm{Re}, \mathrm{Pr}, z/d) \tag{2.11}$$

where the Reynolds number exponent was 0.33. Rao and Trass (1964) obtained a correlation for the local (mass) heat transfer beneath a turbulent jet ($25\,000 \leq \mathrm{Re} \leq 125\,000$) at $r/d > 4.5$:

$$Sh = 1.3\,\mathrm{Re}^{0.84}(r/d)^{-1.27} \tag{2.12}$$

The Reynolds number dependence of 0.84 represented the typical value for turbulent flows. Jambunathan et al. (1992) suggested that the simplest correlations for local heat transfer coefficient should be of the form:

$$Nu = f(\mathrm{Re}, z/d, r/d, \mathrm{Pr}) \tag{2.13}$$

The correlation, however, would not account for the significant effects of nozzle geometry, confinement, and the generation of turbulence upstream of the jet nozzle. Based on published experimental data, correlations for local heat transfer were obtained for single impinging jet in the form:

$$\frac{Nu}{\mathrm{Re}^{f(z/d,r/d)}} = f_1(z/d, r/d) \tag{2.14}$$

The expression assumed Nusselt number as a function of Reynolds number raised to an exponent which in turn depended on the nozzle-to-plate spacing and the radial distance from the stagnation point. However, a significant increase in the exponent was seen in the range $0.6 \leq r/d \leq 2.5$, owing to flow transition of the wall jet from laminar to turbulent. In the region $r/d \geq 4$, the local heat transfer became independent of nozzle-to-plate spacing mainly due to considerable loss of momentum of the wall jet at far downstream distances.

Gordon and Cobonpue (1962) correlated average heat transfer beneath a single impinging jet by the equation:

$$\overline{Nu} = 1.811\,\mathrm{Re}^{0.55}\,\mathrm{Pr}^{0.33}(z/d)^{-0.55}(R/d)^{-0.45} \tag{2.15}$$

which covers $z/d > 12$, $\mathrm{Re} > 2000$ and $0 < R/d < 12$. A similar expression was proposed by Goldstein et al. (1986) for an impinging jet discharging from a contoured nozzle:

$$\frac{\overline{Nu}}{\mathrm{Re}^{0.76}} = \frac{24 - |z/d - 7.75|}{533 + 44(R/d)^{1.394}} \tag{2.16}$$

The expression is valid for z/d ≥ 6 and 0.5 ≤ R/d ≤ 32 in the range 61 000 ≤ Re ≤ 124 000. Average heat transfer coefficient for an impinging jet was also correlated by Lytle and Webb (1991) for small nozzle-to-plate spacings (0.1 ≤ z/d ≤ 1) and 3600 ≤ Re ≤ 27 600 by the expression:

$$\overline{Nu} = 0.424\mathrm{Re}^{0.57}(z/d)^{-0.33} \tag{2.17}$$

A comprehensive empirical correlation for local heat transfer beneath a single impinging jet with crossflow has so far not been obtained due to its highly complex and unsymmetrical nature. Nonetheless, several average heat transfer correlations have been obtained for multiple impinging jets with crossflow. Metzger and Korstad (1972) studied experimentally the effects of crossflow on heat transfer characteristics of a single row of circular impinging air jets. A correlation for average heat transfer was presented with the use of the Reynolds number based on individual jet diameter:

$$\overline{St} = 0.0822M^{*-0.049}\,\mathrm{Re}^{-0.338} \tag{2.18}$$

the expression covered the ranges of independent parameters for -10 ≤ l/d ≤ 10, z/d = 2, 1 ≤ M^* ≤ 3, 2.5 ≤ c_n/d ≤ 5, 2000 ≤ Re_{es} ≤ 6000. Convective heat transfer from a flat surface to a row of impinging, submerged air jets formed by square-edged orifices having a length-to-diameter ratio of unity have been obtained by Obot and Trabold (1987). Viskanta (1993) subsequently correlated the local Nusselt numbers over the spanwise direction by the equation:

$$\frac{\overline{Nu}}{\mathrm{Re}^{0.7}} = \frac{2.9\exp\left[-0.09(x/d)^{1.4}\right]}{22.8 + (c_n/d)(z/d)^{1/2}} \tag{2.19}$$

The correlation is valid for $2 \leq z/d \leq 6$, $4 \leq c_n/d \leq 8$, $0 \leq x/d \leq 6$, $10\,000 \leq Re \leq 40\,000$.

2.3.4 Effects of Turbulence on Jet Impingement Heat Transfer

The prominent role of turbulence on the heat transfer characteristics of impinging jets has long been recognised, Kestin et al. (1961a and 1961b). Heat transfer enhancement due to turbulence can be described by the characteristics of the jet prior to impingement and the subsequent flow development at downstream distances. Gardon and Akfirat (1965) studied the influence of turbulence on both axisymmetric and two-dimensional jet impingement heat transfer. A turbulence promoter, in the form of a wire mesh screen, was inserted into the nozzle in order to artificially adjust the turbulence level at the jet exit between 2.5% and 18% for a constant Reynolds number of 11 000. The stagnation heat transfer coefficient was augmented as the turbulence level was increased; most noticeably for $z/d \leq 6$. The lateral variation in heat transfer rate was also affected. Hoogendoorn (1977) studied experimentally the effect of turbulence on stagnation heat transfer for air jets issuing from a contoured nozzle and straight pipe respectively. Both jet configurations showed an increasing Nusselt number in the stagnation region for $4 \leq z/d \leq 8$ due to growing turbulence level on the jet axis. Hrycak (1983) investigated the heat transfer characteristics of an axisymmetric jet discharging with a uniform velocity profile for $14\,000 \leq Re \leq 67\,000$. Maximum stagnation heat transfer was attained when the impingement surface was located at $z/d \approx 7$, where the highest levels of axial turbulence have been reported by Gardon and Akfirat (1965) and Schlunder and Gnielinski (1967). To promote the generation of turbulence, Ali Khan et al. (1982) placed a perforated plate just upstream of the target surface through which the stagnation heat transfer coefficient was augmented up to four-fold for small nozzle-to-plate spacings.

In the wall jet region, the influence of turbulence on surface heat transfer is manifested particularly as the flow develops from laminar into turbulent. The radial variation in surface heat transfer coefficient beneath an axisymmetric impinging air jet has been considered by Gardon and Cobonpue (1962) and Gardon and Akfirat (1965). For small nozzle-to-plate spacings ($z/d \leq 4$) and Reynolds numbers greater than 14 000, a

local minimum in heat transfer coefficient was observed at the stagnation point whilst two distinct maxima were reported at r/d ≈ 0.5 and r/d ≈ 1.9. Similar observations were made by Button and Wilcock (1982), Gillespie et al. (1996) and more recently by Meola et al. (2000). Several explanations were given on the formation of the two local maxima in heat transfer coefficient. Based on the theoretical work of Kezios (1956), Gardon and Akfirat (1965) associated the primary maximum in heat transfer to thinning of the boundary layer. Kataoka and Mizushina (1974) and Gillespie et al. (1996) attributed it to the convection of large-scale turbulence structure from the edge of the jet onto the laminar boundary layer. The secondary maximum in heat transfer coefficient has been linked to transition of the wall jet from laminar to turbulent flow which occurs in the region $1 \leq r/d \leq 2$, Gardon and Akfirat (1965). The influence of turbulence around the stagnation region was investigated by den Ouden and Hoogendoorn (1974), who found that the secondary maximum in heat transfer coefficient coincides with the maximum in the product of local turbulence level and the highest velocity in the boundary layer. Popiel and Trass (1982 and 1991) ascribed the contribution of wall eddies, induced by large-scale toroidal vortices impinging on the plate, to the enhancement of local momentum, mass and heat transfers. The ring-shaped wall eddies coalesced abruptly with the radially-diverging toroidal vortices (at $1 \leq r/d \leq 2$) while the flow developed into a turbulent radial wall jet.

The various effects of near wall flow characteristics have been correlated to surface heat transfer for a semi-confined axisymmetric impinging jet, Ashforth-Frost et al. (2001). For z/d = 2, the primary maximum in local heat transfer coefficient is ascribed to the impinging large-scale turbulence convected from the edge of the jet that leads to thinning and, transition of the wall jet from laminar to turbulent flow. The secondary maximum is linked to the continuous increase in turbulence level whilst the flow velocity in the vicinity of the wall (i.e. y/d = 0.005) remains constant. For nozzle-to-plate spacings greater than the potential core length of the jet ($z/d \geq 5.5$), the radial variation in heat transfer coefficient assumes a characteristic bell-shape profile where a maximum is located at the stagnation point with no discernible secondary maxima, Gardon and Cobonpue (1962). As the shear-generated turbulence diffuses towards the jet axis with increasing downstream distances, the jet is effectively turbulent on impact. Thus,

transition of the wall jet from laminar to turbulent flow does not occur. Ashforth-Frost et al. (2001), amongst others, have shown that the local maximum in heat transfer coefficient (for z/d = 6.5) coincides with a local peak in turbulence. As turbulence levels (both absolute and normalised) decline at downstream distances, local heat transfer coefficients decrease accordingly.

A secondary maximum in heat transfer, which coincides to that observed for single impinging jets at low nozzle-to-pate spacings ($z/d \leq 4$) , was reported for an array of slot jets by Whidden et al. (1992). This indicated that there is a close characteristic link between turbulent single and array impinging jets. Although the presence of a crossflow promotes turbulence through the mixing process, there is a considerable loss of jet momentum, which needs to be justified in order to achieve an overall increase in heat transfer coefficient. This is important particularly for larger nozzle-to-plate spacings ($z/d \geq 4$) when the momentum loss caused by the crossflow becomes significant.

2.3.5 Effects of Jet Outlet Conditions and Nozzle Geometry on Heat Transfer

Characterisation of jet outlet conditions is important for obtaining an insight into jet impingement heat transfer. According to Hollworth and Berry (1978), jet discharge stream conditions affect the flow field and are believed to account for much of the discrepancies between results of various investigators.

Nozzle geometry strongly affects the jet outlet conditions, which in turn influence the behaviour of the toroidal vortices around the jet circumference and the turbulence level generated in the shear mixing layer, Jambunathan et al. (1992). The turbulent behaviour also affects the mixing of the jet with ambient air and so the rate of velocity decay. All these suggest the considerable impact of nozzle design on local heat transfer coefficients.

Hoogendoorn (1977) highlighted the marked effects of nozzle geometry (i.e. contoured and orifice entry) on turbulence level and local heat transfer coefficient in the

stagnation region, particularly for smaller nozzle-to-plate spacings. The effects of nozzle inlet geometry and nozzle length to diameter ratio (l/d) on impingement heat transfer have been investigated experimentally by Obot et al. (1979). Five nozzle lengths were examined for a jet Reynolds number range of 15 000 to 60 000 and nozzle-to-plate spacings (z/d) of 2 to 12. The values of stagnation heat transfer coefficients for sharp-edged nozzle were found to be significantly higher than those for contoured nozzles. The discrepancies (caused by the different nozzle inlet geometry) were most pronounced for short nozzle, moderate for nozzles of 10 and 20 diameters long, but negligible for nozzles of 40 or more diameters long. Beyond z/d of 12, stagnation and average heat transfer coefficients become independent of nozzle inlet geometry and nozzle length.

Popiel and Boguslawski (1986 and 1988) studied the rate of local mass transfer in impinging single round jets discharging from a bell-shaped nozzle and sharp-edged orifice. Comparisons revealed that the contraction phenomenon at the entry of the sharp-edged orifice resulted in constantly higher mass transfer rates at all exit Reynolds numbers and nozzle-to-plate spacings considered. The latter study showed that typical area mean heat transfer due to an impinging jet discharging from a contoured nozzle is 25 percent lower than that from a sharp-edged orifice for z/d = 4, Re = 20 000 and r/d = 1. In contrast, Gillespie et al. (1996) reported that impingement heat transfer rates were clearly higher for a radiused entry and exit hole profile when compared to a sharp-edged orifice. The heat transfer enhancement was attributed to the broader jet that remained attached to the smooth radiused hole. Gundappa et al. (1989) compared the heat transfer and axial velocity characteristics of impinging jets discharging from orifices and pipes (l/d = 10). For z/d = 7.8, local heat transfer coefficients were higher for an impinging pipe jet at all radial positions. This was linked to the slower decay of axial velocity in the case of a jet discharging from a pipe.

The influence of semi-confinement on impingement heat transfer for single round uniform jets at 18 000 $\leq$ Re $\leq$ 80 000 and 2 $\leq$ z/d $\leq$ 16 was quantified by Obot et al. (1982). It was shown that the semi-confined geometries consistently degraded heat transfer rates although the heat transfer distributions were similar. The effect was most

significant at z/d = 2 where the semi-confinement effectively restricted the entrainment of and mixing with surrounding fluid. Beyond z/d = 12, the heat transfer was unaffected by the semi-confinement. Similar investigations were undertaken by Ashforth-Frost and Jambunathan (1994, 1996a), who studied the axial flow development and the stagnation point heat transfer of semi-confined and unconfined flat and fully developed jets. Comparison showed that the fully developed jet had a longer potential core and provided slightly higher heat transfer than the flat jet at the optimal nozzle-to-plate spacing. The different potential core lengths and heat transfer coefficients were attributed to the variation in turbulent behaviour resulted from altering the degree of confinement.

2.4 Flow Visualisation

Flow visualisation is a popular aid for physical understanding of the fluid flow and heat transfer phenomena of impinging jets. Popiel and Trass (1991) employed the smoke-wire flow visualisation technique to silhouette free and impinging round axisymmetric jets for nozzle-to-plate spacings of 1.2d and 2d and $3500 \leq Re \leq 20\,000$. It was found that the development of large-scale toroidal vortex structures around the circumference of the jet considerably enhanced the entrainment rate and mixing processes. The impinging vortex structures also induced ring-shaped wall eddies which were said to account for additional enhancement of local momentum and heat or mass transfer.

Smoke-wire visualisation was also used by Cornaro et al. (1999) to correlate the formation of regular vortex structures of free and impinging round jets to local velocity and turbulence intensity measurements. Large vortex structures emerged consistently when the turbulence intensity in the shear layer at the jet edge fell to below 10% but disappeared when the turbulence intensity exceeded 14%. It was therefore concluded that a low turbulence intensity in the shear layer at the jet edge promotes the development of regular large vortex structures. Popiel and Trass (1991), however, emphasised that regular vortex structures could only exist in a jet issuing from a bell-shaped convergent nozzle, having an essentially uniform exit velocity profile and low turbulence.

Yokobori et al. (1979) adopted the hydrogen bubble and dye-injection techniques to visualise the flow field of a round water jet issuing at $1000 \leq Re \leq 67\,000$ and $2 \leq z/d \leq 12$. In the potential core region ($z/d \leq 4$), the jet was essentially a laminar-like pulsating flow with fine scale circumferential turbulence imposed. Beyond $z/d \geq 4$, however, the stagnation flow field is increasingly trembled by the large-scale turbulence, causing a significant increase in the heat transfer rate. In addition, the instantaneous stagnation point of the jet started to fluctuate about the geometrical stagnation point, a phenomenon also observed by Popiel and Trass (1991) for an air jet.

The structure of counter-rotating vortex pairs of a impinging round jet with crossflow was visualised by Kim and Park (2000) using laser tomography. The impinging jet was seeded with aerosols and illuminated by a thin laser sheet in order to visualise the interface with the crossflow for Re = 1050 and a jet-to-crossflow velocity ratio of 3.3. It was shown that the counter-rotating vortex pair was initiated from the quasi-steady hanging vortices originated near the lateral edges of the jet column.

2.5 Theoretical Models of Stagnation Flow and Heat Transfer

Turbulent impinging jets serve as an excellent reference for the development and validation of turbulence models for recirculating flow, Cooper et al. (1993). To date, several theoretical models have been made available to predict the stagnation flow and heat transfer characteristics of impinging jets, e.g. Schlichting (1968). However, all the models built are only valid for axisymmetrical single impinging jets without crossflow.

Solutions of the Navier-Stokes equations for laminar stagnation flow have been obtained for both two-dimensional (slot) and three-dimensional (axisymmetric) impinging jets in the form of Hiemenz and Homann flows respectively. Hrycak (1981) developed an expression for stagnation heat transfer of impinging round jets based on laminar theoretical solution of stagnation flow, e.g. Froessling (1940), and experimentally derived parameters.

According to Popiel and Trass (1991), the flow field at the stagnation point of an axisymmetric impinging round jet is very close to Homann's analogy (1936) at low nozzle-to-plate spacings. Further downstream from the stagnation region the radial flow and heat transfer phenomena become very complex and cannot be predicted with existing theoretical models. Beltaos and Rajaratnam (1977) analysed the growth of an impinging jet issuing at $30\,000 \leq Re \leq 54\,000$ and $2.21 \leq z/d \leq 5.17$ from the stagnation point to the wall jet region. The stagnation flow solution was found valid only in a very small region of about $-0.14 \leq r/d \leq 0.14$ surrounding the stagnation point.

Theoretical models of stagnation flow and heat transfer are also useful for the validation of an experimental data set, besides helping to identify regions of flow transformations (e.g. laminar to turbulent transition) beyond which the flow becomes unpredictable.

2.6 Concluding Remarks

A comprehensive review of turbulent impinging jets with, and without, crossflow has been provided. Descriptions of the physical geometry and flow field under consideration have been included to facilitate the discussion of the results. Heat transfer characteristics of single impinging jets with, and without, crossflow have been discussed. The most pertinent empirical correlations for heat transfer have also been presented for both laminar and turbulent jets to assist in comparison of results. The influences of turbulence, outlet conditions and nozzle geometry on jet impingement heat transfer have been highlighted. Flow visualisation studies have also been cited for single impinging jets with, and without, crossflow. Finally, a summary of the theoretical models for prediction of stagnation flow and heat transfer characteristics for axisymmetric impinging jet has been given.

It is apparent from the literature review, e.g. Cooper et al. (1993) and Ashforth-Frost (1994), that heat transfer due to single impinging jets without crossflow is

dominated by the near wall hydrodynamic characteristics, in particular the near wall turbulence. Viskanta (1993) also highlighted the prominent role of hydrodynamic and thermal boundary interaction on local heat transfer in the stagnation and wall jet regions beneath single impinging jets with crossflow.

The interaction between a single impinging jet and upstream crossflow produces a completely different fluid flow and heat transfer phenomena, which vary largely with the jet configurations and flow parameters. The near wall flow and heat transfer distributions become so complex that no theoretical model has been established with satisfactory accuracy. There is also a paucity of information on impinging jets with crossflow, despite the fact that almost all impingement situations involve crossflow.

The sophisticated flow and heat transfer phenomena of array impinging jets with crossflow, particularly at low nozzle-to-plate spacings, require further systematic investigation. The close characteristic link between single and array impinging jets, as shown by Whidden et al. (1992), reinforces the basis for the reduction of the task to that of a single impinging jet for simplicity and clarity. Only when the behaviour of the horseshoe vortex due to the jet interaction with upstream crossflow is resolved will the efficiency of array jet impingement be maximised. This can be accomplished through a well-executed experimental programme combined with state-of-the-art measurement techniques.

CHAPTER 3
EXPERIMENTAL INVESTIGATION

This Chapter explains in detail the development and validation of the experimental arrangements and measurement techniques. The design of the jet impingement facility is described with an evaluation of its stability performance. In-depth analysis, conducted throughout the initial design phase, has been included with particular attention given to the heat transfer measurement techniques and procedures.

The calibration methods and data reduction techniques for liquid crystal thermography, hot-wire anemometry, cold-wire thermometry are presented. The uncertainties associated with the data acquisition and reduction techniques have been determined and discussed. Finally, the experimental method adopted for the smoke-flow visualisation study is described.

3.1 Design of Jet Impingement Facility

The following section details the experimental facility for jet impingement with, and without, crossflow. An isometric diagram of the jet facility is shown in Figure 3.1. The rig consisted of an impingement wind tunnel with a mesh heater, a channel working section and a purpose-built crossflow wind tunnel.

The impingement wind tunnel was developed from an existing facility designed and commissioned by Whitney (1996) and Ball (1998). The major components of this wind tunnel were; a centrifugal fan, flexible sleeve, horizontal diffuser, vertical diffuser, honeycomb holder, settling chamber, heater mesh, nozzle adaptor and a nozzle contraction. All components, with exception of the fan, flexible sleeve, heater mesh and contraction, were fabricated in 16 gauge mild steel plate. The centrifugal fan, supplied by Kiloheat Ltd (model no. SEAe-01-280-4), was cased in galvanised steel and fitted with a direct drive motor (Claude Lyons Ltd. type Regulac RK8-M) capable of 0 - 100 % speed control facilitated by a variable transformer. It enabled a pressure rise of 425 N/m^2 to be

produced at the maximum required flow rate of 0.15 m^3/s. This fan was mounted on a support frame, via a set of rubber dampers, and connected to the diffuser with a flexible sleeve that minimised vibration from the fan to the wind tunnel.

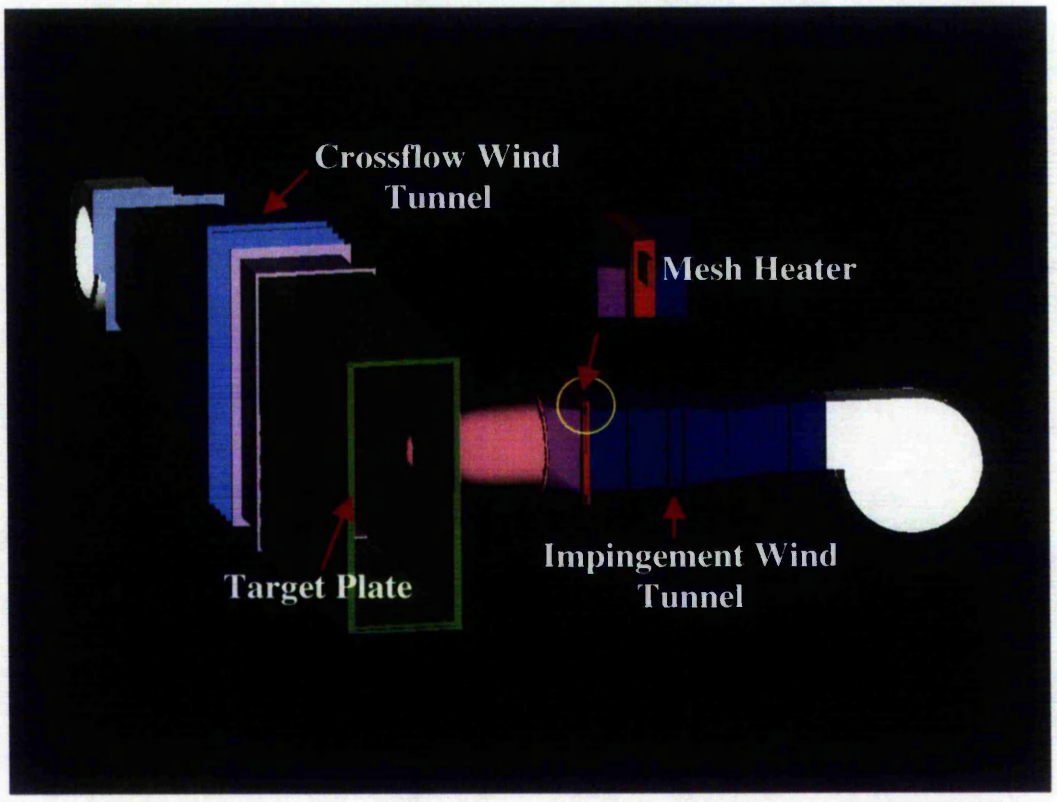

Figure 3.1: Isometric diagram of the experimental jet facility.

The diffuser section, immediately downstream of the fan, consisted of two chambers; one expanding in the horizontal direction and the other expanding vertically. A total expansion angle of 18.6° in the horizontal plane is characterised as a 'wide-angle' diffuser by Mehta (1977) due to the rapid increase in the cross-sectional area, such that separation can only be avoided by using boundary layer control. To suppress separation, curved mesh screens were carefully installed at the entrance to the diffuser chambers with the screens being curved in the plane of expansion. Flow leaving the wide-angle diffuser was effectively straightened through an aluminium honeycomb that reduced the transverse and swirl velocity components. The honeycomb section was 40 mm in length

and hexagonal in nature with a cell size of 5 mm across flats. A small aperture mesh screen, with a wire diameter of 0.22 mm and open area ratio of 0.745, was installed downstream of the honeycomb in order to remove large scale turbulent structures still present in the flow. Two additional mesh screens were introduced into the air stream to further reduce the level of turbulence in the settling chamber. According to Mehta (1977), the full benefits of a multiple screen combination are only experienced when the distance between successive screens is set to at least 500 times the wire diameter, i.e. approximately 110 mm for the present case. This ensures that the turbulence in the wire wakes of one screen decay before the successive screen is reached.

A planar heater mesh, similar to that described in Gillespie et al. (1995), was mounted upstream of the nozzle adaptor for initiating thermal transient flow. It comprised a fine mesh of 40 μm diameter stainless steel wires in a woven arrangement yielding 38% open area. The mesh, soldered to two conductive copper bars at the top and bottom ends, was held taut by using two Perspex frames clamped to one another. Heat was supplied to the mesh by a three-phase AC power unit (Merlin 210), via the copper bars. The copper bars were encased in a Perspex enclosure for protection from electrical shock. The heater provided excellent temporal response and uniformity of the jet temperature to within 0.2°C over the entire cross section. An interchangeable mesh screen with coarser wire, also fitted on a Perspex frame, was used to replace the heater mesh for smoke flow visualisation study. A flow adaptor was attached to the heater mesh to transform the rectangular wind tunnel cross-section into a 250 mm diameter circular orifice from which a three-dimensional contraction to the jet was designed. The optimal contraction profile was calculated with the aid of a BBC computer programme as described by Button and Tura (1984), based on known inlet and outlet dimensions, for various lengths. The profile for the eventual contraction ratio of 2.5 : 1 was curved so as to prevent boundary separation which can be induced in the presence of adverse pressure gradient, especially on the walls, at each end of the contraction. To minimise heat loss to the surroundings, both the flow adaptor and nozzle contractor were thermally insulated on the outer surfaces using Polyethylene foams.

The channel working section was designed to simulate engine representative geometries, e.g. turbine guide vane cooling. It was constructed from 20 mm clear Perspex sheet with operational dimensions of 300 mm x 800 mm x 1200 mm, which corresponded to normalised dimensions of z/d = 1 to 3 (variable), x/d = ±4 and r/d = ±6. The upper confinement plate formed an integral part of the nozzle exit and was mounted flush with the end of the contraction, parallel to the target impingement plate. The target plate was secured in position and accurately located via sliding slots on the side confinement plates. The verticality and the horizontality of the upper confinement and target impingement plates were ensured by spirit level measurements. The left end of the Perspex working section was connected to the outlet of the crossflow wind tunnel.

The crossflow wind tunnel was designed and fabricated according to the specifications of Mehta (1977). The major components of this wind tunnel were; a centrifugal fan, flexible sleeve, horizontal diffuser, vertical diffuser and a settling chamber. All components were fabricated using the same materials as that for the impingement wind tunnel. The centrifugal fan, also supplied by Kiloheat Ltd (model no. SEAe-11-280-4) and facilitated by a variable speed control transformer, was capable of producing a pressure rise of 500 N/m^2 at a maximum flow rate of 0.5 m^3/s.

The diffuser section consisted of two chambers; one expanding in the horizontal direction and the other expanding vertically, forming a 'wide-angle' diffuser with a total expansion angle of 18.3°. Mesh screens were also installed at the entrance to the diffuser chambers with the screens being curved in the plane of expansion. Flow leaving the wide-angle diffuser was monitored through an aluminium honeycomb that reduced the transverse and swirl velocity components, and a series of mesh screens that further suppressed turbulence and flow separation. The outlet of the settling chamber was mounted with the inlet to the Perspex working section via a rubber damper that helped to minimise vibrations.

Photographs of the wind tunnel facility and associated equipment are shown in Figure 3.2.

Figure 3.2: Photographs of the wind tunnels facility and ancillary equipment.

3.1.1 Wind Tunnel Stability

The stability of the air jet issuing from the impingement wind tunnel was verified from readings of velocity, turbulence and temperature over continuous four-hour

operating intervals. The wind tunnel was set for a two-hour initial warm up period before the jet exit centreline characteristics were measured using a special dual hot/cold-wire probe. Figure 3.3 shows that all the parameters were steady over long periods. Specifically, variation in the exit centreline velocity, U_{CL}, and turbulence, u', were limited to 2 % ad 6 % respectively. The jet exit temperature, T_j, also remained constant to within 1 %.

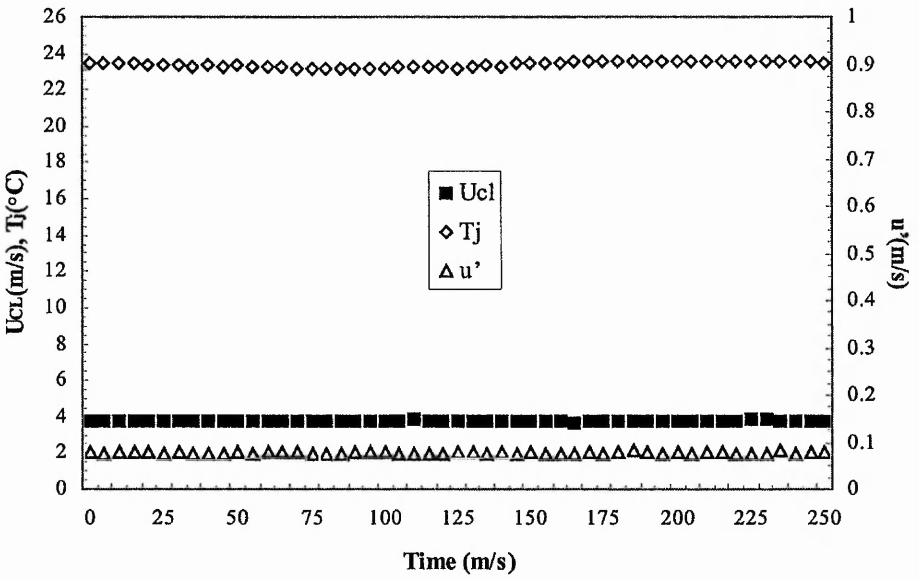

Figure 3.3: Wind tunnel stability.

3.2 Heat Transfer Investigation

3.2.1 Thermochromic Liquid Crystals

Liquid crystal thermography (LCT) offers an accurate and convenient means of measuring high-density full surface temperature and heat transfer distributions. Liquid crystals display colours by reflecting incident white light; the specific wavelength is dependent on temperature. At lower temperatures within a liquid crystal bandwidth a longer wavelength is transmitted, resulting in red colour. As the temperature rises the transmitted wavelength decreases through the spectrum, ending at blue. The colour

change of liquid crystals is both reversible and repeatable and the favourable properties are utilised for measurements of temperature and local heat transfer coefficients.

General descriptions, including the application of liquid crystals in heat transfer and fluid flow studies, have been provided by Jones (1991), Ashforth-Frost (1994) and Ireland et al. (1999). Liquid crystals are categorised, according to their molecular structure, into three groups; smectic, nematic and cholesteric. Fergason (1964) highlighted the most attractive optical characteristic of cholesteric structure is their colour change with temperature. Due to the high sensitivity of colour change with temperature, the cholesteric liquid crystals are also called thermochromic liquid crystals (TLCs). Nematic liquid crystals can be made to become cholesteric by adding with a chiral group, Jones et al. (1992), forming chiral nematic liquid crystals. Liquid crystals are organic compounds that degrade when exposed to chemical contamination and to ultraviolet UV light, Baughn (1995). This degradation can be reduced and stability increased by micro-encapsulation; a process that encloses liquid crystals in polymer spheres which can be as small as a few microns. The encapsulation of the material provides mechanical and chemical influences and allows its use as a thermometer, Ireland et al. (2000). In typical liquid crystal experiments, a single narrow band liquid crystal is all that is necessary to determine the heat transfer coefficient, h.

The present study employed two narrow-band micro-encapsulated chiral nematic liquid crystals type BM/R25C1W/C17-10 and BM/R30C1W/C17-10 manufactured by Hallcrest Ltd. The first code indicates a claimed red start temperature of 25°C and a bandwidth, across which a full colour spectrum is displayed, of 1°C. Likewise the second code indicates a red start temperature of 30°C and a bandwidth of 1°C. The specified temperature tolerance for the liquid crystals, which depends on the coating thickness, surface texture and application conditions, is ± 0.5°C. In order to maximise accuracy of the heat transfer measurements the liquid crystals were calibrated in-situ. The liquid crystal colour play on the jet target impingement surface was captured by a CCD camera onto a video tape. The data was subsequently digitised to yield the temperature history of

the model surface. Further data reduction to determine adiabatic wall temperature and local heat transfer coefficients is performed numerically.

3.2.2 Double-crystal Measurement Method

A typical heat transfer experiment requires the knowledge of the initial surface temperature, T_0, at all points. In experiments which start with the model at room temperature, care has to be taken to ensure that the model temperature is initially uniform. For this reason the double crystal method was introduced by Ireland and Jones (1987) to enable heat transfer coefficient, h, to be calculated without the need to measure the local initial temperature. A solution procedure that is equivalent to writing the equation for surface temperature at each measurement position twice can be adopted, Ireland and Jones (2000):

$$T_1 = T_0 + f(h, t_1, T_{aw}) \tag{3.1}$$

$$T_2 = T_0 + f(h, t_2, T_{aw}) \tag{3.2}$$

where T_1 and T_2 represent the event temperatures of the first and second crystals respectively, t_1 and t_2 are the times from initialisation to crystal colour change for the first and second crystals, and T_{aw} is the adiabatic wall temperature. The simultaneous equations are usually solved numerically for the unknown initial temperature and the heat transfer coefficient. This method recognises that if the time ratio of the two crystals passing over a given location, t_2/t_1, varies over the model it must do so smoothly in accordance with the variation of T_0. Based on this knowledge a more accurate value of h can, therefore, be determined. Ireland and Jones (1987) performed a comprehensive error analysis on this double-crystal method and demonstrated the importance of the choice of the starting and liquid crystal colour change temperatures. For maximum accuracy it was recommended that T_1 and T_2 should be close to each other to minimise the errors due to

the gas temperature errors, whilst the non-dimensional temperatures of the first crystal, θ_1, and second crystal, θ_2, must be well separated.

3.2.3 Selection of Heat Transfer Measurement Technique

The selection of an appropriate surface temperature measurement technique was essential for experimental study of jet impingement heat transfer. There are, in general, two different approaches to measure local heat transfer coefficients using liquid crystals as thermal indicators.

The first is the steady-state technique, which requires the experimental conditions to be maintained during the course of the test, most commonly, by imposing a constant heat flux boundary condition. The test surface is often heated electrically with the thermal indicator (i.e. liquid crystals) placed on top and subjected to a flow field. For this reason the steady-state technique is often referred to as heated-coating method. The three common types of heating elements are graphite impregnated paper, vapour or vacuum-deposited gold on polycarbonate, and thin stainless steel foil. To measure local surface heat transfer, the input power to the heating element is increased until the liquid crystal transmits a pre-calibrated colour at the desired measurement position. The local heat transfer coefficient, h, is calculated based on energy balance on the heating element:

$$h = \frac{Q}{A(T_w - T_j)} \tag{3.3}$$

where A and Q represent the area and input power to the heating element respectively, T_w is the heated wall temperature and T_j is the jet temperature. This technique has been used by many workers e.g. Simonich and Moffat (1982), Hippensteele (1981) and Kasagi (1981). Since it demands uniform heating of the test surface, the relative rigidity of the heating elements has restricted the application of this technique to only uniform surfaces.

The second is the transient technique where heat transfer coefficients are deduced from the thermal response of the test surface subjected to a sudden temperature change of the local steady fluid flow, within an elapsed time. This transient inverse way of temperature measurement using liquid crystals was pioneered by Ireland and Jones (1985 and 1986). The primary requirement of the technique is that the test specimen, coated with liquid crystal, be swiftly introduced to a uniform, quantifiable, heated flow field. The rate of the heating test specimen is recorded by monitoring the colour change in the liquid crystal with respect to time. The duration of a transient experiment must be sufficiently short that the thermal pulse is not affected by the thermal boundary conditions at remote surfaces of the specimen. By using a specimen having constant material properties and low thermal conductivity, a semi-infinite boundary condition can be used to relate the surface temperature to the fluid temperature and unknown heat transfer coefficient. A summary of five common analytical solutions that quantify changes in surface temperature to the fluid temperature can be found in Ireland and Jones (2000). For accurate measurement, the transient technique usually requires a uniformly heated flow field that can be achieved in a thermal wind tunnel.

While the steady-state technique approximates a constant heat flux surface, the transient technique more closely resembles a constant temperature surface, Moffat (1990). The difference in the boundary conditions is known to have a large effect on the magnitude of heat transfer coefficients, most notably in laminar flow. A comparison of the steady-state and transient methods was performed by Baughn et al. (1989) for calculation of local heat transfer coefficients on a pin fin. The two methods compared well near the centre stagnation point of the pin fin where the difference in the thermal boundary condition has negligible effect. The results in other regions were close but somewhat different. According to Moffat (1990), the steady-state technique, which applies a uniform heat flux boundary condition, will yield higher heat transfer coefficients than would tests conducted with a uniform wall temperature boundary condition. The difference is small in turbulent flows, about 7 %, but can approach 50 % in laminar flow. Arguably, the two techniques reviewed herein could be utilised for the present investigation provided the thermal boundary condition is specified appropriately. The

main restriction, however, lies in the requirement of the steady-state technique for a complex uniform electric heater on the surface.

Valencia et al. (1995) (see Ireland and Jones, 2000) numerically assessed the influence of lateral heat conduction on heat transfer experiments and concluded that transient experiments were less prone to error than steady-state experiments. Ball (1998) evaluated the two different experimental techniques, using the procedure detailed in Kline and McClintock (1953), Moffat (1985) and Coleman and Steele (1989), for surface heat transfer measurement beneath single impinging jets. The transient technique, which assumes a constant temperature boundary condition, Baughn (1995), yielded lower level of uncertainty when the heat transfer coefficient is below 60 W/m^2K. Based on previous works, Ashforth-Frost et al. (1996, 1997), Whitney (1996), the maximum level of heat transfer coefficient was estimated to be less than 50 W/m^2K. The transient technique was, therefore, selected due to its relative simplicity in establishment and lower experimental uncertainty in the operating domain of the present experiments.

3.2.4 Establishment of Thermal Transient

A number of methods have been used to establish the temperature difference between the fluid and the test model starting temperature to drive the heat transfer process. Clifford et al. (1983) employed large electrical heaters that took time to stabilise at the required temperature for heat transfer study within gas turbine cooling passages. Plumbing was used to allow the flow to by-pass the test section during the heating up period. Once a steady temperature was reached, fast acting valves were released to initiate the heat transfer experiment. Similarly, Kim and Metzger (1995) used a uniform temperature wall and suddenly discharged the heated air to the test section using a diverter valve. Rapid-withdrawing shutters have also been used to isolate the preheated (or pre-cooled) models from the major flow until the test is initiated, Martinez-Botas et al. (1995).

Jones and Hippensteele (1987) used in-situ heating of a wind tunnel wall before initiating the flow using a diverter door. Multiple liquid crystal coatings were applied onto on the model surface to reduce the dependence of the results on the initial wall temperature distribution. Camci et al. (1991b) preheated the walls of their transition duct test section before initiating an ambient temperature airflow using a pneumatically controlled diverter door. Other approaches include rapid insertion or exposure of preheated models in the test sections. Yan et al. (1992) and Ball (1998) preheated their Styrofoam protected test plates in ovens before securing them in position beneath ambient air jets. The Styrofoams were then suddenly removed and the thermal response of the liquid crystal coated surfaces recorded. Butler and Baughn (1995) introduced a variation of transient heating method referred to as shroud–heating. In this method a model is preheated inside a removable shroud to a uniform and constant temperature before suddenly exposed to an ambient temperature flow by ejecting the shroud.

Gillespie et al. (1995) invented a fine electrical heater that has greatly simplified the establishment of the thermal transient for heat transfer experiments. The mesh heater, which spans the duct and changes the flow temperature over a very short downstream distance, eliminates the use of complex fast-acting valves and model positioning activators. The high convective efficiency of the mesh heater enables a rapid flow temperature rise to be achieved with minimal time and effort. The system has been successfully applied in many other studies, including for turbine blade cooling systems e.g. Wang et al. (1998), and for film cooling system, Allen (1996). This flow heating method has been adopted in the present investigation and will therefore be explained in greater detail.

3.2.5 Concept of the Mesh Heater

The construction of the mesh heater is relatively simple and is described in Section 3.1. The mesh convective efficiency, which is a function of the air speed, is defined as:

$$\eta = \frac{T_{down} - T_{up}}{T_{mesh} - T_{up}} \tag{3.4}$$

where T_{mesh}, T_{up} and T_{down} represent the temperature of the wire mesh, and flow temperature upstream and downstream of the heater respectively. A typical value of η is approximately 0.55. This means that the wire mesh overheat can be modest and problems associated with the hot mesh wires in the wind tunnel are avoided, Ireland et al. (1999). The mesh heater was manufactured to deliver uniform downstream flow temperature needed for transient heat transfer experiments.

Gillespie et al. (1995) characterised the performance of the planar mesh heaters through a combination of theory and experiments. It was found that using a smaller wire diameter (i.e. 40μm) improved the convective efficiency and the dissipation of turbulence produced by the mesh heater. In situation where pressure loss caused by the heater needs to be minimised, the mesh area is kept large and the flow contracted downstream, Neely et al. (1998). The mesh heater exhibits negligible heat losses through radiation and conduction such that all the supplied electrical power is effectively converted into convective heat. For a known power level the average temperature rise generated by the heater can be expressed as:

$$T_{down} - T_{up} = \frac{IV}{\dot{m}c_p} \tag{3.5}$$

where I and V represent the input current and voltage respectively, $\dot{m}$ is the mass flow rate and c_p is the specific heat at constant pressure. The agreement between the calculated and the measured temperatures has been validated by Tsang and Ireland (1998).

The transient experiment is initiated when power is switched to the mesh. However, the step change in power supplied does not cause the flow temperature to

change as a step. Gillespie et al. (1996) has shown that the fluid temperature changes exponentially, giving a time constant which can be expressed as:

$$\tau = \frac{0.111}{U_{mesh}^{0.914}} \tag{3.6}$$

where U_{mesh} is the air velocity through the mesh heater which is written as:

$$U_{mesh} = \frac{\dot{m}}{\rho A_{mesh}} \tag{3.7}$$

The mass flow rate, $\dot{m}$, is determined from the pressure drop across the contraction, the density, ρ, is calculated using the equation of state at the heated gas temperature and atmospheric pressure. The mesh area, A_{mesh}, corresponds to the cross-sectional area of the plenum. The time constant in Eqn. 3.6 must be added to the time taken for the air to travel from the heater to the target surface which is given by:

$$\tau_t = \frac{V}{(\dot{m}/\rho)} \tag{3.8}$$

where V is the total inner volume of the wind tunnel sections downstream of the heater mesh.

3.2.6 Transient Conduction in a Semi-infinite Solid

The transient technique involves a sudden onset of steady flow and recording of surface temperature response, as indicated by a liquid crystal colour play. The fundamentals of the transient liquid crystal technique and the data reduction process have been detailed by Ireland and Jones (1985, 1986). When a solid, initially uniform in temperature, is suddenly subjected to flow at another temperature, the subsequent variation of surface temperature with time can be used to calculate the local heat transfer coefficients based on the one-dimensional transient conduction equation. The semi-

infinite description is appropriate as long as the transient temperature penetration does not exceed the thickness of the model material during the course of the test. This requires the use of a material which has constant properties and a low enough thermal conductivity so that the effect of lateral conduction is negligible. Yan et al. (1992) performed a two-dimensional numerical unsteady heat conduction analysis for their Plexiglass target plate with the measured radial Nusselt number distribution (assuming one-dimensional conduction) beneath an air jet as the boundary condition. They compared the surface response for the two-dimensional case with that using the one-dimensional assumption and concluded that two-dimensional effects were completely negligible.

A guideline for deciding the minimum thickness of the test specimen, x, was written by Schultz and Jones (1973) and is given below:

$$x > 4\sqrt{\alpha t} \tag{3.9}$$

Numerical and analytical techniques can be used to solve the one-dimensional transient conduction equation:

$$\frac{\partial T}{\partial t} = \alpha \frac{\partial^2 T}{\partial x^2} \tag{3.10}$$

where the temperature, T, is a function of distance from the surface, x, and time, t, or expressed mathematically $T = T(x,t)$. When a test surface is subjected to a fluid flow of temperature, T_j, and a convective heat transfer coefficient of, h, a single initial condition and two boundary conditions can be specified:

Initial condition:

$$T(x,0) = T_0 \tag{3.11}$$

This means that the entire semi-infinite solid is at a uniform temperature, T_0, at the initial time of $t = 0$. One of the boundary conditions states that the material temperature at a large distance from the surface never changes with time:

$$T(\infty, t) = T_0 \tag{3.12}$$

The heat flux at the surface is given by:

$$q = h\left[T_j - T(0,t)\right] = -k\left(\frac{\partial T}{\partial x}\right)_{x=0} \tag{3.13}$$

The one-dimensional transient conduction solution to Eqn. 3.10, subject to the initial condition (Eqn. 3.11) and the two boundary conditions (Eqn. 3.12) and (Eqn. 3.13), is given in Schneider (1955) (see Kreith and Black, 1980). Under a normal step change in fluid temperature and a uniform initial temperature the thermal transient at the model surface is governed by:

$$\frac{T(0,t) - T_0}{T_j - T_0} = 1 - e^{\eta} erfc\sqrt{\eta} \tag{3.14}$$

where

$$\eta = \frac{h^2 \alpha t}{k^2} = \frac{h^2 t}{\rho c k} \tag{3.15}$$

ρ, c and k represent the model density, specific heat and thermal conductivity. The exact values of the Gauss error function, *erfc*, have been tabulated by Kreith and Black (1980).

The above solution was modified by Gillespie (1996) for transient heating using the mesh heater (described in Section 3.2.5) that produces an exponential fluid

temperature rise with an asymptote of T_j and time constant τ. The modified solution used the adiabatic wall temperature, T_{aw}, in place of the jet temperature (further details in Section 3.2.7). The response of the surface temperature, $T(0,t) = T_s$, under a driving fluid temperature which changes exponentially with time is given by:

$$\frac{T_s - T_0}{T_{aw} - T_0} = 1 - \frac{\rho ck / h^2\tau}{\left(1 + (\rho ck / h^2\tau)\right)} e^{h^2 t / \rho ck} erfc\left(\frac{h\sqrt{t}}{(\rho ck)^{1/2}}\right)$$
$$- e^{-t/\tau} \frac{1}{1 + (\rho ck / h^2\tau)} \left\{1 + \frac{(\rho ck)^{1/2}}{h\sqrt{t}}\left(\frac{1}{\pi}\sqrt{\frac{t}{\tau}} + \frac{2}{\pi}\sum_{1}^{\infty}\frac{1}{n} e^{-n^2/4} \sinh n\sqrt{\frac{t}{\tau}}\right)\right\} \tag{3.16}$$

The equation is solved numerically for the local heat transfer coefficients from the time, t, the surface takes to reach a liquid crystal event temperature. For this purpose a data reduction computer program has been developed at Oxford University using Matlab (see Section 3.2.12.2).

3.2.7 Definition of Heat Transfer using Adiabatic Wall Temperature

With the transient technique the thermal boundary condition created on the test surface is non-uniform. The choice of the reference temperature used in defining the heat transfer solution (Eqn. 3.16) can therefore be critical. According to Moffat (1990), there are four options for the reference temperature; the temperature far from the test surface, T_∞, the mixed mean temperature, T_m, the channel inlet temperature, T_{in}, and the adiabatic wall temperature, T_{aw}.

Variations in the definition of reference temperature often result in considerable differences in the heat transfer values from one set of boundary conditions to another. For the present investigation, variation could arise by referencing the mixed mean temperature, T_m, yielding h_m which must account for both the flow and thermal characteristics of the heated impinging jet coupled with an ambient crossflow. In this situation, the surface heat transfer rate would no longer just depend on the fluid

mechanics but also on the thermal boundary condition of the mixing jets. This dilemma would limit the transfer and comparison of experimental data obtained under different conditions.

There are two solutions to the problem. The first is to apply superposition, which requires redesigning of almost all jet impingement heat transfer experiments, to solve the non-uniform boundary conditions. The second solution is to define the heat transfer coefficient in terms of adiabatic wall temperature, which serves to describe the effective temperature the target wall would reach if it had no heat losses. The use of adiabatic wall temperature separates the effects of fluid mechanics of the jets from the thermal boundary conditions. Under these circumstances, the heat transfer coefficient is virtually independent of the thermal boundary condition and reflects only the influence of fluid mechanics. This not only facilitates the performance analysis of the different impinging jets but also makes heat transfer coefficients measured under one set of boundary conditions transferable to those measured under another set. Baughn (1995) has shown that by using the adiabatic wall temperature in the definition of heat transfer coefficients, the results from ambient and heated impinging jets compared favourably.

The adiabatic wall temperature was derived numerically and used in the definition of heat transfer coefficients in the present study.

3.2.8 Jet Effectiveness

The term jet effectiveness is used to describe the effective gas temperature the target surface would reach under the impact of the heated impinging jet coupled with crossflow. It is a dimensionless expression of adiabatic wall temperature in the form of: -

$$\Theta = \frac{T_{aw} - T_c}{T_j - T_c} \tag{3.17}$$

where T_c represents the crossflow temperature, which is equivalent to the ambient air temperature, and T_j is the temperature of the heated impinging jet. In regions of maximum jet effectiveness (i.e. 1) the adiabatic wall temperature is essentially the heated jet temperature. For the present set-up, jet effectiveness is proportional to the jet-to-crossflow velocity ratio and therefore is expected to be low (ideally 0) in regions where the crossflow is dominant.

3.2.9 Uncertainty Analysis for the Determination of Heat Transfer Coefficients

The present investigation employed a mixture of two types of liquid crystals to determine the adiabatic wall temperature and local heat transfer coefficients. This method required careful selection of the starting and liquid crystal colour change temperatures to maximise the accuracy. A comprehensive uncertainty analysis on heat transfer measurement using the double-crystal method has been performed by Ireland and Jones (1987) and is summarised herein.

For a transient experiment involving a step change in fluid temperature and a uniform initial surface temperature, the equation (Eqn. 3.14) could be written twice, yielding the non-dimensional temperature of the first crystal, θ_1, and second crystal, θ_2. Through an error propagation process, it was demonstrated that when the difference in the two liquid crystal event temperatures, T_1 - T_2, is small compared to the difference in the driving gas and the initial temperature, $T_j - T_0$, the error in the calculated heat transfer coefficient, h, would be high. In addition, the error could increase further if the non-dimensional temperatures, θ_1 and θ_2, are not well separated. This is counter to the requirement that the crystals event temperatures, T_1 and T_2, should be sufficiently close to minimise the effects of measurement errors in the gas temperature. Current liquid crystal event temperatures represented a trade-off between the different criteria to achieve accurate heat transfer measurement.

3.2.10 Preparation of the Impingement Plate

The target impingement plate for the transient heat transfer measurements was constructed from 20 mm thick clear Perspex sheet with an operational area of 800 mm x 1200 mm. The sheet was marked at right angles using a scribe and further graduated with a 10 mm grid. White chalk was rubbed into the scribed lines to improve the viewing clarity of the grid.

Three Rhopoint ultra fast response surface thermocouples (type 20102 – 1 (T)), of 5μm thickness, were attached to the target plate using the strain gauge technique. Prior to that, the areas attaching the strain gauges were carefully prepared to achieve chemical cleanliness and a roughness appropriate for strong and durable gauge bondages. The thermocouples were positioned with the measuring junctions located at r/d = 0, 2 and 4 and the leads in the bottom half of the plate. This was to ensure consistency of liquid crystal colour play throughout the top half of the plate from which temperature data would be monitored continuously. The ends of each thermocouples were welded to a 2000 mm long (type T PTFE insulated) extension lead according to British Standard 1041-4: 1992, thereby providing a total working length of 2150 mm. To minimise flow disturbance in the test section, three small holes of 1 mm diameter were drilled through the target plate to allow the extension wires to be channelled out from another side of the plate. The target surface area was then degreased to obtain fine and uniform viewing clarity from the other side of the plate. The thermocouples were then tested against a pre-calibrated thermocouple and were proven to be accurate to within 0.1°C.

The target surface was left to dry before the mixture of two micro-encapsulated liquid crystals (BM/R25C1W/C17-10 and BM/R30C1W/C17-10), equal in quantity, was applied. Four thin and uniform coatings of the mixed liquid crystals were sprayed using an artists air brush. A thin coating of black paint (Hallcrest BB-G1) was then added to the top of the surface. The liquid crystals isotherms were to be viewed through the Perspex plate so the black paint helped to absorb unreflected light and provide an invariable

viewing contrast behind the liquid crystals. The combined thickness of the dry coatings in this case was approximately 20 μm.

3.2.11 Heat Transfer Data Acquisition and Procedure

A schematic diagram of the experimental arrangement for the heat transfer measurement is shown in Figure 3.4. The liquid crystal colour plays were viewed and recorded through the Perspex substrate using a Pulnix colour CCD camera and a VSH recording system. A Panasonic time generator was connected to the video recorder to display the elapsed time of the transient test. Electrical current to the heater mesh was delivered from an AC power supply unit (Merlin 210). A digital multimeter (Keithley 2001), which also stored a scanner card, was used to detect voltages on the three surface thermocouples. The junctions connecting the scanner card and the thermocouple extension leads were immersed into a Dilvac thermoflask filled with crushed ice, capable of maintaining a cold reference point of 0°C to within ± 0.05°C. The multimeter was interfaced with a Pentium 133 MHz PC through the IEEE interface protocol. A software was developed using Microsoft Visual C++ programming syntax to facilitate the control, collection and storage of temperature data (see Appendix B). In order to synchronise the heat transfer test a relay circuit was built across the power supply, the digital multimeter, and the time generator.

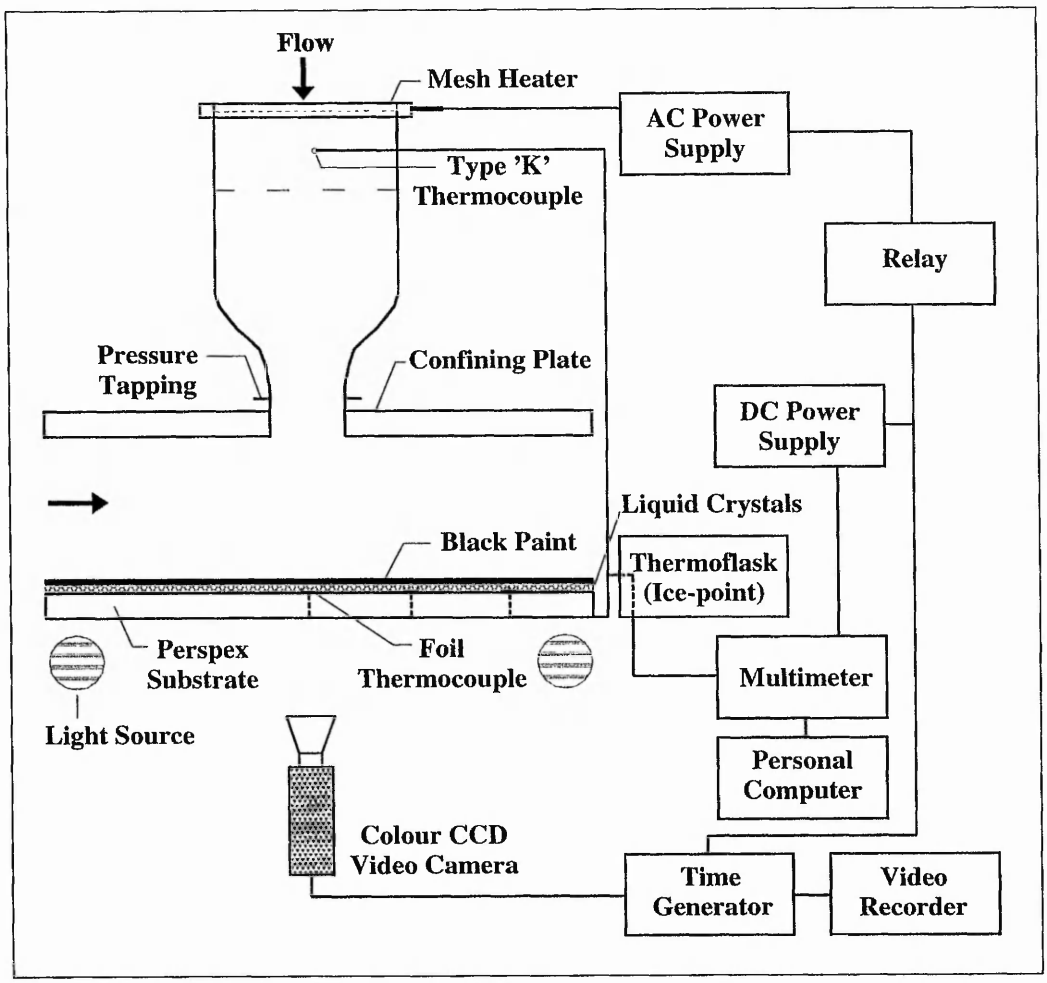

Figure 3.4: Schematic diagram of the experimental set-up for the heat transfer investigation.

Illuminations were provided by two fluorescent strip lights placed at each corner behind the target impingement plate. The strip lights were covered with black shields at the sides so that only the surface area of interest was illuminated. This helped to maximise the optical quality of the liquid crystal colours recording. The velocity of the impinging jet and the crossflow were set to the desired levels using a calibrated hot-wire measuring probe (details in Section 3.3.8). To ensure steady flow conditions, the wind tunnels were allowed a settling period of at least 30 minutes before any measurement was taken. Once stable, the jet exit discharge velocity was closely monitored using the static pressure difference across the contraction (see Section 3.7), which was detected by the

pressure tappings. The experiment was discarded if the jet discharge velocity varied by more than ± 2.5 % during the course of the test. The temperature of the impinging jet was measured to within 0.1°C using a calibrated type 'K' thermocouple placed downstream of the mesh heater. The crossflow temperature was measured, just before the start of the test, to within 0.1°C using a calibrated cold-wire sensor (see Section 3.3.8).

The transient technique adopted in this study utilised the thermal response of the liquid crystal coated surface subjected to the impinging jet that underwent an exponential change in temperature. The two narrow-band liquid crystals were calibrated in-situ against the surface temperatures, detected by the three type 'T' foil thermocouples, to within 0.1°C. The start of the heat transfer test was indicated by the time marker, triggered when the power was switched to the heater mesh, on the VSH recorder. Simultaneous temperature scanning was also triggered for approximately 2 minutes with a scan interval of 0.2s. Upon completion of the test, the temperature readings (in voltages) were transferred to and stored in the PC. The temperature history was subsequently analysed together with the recorded liquid crystal colour play using an advanced image processing and data reduction system (see Section 3.2.12.2).

3.2.12 Liquid Crystal Calibration

3.2.12.1 Colour Definition and Processing

Colour may be defined as a psychophysical property of light, specifically, the combination of those characteristics of light that produces the sensations of hue, saturation and intensity (HSI) in a normal human observer, Camci et al. (1991a). A colour can be described in quantitative terms using a three-dimension HSI based quantification. Hue corresponds to the dominant wavelength of light and therefore determines the position of a colour in the visible spectrum and its relation to other colours. Saturation refers to the strength, purity or richness of a colour in proportion to its brightness, or the amount of white contained in a specific colour. Intensity or brightness describes the relative amount of light reflected by a coloured object compared to white under the same

illumination, or the position of a colour as compared to a black to white scale. An in-depth discussion of colour phenomenon is provided by Chamberlin and Chamberlin (1980).

The HSI definition provides all the information about a colour and enables an image processing system to be used in the determination of surface convective heat transfer coefficients with liquid crystals as the thermal indicator. The image processing system serves to bridge the perceived quantitative colour information and the local temperature at a specific point on a liquid crystal coated surface. As the TLC surface passes through the optically active range, the surface optical response can be deduced using true-colour processing or intensity-based (monochromatic) processing.

True-colour processing analyses the red, green and blue (RGB) tristimulus signals and is less sensitive to variations in strength of illumination. The derived signals hue and saturation are both independent of intensity and are produced using look-up tables in commercially available colour framegrabbers, Ireland and Jones (2000). True-colour processing can be further divided into chromaticity processor e.g. Hollingsworth et al. (1990) and spectral intensity method e.g. Akino et al. (1986) and (1989). The chromaticity processor uses a calibration in terms of the dominant wavelength versus temperature while the spectral intensity method uses intensity versus wavelength, parametric in temperature, Moffat (1990). True colour processing works well with wide-band liquid crystals. In intensity-based processing, the peak intensity value is calibrated relative to a foil thermocouple and the time at which the surface reaches the temperature can thus be determined for any pixel. In general, narrow-band liquid crystals are preferred in intensity-based processing to reduce the temperature-uncertainty associated with the perceived colour.

In order to maximise accuracy of the present heat transfer measurements, narrow-band liquid crystals were selected and calibrated in-situ before data reduction was performed using an intensity-based image processing system.

3.2.12.2 Intensity-based Liquid Crystal Calibration and Image Processing

The recorded liquid crystal colour play (from Section 3.2.11) was analysed using an advanced image processing and data reduction facility at Oxford University. A frame grabbing card, fitted to a Pentium PC, was used to digitise the images and the data stored directly in the computer RAM. The computer has 512 Mbytes of RAM and was capable of acquiring 500 full successive frames. Each frame was captured at a particular time from the start of the heat transfer experiment. The time marker shown in the frame was used to reference the intensity signal to the elapsed time.

A numerical program developed in Matlab was used to facilitate the calibration of liquid crystals and the calculations of adiabatic wall temperature, local heat transfer coefficients and jet effectiveness. To calibrate the liquid crystals the intensity history of the local pixel (on which the thermocouple measuring junction lays) was plotted against the recorded temperature data. Figure 3.5 shows a typical calibration curve with two significant peaks in intensity that corresponded to the event temperature of the double crystals.

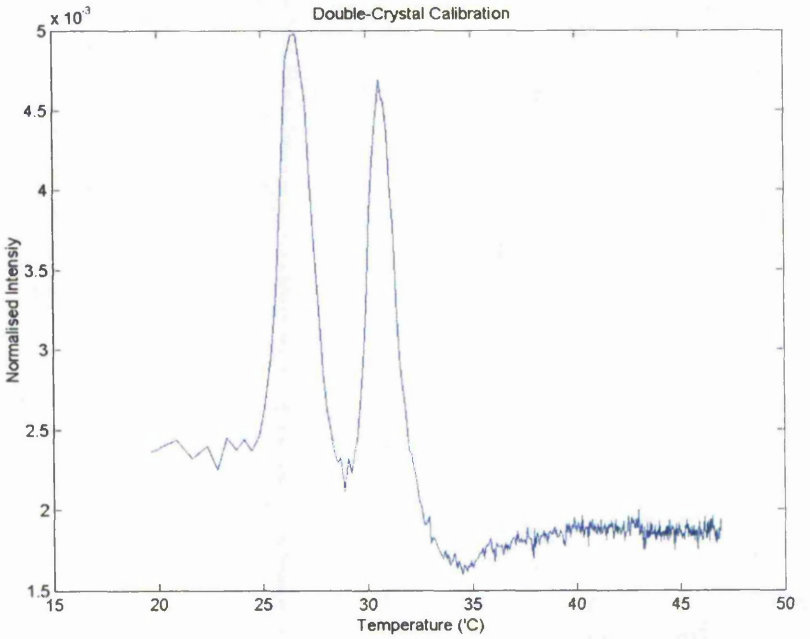

Figure 3.5: Calibration curve of intensity versus temperature.

The intensity-temperature relationship was used to determine the temperature history for each pixel on the target surface. From the calibration a look-up table of the ideal intensity histories was generated for the possible combinations of h and T_{aw} values. From the true response of the double liquid crystals, the experimental intensity history was then matched with the ideal intensity history. The combination of h and T_{aw} with the minimum fit error was selected to represent the heat transfer behaviour of the local pixel. This enabled mappings of the entire surface heat transfer distribution and jet effectiveness, which are essential for the understanding of the complex impingement phenomena. The numerical program has been validated and detailed by Ling et al. (2001).

3.3 Hot-wire Anemometry (HWA)

3.3.1 Background and Principle of Operation

Hot-wire anemometry has become the principal research technique in experimental fluid mechanics for measurement of air and gas in low and moderate turbulence intensity flows (less than 25 %), Bruun (1995). A hot-wire is essentially a fine resistance element which is heated and controlled at an elevated temperature. Based on the concept of convective heat transfer, the amount of electrical energy dissipated from the heated sensor when exposed to a fluid flow is a direct measure of the variation in flow condition. The continuous signal detected by a HWA system can be monitored via several electronic methods to provide useful information such as instantaneous velocity and temperature at a point of flow. More specific applications include measurements of wall shear stress, vorticity, gas mixture concentration and phase changes in multi-phase flows.

Figure 3.6 shows a typical single-sensor hot-wire probe. The sensing wire is manufactured from materials with good thermal properties, usually tungsten, platinum or platinum alloy. The wire is attached to two prongs that are usually made of stainless steel or nickel. The active part of the wire element may extend to the prongs, or may be restricted to a central part by using plated wire ends to reduce interference from the prongs.

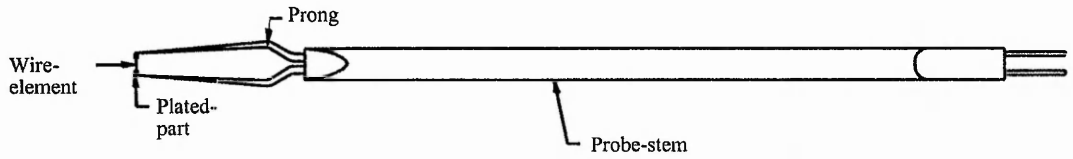

Figure 3.6: Single-sensor hot-wire probe (plated type).

A hot-wire anemometer can be operated under two modes. When operated in a constant-temperature mode (hot-wire) the sensor is connected to a feedback circuit that helps to maintain the wire at a constant resistance and hence constant temperature. Variation in the cooling of the sensor causes change in the wire current or voltage, which is amplified and converted to the desired form such as fluctuation in velocity. In the constant-current mode (cold-wire) the current in the wire is kept constant so that variations in the wire resistance, caused by the flow temperature, are measured by monitoring the voltage drop across the sensor. A cold-wire can be used concurrently with a hot-wire to measure and compensate for temperature fluctuations in the constant temperature anemometer. In the present investigation, both hot-wire and cold-wire were employed for independent measurements of velocity and temperature respectively.

3.3.2 Idealised Heat Balance

When a current is passed through a sensor wire of finite length, heat, I^2R_w, is generated. In the stage of equilibrium, there must be a balance heat loss primarily through convection to the surrounding fluid. The idealised heat transfer can be defined in the governing equation:

$$\frac{dE_{in}}{dt} = W - H \tag{3.18}$$

Expanding Equation (3.18) yields:

$$m_w c_w \delta T_w = I^2 R_w \delta t - H_0 \delta t \tag{3.19}$$

For a small increment, δt, and retaining first order terms only, the differential form of this equation can be written as:

$$m_w c_w \frac{dT_w}{dt} = I^2 R_w - H_0 \tag{3.20}$$

Taking T_0 as the reference temperature and R_0 as the reference resistance (equal to the wire resistance at ambient air temperature), the hot resistance of the sensor can be defined as:

$$R_w = R_0[1 + \alpha(T_w - T_0)] \tag{3.21}$$

This equation enables T_w and T_0 to be expressed in terms of R_w and R_0. The rate of heat transfer from the sensor is equal heat flux transferred to the fluid per unit area, H_0 / A, divided by the product of the thermal conductivity of the fluid and a typical temperature gradient, Bradshaw (1971). The Nusselt number can be written as:

$$Nu = \frac{H_0 / (\pi d l)}{\lambda_0 (T_w - T_0)/d} \tag{3.22}$$

Rewriting equation (3.20) by substituting equations (3.21) and (3.22) to give:

$$\left[\frac{m_w c_w}{\alpha R_0}\right]\frac{dR_w}{dt} = I^2 R_w - \left[\frac{\pi \lambda_0 l}{\alpha}\right]\left[\frac{R_w}{R_0} - 1\right]Nu \tag{3.23}$$

In general, R_w, I and Nu may vary with time while other parameters should be kept constant for the given physical properties of fluid and wire, Ball (1998).

3.3.3 Constant Temperature (CT) Operation

HWA operated in the CT mode is based on the principle of thermal resistance whereby the wire temperature is kept virtually constant by a feedback current. Figure 3.7 illustrates a standard CT circuit which incorporates a resistor with a hot resistance, R_w, a Wheatstone Bridge, an electronic-testing subcircuit and a feedback amplifier to maintain R_w constant up to a frequency of 20 kHz.

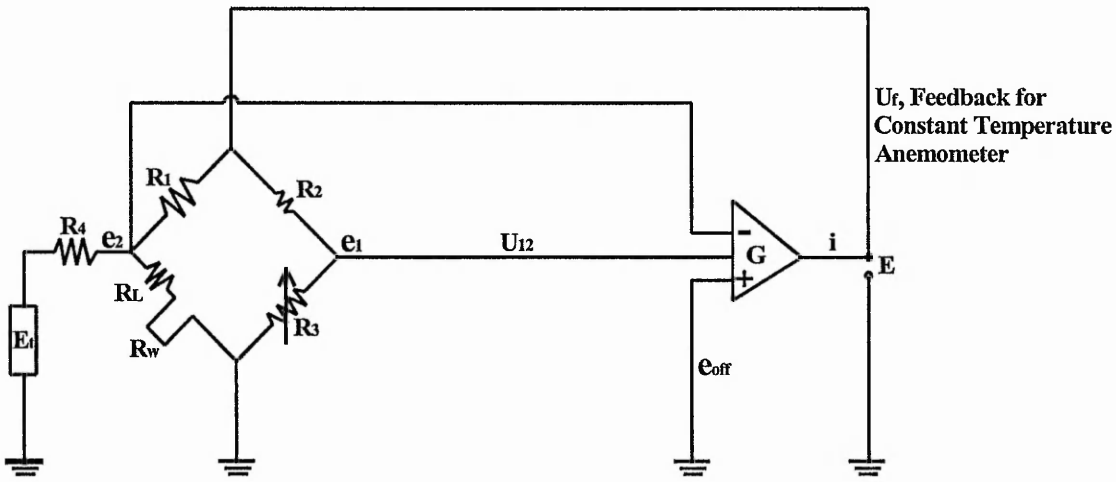

Figure 3.7: CT circuit incorporating a Wheatstone bridge, a feedback amplifier, and an electronic-testing subcircuit.

A change in the flow condition will cause a corresponding fluctuation in the operating wire resistance and thus produce an error voltage, $e_1 - e_2$, which will be the input to the operational amplifier. The output current, *i*, from the amplifier is inversely proportional to the resistance change, ΔR_w, in the sensor. Feeding the output current, *i*, back to the top of the bridge will maintain the sensor resistance, R_w, and thus the sensor temperature T_w. A step-by-step description of the operation would be as follows: -

i. A velocity increase past the hot-wire probe cools the sensing element, thus reducing the temperature T_w and the resistance R_w.

ii. The reduction in voltage at the negative input to the amplifier causes the voltage, U_{12}, to increase.

iii. The higher amplifier input voltage, U_{12}, increases the output voltage of the amplifier, U_f and thus the feedback voltage to the bridge to cause an increase in the sensor current, *i*.

iv. The increased current heats up the sensor, resulting in a decrease in U_{12} until an equilibrium stage is achieved in the entire system.

The above steps are continuous and virtually simultaneous such that an increase in the velocity can be seen as an increase in the anemometer output voltage, E. Since the sensor temperature is automatically and rapidly adjusted when the flow conditions vary, the thermal inertia term in Equation (3.23) can be neglected:

$$I^2 R_w = \left[\frac{\pi \lambda_0 l}{\alpha}\right]\left[\frac{R_w}{R_0} - 1\right] Nu \tag{3.24}$$

Substituting $E = IR_w$ into Equation (3.24) yields:

$$E^2 = C\left[\frac{R_w}{R_0} - 1\right] Nu \tag{3.25}$$

The overheat ratio, R_w / R_0, is proportional to the velocity sensitivity but inversely proportional to the temperature sensitivity of the sensing element. It is therefore essential to operate the hot-wire at a high temperature but below 300°C to avoid oxidisation on the sensor. For maximum effectiveness, the overheat ratio for a tungsten probe is usually set to a value less than 2, with 1.8 being recommended, Bruun (1995). The velocity and temperature sensitivities can be expressed as follows: -

$$S_u = \frac{\partial E}{\partial U} \tag{3.26}$$

$$S_\theta = \frac{\partial E}{\partial \theta} \tag{3.27}$$

Where θ represents a small fluctuation in the fluid temperature, T_a. The fluctuating wire voltage signal, e_w, can be related to velocity, u and temperature fluctuations, θ by:

$$e_w = S_u u + S_\theta \theta \tag{3.28}$$

For practical applications, the equation is often expressed in terms of fluctuating anemometer voltage, e, by:

$$e = S_u u + S_\theta \theta \tag{3.29}$$

3.3.4 Calibration and Linearisation Equations

A hot-wire must be calibrated to determine the relationship between the anemometer output voltage and the fluid velocity. Over the years a number of linearisation algorithms have been proposed. The most common algorithms, which cover the majority of applications, are:

1. Polynomials

$$U = C_0 + C_1 E + C_2 E^2 + C_3 E^3 + C_4 E^4 + ...C_n E^n \tag{3.30}$$

where U is velocity, E is the anemometer output voltage and C_0 to C_n are calibration constants determined from a standard least square curve-fitting.

2. Power law (King's law)

$$E^2 = A + BU^C \tag{3.31}$$

where the exponent, C, ranges between 0.3 to 0.6, depending on the Reynolds number. The constants A and B can be determined through fitting of a set of calibration data expressed as E^2 against U^C.

3. Look-up tables

Polynomial curve-fitting or look-up tables provide the best accuracy, up to ± 5 %, in all cases whereas Power law is unreliable particularly at low velocity (≤ 1m/s) due to the velocity sensitivity of the exponent C, Jorgensen (1996). The present investigation employed Polynomials curve-fitting due to its high and consistent accuracy.

3.3.5 Temperature Compensation in Non-isothermal Flows

The output voltage from a constant-temperature anemometer is a direct function of the cooling effect of an air stream flowing pass the sensing element. In non-isothermal flows the hot-wire tends to response indistinctly to changes in velocity and temperature. This can lead to considerable errors in the measured velocity particularly when the change in fluid temperature becomes large. Lemieux and Oosthuizen (1984) showed that at 3 m/s a relative error in velocity measurement, reduced using the Power law, was about 1.5 % per degree Celsius for an uncompensated system.

To account for the effect of ambient temperature variation on the anemometer output voltage, two main approaches for temperature correction have been introduced. The first approach compensates by dynamically adjusting the hot-wire sensor temperature to maintain the same voltage at the same velocity. This can be achieved by incorporating an additional temperature sensitive element into the bridge circuit to enable constant automatic overheat adjustment. In this way it is possible to measure at different temperatures without having to correct for the probe voltages. Such circuits for temperature compensation of varying complexity have been detailed by Chevray and Tutu (1972) and Hishida and Nagano (1978).

The second approach utilises an additional temperature sensor (a cold-wire or temperature probe), placed in close proximity to the hot-wire, to measure instantaneous temperature for correction of hot-wire voltages. It entails analytic and predictive interpretation of the influence of temperature variation on hot-wire readings. The method is simple but yet effective for a small fluid temperature variation ($\Delta T_f \approx 40°C$), Bruun (1995), and can be easily implemented on a digital computer, Ball (1998). A large number of analytic methods for temperature corrections have been made available but the majority of them were developed from the Power law formulations proposed by Collis and Williams (1959). Abdel-Rahman et al. (1987) evaluated the different methods and found that the most consistent compensation was obtained using the original formulations of Collis and Williams (1959). Simplified versions of the formulations have been suggested by Bearman (1971) and Kanevce and Oka (1973). The latter developed a compensation formula, which assumed negligible change in the fluid properties of the form:

$$E_c = E^2 \frac{(T_w - T_0)}{(T_w - T_f)} \tag{3.32}$$

where E_c is the corrected voltage, E is the measured hot-wire voltage, T_w is the hot-wire sensor temperature, T_0 is the reference temperature at which the hot-wire was calibrated and T_f is the measured fluid temperature. The expression is valid for velocities not less than 0.6 m/s. At lower velocities natural convection and heat conduction to the prongs become significant that heat losses are no longer dependent solely on the temperature difference, but also on the change of coefficient, h. Using linear dependence of wire resistance on temperature and an approximation technique a correction for low-velocity measurements ($0 \leq U \leq 0.6$ m/s) was obtained in the form of:

$$E_c^2 = E^2 \left[\frac{(R_w - R_0)}{(R_w - R_f)} \right]^2 + E_{0.6}^2 \left[1 - \frac{(R_w - R_0}{(R_w - R_f)} \right] \tag{3.33}$$

where R_w is the resistance at working temperature of hot-wire sensor, R_0 is the reference resistance, R_f is the wire resistance at fluid temperature and $E_{0.6}$ is the voltage drop for $U = 0.6$ m/s at reference temperature.

The analytic temperature correction method used for the present investigation, whereby the more accurate Polynomials curve-fitting was selected, can be expressed as:

$$E_c = E\left[\frac{(T_w - T_0)}{(T_w - T_a)}\right]^{0.5.(1\pm l)} \tag{3.34}$$

where T_a is the measured ambient temperature and l is the predetermined temperature loading factor to be added or subtracted for increasing and decreasing temperatures, respectively.

3.3.6 Constant Current (CC) Operation

A hot-wire operated in the CC mode is essentially a resistance thermometer, which is commonly used for the measurement of fluctuating fluid temperatures in non-isothermal turbulent flows. A typical CC circuit incorporating a Wheatstone bridge and an R-C compensator is shown in Figure 3.8.

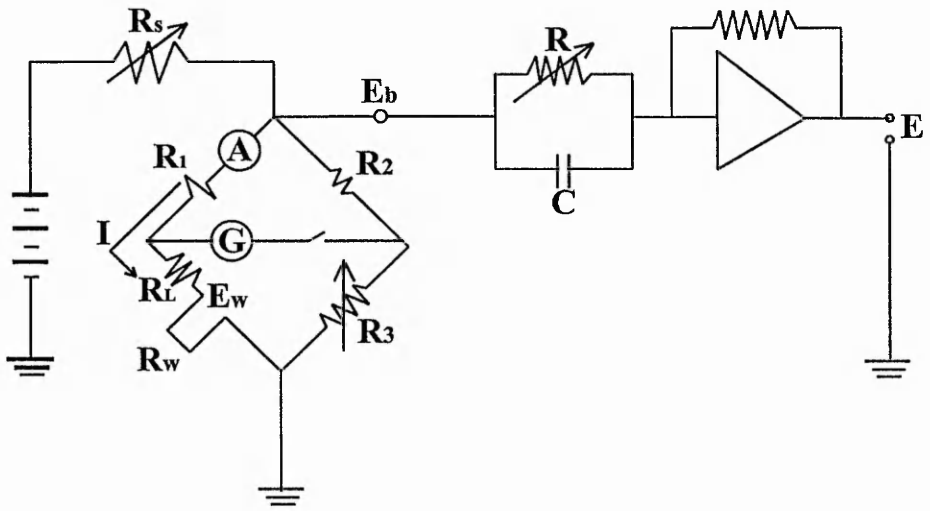

Figure 3.8: CC circuit incorporating a Wheatstone bridge and an R-C compensator circuit (from Perry, 1982).

A low overheat ratio, usually 1, is applied to a CC (cold-wire) probe to minimise the velocity sensitivity of the sensor so that temperature signal can be read with negligible contamination. The wire temperature is simply taken as equal to the surrounding fluid temperature. The bridge is balanced by adjusting the resistances R_s, and R_3 using the galvanometer, G. Having balanced the bridge and fixed the overheat ratio and velocity, the value of R_w can be set by adjusting R_3 using the relationship,

$$\frac{R_w + R_L}{R_1} = \frac{R_3}{R_2} \tag{3.35}$$

The fluctuating signal, e_w, from the resistance-wire can be related to the temperature and velocity fluctuations by:

$$e_w = S_{\theta,cc}\theta + S_{u,cc}u \tag{3.36}$$

LaRue et al. (1975) showed that an extremely fine 0.25 μm diameter cold-wire can follow temperature fluctuations of up to a frequency of 13 KHz if the air velocity is sufficiently high. They also demonstrated that the velocity sensitivity of a cold-wire is proportional to the square of the current and inversely proportional to the velocity and the square of the wire diameter. The choice of wire diameter is determined by the desired frequency response but the velocity is generally not a selectable parameter. Therefore, in order to achieve the most accurate temperature measurements with low velocity sensitivity a suitably low sensor current (i.e. 0.2 mA) should be selected.

Again, based on the temperature dependence of the wire resistance (Eqn. 3.21), variations in the output voltage, E, due to the change in fluid temperature, $T_f = T_w$, can be expressed linearly by:

$$E = KIR_0\alpha_0(T_w - T_0) \tag{3.37}$$

where K is the amplifier gain and I is the sensor current measured by the ammeter, A. The equation can be further simplified to:

$$E = A + BT_w \tag{3.38}$$

where A and B are the linear constants determined through fitting a set of calibration data expressed as E against T_w.

3.3.7 Design of Special Dual Hot/cold-wire Probe

In a non-isothermal flow, velocity and temperature data can be obtained simultaneously or separately using a special dual-sensor probe with an additional fine cold-wire mounted close to the hot-wire. A schematic diagram of the probe geometry is shown in Figure 3.9 with the probe stem orientated parallel to the mean flow direction along the wall. The probe was similar to the standard Dantec boundary layer probe with

the prongs being offset from the probe-stem by a distance of approximately 3 mm to enable measurement in close proximity to the solid wall. The velocity sensor was made of a 5 μm diameter platinum-plated tungsten wire, gold-plated at the ends for minimum prong interference, giving an active length of 1.25 mm. The temperature sensor consisted of a 2.5 μm diameter unplated platinum wire, also gold-plated at the ends to provide an active length of 1.25 mm.

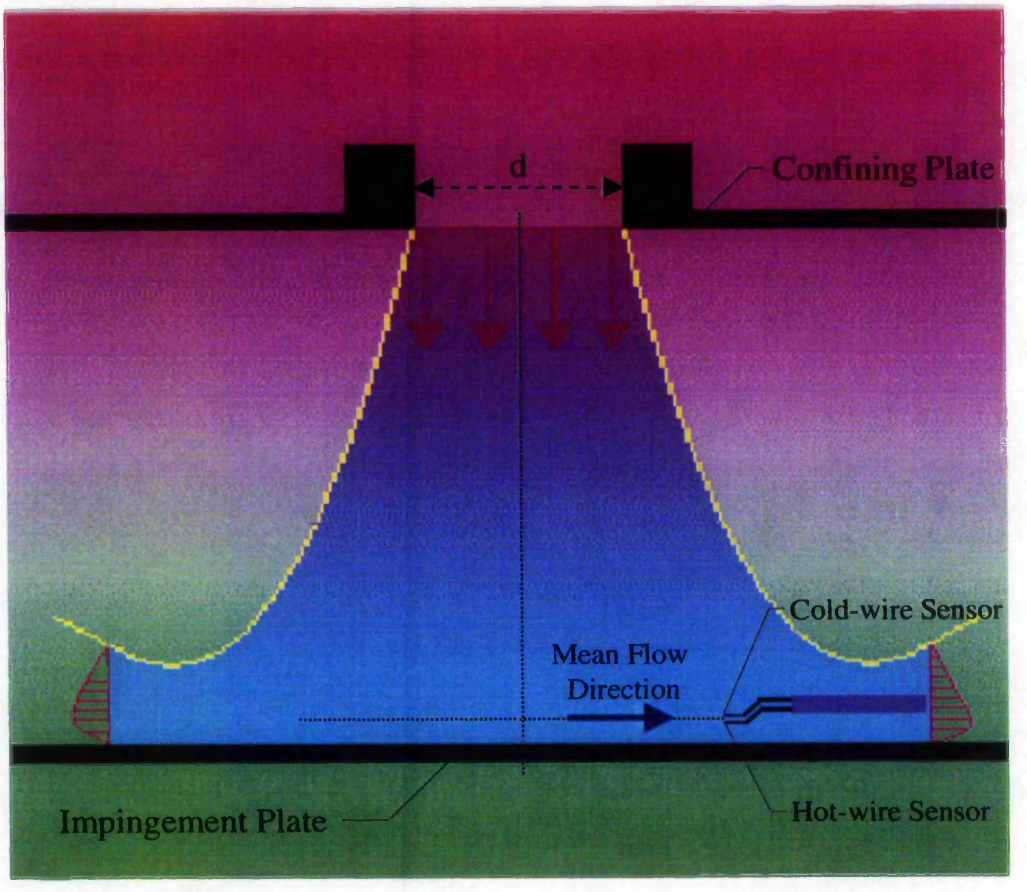

Figure 3.9: Schematic diagram of the dual hot/cold-wire probe geometry.

It is essential to optimise the relative positions of the sensing wires in space to counter for wake interference. The effect of the wake becomes significant when the sensors are mounted too close where the velocity sensor is likely to pick up signals from the upstream temperature sensor. Likewise, in the vicinity of the wall, heat generated around the velocity sensor is likely to rebound and be convected to the upstream

temperature sensor, thus resulting in erroneous measurement. The region of wake interference between two sensors spaced in the horizontal up/downstream plane was investigated by Hishida and Nagano (1978), who performed probe orientation tests. It was demonstrated that the effect of upstream wakes on the hot-wire became significant when the distance separating the two sensors was less than 150 wire diameters. With a standard 2.5 μm diameter upstream temperature sensor the spatial resolution would fall considerably. To account for this factor the sensors were separated in the vertical direction by a distance of 200 μm to avoid mutual interference, Ball (1998). The separation distance was negligible compared to the jet outlet size (100 mm in diameter) such that the sensors were considered measuring velocity and temperature data at the same point of flow.

3.3.8 Set-up Procedures for Dual Hot/cold-wire Probe

Detailed set-up and operating procedures for the hot-wire anemometer are provided in the StreamLine/StreamWare Installation and User's Guide, Dantec (2000). The StreamLine system used for the present study integrated a CTA, a CCA and a personal computer. A standard application software (StreamWare 3.0) was used to set up the anemometer modules, and to interface with a traversing mechanism and an A/D converter board for data acquisition and control. The basic set-up procedures are described in the following section.

A project was first created within the StreamWare application to record and to organise the experimental database. The probe supports and cables were connected to the front panel of the hot-wire module, cold-wire module and the controller unit which housed the system temperature module. The entire system was then configured using the software. For hardware set-up, a shorting probe was inserted into the circuit to determine the probe support and cable resistances. The values were stored in memory and automatically subtracted from all subsequent measurements. The dual-sensor probe was then inserted into the circuit in place of the shorting probe to determine the cold resistance, R_0, of the hot-wire sensor at the maximum calibration velocity and at ambient

temperature, T_0. For optimum operation of the hot-wire, the overheat ratio was set to 1.8 by default. The operating resistance of the probe was calculated automatically based on the relationship:

$$R_w = R_0 + \alpha_{20} R_{20} (T_w - T_0) \tag{3.39}$$

where T_w is set at approximately 250°C, and R_{20} and α_{20} are the respective sensor resistance and temperature coefficient of resistance at 20°C determined by the manufacturer.

The cold-wire sensor was set-up manually from the front panel of the module. To facilitate the process, the signals from the module were output to and displayed on a Gould 465 digital oscilloscope. The current through the sensor was set to the desired level (i.e. 0.2 mA) using the current switch. Similarly, the value of gain was set to a level (i.e. 200) at which the transducer's voltage output ($0 - 5$ volts) was fully utilised. To ensure that the temperature range of interest had been encompassed, the value of offset was also adjusted through the offset knob. The dual-sensor probe was calibrated before being used for measurements of velocity and temperature fluctuations in non-isothermal flows.

3.3.9 Calibration of Dual Hot/cold-wire Probe

The most satisfactory calibration of the hot-wire sensor should be performed in the facility in which the measurements are to be taken, Bruun (1995). For this reason the wind tunnel facility was designed and constructed in a way which allowed dynamic and in-situ calibrations of the hot-wire and cold-wire sensors to be performed at the jet exit. This calibration method was preferred over a static calibration using a separate facility to ensure the effects due to velocity on the cold-wire and discrepancies between facilities were eliminated. Thus, the accuracy of velocity and temperature measurements could be improved significantly.

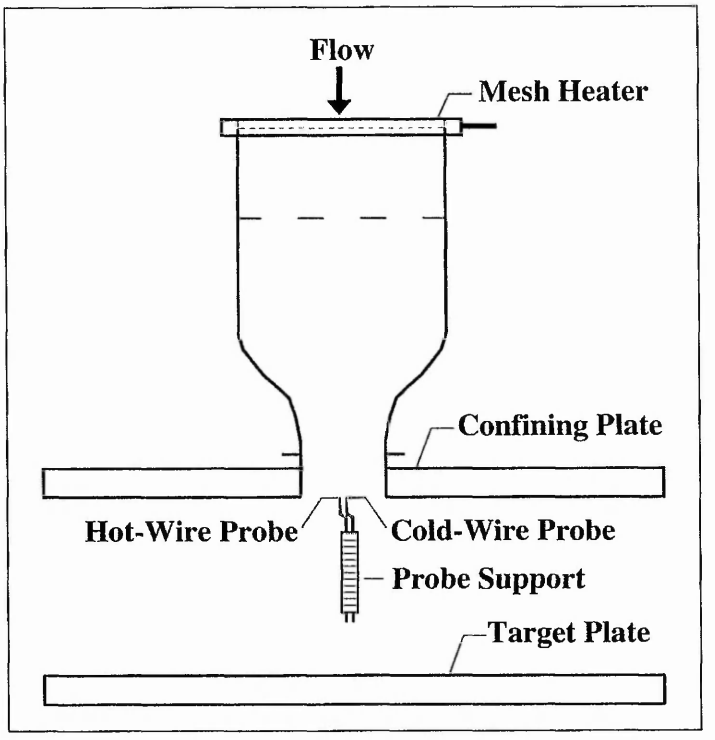

Figure 3.10: Schematic diagram of the wind tunnel facility and probe orientation.

A schematic diagram of the wind tunnel and the calibration arrangement is shown in Figure 3.10. Compressed air was supplied via the centrifugal fan (Kiloheat Ltd. type SEAe-01-280-4) driven though the variable transformer (Claude Lyons Ltd. type Regulac RK8-M) by a 8A motor. The mesh heater, similar to that described by Gillespie et al. (1996), was powered by a variable AC supply to produce temperature escalation of the jet. The dual hot/cold-wire probe was orientated such that the probe-stem laid parallel to the axis of the impinging jet. This was to avoid the effect of forced convection between the sensors during calibration. Using the traverse mechanism the probe was carefully positioned at the exit centreline of the jet. The axial flow velocity was monitored using a BS1042:1983 Pitot-static tube and digital micro-manometer arrangement. The Pitot-static tube was placed in the outlet plane of the wind tunnel a small distance ($\approx$ 2 mm) radially away from the hot-wire sensor to avoid any mutual interference. It was aligned at 90° to the jet exit plane with an estimated yaw angle of $\pm$ 2.5°, giving a 0.1 % error in the

dynamic pressure reading, Whitney (1996). The jet exit temperature was measured to within 0.1°C using a calibrated type 'K' thermocouple placed in close proximity (≈ 2 mm) to the cold-wire sensor.

The hot-wire was calibrated in an isothermal flow over a velocity range of $0 - 8.2$ m/s. Within this specified range of interest sixteen velocities were chosen and visited at random with the frequency being gradually decreased from low to high velocities. This helped to minimise calibration uncertainty at low velocities where the effects of natural convection and heat conduction to the prongs became significant. The measured dynamic pressure was converted into velocity and stored in the StreamWare application software together with the corresponding hot-wire voltage. A fourth-order polynomial algorithm was selected for calibration fitting accurate to within ± 1.5 %.

The cold-wire sensor was calibrated at a constant velocity over a temperature range of 20°C to 40°C. The calibration procedure was similar to that used for the hot-wire except that instead of the flow velocity, the flow temperature was varied over the range of interest. Twelve voltages obtained with the cold-wire sensor were plotted against the corresponding temperatures measured using the thermocouple. A linear regression (as in Eqn. 3.38) was performed on the calibration data, giving an accuracy of up to ± 0.26 %.

The calibration data were saved in the project defined within the application and used as transfer functions of voltages into velocity and temperature in subsequent measurements.

3.3.10 Determination of Optimum Sample Frequency and Size

The present hot-wire measurements involved amplitude domain statistics (e.g. mean velocity and turbulence) which require uncorrelated samples. It is therefore essential to ensure that the sampling interval (or dead time) is not less than two times the integral time scale. This was achieved by identifying the largest time scale of the jet from an autocorrelation plot and selecting an optimum sampling frequency to obtain non-

correlation between two successive measurements. Autocorrelation was performed with the dual-sensor probe placed at the exit centreline of the jet and with a fixed nozzle-to-plate spacing of 3d. A sampling frequency of 500 Hz was selected as the optimum speed to obtain statistically independent data in the shortest time-span.

To determine the optimum sample size for the measurements, it was essential to examine the initial scatter and subsequent convergence of ensemble-averaged data with respect to increasing sample size. This was conducted by varying the sample size from 1 to 65536 with an increment factor of 2 each time. The variations in jet exit centreline velocity and turbulence as a function of sample size are shown in Figure 3.11.

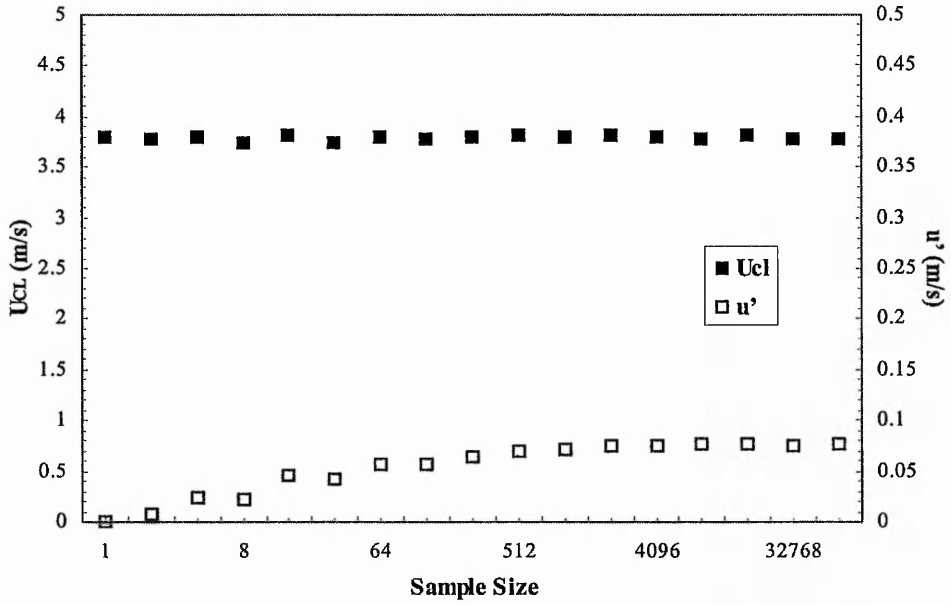

Figure 3.11: Jet exit centreline velocity and turbulence as a function of sample size.

The variations in the measured velocity and turbulence are considerable when the sample size is less than 2048, beyond which convergence is realised for both the parameters. Figure 3.12 shows the variations in the jet exit centreline temperature and temperature fluctuation as a function of sample size. The measured temperature is almost independent of the sample size. However, the measured value of temperature fluctuation becomes stable only when the sample size exceeds 512. Based on these observations, a

sample size of 4096 was selected for both the velocity and temperature sensors to ensure convergence of the measured data.

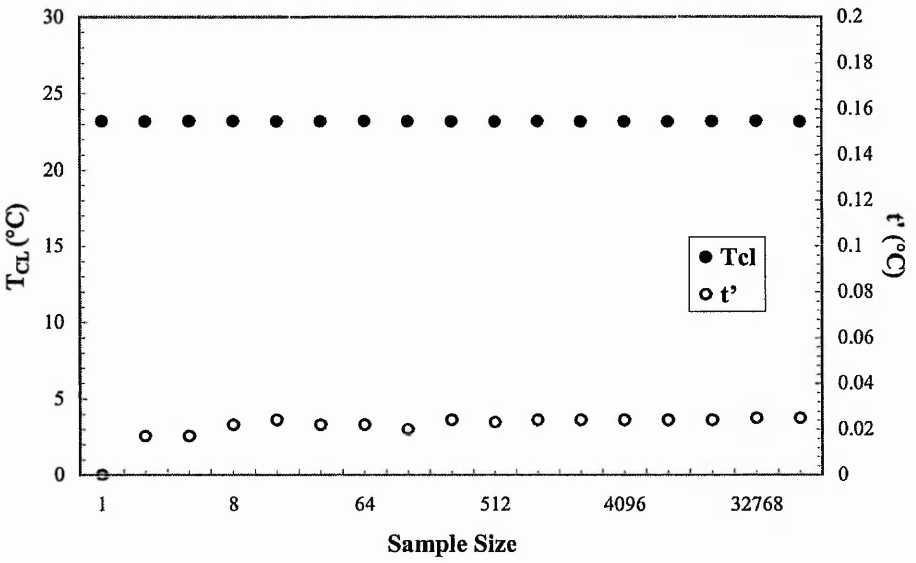

Figure 3.12: Jet exit centreline temperature and temperature fluctuation as a function of sample size.

3.3.11 Signal Interpretation of Hot-wire Sensor

Unlike temperature data which is in scalar form, velocity data inferred by the hot-wire sensor requires careful interpretation. When exposed to a complex three-dimensional fluid flow, a hot-wire sensor responds differently to three mutually perpendicular velocity components. The sensitivity to the tangential velocity component is particularly small, Bruun (1995). One of the common ways to account for this problem is by identifying the predominant flow direction in the measurement region, e.g. through flow visualisation study so that the measuring sensor is placed normal to the mean flow. To simplify the present case of a three-dimensional jet, hot-wire measurement was taken with the sensor placed on the centre of at least one of the flow axes. Thus the mean flow was considered two-dimensional and can be expressed as:

$$V_m = \sqrt{U^2 + V^2} \tag{3.40}$$

At the jet exit centreline the contribution of the radial velocity component, V, is negligible that the mean velocity obtained by the hot-wire sensor is considered to be equivalent to the axial velocity component, U. Similarly, for measurements in the vicinity of the target plate and at radial positions r/d ≥ 0.5 the component, V, is expected to be dominant with negligible U. Similar assumptions can be applied for the fluctuating axial and radial velocities, u' and v', which are interpreted as in the direction of the mean velocity vector, Cooper et al. (1993).

A qualitative smoke-flow visualisation has been undertaken for confined single impinging jets with, and without, crossflow. Details of the flow regimes can be found in Section 5.1.

3.3.12 Data Acquisition and Control System

A schematic diagram of the hot and cold-wire data acquisition and control system is shown in Figure 3.13. A large part of the system was formed by the standard Dantec StreamLine system. The StreamLine Analyser was used to operate the hot and cold-wire sensors in constant temperature and constant current modes, respectively. The major components of the main analyser frame were; a controller (90N10) unit with a system temperature sensor, a CTA module (90C10), a CCA module (90P20), a signal conditioner, a RS232 interface and an analogue output port. The signals on the hot and cold-wire circuits and the system temperature sensor were sent to an A/D input connector. The connector transferred the data to an A/D converter board, stored in the personal computer, via an UL type cable (E34856). The A/D converter (United Electronic Win-30 DS Win95) had a 12-bit resolution, an input range of ± 5V and a maximum sampling rate of 750 kHz.

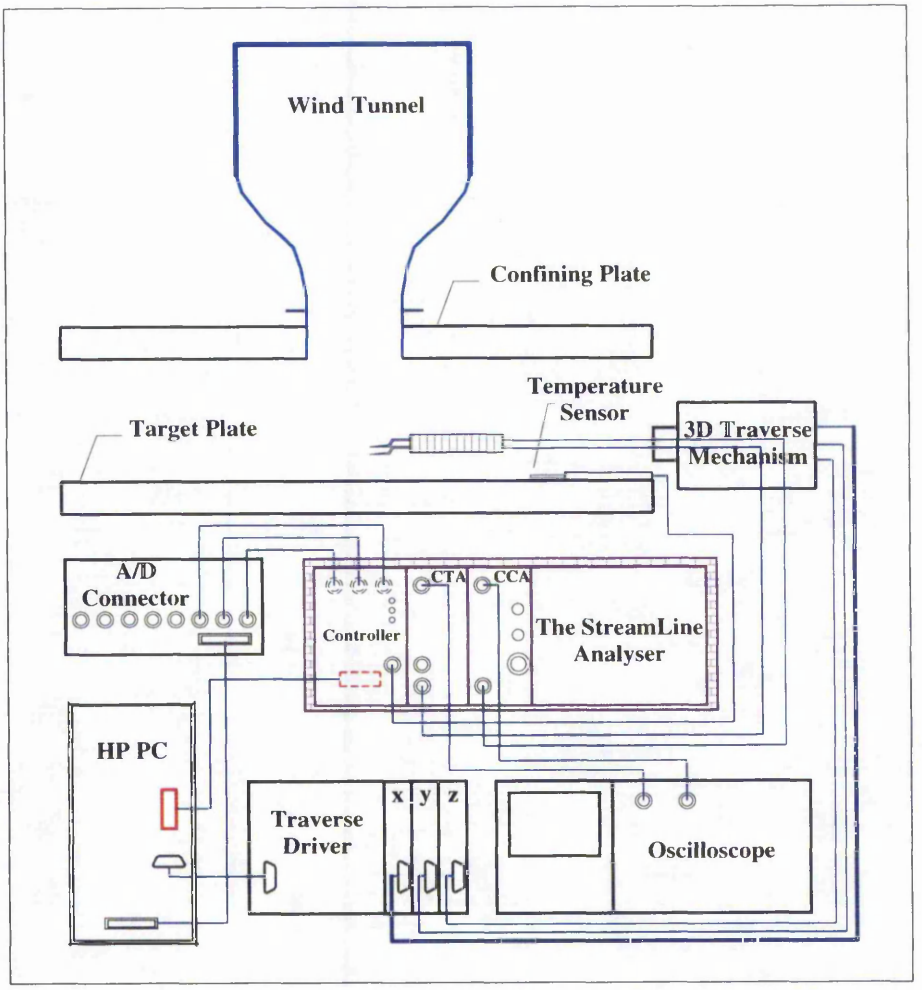

Figure 3.13: Schematic diagram of the hot/cold-wire data acquisition and control system.

The data acquisition and control process was monitored by the main controller, which communicated with the computer (HP Vectra 650MHz) via an RS232 interface. The computer also controlled the driver unit for the three-dimensional lightweight traverse through a 32-bit PCI serial port. The traverse mechanism had a working length of 580 mm on each of the three axes and a spatial resolution of approximately 30 μm. The dual-sensor probe, together with the probe holder, was fixed onto a supporting mechanism which had one of its ends mounted onto the body of the traverse. This enabled the measurement positions to be accurately controlled using the computer. Finally,

instantaneous velocity and temperature signals on the hot and cold-wire modules were displayed on a two-channel Gould 465 digital oscilloscope.

3.3.13 Measurement Arrangement and Probe Positioning

A schematic diagram showing the co-ordinate system for the near wall measurements and the orientation of the probe is provided in Figure 3.14. The dual boundary layer probe was positioned within the measurement volume using the three-dimensional traverse system, controlled and programmed via the StreamWare application.

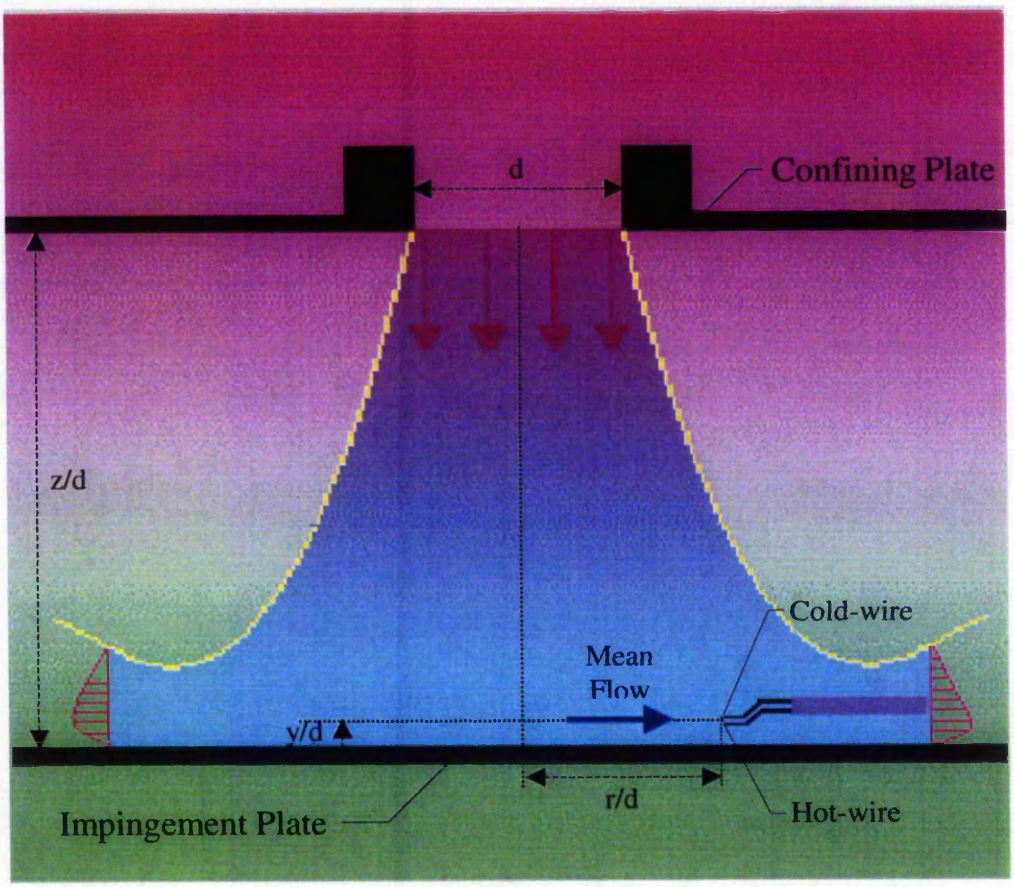

Figure 3.14: Hot and cold-wire measurement co-ordinate system and probe orientation.

As the flow velocity reduced significantly in close proximity to the wall, the combined effect of heat conduction to the prongs, natural convection and forced

convection between the sensors became significant. To avoid this problem, measurements of fluctuating velocity and temperature were performed separately. The hot-wire measurement was conducted in an unheated flow and temperature inferred by the system temperature probe was, instead, used for temperature correction. The cold-wire measurement was carried out in a steady heated flow with the CTA switched off.

To facilitate the positioning of the measuring probe, the impingement plate was marked at right angles and further graduated with a 10 mm grid. Its position relative to the centre of the jet exit was confirmed through spirit level and ruler measurements. The reflective property of the Perspex target plate was utilised for the positioning and alignment of the probe accurate to ± 0.5°. The probe was first located along the jet centreline and moved in the negative y-direction until the lower hot-wire sensor visibly came into contact with the solid wall. At this point the absolute position of the probe was set to zero in the project defined in the software. Locating the probe against the wall using this method was accurate to within ± 0.001d, Whitney (1996). The probe was then reversed a distance of 0.9 mm away from the wall. Since the hot and cold-wire sensors were separated in the y-direction by 0.2 mm, the initial measurement position was taken to be sum of the distance from the wall plus half of the separation distance of the sensors i.e. 1.0 mm or y/d = 0.01. The sensor separation distance was considered negligible compared to the jet outlet diameter (100 mm), so the measurements of velocity and temperature were essentially taken at the same point in the flow even though they were performed separately.

The measurement positions were predefined in the software such that the probe would travel from r/d = 0 to 5.5 with a small interval of 0.1d. Upon completion of the first run, the probe was moved to the next vertical position away from the wall. The vertical interval was gradually increased from y/d = 0.01 to 0.6 to obtain illustrative hydrodynamic and thermal boundary layer profiles. During data acquisition the jet velocity was closely monitored through measurement of the static pressure difference across the contraction (see Section 3.7). The results were discarded and the experimental

run be repeated if the starting and ending values of velocity or temperature differed by more than 2 %.

3.3.14 Data Acquisition and Analysis

The instantaneous axial velocity, U_i, at a given measurement position was defined as a fourth-order Polynomial function of the temperature corrected voltage, which can be expressed as:

$$U_i = C_0 + C_1 E + C_2 E^2 + C_3 E^3 + C_4 E^4 \tag{3.41}$$

Data reduction was performed within the StreamWare application. The mean velocity, U, was inferred automatically using:

$$U = \frac{1}{N}\sum_{i=1}^{N} U_i \tag{3.42}$$

The instantaneous velocity fluctuation, u_i, was determined using:

$$u_i = U_i - U \tag{3.43}$$

The turbulence was defined as the root-mean-square (RMS) of the velocity fluctuation, or the standard deviation, σ, where:

$$\sigma = \left[\frac{1}{N}\sum_{i=1}^{N}(U_i - U)^2\right]^{0.5} \tag{3.44}$$

The same data reduction equations were used to infer the radial velocity, V, and turbulence, v'.

The instantaneous temperature, T_i, at a specific point of flow were determined by inverting the linear Equation 3.38:

$$T_i = \frac{E - A}{B} \tag{3.45}$$

Similarly, the mean temperature, T, was reduced within the StreamWare application using:

$$T = \frac{1}{N}\sum_{i=1}^{N} T_i \tag{3.46}$$

The instantaneous temperature fluctuation, t_i, was calculated using:

$$t_i = T_i - T \tag{3.47}$$

Finally, the temperature fluctuation was determined using:

$$\sigma = \left[\frac{1}{N}\sum_{i=1}^{N}(T_i - T)^2\right]^{0.5} \tag{3.48}$$

3.3.15 Uncertainty Analysis for the Measurement of Velocity and Temperature.

Early work of uncertainty analysis was undertaken by Kline and McClintock (1953). Since then, there has been increasing concerns and application of uncertainty analysis as a mean to evaluate experimental accuracy e.g. Moffat (1985). Coleman and Steele (1999) documented a comprehensive approach to experimental uncertainty analysis that covered planning, design, construction, debugging, execution, data analysis and reporting. Uncertainty specifications for statistical quantities and amplitude domain analysis

for fluid flow measurements have also been summarised in Bruun (1995) and Benedict and Gould (1996).

Collis and Williams (1959) suggested that HWA could lead to large uncertainties in the measured quantities, and partially attributed it to the use of inappropriate heat-transfer relations. In response to that, much effort has been input to improve the performance and reliability of HWA. Ball et al. (1999), amongst others, employed a temperature compensation technique using a hot/cold-wire probe for simultaneous measurement of instantaneous velocity and temperature. The technique achieved measurement accuracy of ± 2.2 % for velocities in excess of 3 m/s and over 20 - 60°C temperature range. Jorgensen (1996) demonstrated that constant-temperature anemometer might be considered a 1 % instrument in the case of single-wire measurement.

A comprehensive uncertainty analysis for airflow measurement beneath a non-isothermal jet issued at Reynolds numbers of 0 - 40 000 has been undertaken. The approach was adopted from Coleman and Steele (1999) to determine random and systematic uncertainties associated with hot-wire calibration, curve-fittings and measurement expressed as a function of airflow speed. The structural illustration of the uncertainty elements is shown in Appendix A. Typical overall uncertainty of the measured mean velocity, V_m, at $Re \approx 20\,000$ (i.e. $U_{CL} \approx 3.04$ m/s) is 3.31 %.

Since the present investigation employed the more consistent Polynomials algorithm, the accuracies of calibration and curve-fitting could be improved significantly. Using a fourth-order polynomial fitting for velocity measurement and a first-order (linear) fitting for temperature measurement, the uncertainties of the measured velocity and temperature were estimated to be below 3.0 % and 1.5 % respectively over the entire experimental domain (0 - 8.0 m/s and 15 - 40°C).

3.4 Selection of Surface Thermal Boundary Condition

The selection of surface thermal boundary condition is essential to allow convective heat transfer to be correctly quantified. There are three common thermal boundary conditions; uniform temperature, uniform heat flux and transient conditions. The thermal boundary condition can vary the results of heat transfer measurement even for the same geometry and flow conditions. For a laminar flat plate boundary layer it is known from theory that the local heat transfer for a uniform heat flux boundary condition is 36 % higher than that for uniform temperature boundary conditions, Butler and Baughn (1996).

Taylor et al. (1989) demonstrated that the thermal boundary condition had a marked influence on the surface heat transfer from a flat plate. A measurable difference of $5 - 15$ % was reported between the heat transfer for constant wall temperature and constant heat flux techniques. Baughn and Saniei (1991) (see Baughn, 1995) compared the heat transfer coefficients obtained with a uniform wall temperature technique to those of a uniform heat flux technique for a cylinder in crossflow. The stagnation point values were almost identical for both thermal boundary conditions. However, as the boundary layer developed around the cylinder significant differences in the heat transfer were found. Similar comparison of constant wall temperature and constant heat flux was performed by Chupp et al. (1969) for internal impingement cooling of the leading edge of gas turbine airfoils. The heat transfer results were also identical for the stagnation strip beyond which differences in local Nusselt number of up to 15 % was shown. For the present measurement of hydrodynamic boundary layer using the hot-wire sensor, a constant temperature boundary condition was used.

3.4.1 Constant Surface Temperature Boundary Condition

To assume a uniform surface temperature boundary layer condition, the Perspex target plate was exposed to the ambient temperature jet for approximately an hour to reach steady-state temperature before hot-wire measurement was initiated.

The resultant temperature uniformity on the experimental target surface was estimated to be within 0.5°C. For an average working temperature of about 22°C this represented a discrepancy of less than 2.3 %, which was sufficiently small for the target plate to be assumed having a uniform temperature boundary condition.

3.5 Qualification of the Jet Flow Symmetry

The degree of jet flow symmetry issuing from the impinging wind tunnel has been quantified by Ball (1998). To ensure that the full confinement of the impinging jet was not causing spurious results through end effects, the velocity and turbulence profiles across the nozzle exit were validated. The results are shown and discussed in Section 6.1.1.

3.6 Flow Visualisation

A detailed flow visualisation study was undertaken to facilitate the understanding the flow structures for subsequent interpretation and corroboration of quantitative experimental data. The experimental arrangement and data acquisition procedure are described in the following section.

The translucent target Perspex plate, with operational dimensions measuring 20 mm x 800 mm x 1200 mm, was secured in position parallel to the confinement plate. The edges of both the target plate and the confinement plate were marked with 50 mm grids made visible in dark conditions using fluorescent colour. The seeding media to the flow field was smoke, delivered by vaporising Propylene Glycol in a smoke generator unit manufactured by Concept Smoke Systems. This produced typical smoke particles (technically fog) of 0.2 – 0.3 μm diameter, which are assumed to be spherical. The control unit was fitted with a nozzle from which a steady stream of smoke was introduced to the impingement tunnel via the inlet of the compressor fan. This ensured a minimal disruption to the flow field and uniform distribution of the smoke particles at the nozzle

exit. In order to facilitate the characterisation of the hydrodynamic turbulent behaviour of single impinging jets, a range of experimental parameters (see Table 5.1) was considered. The velocities at the nozzle exit and the crossflow channel were monitored continuously to ensure consistent hydrodynamic boundary condition.

The cross-sectional plane along the impingement axis was illuminated by a light sheet, produced by passing a light beam from an 800 W Arrilite Halogen light source through a slit having a 1 mm x 600 mm opening. The seeded flow field was captured normal to the illuminating light sheet using a Pulnix CCD camera and recorded on a VHS video tape. To obtain an invariable viewing contrast, the test section and the area surrounding the CCD camera were covered with black cardboards and light reflector shield respectively.

3.7 Pressure Measurement

During data acquisition the velocity of the impinging jet was closely monitored using the static pressure difference across the contraction, which was detected by two sets of pressure tappings designed in accordance with clause 6 of British Standard 848 part 1 (1980). The pressure tappings were located at 75.4 mm and 363.3 mm upstream of the contraction outlet plane, and equally spaced around the circumference of the contraction. The pressures were hydraulically averaged at each section before being read on a Perflow Instruments Ltd. digital micro-manometer. The differential pressure was then converted into velocity using the equation:

$$p_1 - p_2 = \frac{1}{2}\rho U_2^2\left[1-\left(\frac{A_2}{A_1}\right)^2\right] \tag{3.49}$$

where p_1 and p_2 represent the respective pressure at the first and second sections (i.e. at 363.3 mm and 75.4 mm), A_1 and A_2 are the respective cross-sectional areas, ρ is the air density and U_2 is the mean jet velocity.

3.8 Thermocouple Calibration

The type 'K' thermocouples used for the present investigation were calibrated to within 0.1°C in a Townson and Mercer constant temperature water bath over the temperature range of interest (15°C - 90°C). The thermocouple measuring junctions were placed in a test tube filled with deionised water and partially submerged in the bath. The reference junctions were placed in a Dilvac thermoflask filled with crushed ice, capable of maintaining a cold reference point of 0°C to within ± 0.05°C. A twelve-point temperature calibration was performed against a primary standard (BS1704: 1951) mercury-in-glass thermometer with the corresponding voltages being recorded on a Keithley 2001 digital multimeter. A linear regression analysis was undertaken to establish the equations for the individual thermocouples.

3.9 Concluding Remarks

The design, development and testing of the experimental wind tunnels facility and the associated data acquisition and analysis systems have been described. In particular, the selections of the heat transfer measurement techniques and procedures have been elaborated. The calibration methods and data reduction techniques for liquid crystal thermography, hot-wire anemometry, cold-wire thermometry and smoke-flow visualisation have been discussed.

The transient liquid crystal technique, which has been explained in depth, was selected for heat transfer measurements of the impinging jets. Adiabatic wall temperature emerged as the preferred reference temperature for defining surface heat transfer. With the use of the double-crystal method and mesh heater transient technique, the uncertainty in the measured heat transfer coefficient is estimated to be below 6 %. Whereas the uncertainties in velocity and temperature measurements using the hot/cold–wire are estimated to be less than 3.0 % and 1.5 % respectively over the entire experimental domain.

CHAPTER 4
THEORETICAL INVESTIGATION

Theoretical treatments have been applied for the investigation of single axisymmetric impinging jets. Specifically, the measured near wall flow fields beneath single impinging jets were compared with predictions based on theoretical models. The main objective was to evaluate the applicability of selected theoretical solutions for jet impingement study. It also served to cross-examine the reliability of hot-wire measurements in the hydrodynamic boundary layer, and to identify regions of flow transition from laminar to turbulent.

4.1 Theoretical Models for Flow Predictions

Solutions of the Navier-Stokes equations have been obtained for laminar stagnation flow beneath three-dimensional (axisymmetric) impinging jets, Schlichting (1968). The flow field in the inviscid region (outside the hydrodynamic boundary layer) of the jet is predicted herein using the solution for stagnation three-dimensional flow (Homann model (1936) – see Schlichting (1979), p100). The viscous flow field (within the hydrodynamic boundary layer) is predicted using the near wall viscous flow solution for an axisymmetric case (Froessling model (1940) – see Schlichting (1979), p98). The predicted flow fields were then compared with data obtained experimentally using a hot-wire boundary layer probe.

4.2 Experimental Apparatus and Procedures

4.2.1 Hot-wire Calibration

Figure 4.1 illustrates the hot-wire calibration arrangement and the associated uncertainty elements, which are elaborated further in Appendix A. A Dantec 55P15 near wall hot-wire probe connected to the IFA 100 Constant-Temperature (CT) Anemometer was first calibrated at the exit of the impingement wind tunnel. The air jet speed was

altered from 0 to 6.5 m/s (i.e. Re = 0 - 40 000) to obtain the corresponding hot-wire voltage signals on the anemometer. Simultaneous exit dynamic pressure was recorded to within 1% using a Perflow PMM600 digital manometer which was connected to a BS1042:1984 pitot-static tube placed in close proximity to the hot-wire.

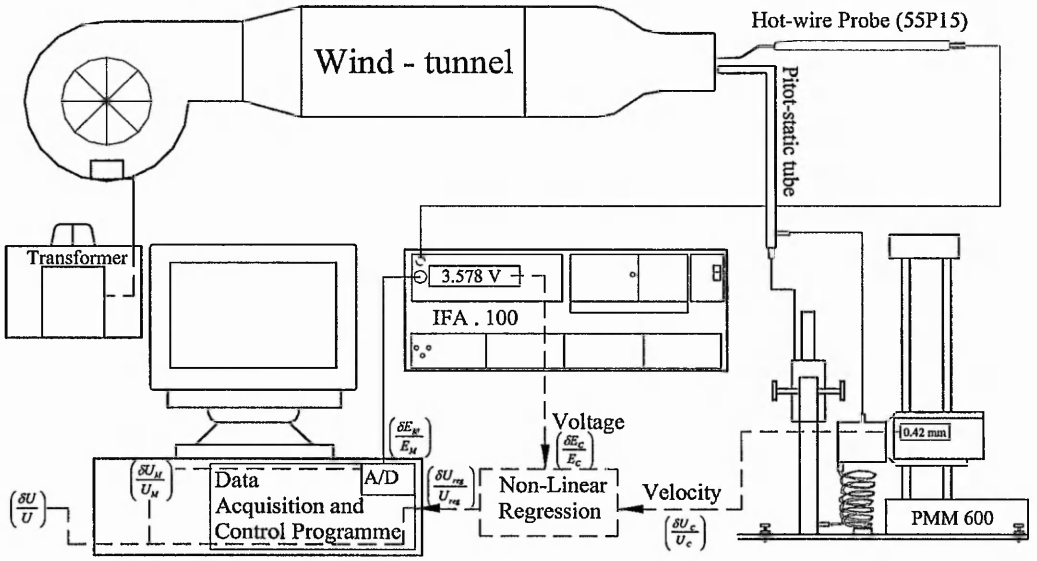

Figure 4.1: Hot-wire calibration arrangement.

The dynamic pressures at different airflow speeds were converted into velocities for a regression analysis against the corresponding hot-wire voltage readings. The regression was then programmed into an in-house data acquisition and analysis software.

4.2.2 Hot-wire Measurement

A schematic diagram of the hot-wire measurement arrangement is presented in Figure 4.2. Two nozzle-to-plate spacings, z/d, of 2 and 6.5 were considered. The air jet was discharged from the 100 mm diameter nozzle to impinge onto the Perspex plate, measuring 700 x 400 mm, at a constant turbulence intensity of 1.5 - 1.7%. Near wall hot-wire data were obtained by traversing the probe parallel to the impingement plate using a computer-interfaced three-dimensional mechanism with a spatial resolution of 2.5 μm.

Small measurement intervals (i.e. r/d = 0.1) were used to precisely locate local maxima in near wall velocity and turbulence. The vertical measurement interval was gradually increased from 0.5 – 5 mm (y/d = 0.005 – 0.05) to obtain illustrative boundary layer profiles.

The reflective nature of the Perspex impingement plate was utilised for accurate positioning of the probe adjacent to the surface where the radial wall jet is dominant. Each set of measurements was intercepted between a single point velocity taken at a fixed central position beneath the jet. The experiments were discarded and repeated if the 'before' and 'after' centreline velocity differed by more than 2%.

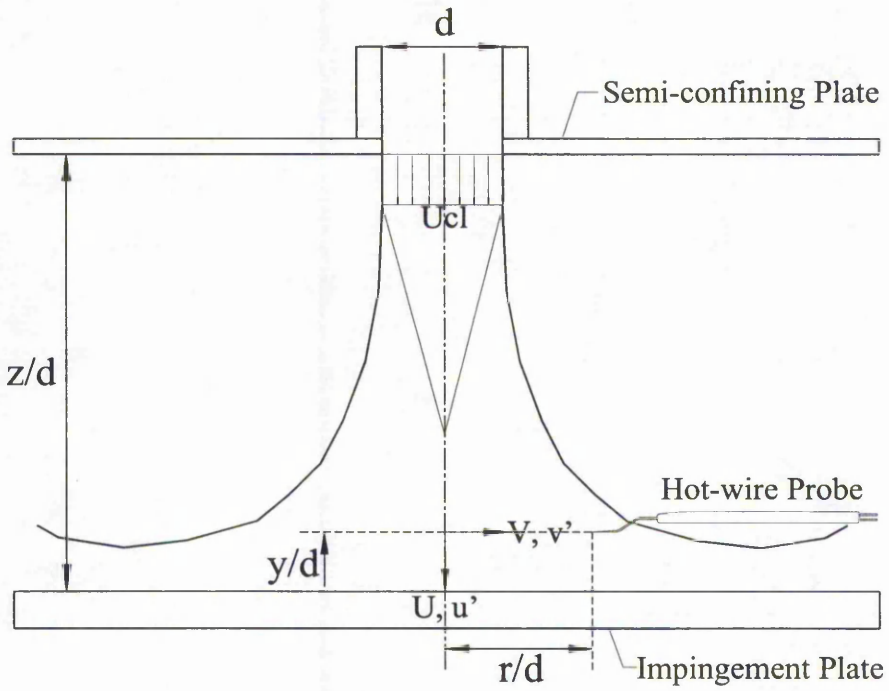

Figure 4.2: Hot-wire measurement arrangement.

The time varying hot-wire signal was output to the A/D converter card which sampled at a specific rate of 360 Hz to accommodate medium to large-scale turbulent flow structures. The sampling rate represented the optimum speed to obtain statistically

independent data in the shortest time-span. A sample size of 8000 was selected for each independent measurement to obtain an ensemble average of the airflow speed.

4.3 Theoretical Treatment

During the test, the air jet impinged orthogonally onto the target plate. The bulk fluid then diverted and accelerated radially outwards to develop into a wall jet. By specifying the boundary conditions, the flow field in the inviscid region (outside the boundary layer) was predicted using the three-dimensional stagnation model, and compared with the measured hot-wire data.

For this analysis, the stagnation point is taken as the datum and the axial and radial components of inviscid frictionless jet flow are denoted by U and V respectively. The flow components in the viscous boundary layer are written as $u = u(r, y)$ and $v = v(r, y)$. According to Schlichting (1979), the Navier-Stokes equations for a rotational symmetrical flow can be expressed as:

$$v\frac{\partial v}{\partial r} + u\frac{\partial v}{\partial y} = -\frac{1}{\rho}\frac{\partial p}{\partial r} + \upsilon\left(\frac{\partial^2 v}{\partial r^2} + \frac{1}{r}\frac{\partial v}{\partial r} - \frac{v}{r^2} + \frac{\partial^2 v}{\partial y^2}\right)$$

$$v\frac{\partial u}{\partial r} + u\frac{\partial u}{\partial y} = -\frac{1}{\rho}\frac{\partial p}{\partial y} + \upsilon\left(\frac{\partial^2 u}{\partial r^2} + \frac{1}{r}\frac{\partial u}{\partial r} + \frac{\partial^2 u}{\partial y^2}\right)$$

$$\frac{\partial v}{\partial r} + \frac{v}{r} + \frac{\partial u}{\partial y} = 0 \qquad (4.1)$$

The boundary conditions are defined as:

$$y = 0 \quad v = 0 \quad u = 0; \qquad y = \infty \quad v = V \qquad (4.2)$$

One solution that satisfies the continuity equation is:

$$\text{Axial, } U = -2ay \tag{4.3}$$

$$\text{Radial, } V = ar \tag{4.4}$$

Where a is a constant which is determined from the gradient of the measured velocity profile along the jet centreline. Note that the hot-wire signal at this location was contributed only by the axial impinging component flowing in the negative y direction. Differentiating the velocity component along the jet centreline yields,

$$\left(\frac{\partial U}{\partial y}\right)_{r/d=0} = -2a \qquad \Rightarrow \qquad a = -\frac{1}{2}\left(\frac{\partial U}{\partial y}\right)_{r/d=0}$$

From the gradient of the measured velocity profile at r/d = 0 (shown in Figure 4.3),

$$\left(\frac{\partial U}{\partial y}\right)_{r/d=0} = \frac{1.07U_{CL}}{0.5d} \qquad \Rightarrow \qquad a = \frac{-1.07U_{CL}}{d}$$

Deriving the predicted mean flow velocity in the inviscid region,

$$V_m = \sqrt{U^2 + V^2} = \sqrt{4a^2y^2 + a^2r^2}$$

$$= a\sqrt{4y^2 + r^2}$$

Normalising the mean flow velocity against the jet exit centreline velocity,

$$V_m = \frac{ad}{U_{CL}}\sqrt{4\left(\frac{y}{d}\right)^2 + \left(\frac{r}{d}\right)^2} \qquad \Rightarrow \qquad V_m = -1.07\sqrt{4\left(\frac{y}{d}\right)^2 + \left(\frac{r}{d}\right)^2}$$

Figure 4.3 shows that for z/d = 2, predictions based on the stagnation three-dimensional model compare favourably with the measured flow field in the inviscid region and r/d ≤ 0.4. As expected, the accuracy of the prediction falls as the core of the impinging jet (at r/d = 0.5) is approached. This is inline with Popiel and Trass (1991),

who found that the stagnation flow field of an axisymmetric impinging jet matched closely with the model of Homann (1936) at low nozzle-to-plate spacings.

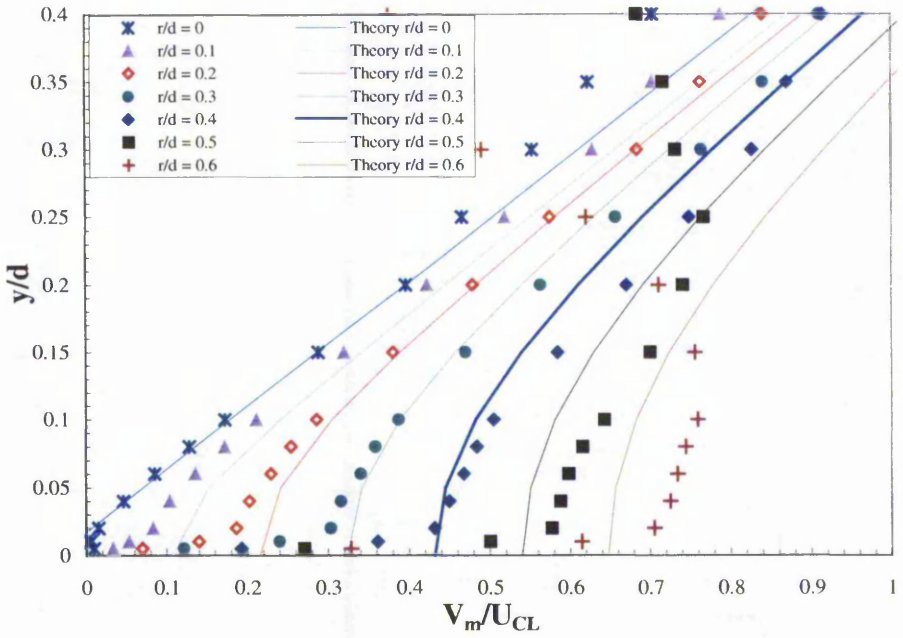

Figure 4.3: Measured and predicted near wall velocity profiles for stagnation in 3-D flow, z/d = 2.0, 0 ≤ r/d ≤ 0.6.

The viscous flow field within the hydrodynamic boundary layer (y/d ≤ 0.02) is predicted using the solution for the near wall viscous flow for an axisymmetric case. The solution assumes that the dimensionless velocity distribution parallel to the wall, v/V, and the boundary layer thickness, δ, are independent of the radial distance, r. The parameter, v/V, and its corresponding value, $\sqrt{(2a/v)}y$, have been tabulated by Froessling (1940). The following steps have been taken to convert the measured hot-wire data into the similar form for comparison:

$$\sqrt{\frac{2a}{v}}y = \sqrt{2}\xi \qquad \Rightarrow \qquad y = \frac{\sqrt{2}\xi}{\sqrt{2}} \cdot \frac{\sqrt{v}}{\sqrt{a}}$$

$$a = \frac{1.07U_{CL}}{d} \qquad \Rightarrow \qquad y = \frac{\sqrt{2}\xi}{\sqrt{2}} \cdot \frac{\sqrt{\nu}}{\sqrt{1.07}} \cdot \frac{\sqrt{d}}{\sqrt{U_{CL}}}$$

$$\nu = \frac{U_{CL}d}{\mathrm{Re}} \qquad \Rightarrow \qquad y = \frac{\sqrt{2}\xi}{\sqrt{2}} \cdot \frac{d}{\sqrt{1.07}\sqrt{\mathrm{Re}}}$$

Normalising y against the nozzle diameter, d ,

$$y/d = \frac{\sqrt{2}\xi}{\sqrt{2}\sqrt{1.07}\sqrt{\mathrm{Re}}}$$

Converting the measured hot-wire data into the similar form for comparison,

$$V_\infty = ar = \frac{1.07U_{CL}}{d}.r$$

$$\frac{V}{V_\infty} = \frac{V}{U_{CL}} \cdot \frac{U_{CL}}{V_\infty} = \frac{V}{U_{CL}} \cdot \frac{d}{1.07r} = \frac{V}{U_{CL}} \cdot \frac{1}{1.07(r/d)}$$

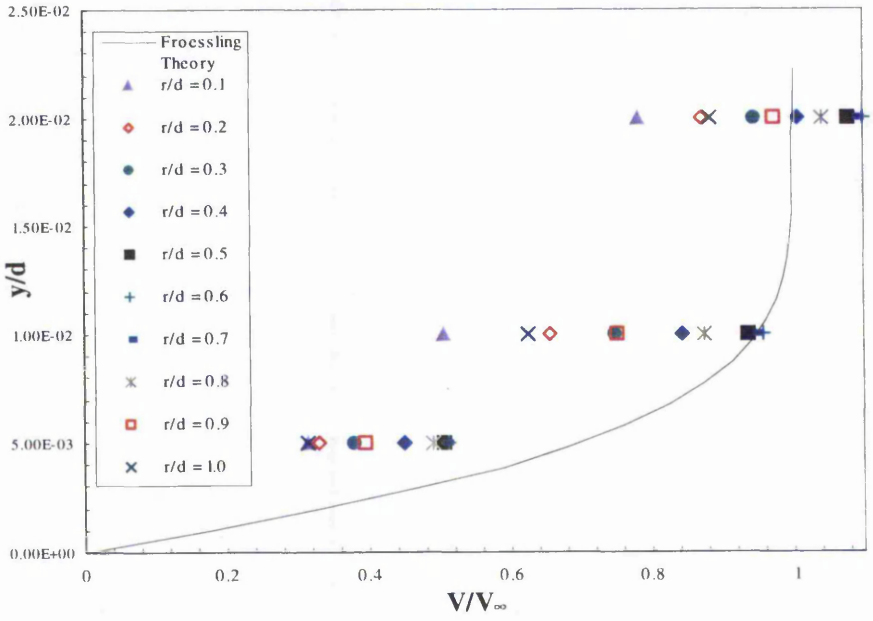

Figure 4.4: Measured and predicted viscous boundary layer profiles for axisymmetric jet flow, z/d = 2.0, 0.1 ≤ r/d ≤ 1.0.

Figure 4.4 shows that the predicted velocity profiles in the hydrodynamic boundary layer deviate significantly with the measured data at r/d ≤ 0.4. This is due to the incompatibility of the dimensionless radial velocity distribution, v/V, at r/d ≤ 0.4 where the mean flow is dominated by the axial impinging component. The near wall flow later diverts in the direction parallel to the wall at 0.4 ≤ r/d ≤ 0.8, whereby a reasonable agreement between the measured and the predicted wall jet profiles is observed. The prediction degrades further downstream at distances r/d ≥ 0.8 as the wall jet becomes increasingly turbulent due to laminar to turbulent transition, which commences at r/d ≈ 0.7.

It should be noted that the boundary layer velocity profile, contrary to the assumption, does change due to acceleration or deceleration of the radial wall jet as well as the loss of momentum for overcoming wall friction. The changing flow field complicates the definition of the wall jet thickness and, to a large extent, has contributed to the discrepancies between the measured and the predicted profiles.

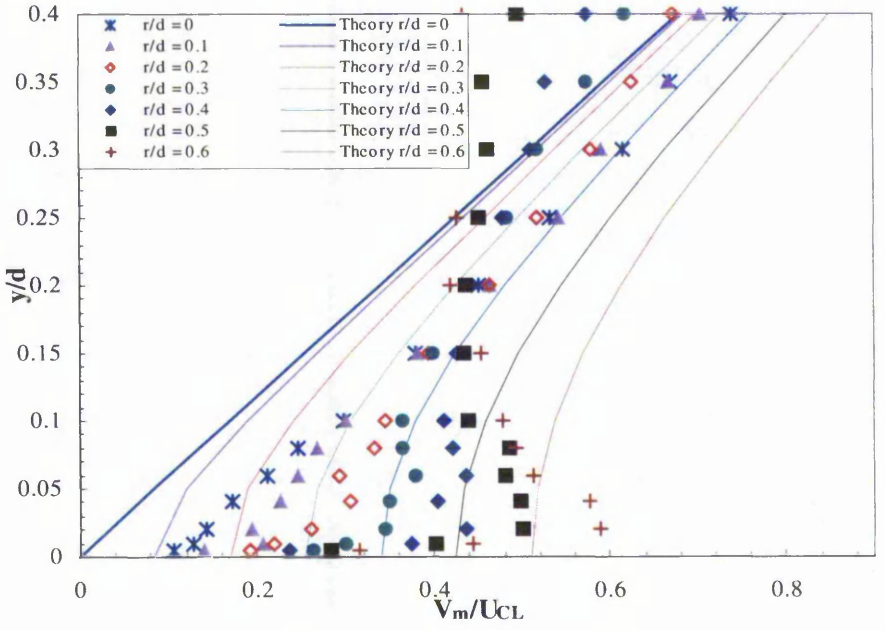

Figure 4.5: Measured and predicted near wall velocity profiles for stagnation in 3-D flow, z/d = 6.5, 0 ≤ r/d ≤ 0.6.

Figure 4.5 shows that for z/d = 6.5, the predicted flow fields deviate significantly with the measured data. This is because at this nozzle-to-plate distance, the target plate lies beyond the laminar potential core of the impinging jet (i.e. z/d ≥ 5.5) and the near wall flow field is therefore highly turbulent and unpredictable. Likewise, the prediction of the boundary layer velocity profiles using the solution for the near wall viscous flow for an axisymmetric case (shown in Figure 4.6) results in large errors. This indicates that the turbulent impinging jet has effectively penetrated into the immediate vicinity of the wall due to the mixing with the surrounding fluid.

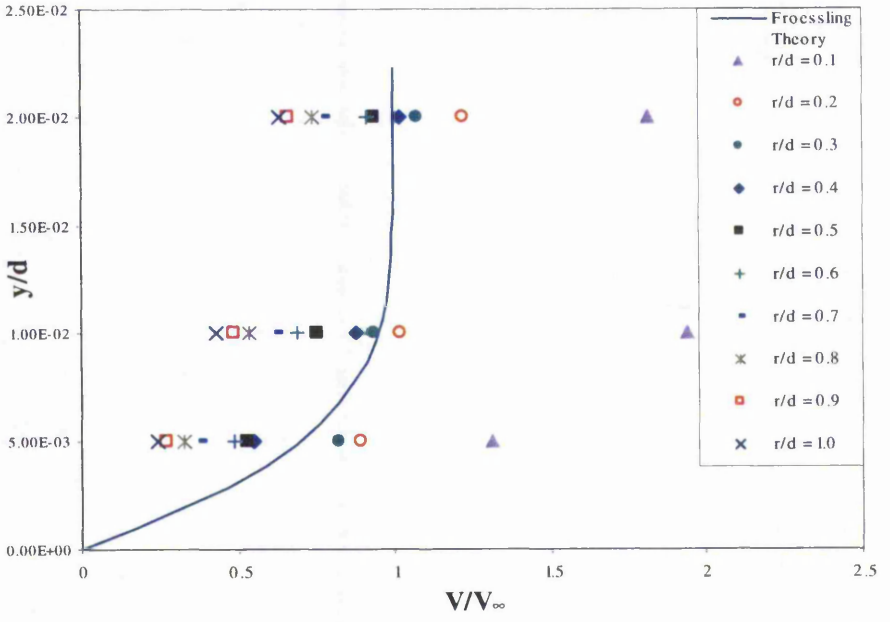

Figure 4.6: Measured and predicted viscous boundary layer profiles for axisymmetric jet flow, z/d = 6.5, 0.1 ≤ r/d ≤ 1.0.

4.4 Concluding Remarks

Theoretical models have been used to predict near wall flow field beneath a single impinging jet for z/d = 2 and 6.5. For z/d = 2, velocity profiles in the inviscid region of the near wall flow can be predicted accurately using Homann's stagnation three-dimensional flow model, up to r/d ≤ 0.5. Further downstream from the stagnation region the radial flow phenomena become very complex and cannot be predicted with existing theoretical models. Prediction of boundary layer profiles using theoretical solution for viscous flow for an axisymmetric case (Froessling's theory) is also reasonable as long as the local bulk flow remains laminar and dominated by the radial wall jet. For z/d = 6.5, the near wall flow field becomes very turbulent and predictions using the stagnation three-dimensional model and the viscous flow for an axisymmetric case are both inappropriate.

Although the outcomes have been expected, it is nevertheless important for the current work to be quantified for a jet impingement study. As far as the author is aware, prior to this no such work has been undertaken for a semi-confined jet configuration.

CHAPTER 5
FLOW VISUALISATION

Smoke-flow visualization patterns of single impinging jets with, and without, crossflow are presented and discussed in this chapter. The objective of the investigation was to gain a deeper insight into the flow structures of impinging jets and to help substantiate the quantitative hydrodynamic results in the following chapter.

The tests covered a Reynolds number range from 5000 to 40 000, and jet-to-crossflow velocity ratios of 1, 2 and 5. The range of flow parameters considered would enable validation of the experimental rig and equipment against previously published data, and would further the knowledge of the complex flow phenomena of impinging jets under a varying condition. In addition, the effectiveness of the impinging jet under the influence of a crossflow could be examined to enable selection of flow parameters for quantitative near wall measurements. The Chapter ends with a brief summary of the main findings from the flow visualisation study.

5.1 Flow Visualisation

Details of the experimental arrangement and procedures can be found in Section 3.6. Table 5.1 lists the range of experimental parameters under consideration. A nozzle-to-plate spacing of 3d was investigated for the varying flow parameters to complement the hydrodynamic data and to help to characterize the flow structure. Flow fields created by the impinging jets were silhouetted using smoke particles, produced by vaporising Propylene Glycol in a smoke generator. Images were captured using a CCD camera positioned at the outlet of the test section, directly opposite to the exiting spent air. This allowed the flow field to be viewed clearly without the effect of reflection caused by the Perspex walls. The flow fields were recorded on a VHS video for analysis and interpretation.

Parameter	Range
Re	5000, 10 000, 20 000 and 40 000
z/d	3
Jet-to-crossflow ratio	1, 2, 5 and no crossflow

Table 5.1. Experimental parameters for flow visualization study.

Considering first the axisymmetric impinging jet at a low Reynolds numbers of 5000. Figure 5.1 shows that within the central potential core region, the jet is seen to flow axially downstream in a regular, ordered manner, influenced only by small-scale turbulent fluctuations. The low-turbulence jet is surrounded by a thin laminar shear layer that is intrinsically unstable. Consequently, periodic toroidal vortex structures develop just downstream from the edge of the nozzle and are transported in the shear layer, around the circumference of the jet, towards the target plate. As the jet travels further downstream, the vortices roll-up due to the shearing action of the flow and grow in diameter and strength. As a result, ambient fluids are entrained into the jet, resulting in a spreading of the jet width.

The large-scale vortex structures eventually impinge upon the developing wall jet at $x/d \approx 0.6 - 0.7$. The impinging vortex structures consecutively induce ring-shaped wall eddies which are rolled up and diverged in the radial direction along the plate surface. Similar observations were made by Popiel and Trass (1991), who suggested that the wall eddies are responsible for additional enhancement of local momentum and heat or mass transfer. Over the interval $1 \leq x/d \leq 2$ the stretched but coherent wall eddies are suddenly destroyed. At further lateral distances ($x/d \geq 2$), flow in the outer wall jet shear layer region rolls-back upon itself to create a large recirculation zone bounded by the upper confining plate.

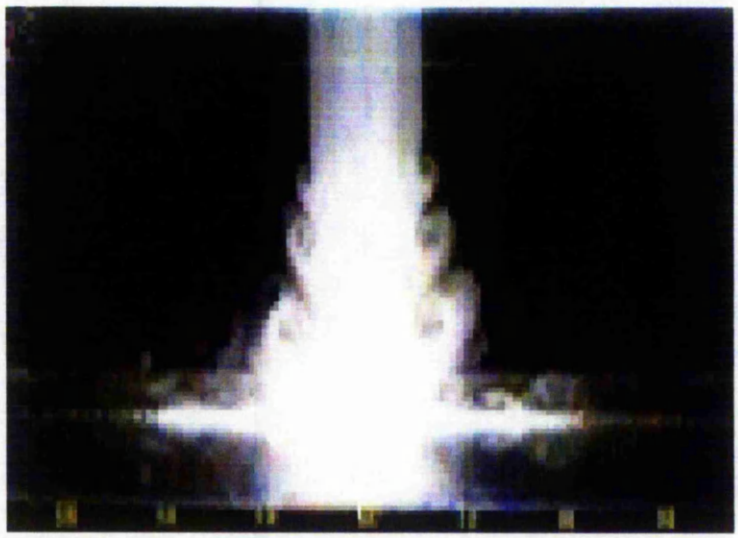

Figure 5.1: Smoke-flow visualisation, z/d = 3, Re = 5000, no crossflow.

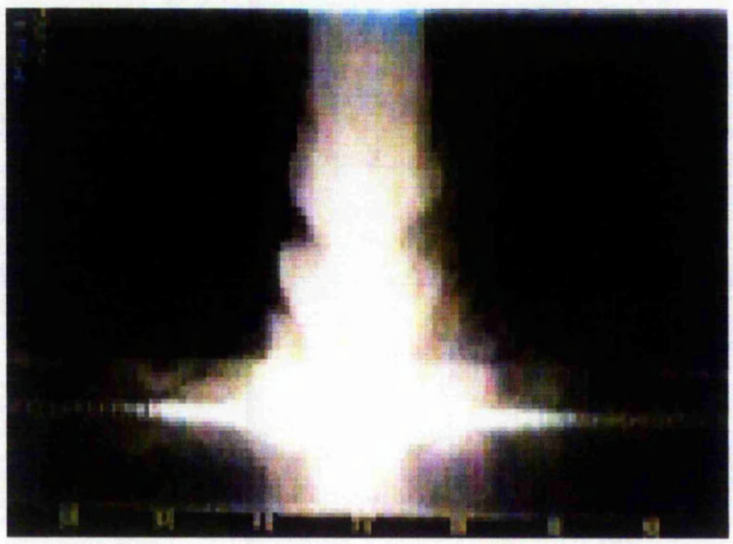

Figure 5.2: Smoke-flow visualisation, z/d = 3, Re = 10 000, no crossflow.

Figure 5.2 exhibits that when the exit Reynolds number is increased to 10 000, the formation of toroidal vortex structures around the jet core is reduced. This lends support to the work of Fondse et al. (1983) who found that the entrainment rate is considerably lower for a turbulent exit boundary condition than for a laminar one. A slight lateral contraction and expansion of the potential core region is also observed due to the shearing action of the surrounding vortex structures.

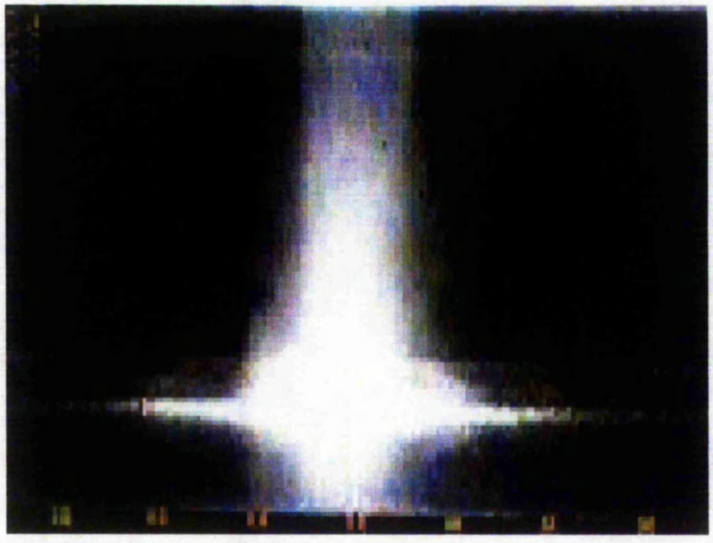

Figure 5.3: Smoke-flow visualisation, z/d = 3, Re = 20 000, no crossflow.

Figure 5.3 displays the flow field of the axisymmetric impinging jet at Reynolds number of 20 000. The impinging jet is essentially turbulent in nature and toroidal vortex structures only appear intermittently around the circumference of the jet. This substantiates the finding of Cornaro et al. (1999), who demonstrated that vortex structures are present when the turbulence intensity level in the shear layer is below 10 %, and disappear when the turbulent intensity level exceed 14 %. This, however, could only be confirmed if the images were recorded using a camera with a much higher frequency (e.g. 100 frames/second). The core of jet is dominated by large-scale turbulent structures which are convected onto the target plate at the lateral location of about ± 0.6d. These impinging large-scale turbulent structures, which cause thinning and transition of the wall jet from laminar to turbulent flow, have been proven to incite a local maximum in heat transfer coefficient, Kataoka and Mizushina (1974) and Gillespie et al. (1996). In addition, the instantaneous stagnation point of the impinging jet is seen oscillating about the geometrical centre, an observation also made by Yokobori et al. (1979) and Popiel and Trass (1991).

Under the influence of a crossflow, the flow structures of the impinging jet differ significantly. Figure 5.4 shows that for a Reynolds number of 20 000 and a jet-to-crossflow velocity ratio, U_j/U_c, of 5, the collision with the crossflow fluid results in a growth in jet diameter and turbulence level in the mixing region surrounding the potential core. Notably, the jet impinges directly on a much larger spanwise area of x/d $\approx \pm$ 1.5. Although not clearly depicted in this image, when observed in the plane parallel to the crossflow direction, a deflection of the impinging jet was apparent. The crossflow causes the jet to deflect radially (towards the direction of the camera) and impinge in big lumps of wave-like fluids on a quick but periodic basis. More interestingly, the amplitude of jet oscillation about the geometrical centre increases dramatically. This is due to the influence of the crossflow which distorts the stability of the already turbulent jet.

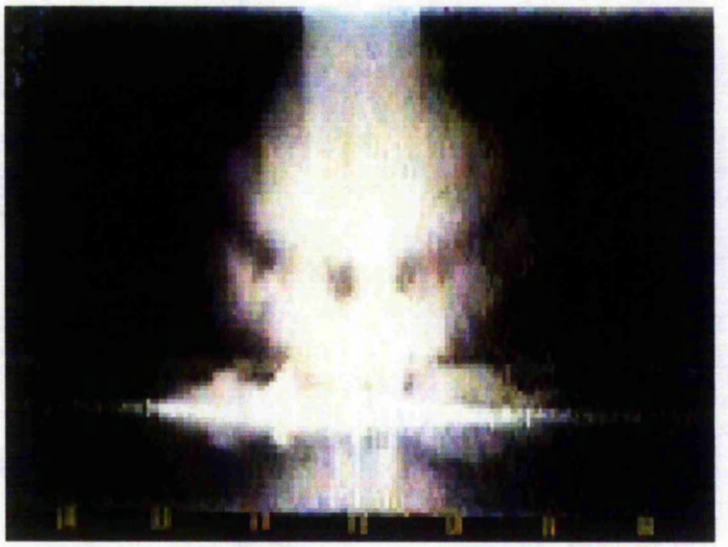

Figure 5.4: Smoke-flow visualisation, z/d = 3, Re = 20 000, $U_j/U_c = 5$.

The flow field at a jet-to-crossflow velocity ratio of 2 is shown in Figure 5.5. The deflection of the jet becomes considerable such that, when viewed in the plane parallel to the crossflow direction, only a fraction of the impinging fluid reaches the target plate at far downstream distances from the geometrical centre. The core of the jet extends to approximately 1d from the nozzle exit before taking a radical sway towards the outlet of the test section. This means that the effectiveness of the impinging jet is reduced drastically when the strength of the crossflow becomes comparable to the primary

impinging jet. This is in line with the conjecture of Obot and Trabold (1987), who found that the average surface heat transfer for array jet configurations is severely degraded even under an intermediate strength crossflow condition.

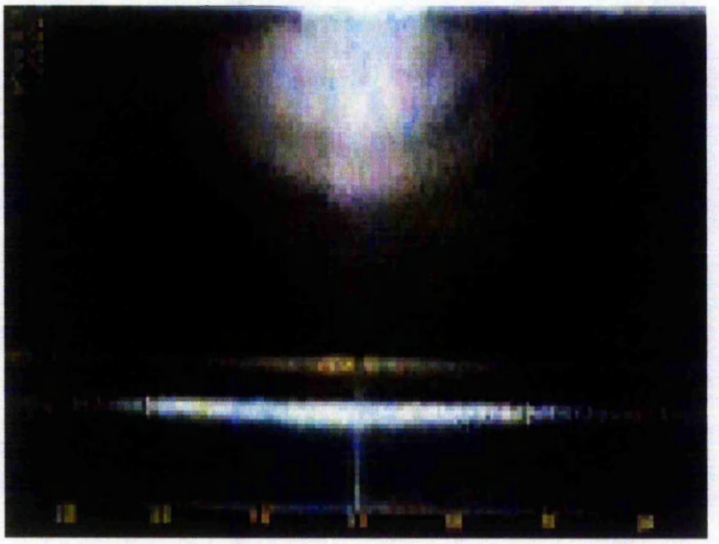

Figure 5.5: Smoke-flow visualisation, z/d = 3, Re = 20 000, $U_j / U_c = 2$.

When the jet-to-crossflow ratio is reduced to 1, the main core of the jet stretches only about 0.6d from the nozzle exit. The strong crossflow forces the primary impinging jet to take a rapid turn immediately after exiting from the nozzle, towards the outlet of the test section. The bulk fluid, as shown in Figure 5.6, is constrained to flow near the upper confinement wall. Under this situation the primary impinging jet is almost futile, leaving the secondary crossflow to dominate the fluid flow and heat transfer characteristics near the target plate.

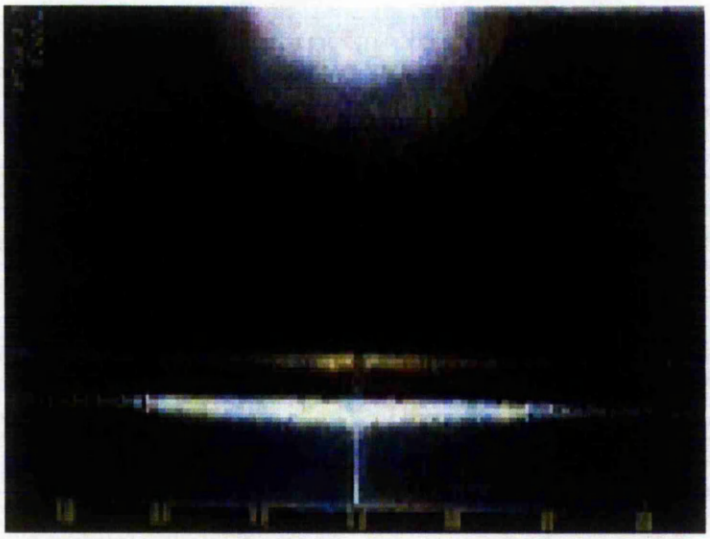

Figure 5.6: Smoke-flow visualisation, z/d = 3, Re = 20 000, $U_j / U_c = 1$.

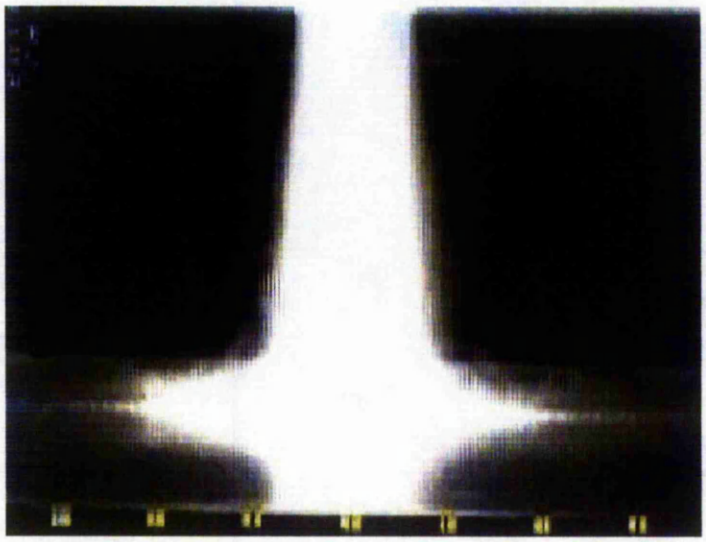

Figure 5.7: Smoke-flow visualisation, z/d = 3, Re = 40 000, no crossflow.

Figure 5.7 displays the flow field of the axisymmetric impinging jet at Reynolds number of 40 000. The impinging jet becomes very chaotic and is dominated by large-scale turbulent fluctuations with the imposed fine-scale turbulence. Coherent vortex structures are no longer present around the circumference of the jet. The impinging bulk fluid diverts radically at x/d ≈ 0.6 and accelerates along the plate under the influence of a favourable pressure gradient before evolving into a typical wall jet. This implies that the

local heat transfer distribution at the radial distance, r/d ≈ 0.6, can be expected to assume a sharp rise since this is an axisymmetric case.

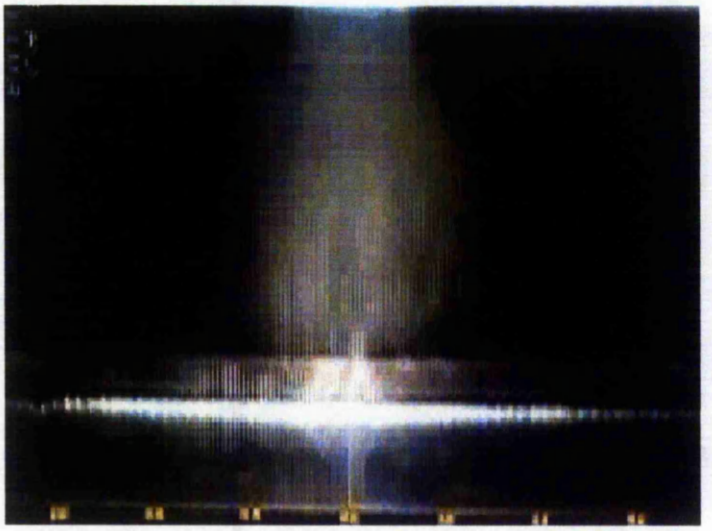

Figure 5.8: Smoke-flow visualisation, z/d = 3, Re = 40 000, $U_j / U_c = 5$.

Figure 5.8 shows that the turbulent jet, when interacting with a crossflow at a velocity ratio of 5, resembles that described for Figure 5.4. The bulk fluid is clearly more disrupted and chaotic. The fluid motion along the jet axis is also random and unsteady.

When the jet-to-crossflow is reduced to 2, the main core of the jet again extends approximately 1d from the nozzle exit before being swayed by the crossflow towards the outlet of the test section (Figure 5.9). Hence, the effectiveness of the impinging jet is reduced drastically.

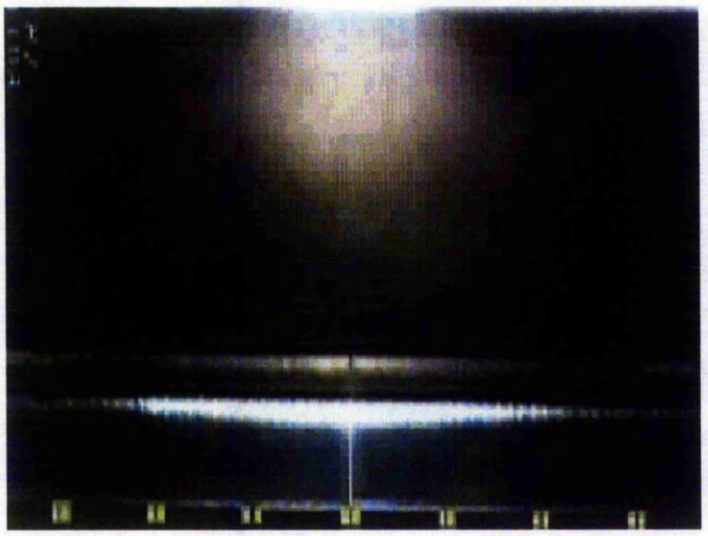

Figure 5.9: Smoke-flow visualization, z/d = 3, Re = 40 000, $U_j / U_c = 2$.

5.2 Concluding Remarks

A smoke-flow visualisation study of single impinging jets with, and without, crossflow has been undertaken. A non-dimensional nozzle-to-plate spacing of 3d has been investigated. The experiments covered varying flow parameters with Reynolds number ranging from 5000 to 40 000, and jet-to-crossflow velocity ratios of 1, 2 and 5. The full flow fields have been analysed, interpreted and compared, wherever possible, with previously published works.

For low Reynolds numbers (Re = 5000 and 10 000), the instability in the low turbulence shear layer at the edge of axisymmetric jets creates disturbances in the flow. This leads to the formation of well-organised vortex structures which roll up and grow in size as they are convected downstream. These toroidal vortices cause entrainment of ambient fluid to the jet centreline and subsequently result in contractions and expansions of the potential core. The vortices eventually impinge on the developing wall jet at r/d ≈ 0.6 – 0.7 and consecutively induce ring-shaped wall eddies which are rolled up in the lateral direction and later destroyed over the interval $1 \leq x/d \leq 2$. At higher Reynolds number (Re ≥ 20 000), toroidal vortex structures around the circumference of the

axisymmetric jet become less evident. Instead, the core of jet is dominated by large-scale turbulent structures which are convected onto the target plate at x/d ≈ 0.6. These large-scale turbulent structures are responsible for thinning and transition of the wall jet from laminar to turbulent flow, and therefore lead to the formation of a local maximum in heat transfer coefficient.

The presence of a crossflow results in a growth in jet diameter and turbulence level particularly in the mixing region surrounding the potential core. Besides distorting the stability of the primary impinging jet, crossflow also deflects the impinging jet to flow radially outwards. The effectiveness of the impinging jet is affected through interaction with the crossflow, and is drastically reduced when the crossflow becomes comparable to the impinging jet ($U_j / U_c \leq 2$). Typically at Re = 20 000 and $U_j / U_c = 1$, the impinging fluid is constrained to flow near the upper confinement wall, and the main bulk flow in the test section is dominated by the crossflow. In general, single impinging jets (with, and without, crossflow) at Re = 20 000 and 40 000 assume similar flow characteristics except at higher Reynolds number the jet becomes more chaotic and dominated by large-scale turbulent fluctuations with imposed fine-scale turbulence.

CHAPTER 6
PRESENTATION AND DISCUSSION OF EXPERIMENTAL NEAR WALL RESULTS

Experimental results obtained from an investigation into the near wall fluid flow and thermal characteristics of confined single impinging jets with, and without, crossflow are presented and discussed in this Chapter. The jet discharged with uniform exit velocity and temperature profiles and impinged onto a smooth flat surface. Two jet exit Reynolds numbers of 20 000 and 40 000 were considered. Particular attention is given to jets at low non-dimensional nozzle-to-plate spacings of 1.5d and 3d, which represent some of the most common engine cooling geometries. A range of jet-to-crossflow velocity ratios of 2, 3, 4 and 5 has been studied.

The majority of this Chapter is focused on the presentation and discussion of detailed near wall velocity, turbulence, temperature and fluctuating temperature data. Measurements were made parallel to the target impingement surface using hot-wire anemometry and cold-wire thermometry. All data are normalised against the jet exit centreline characteristics, unless stated otherwise. The near wall hydrodynamic and thermal data are essential for the analysis of the surface heat transfer phenomena in the next Chapter. A brief summary of the main conclusions drawn from the near wall investigation is provided towards the end of this Chapter.

6.1 Quantitative Validation of Axisymmetric Jet

6.1.1 Exit Velocity and Turbulence Characteristics

The measured discharge velocity and turbulence characteristics of the axisymmetric ambient temperature jet (without crossflow) are presented in Figure 6.1 in terms of U/U_{CL} and u'/U_{CL} respectively. The exit velocity profile of the confined jet is uniform to within 2 % across the central region. At radial distances equal to or greater than the nozzle diameter (r/d $\geq \pm$ 0.5), the streamwise velocity falls to near zero. The

weak velocity signals in these regions are due to recirculation of flow from the outer wall jet shear layer region to the upper confining plate.

The axial turbulence level at the exit is uniform across the central region with $u'/U_{CL} = 0.022316 \pm 0.001$. The sudden increase in the turbulence level at r/d ≥ ± 0.5 confirms the presence of large-scale turbulent structures in the shear layer around the core of the jet. Similar exit velocity and turbulence distributions for contoured nozzles obtained using hot-wire anemometry have been provided by Popiel and Boguslawski (1986) and Ball (1998), amongst others.

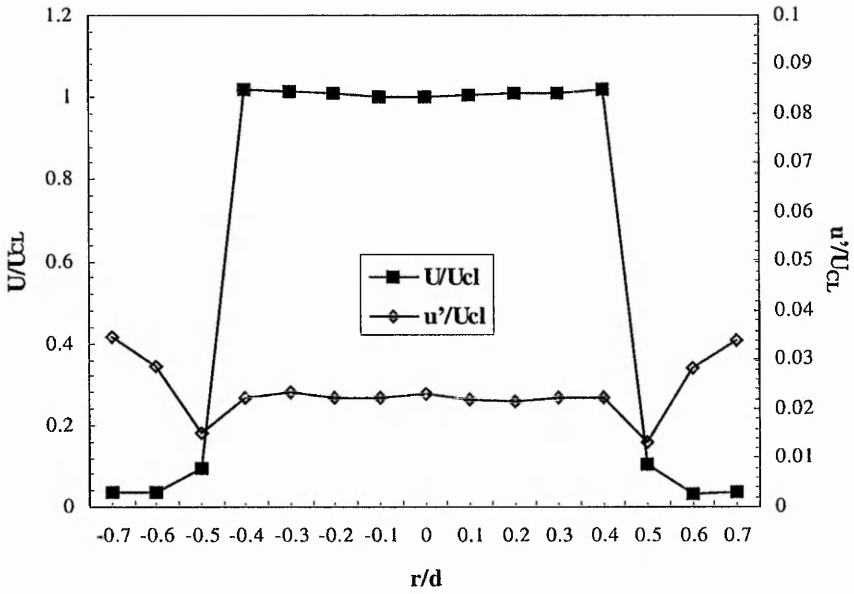

Figure 6.1: Exit velocity and turbulence characteristics.

6.1.2 Exit Temperature and Fluctuating Temperature Characteristics

Figure 6.2 illustrates the distribution of exit temperature, T/T_{CL}, and fluctuating temperature, t'/T_{CL}, of the heated axisymmetric jet. The air was heated using the mesh heater described in Section 3.1. The resulting temperature profile is uniform to within 1 % across the central region of the jet. At r/d ≤ - 0.5 and r/d ≥ 0.5, the effect of flow

recirculation from the wall jet region to the upper confining plate is manifested. This is demonstrated by the increase in the levels of local temperature and temperature fluctuation. Across the central region of the jet the fluctuating temperature remains constant to within $t'/T_{CL} = 0.0018 \pm 0.0003$.

The experiment justifies the use of a cold-wire thermometer for measuring temperature and fluctuating temperature, and a mesh heater for producing uniformly heated flows.

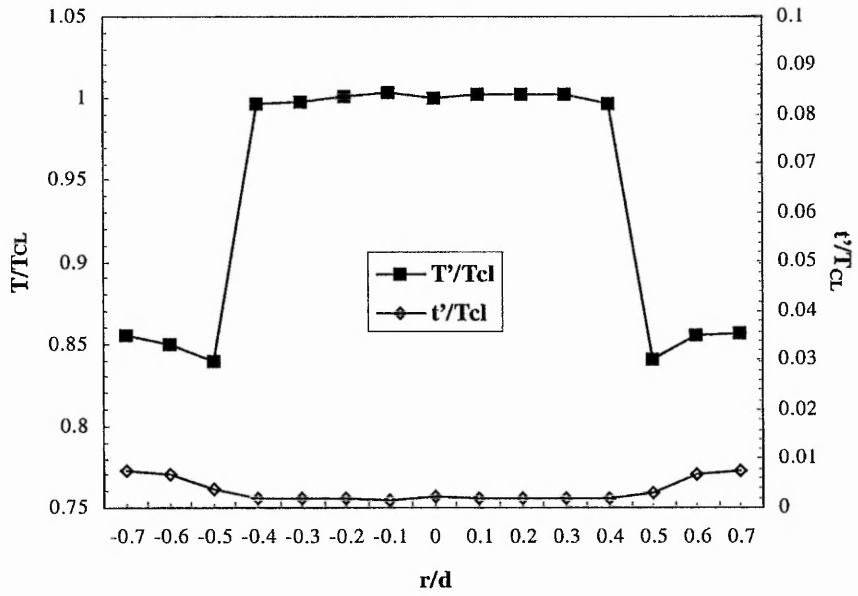

Figure 6.2: Exit temperature and fluctuating temperature characteristics.

6.2 Impinging Jet Measurements

6.2.1 Near Wall Velocity and Turbulence Characteristics

The distributions of near wall mean velocity, V_m/U_{CL}, and turbulence, v_m'/U_{CL}, are presented in the form of contour plots to aid understanding of the complex fluid flow

phenomena, particularly when a crossflow is imposed. Two nozzle-to-plate spacings of 1.5d and 3.0d have been considered. The data are shown as a function of non-dimensional distance from the jet centreline (r/d = 0) to r/d = 5.5 and from the plate between y/d = 0.01 and 0.6. It should be noted that the influence of the axial velocity component, U, on the hot-wire signal increases significantly in the region beyond the wall jet (y/d ≥ 0.15). The mean velocity vector, V_m, in this region is therefore considerably different from the radial velocity component, V. However, within the wall jet region (y/d ≤ 0.15), the measured velocity is dominated by the radial velocity component.

Figure 6.3 illustrates the near wall velocity contour for the axisymmetric ambient temperature jet at nozzle-to-plate spacing of 1.5d and Reynolds number of 20 000. The impinging jet accelerates and spreads slightly prior to striking orthogonally onto the target surface covering -0.6 ≤ r/d ≤ 0.6. At the stagnation point (r/d = 0), the measured velocity in the vicinity of the wall (y/d ≤ 0.01) approaches the theoretical zero value. The bulk fluid then diverts and accelerates radially outwards to develop into a typical wall jet adjacent to the stagnation region.

Figure 6.4 shows that the near wall turbulence level grows significantly at r/d ≥ 0.6. This is largely attributed the convection of large-scale turbulence from the edge of the jet onto the developing wall jet, as described by Gillespie et al. (1996). These impinging turbulent structures prompt a local thinning and transition of the wall jet from laminar to turbulent flow. The flow in the boundary layer (y/d ≤ 0.02) attains a maximum of $V_m / U_{CL} = 0.7 - 0.8$ at r/d ≈ 0.8. Just above this location lies a lump of fast-moving fluid (indicated by the 0.9 – 1.0 colour patch in Figure 6.3) which starts to decelerate at further downstream distances, notably from r/d ≈ 1.35. The location coincides to the point where the static wall pressure reaches almost zero, as reported by Ball (1998), amongst others. A subsequent unsteady separation of the wall jet results in a region of high turbulence in the interval 1.1 ≤ r/d ≤ 1.9 and 0.02 ≤ y/d ≤ 0.15 (Figure 6.4).

The wall jet continues to decelerate at further downstream distances due to flow diffusion and loss of momentum caused by the wall friction. At r/d ≥ 2, a large amount of fluid rolls-back upon itself and recirculates upward towards the upper confining plate. The mean velocity eventually becomes negligible at r/d ≥ 4.4 and y/d ≤ 0.02.

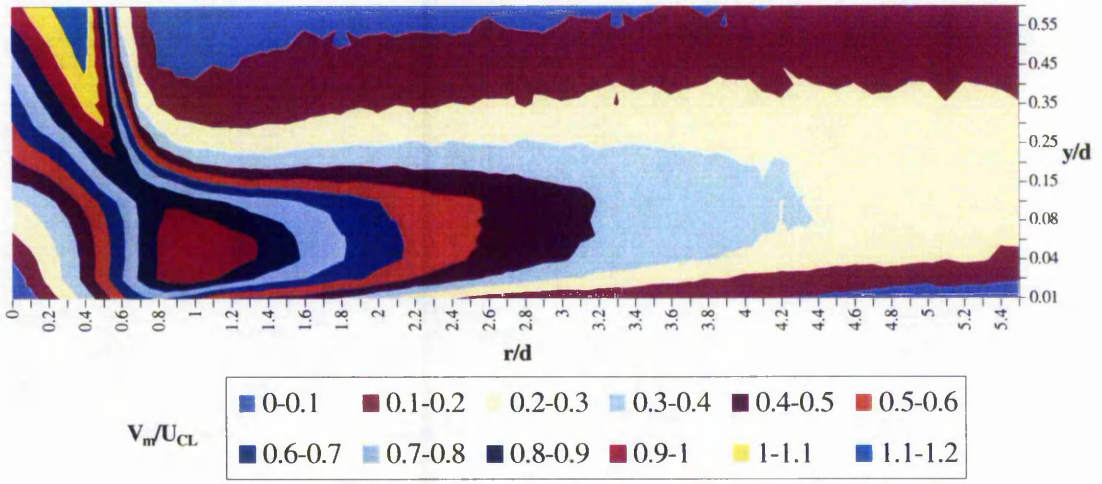

Figure 6.3: Mean velocity contour, z/d = 1.5, Re = 20 000, no crossflow, 0.01 ≤ y/d ≤ 0.6.

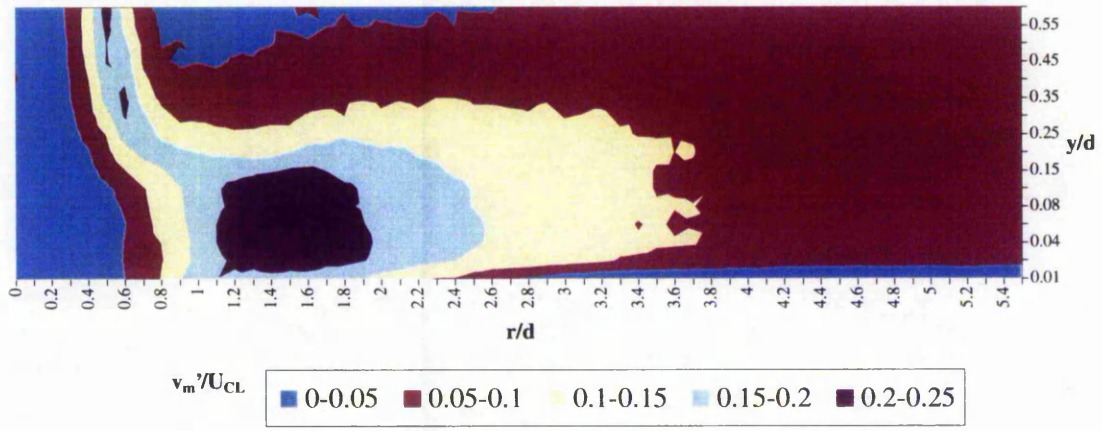

Figure 6.4: Mean turbulence contour, z/d = 1.5, Re = 20 000, no crossflow, 0.01 ≤ y/d ≤ 0.6.

Figure 6.5 illustrates the flow field when an upstream crossflow is imposed from the left of the working section at a jet-to-crossflow velocity ratio, U_j/U_c, of 5. As the

impinging jet collides with the oncoming crossflow, the stagnation point is swayed slightly downstream (by ≈ 0.1d). However, the flow field within the jet core remains undisturbed by the crossflow. This indicates that the primary impinging jet is still dominant over the secondary crossflow. The effect due to the crossflow is more significant in the region outside of the core of the jet. Figure 6.6 shows that the region of high turbulence caused by the unsteady separation of the wall jet (as in Figure 6.4) is diminished. This is because the crossflow suppresses flow separation by forcing the local bulk fluid to re-attach to the wall and transport radially outwards.

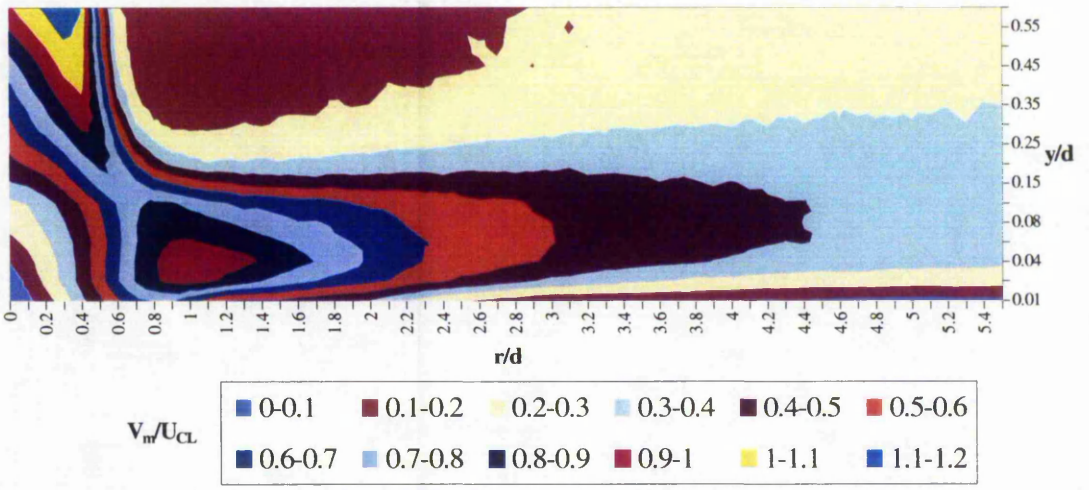

Figure 6.5: Mean velocity contour, z/d = 1.5, Re = 20 000,

$U_j / U_c = 5$, $0.01 \leq y/d \leq 0.6$.

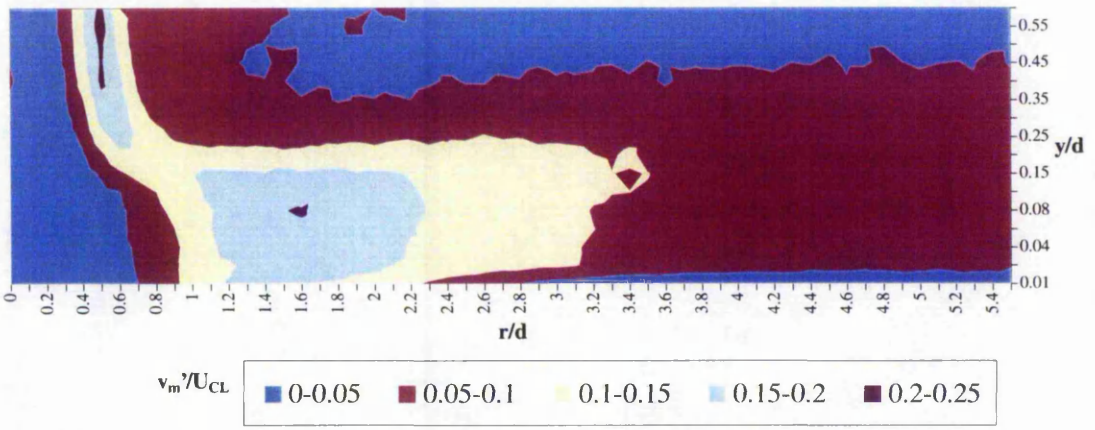

Figure 6.6: Mean turbulence contour, z/d = 1.5, Re = 20 000,

$U_j / U_c = 5$, $0.01 \leq y/d \leq 0.6$.

The mean velocity and turbulence contours for Re = 20 000 and $U_j / U_c = 4$ are presented in Figure 6.7 and 6.8 respectively. The core of the impinging jet is deflected laterally downstream by ≈ 0.16d. The increased crossflow stretches the radial bulk fluid further downstream. Typically, the fluid at $V_m / U_{CL} = 0.4 - 0.5$ extends up to r/d ≈ 4.8. A slight increase in the turbulence level is also seen in the region $1.3 \leq r/d \leq 1.8$ and $0.4 \leq y/d \leq 0.13$, presumably due to intensified mixing caused by the crossflow.

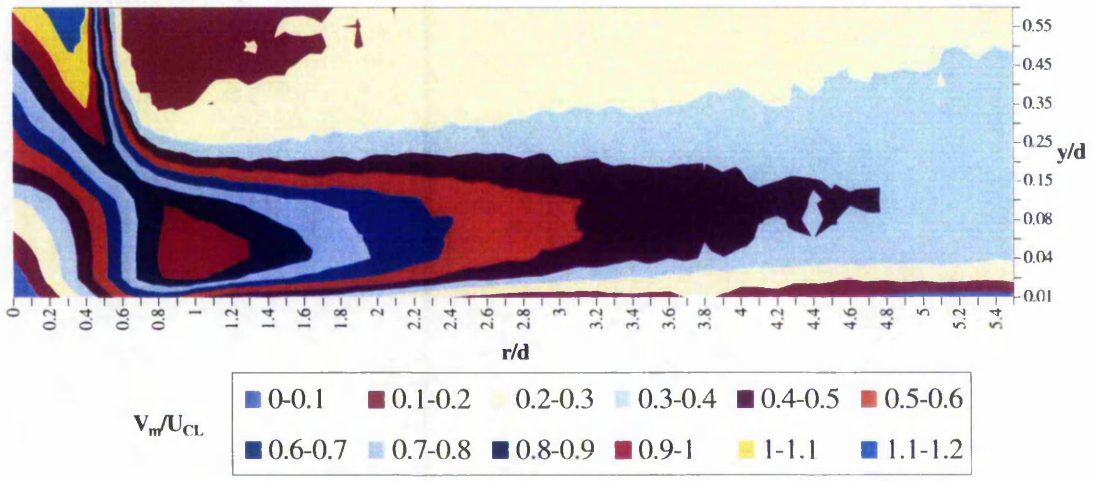

Figure 6.7: Mean velocity contour, z/d = 1.5, Re = 20 000,

$U_j / U_c = 4$, $0.01 \leq y/d \leq 0.6$.

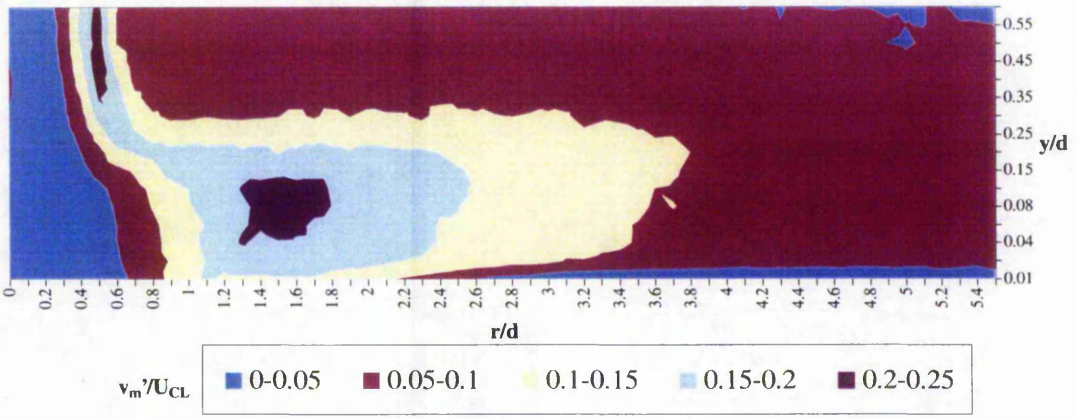

Figure 6.8: Mean turbulence contour, z/d = 1.5, Re = 20 000,

$U_j / U_c = 4$, $0.01 \leq y/d \leq 0.6$.

Figure 6.9 and 6.10 show the respective mean velocity and turbulence contours for Re = 20 000 and $U_j / U_c = 3$. The stronger crossflow drives the upstream impinging fluid (on the left side) towards the core of the jet. This is illustrated by the increased level of turbulence at the geometrical centre (r/d = 0). The stagnation point is deflected by approximately 0.32d downstream. The turbulence level in the wall jet region also continues to rise as a result of increased flow mixing. However, the fluid velocity in the downstream near wall ($y/d \leq 0.2$) region starts to decline under the increased influence of the crossflow.

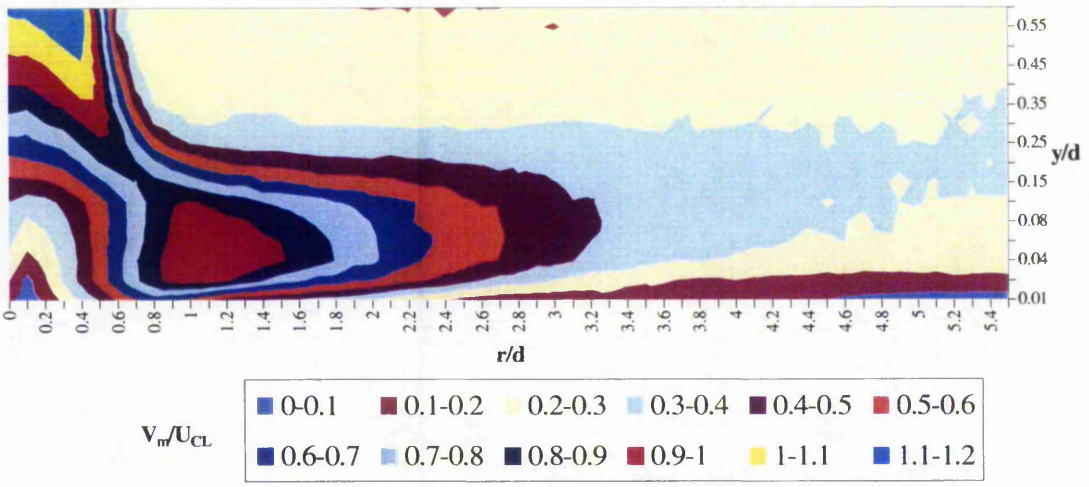

Figure 6.9: Mean velocity contour, z/d = 1.5, Re = 20 000,

$U_j / U_c = 3$, $0.01 \leq y/d \leq 0.6$.

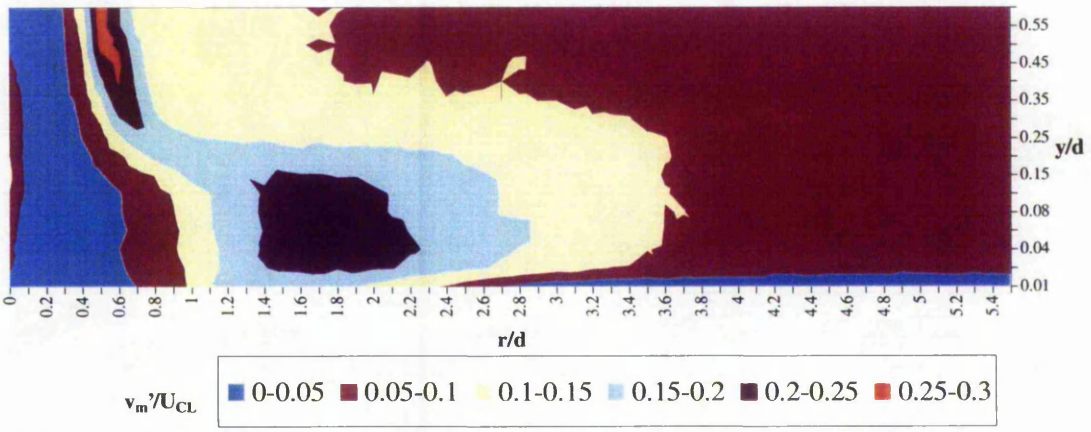

Figure 6.10: Mean turbulence contour, z/d = 1.5, Re = 20 000,

$U_j / U_c = 3$, $0.01 \leq y/d \leq 0.6$.

The impinging jet becomes highly asymmetric when the strength of the crossflow is increased further to $U_j / U_c = 2$. Figure 6.11 and 6.12 indicate that a large part of the jet core that is colliding with the upstream crossflow has been destroyed. The exact location of the stagnation point is arbitrary but the impingement begins at r/d ≈ 0.5. Upon impingement, the bulk fluid decelerates rapidly and rebounds towards the upper confining

plate. The high turbulence level at $1.8 \leq r/d \leq 2.6$ and $0.02 \leq y/d \leq 0.1$ implies that there is a major diffusion of the bulk fluid from the wall jet region.

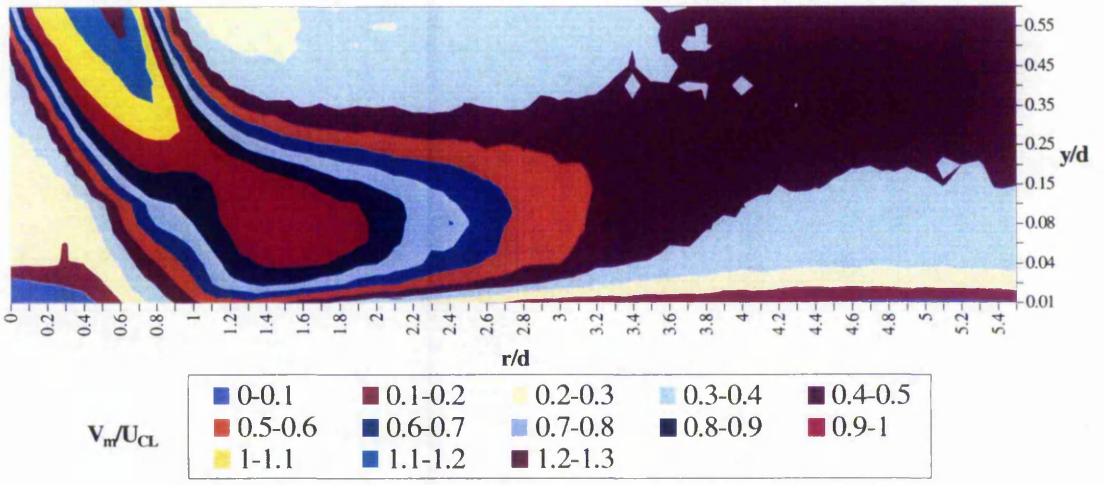

Figure 6.11: Mean velocity contour, z/d = 1.5, Re = 20 000,
$U_j / U_c = 2$, $0.01 \leq y/d \leq 0.6$.

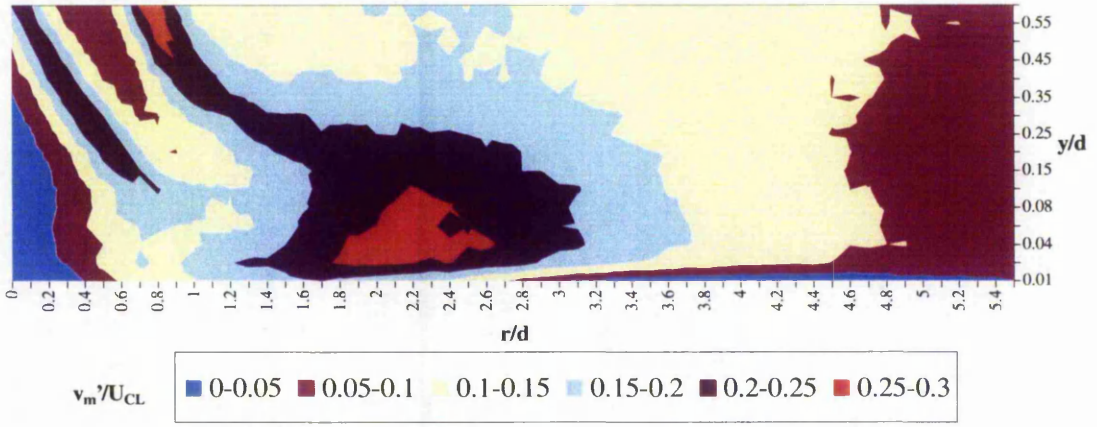

Figure 6.12: Mean turbulence contour, z/d = 1.5, Re = 20 000,
$U_j / U_c = 2$, $0.01 \leq y/d \leq 0.6$.

Figure 6.13 and 6.14 illustrate the respective near wall velocity and turbulence contours for the axisymmetric jet at a nozzle-to-plate spacing of 1.5d and exit Reynolds number of 40 000. The normalised flow field matches closely with that for Re = 20 000. Within the boundary layer ($y/d \leq 0.02$), the flow attains a maximum of $V_m / U_{CL} = 0.8 - 0.9$ at $r/d \approx 0.85$. Again, above it lays a lump of fast-moving fluid

(indicated by the 0.9 – 1.0 colour patch in Figure 6.13) which starts to decelerate at r/d ≈ 1.5 due to the unfavourable local pressure gradient. This leads to an unsteady separation of the wall jet boundary layer and subsequently a region of high turbulence which is exemplified in the interval $1.3 \leq r/d \leq 1.7$ and $0.02 \leq y/d \leq 0.08$ (Figure 6.14).

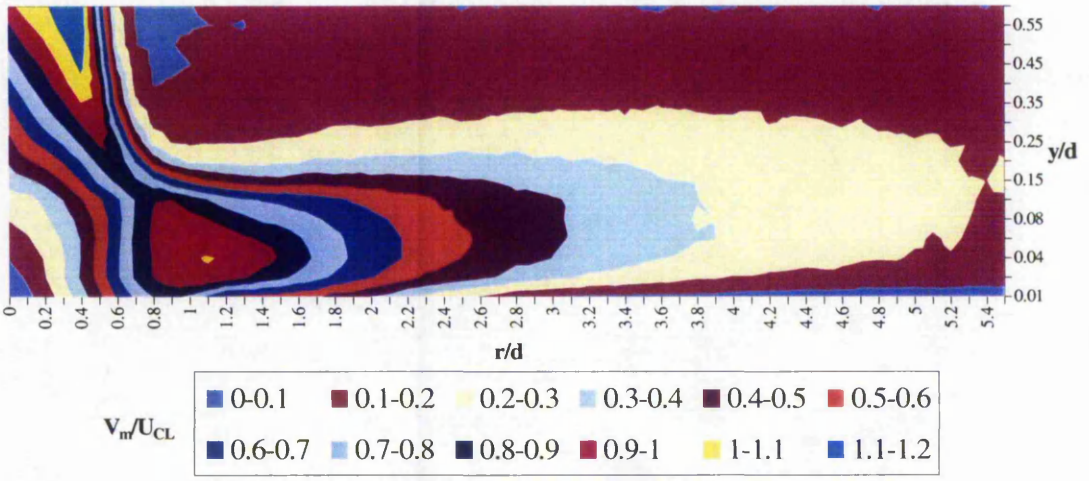

Figure 6.13: Mean velocity contour, z/d = 1.5, Re = 40 000, no crossflow, $0.01 \leq y/d \leq 0.6$.

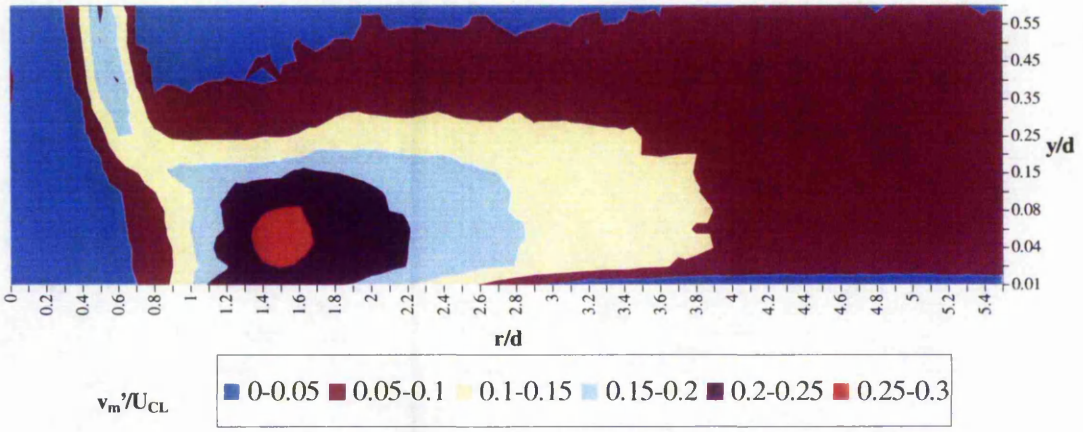

Figure 6.14: Mean turbulence contour, z/d = 1.5, Re = 40 000, no crossflow, $0.01 \leq y/d \leq 0.6$.

When a crossflow is imposed from the left of the working section at $U_J/U_c = 5$, the stagnation point is swayed slightly downstream by ≈ 0.12d. Figure 6.15 and 6.16 indicate that the flow field around the centre of the jet stays intact while the influence of the crossflow manifests outside the core of the jet. Interestingly, the crossflow again helps

to reduce the local turbulence level in the wall jet region. This corroborates with the previous case for Re = 20 000 and $U_j / U_c = 5$ and thereby suggests that unsteady separation of the wall jet could be suppressed through the provision of a moderate crossflow.

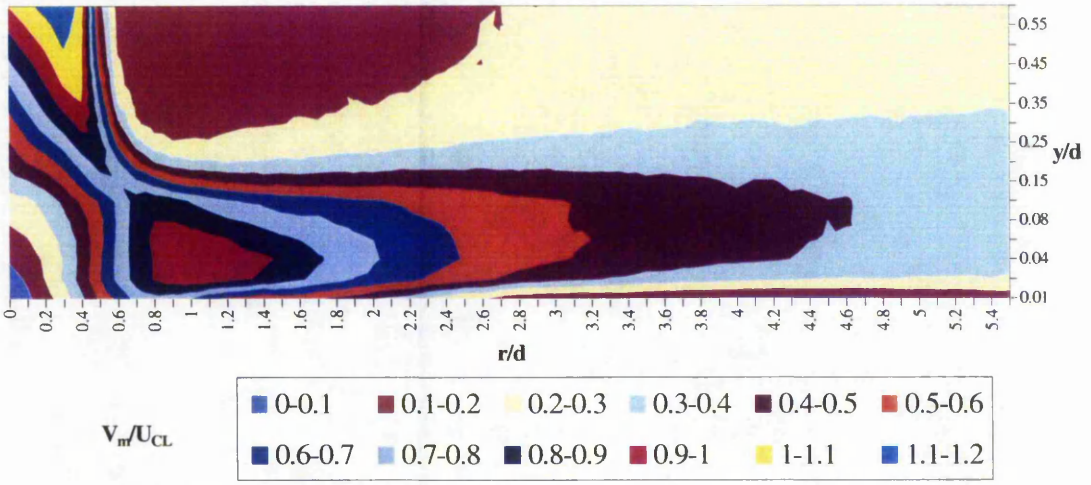

Figure 6.15: Mean velocity contour, z/d = 1.5, Re = 40 000,
$U_j / U_c = 5$, 0.01 ≤ y/d ≤ 0.6.

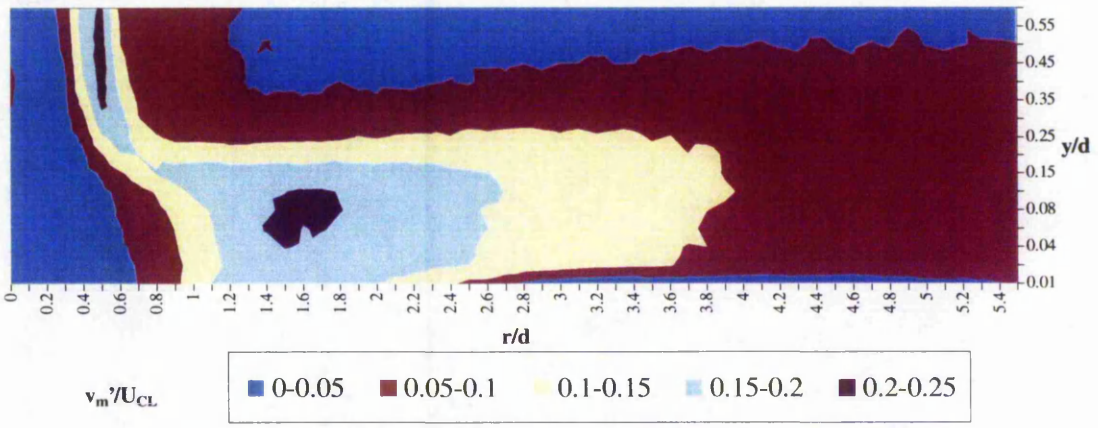

Figure 6.16: Mean turbulence contour, z/d = 1.5, Re = 40 000,
$U_j / U_c = 5$, 0.01 ≤ y/d ≤ 0.6.

Figure 6.17 and 6.18 show the respective mean velocity and turbulence contours for Re = 40 000 and $U_j / U_c = 4$. The central core of the jet is deflected downstream by ≈

0.18d. The fluid velocity in the downstream wall jet region is now adversely affected by the stronger crossflow. The turbulence level of the developing wall jet, notably in the interval $1.2 \leq r/d \leq 2.2$ and $0.01 \leq y/d \leq 0.15$, grows significantly as a result of intensified mixing between the primary jet and the crossflow.

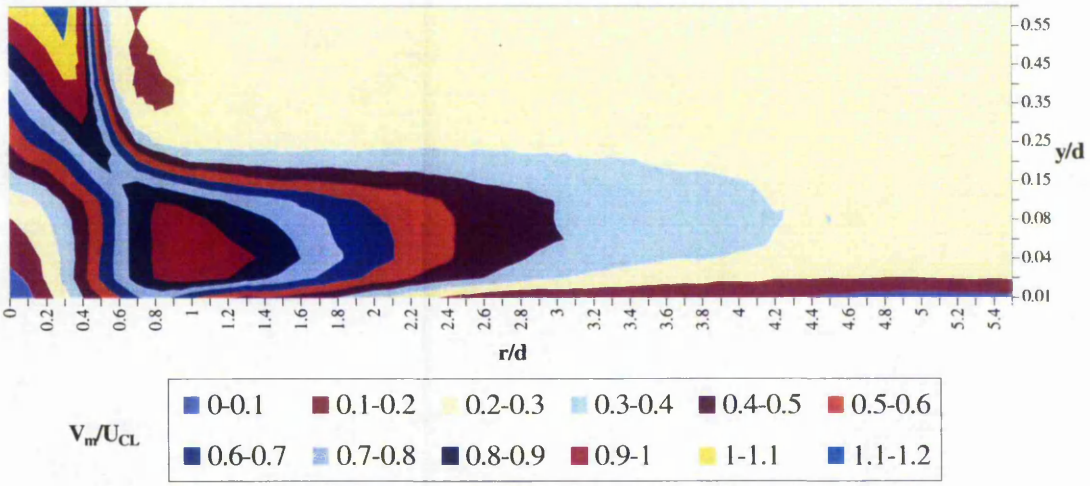

Figure 6.17: Mean velocity contour, z/d = 1.5, Re = 40 000, $U_j / U_c = 4$, $0.01 \leq y/d \leq 0.6$.

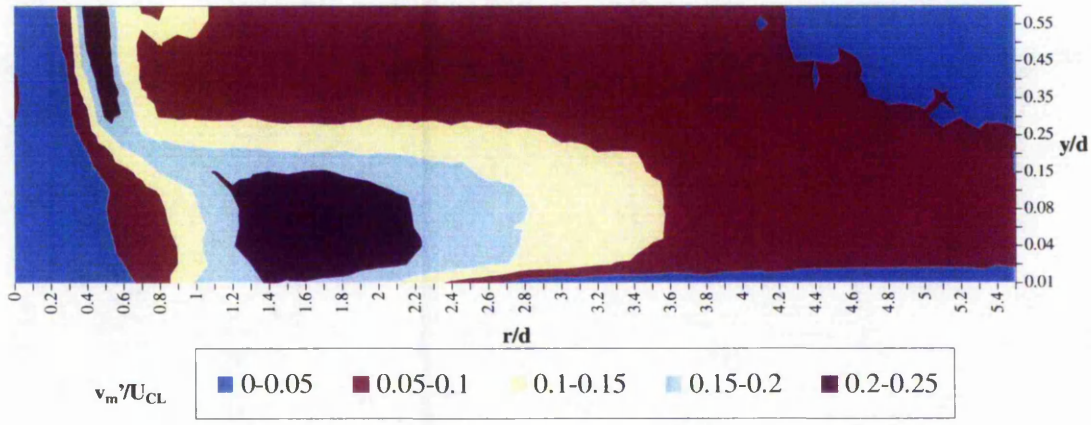

Figure 6.18: Mean turbulence contour, z/d = 1.5, Re = 40 000, $U_j / U_c = 4$, $0.01 \leq y/d \leq 0.6$.

The mean velocity and turbulence contours for Re = 40 000 and $U_j / U_c = 3$ are presented in Figure 6.19 and 6.20 respectively. The stronger crossflow pushes the

upstream impinging fluid towards the core of the jet and subsequently leads to higher turbulence levels in the interacting region, e.g. at r/d = 0. The stagnation point is now shifted by approximately 0.35d downstream. In addition, the turbulence level in the wall jet region continues to rise due to increased mixing with the crossflow fluid.

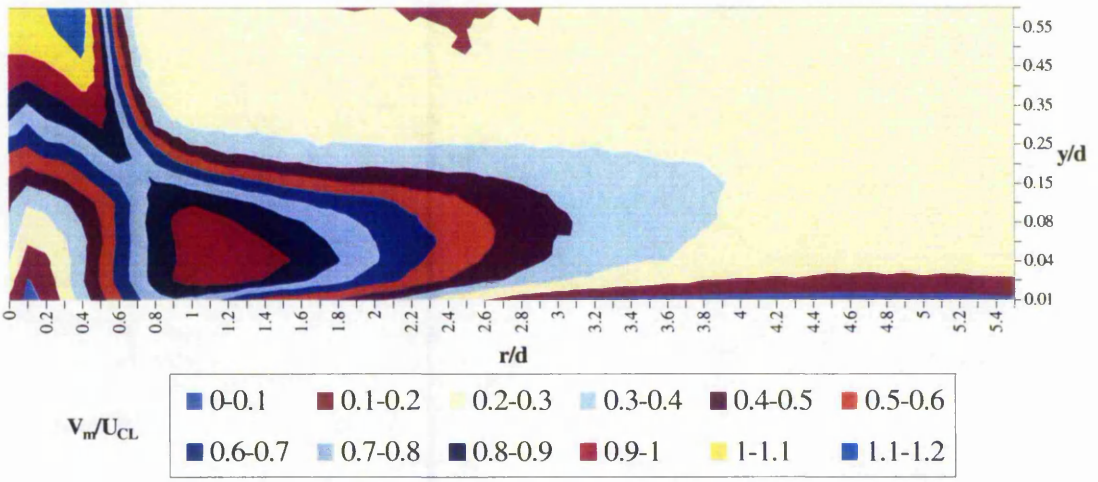

Figure 6.19: Mean velocity contour, z/d = 1.5, Re = 40 000,

$U_j / U_c = 3$, $0.01 \leq y/d \leq 0.6$.

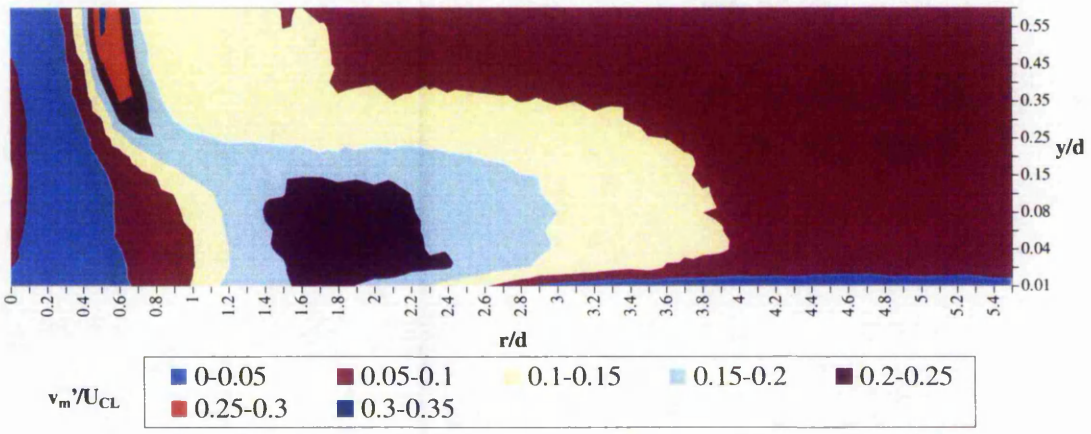

Figure 6.20: Mean turbulence contour, z/d = 1.5, Re = 40 000,

$U_j / U_c = 3$, $0.01 \leq y/d \leq 0.6$.

The symmetry of the impinging jet is destroyed when the strength of the crossflow is increased to $U_j / U_c = 2$. Figure 6.21 and 6.22 indicate that the upstream crossflow

penetrates deep into the potential core of the jet. As a result, the stagnation point becomes ambiguous even though the impingement begins at r/d ≈ 0.6. Upon impingement, the bulk fluid bounces towards the upper confining plate. At r/d ≈ 1.5, the wall jet decelerates and diffuses rapidly. Consequently, a high turbulence region is formed in the interval 1.5 ≤ r/d ≤ 2.7 and 0.01 ≤ y/d ≤ 0.15.

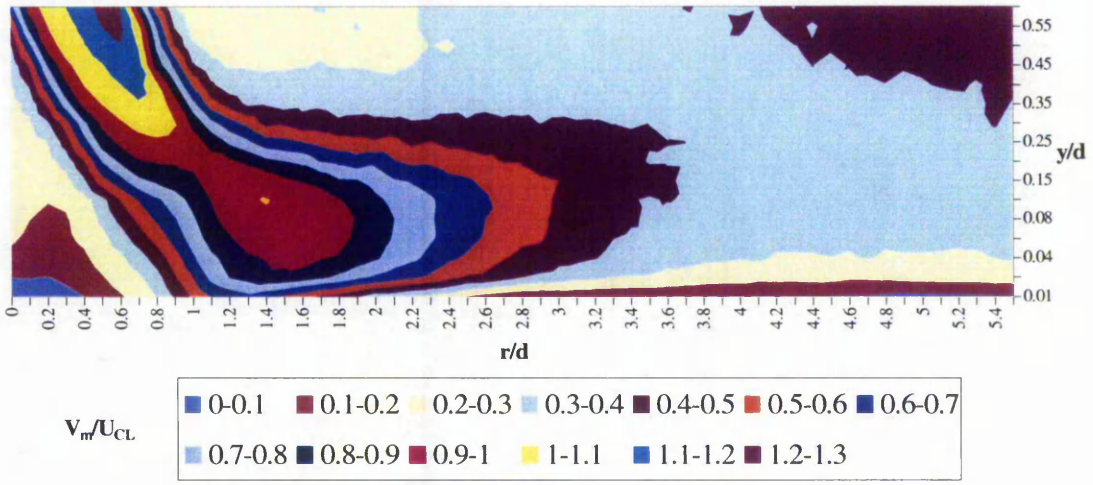

Figure 6.21: Mean velocity contour, z/d = 1.5, Re = 40 000,

$U_j / U_c = 2$, 0.01 ≤ y/d ≤ 0.6.

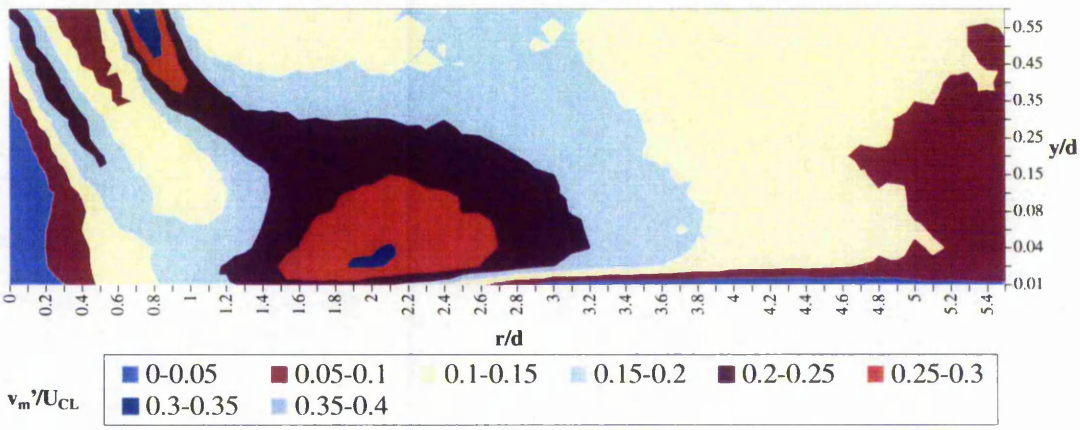

Figure 6.22: Mean turbulence contour, z/d = 1.5, Re = 40 000,

$U_j / U_c = 2$, 0.01 ≤ y/d ≤ 0.6.

The near wall velocity and turbulence characteristics of the axisymmetric jet for a non-dimensional nozzle-to-plate spacing of 3d and Reynolds number of 20 000 are illustrated in Figure 6.23 and 6.24 respectively. The jet also spreads slightly to impinge onto the target surface before diverting and accelerating radially outwards to develop into a typical wall jet. The potential core of the jet is clearly more turbulent (compared to the case for z/d = 1.5) due to the periodic toroidal vortex structures in the surrounding shear layer which grow in size and strength at the larger nozzle-to-plate spacing. The flow in the boundary layer (y/d ≤ 0.02) attains a maximum of $V_m / U_{CL} = 0.8 - 0.9$ at r/d ≈ 0.9. The behaviour of the wall jet resembles that described for z/d = 1.5, whereby a deceleration of the bulk fluid (at r/d ≈ 1.4) leads to an unsteady flow separation and subsequently a region of high turbulence. The velocity becomes negligible at r/d ≥ 4.1 and y/d ≤ 0.02.

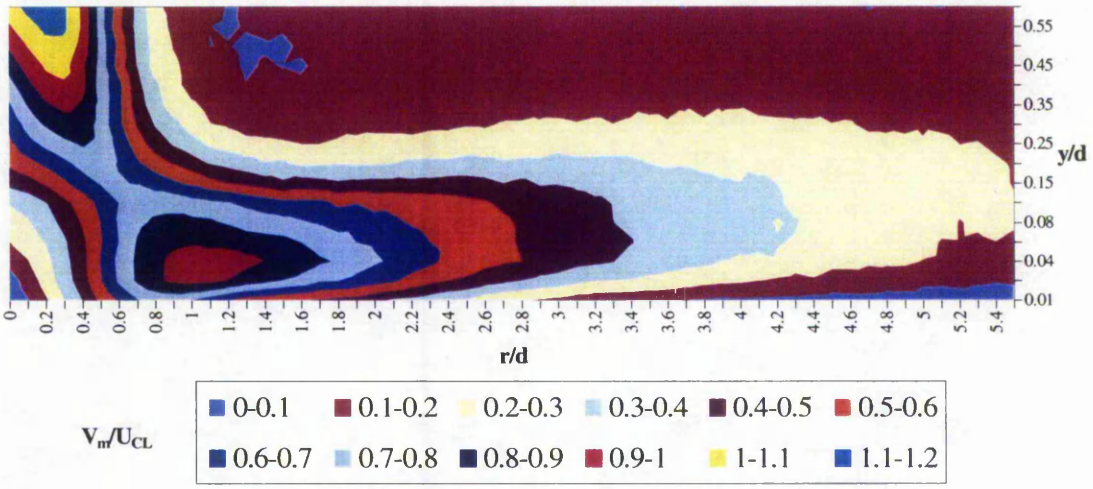

Figure 6.23: Mean velocity contour, z/d = 3, Re = 20 000, no crossflow, 0.01 ≤ y/d ≤ 0.6.

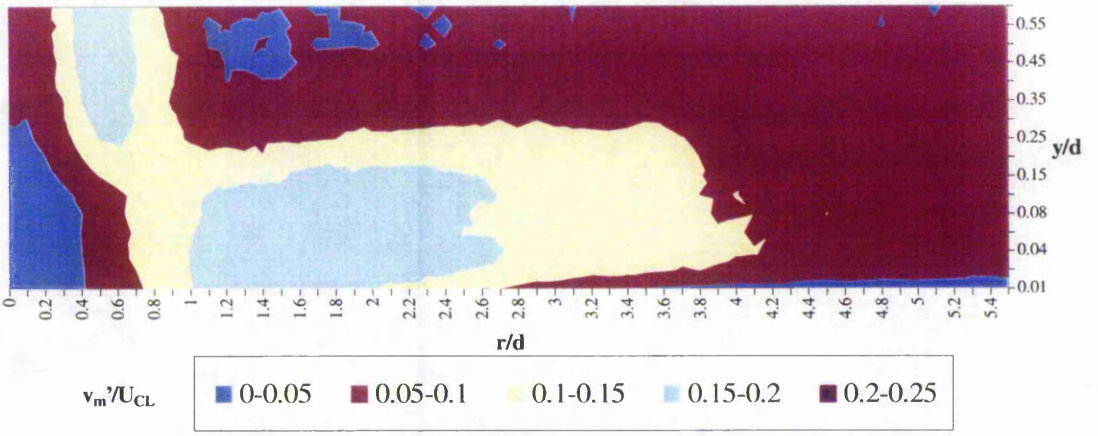

Figure 6.24: Mean turbulence contour, z/d = 3, Re = 20 000, no crossflow, $0.01 \leq y/d \leq 0.6$.

Figure 6.25 and 6.26 demonstrate that when the impinging is coupled with an upstream crossflow at $U_j / U_c = 5$, the stagnation point is deflected downstream by ≈ 0.4d. This corroborates with the work of Sparrow et al. (1975) who reported that the extent of jet deflection is accentuated at a larger nozzle-to-plate spacing. The weak crossflow is capable of disrupting the entire flow field of the intrinsically unstable jet, particularly the upstream jet core that is almost destroyed. Unlike the case for z/d = 1.5, the crossflow tends to promote flow separation through mixing and therefore increase the level of turbulence in the wall jet region.

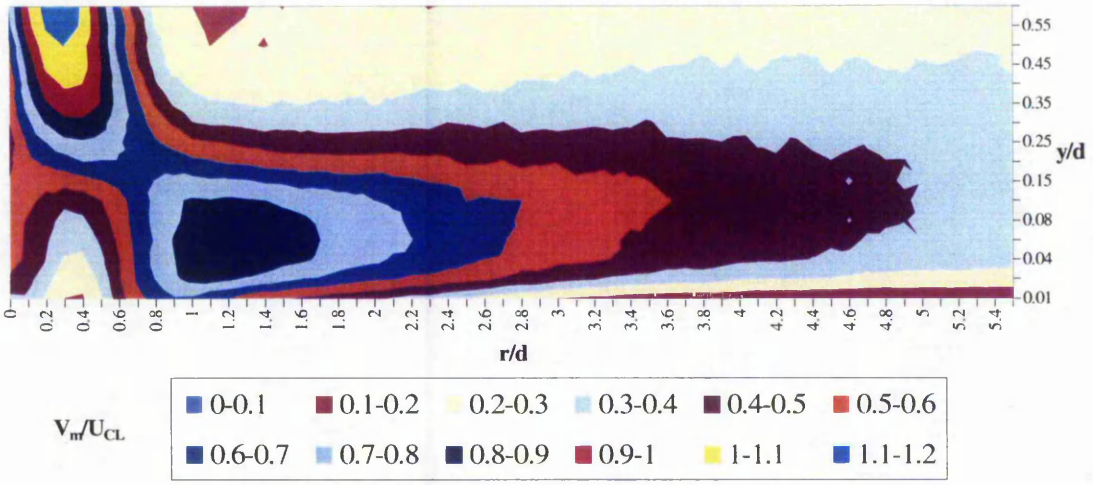

Figure 6.25: Mean velocity contour, z/d = 3, Re = 20 000,

$U_j / U_c = 5$, $0.01 \leq y/d \leq 0.6$.

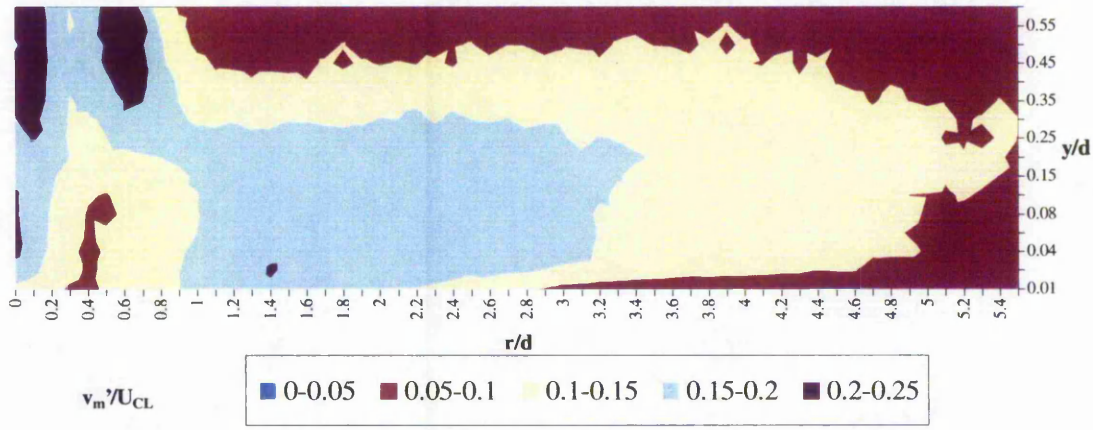

Figure 6.26: Mean turbulence contour, z/d = 3, Re = 20 000,

$U_j / U_c = 5$, $0.01 \leq y/d \leq 0.6$.

The velocity and turbulence characteristics for Re = 20 000 and $U_j / U_c = 4$ are illustrated in Figure 6.27 and 6.28 respectively. The potential core of the impinging jet is destroyed completely by the crossflow. The majority of the bulk fluid impinges at r/d ≥ 0.8 before accelerating radially outwards along the target plate. A unique region of high turbulence is also created around r/d = 0.3 due to the formation of a secondary vortex as the crossflow collides with the impinging fluid.

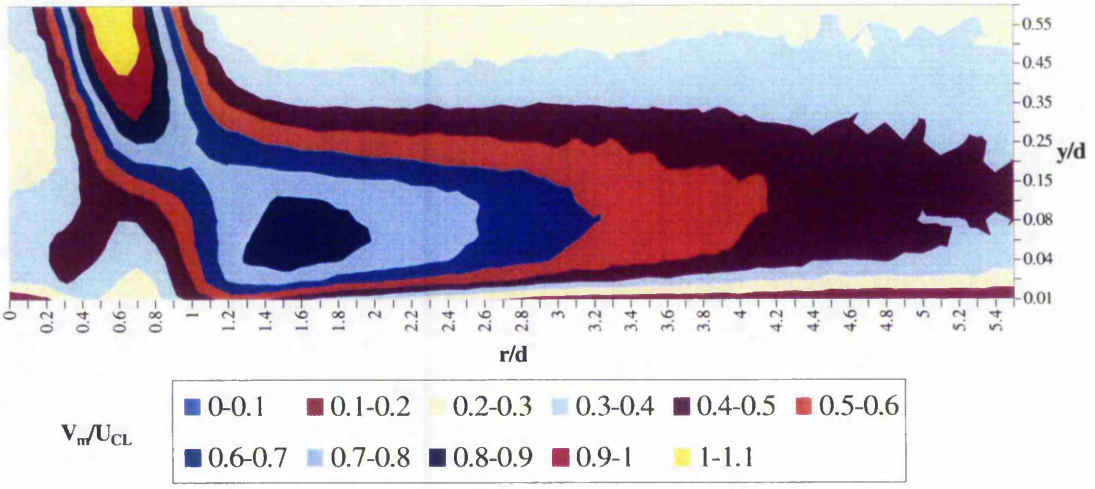

Figure 6.27: Mean velocity contour, z/d = 3, Re = 20 000,

$U_j / U_c = 4$, 0.01 ≤ y/d ≤ 0.6.

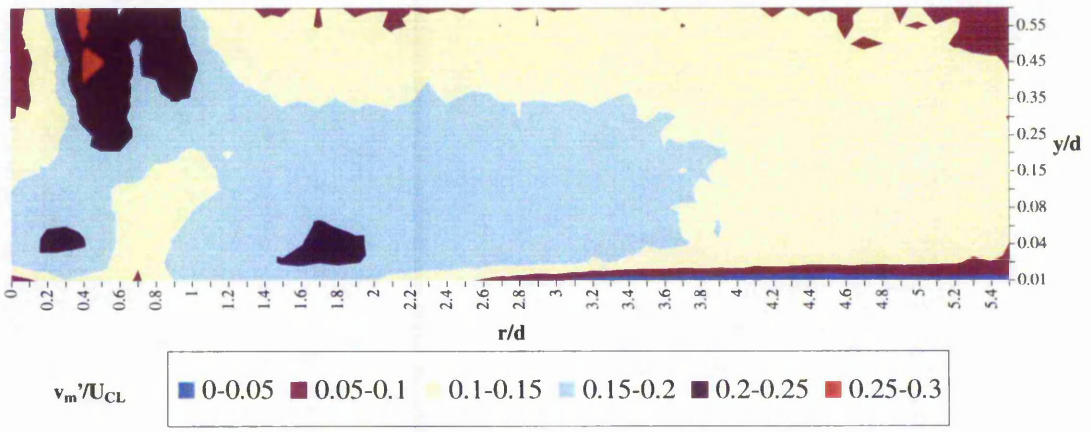

Figure 6.28: Mean turbulence contour, z/d = 3, Re = 20 000,

$U_j / U_c = 4$, 0.01 ≤ y/d ≤ 0.6.

Figure 6.29 and 6.30 indicate that as the crossflow is increased to $U_j / U_c = 3$, the impinging bulk fluid is virtually diverted such that it only hits the target plate from r/d ≈ 1.6 onwards. The near wall hydrodynamic characteristic at r/d ≤ 2.0 is dominated by the mainstream crossflow. The fluid velocity in the boundary layer (y/d ≤ 0.02) reaches a maximum of merely 0.2 - 0.3U_{CL} (at r/d ≈ 2.4). This signifies that the effectiveness of the

impinging jet has been reduced by the crossflow. The flow field is generally turbulent due to enhanced flow mixing between the impinging bulk fluid and the crossflow.

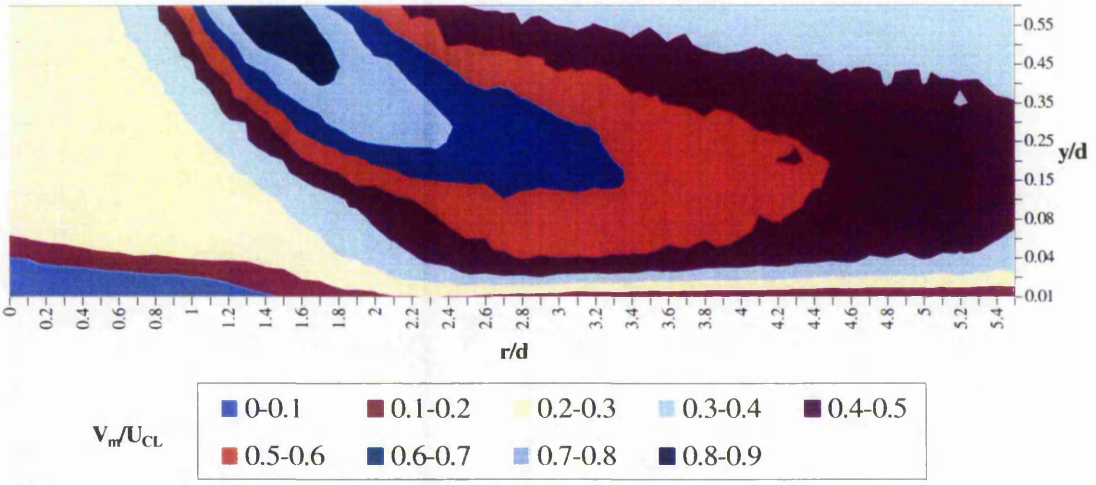

Figure 6.29: Mean velocity contour, z/d = 3, Re = 20 000,

$U_j / U_c = 3$, $0.01 \leq y/d \leq 0.6$.

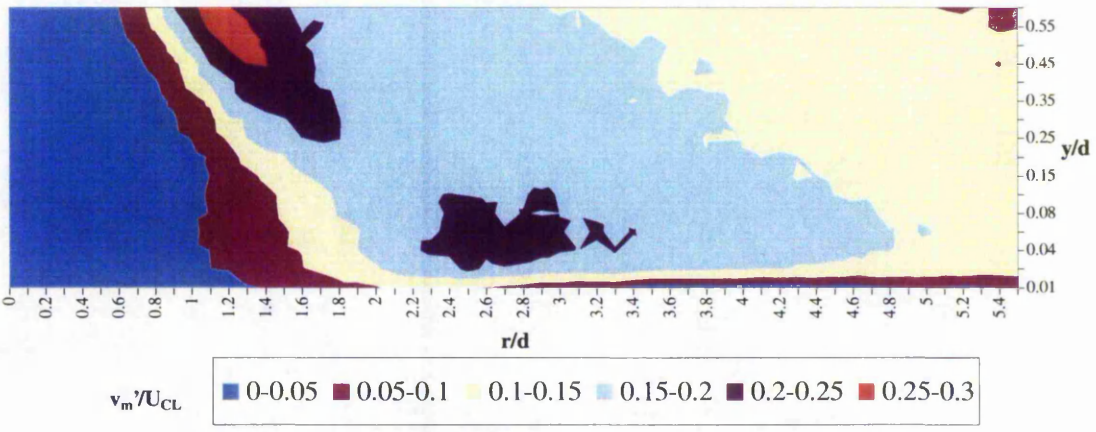

Figure 6.30: Mean turbulence contour, z/d = 3, Re = 20 000,

$U_j / U_c = 3$, $0.01 \leq y/d \leq 0.6$.

The near wall velocity and turbulence characteristics of the axisymmetric jet for a non-dimensional nozzle-to-plate spacing of 3d and Reynolds number of 40 000 are presented in Figure 6.31 and 6.32 respectively. The flow in the boundary layer (y/d ≤ 0.02) attains a maximum of $V_m / U_{CL} = 0.9 - 1.0$ at r/d ≈ 1. Similar to the case for Re = 20 000, a sudden deceleration of the wall jet (at r/d ≈ 1.55) results in an unsteady flow separation and highly turbulent bulk fluid. The near wall velocity eventually becomes negligible at r/d ≥ 4.3 and y/d ≤ 0.02.

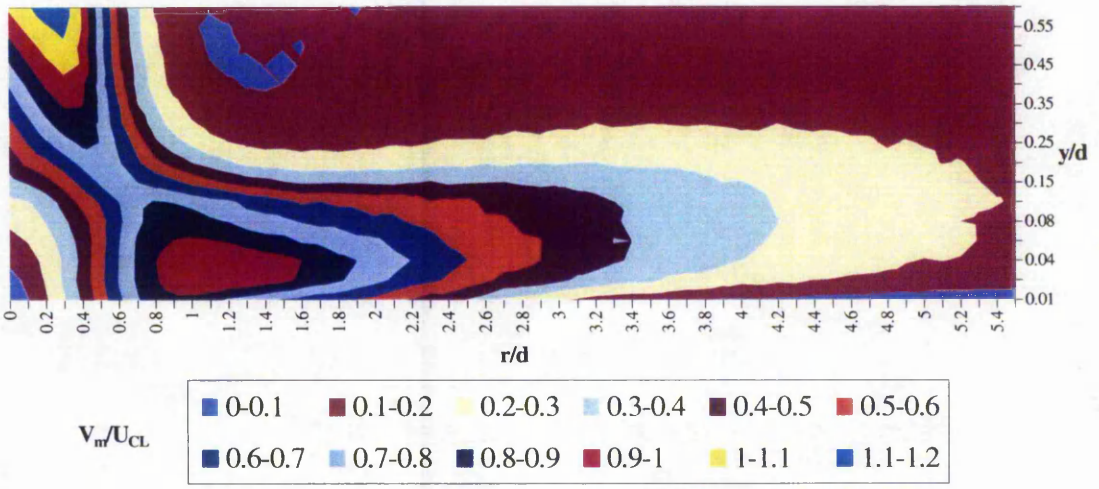

Figure 6.31: Mean velocity contour, z/d = 3, Re = 40 000, no crossflow, 0.01 ≤ y/d ≤ 0.6.

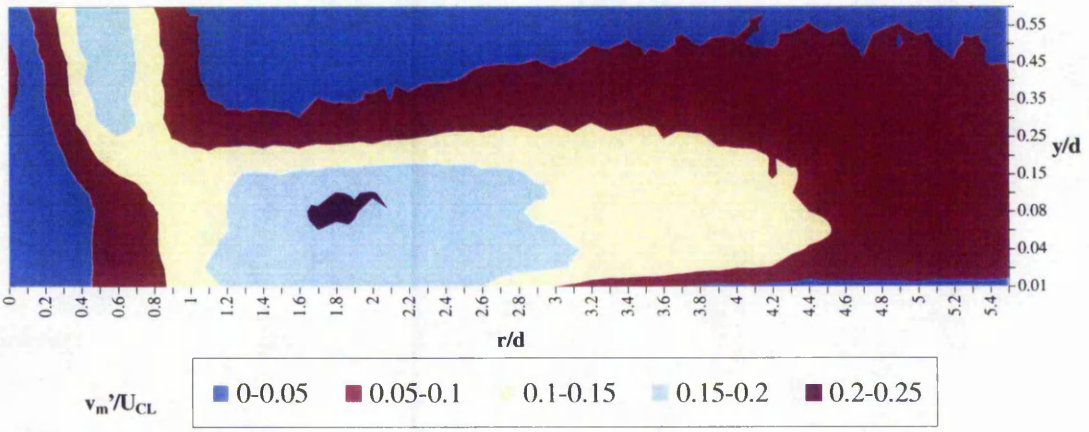

Figure 6.32: Mean turbulence contour, z/d = 3, Re = 40 000, no crossflow, 0.01 ≤ y/d ≤ 0.6.

Figure 6.33 and 6.34 illustrate the respective velocity and turbulence characteristics of the impinging jet in crossflow at a velocity ratio, U_j/U_c, of 5. The crossflow deflects the stagnation point by ≈ 0.5d downstream, and nearly destroys the entire potential core of the jet. The interaction and mixing between the impinging fluid and the crossflow also leads to high turbulence level throughout flow field.

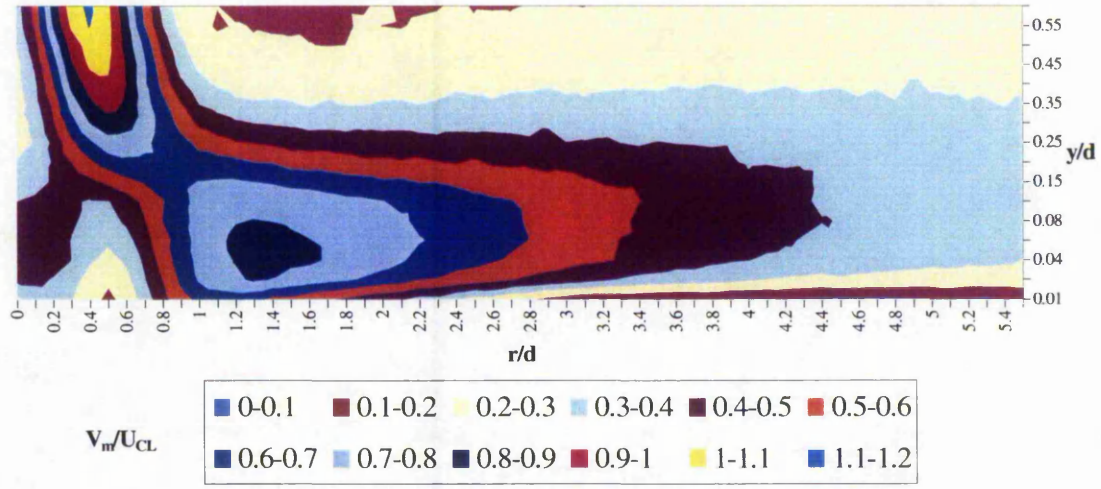

Figure 6.33: Mean velocity contour, z/d = 3, Re = 40 000,

$U_j/U_c = 5$, $0.01 \leq y/d \leq 0.6$.

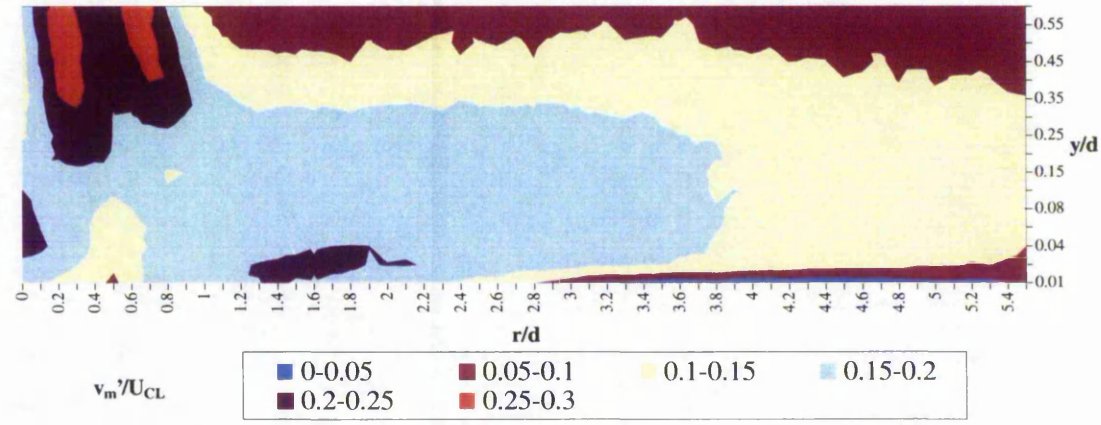

Figure 6.34: Mean turbulence contour, z/d = 3, Re = 40 000,

$U_j/U_c = 5$, $0.01 \leq y/d \leq 0.6$.

Figure 6.35 and 6.36 show that at $U_j / U_c = 4$, the potential core of the impinging jet is destroyed completely by crossflow. The impinging bulk fluid becomes highly turbulent and begins to impinge only at r/d ≈ 1.0 before accelerating radially outwards. The fluid velocity in the boundary layer (y/d ≤ 0.02) attains a maximum of 0.5 - 0.6U_{CL} at r/d ≈ 1.55. A region of high turbulence is also created at 1.1 ≤ r/d ≤ 1.8 following impingement.

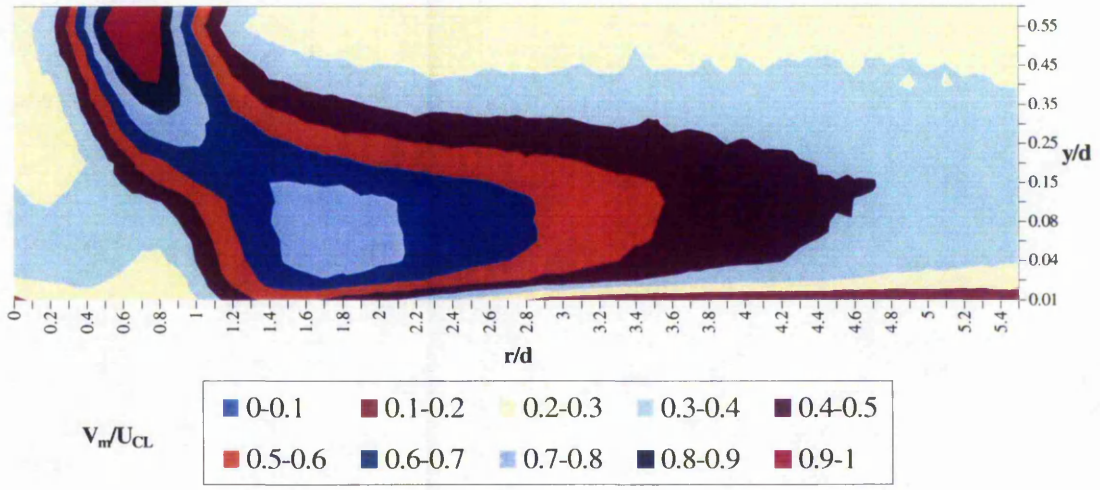

Figure 6.35: Mean velocity contour, z/d = 3, Re = 40 000,

$U_j / U_c = 4$, 0.01 ≤ y/d ≤ 0.6.

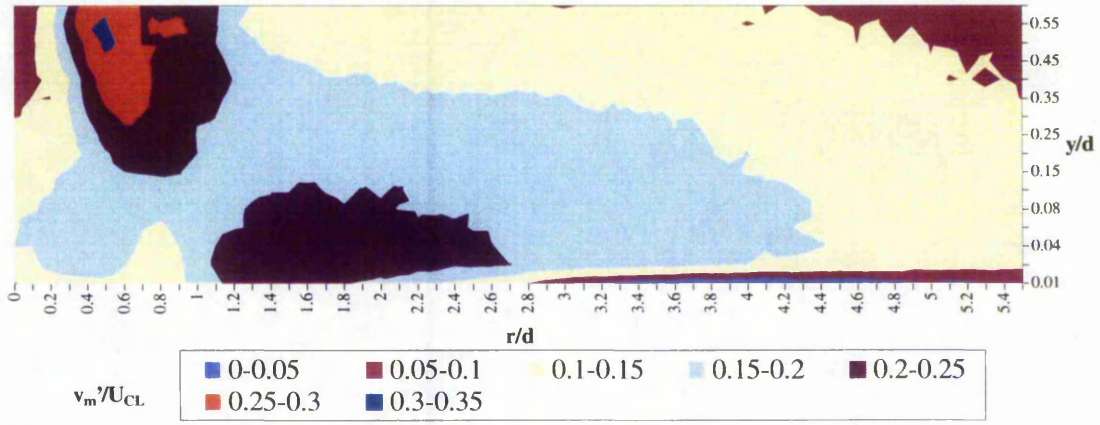

Figure 6.36: Mean turbulence contour, z/d = 3, Re = 40 000,

$U_j / U_c = 4$, 0.01 ≤ y/d ≤ 0.6.

As the crossflow is strengthened to $U_j / U_c = 3$, the impinging bulk fluid is diverted such that it only reaches the target plate from r/d ≈ 1.8 onwards. Figure 6.37 and 6.38 indicate that the near wall hydrodynamic characteristic at r/d ≤ 1.8 is essentially dominated by the upstream crossflow. The fluid velocity in the boundary layer (y/d ≤ 0.02) reaches a maximum of only 0.3 - 0.4U_{CL} (at r/d ≈ 2.6). Hence, the effectiveness of the primary impinging jet has been reduced significantly by the crossflow, which also enhances turbulence through flow interaction and mixing.

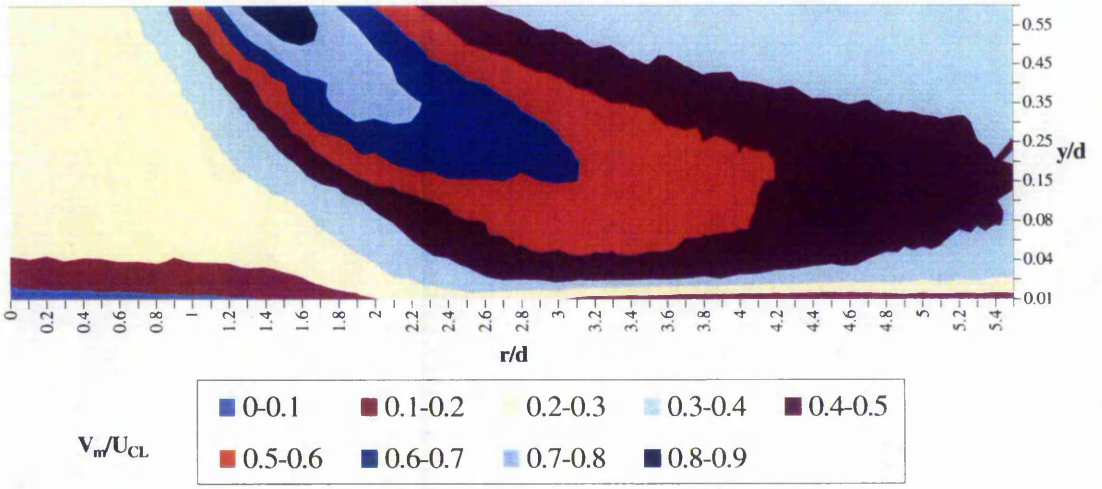

Figure 6.37: Mean velocity contour, z/d = 3, Re = 40 000, $U_j / U_c = 3$, 0.01 ≤ y/d ≤ 0.6.

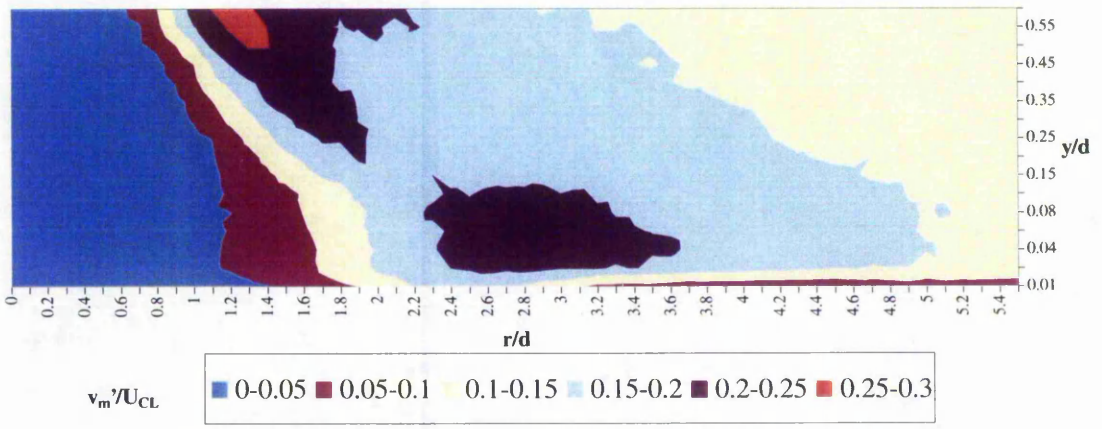

Figure 6.38: Mean turbulence contour, z/d = 3, Re = 40 000, $U_j / U_c = 3$, 0.01 ≤ y/d ≤ 0.6.

6.2.2 Near Wall Temperature and Fluctuating Temperature Characteristics

The near wall thermal boundary layer is described in terms of normalised temperature, $(T - T_{ref})/(T_{CL} - T_{ref})$, and fluctuating temperature, $t'/(T_{CL} - T_{ref})$, where the reference temperature, T_{ref}, is taken as temperature of the ambient (or crossflow) fluid. Two nozzle-to-plate spacings of 1.5d and 3.0d have been considered. The heated jet discharged at a constant Reynolds number of 20 000, and was subjected to an ambient temperature crossflow at velocity ratios, U_j/U_c, of 2, 3, 4 and 5. The temperature profiles are presented as a function of non-dimensional distance from the jet centreline (r/d = 0) to r/d = 5.5 and from the plate between y/d = 0.02 and 0.6.

Figure 6.39 and 6.40 illustrate the respective near wall temperature and fluctuating temperature contours of the heated axisymmetric impinging jet for z/d = 1.5 and Re = 20 000. The temperature within the core of the jet ($r/d \leq 0.5$) stays around 1 until $y/d \leq 0.03$, whereby sharp temperature gradients are recorded. Interestingly, a thinning of the thermal boundary layer is evident at $r/d \approx 0.6$, where a local thinning of the hydrodynamic boundary layer is also seen. These mechanisms are clearly responsible for the formation of the primary maximum in heat transfer coefficient, as reported by Gillespie (1996) and Ball (1998), amongst others. The higher fluctuating temperature in the shear layer around the core of the jet is attributed to the mixing and entrainment of the ambient fluid. Upon impingement, the temperature decreases gradually as the bulk fluid travels radially outwards.

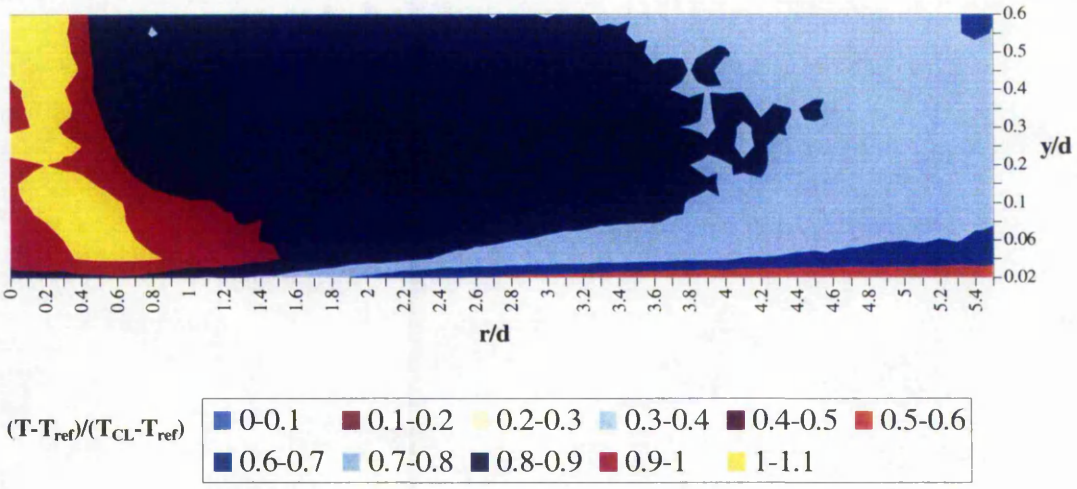

Figure 6.39: Temperature contour, z/d = 1.5, Re = 20 000,
no crossflow, $0.02 \leq y/d \leq 0.6$.

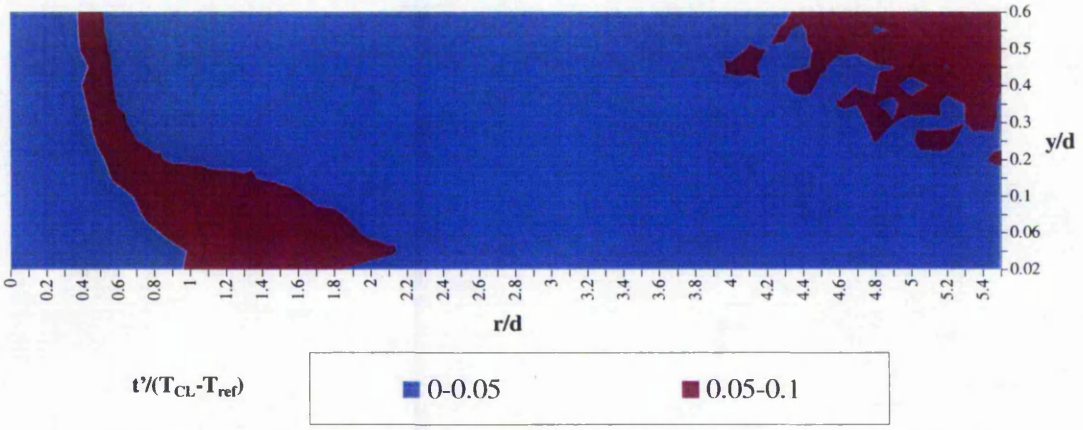

Figure 6.40: Fluctuating temperature contour, z/d = 1.5, Re = 20 000,
no crossflow, $0.02 \leq y/d \leq 0.6$.

Figure 6.41 and 6.42 show the near wall temperature and fluctuating temperature characteristics of the heated impinging jet in an ambient temperature crossflow at a velocity ratio, U_j / U_c, of 5. The potential core of the jet remains thermally undisrupted by the crossflow. However, the temperature in the downstream wall jet region falls rapidly as a result of mixing with the crossflow. This is manifested particularly in the

interval $1.2 \leq r/d \leq 2.2$ and $0.03 \leq y/d \leq 0.25$ where high temperature fluctuations are observed.

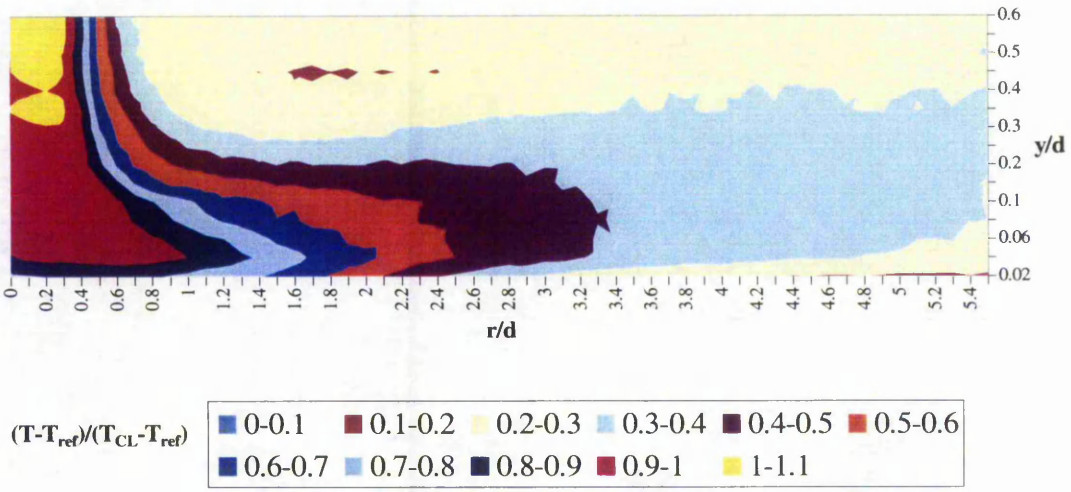

Figure 6.41: Temperature contour, z/d = 1.5, Re = 20 000,

$U_j / U_c = 5$, $0.02 \leq y/d \leq 0.6$.

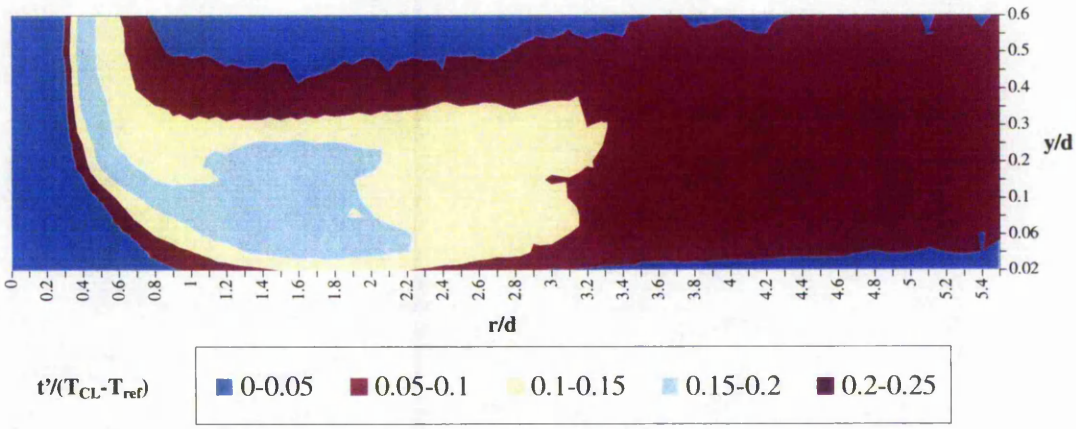

Figure 6.42: Fluctuating temperature contour, z/d = 1.5, Re = 20 000,

$U_j / U_c = 5$, $0.02 \leq y/d \leq 0.6$.

The near wall temperature and fluctuating temperature profiles for z/d = 1.5, Re = 20 000 and $U_j / U_c = 4$ are illustrated in Figure 6.43 and 6.44 respectively. Expectedly, the increased crossflow causes the temperature of the wall jet to fall more rapidly and therefore leads to higher local temperature fluctuations.

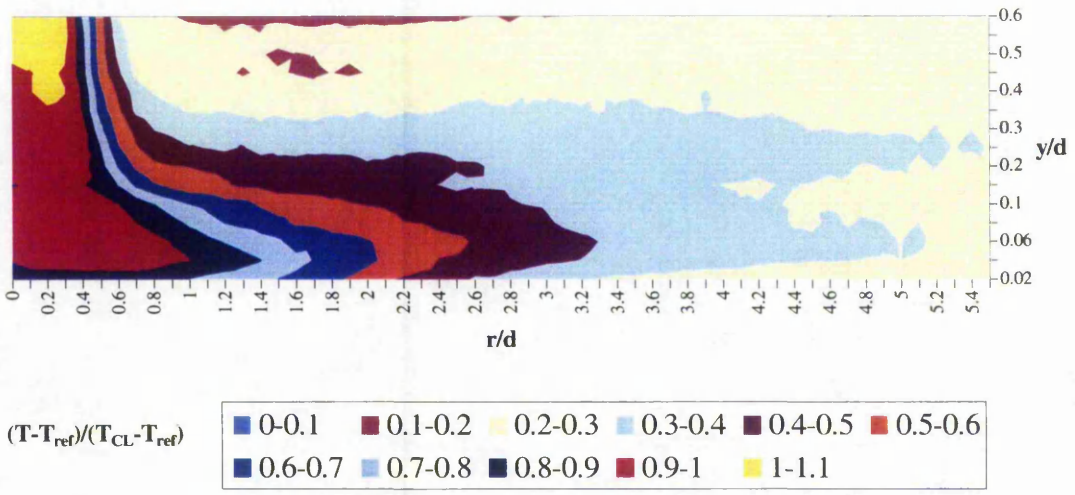

Figure 6.43: Temperature contour, z/d = 1.5, Re = 20 000,

$U_j / U_c = 4$, $0.02 \leq$ y/d ≤ 0.6.

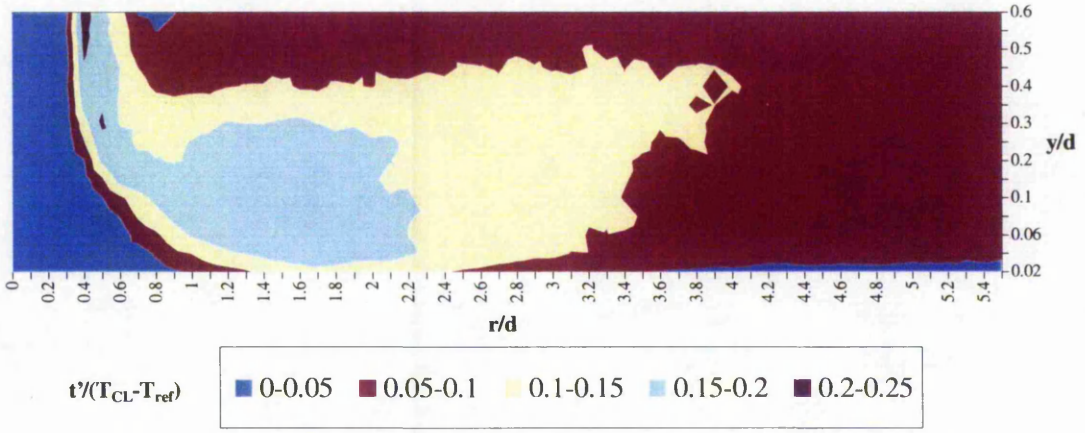

Figure 6.44: Fluctuating temperature contour, z/d = 1.5, Re = 20 000,

$U_j / U_c = 4$, $0.02 \leq$ y/d ≤ 0.6.

At $U_j / U_c = 3$, the influence of the upstream crossflow becomes significant as it penetrates into the core of the jet and undergoes both thermal and hydrodynamic mixings with the impinging bulk fluid. Figure 6.45 and 6.46 demonstrate that the temperature and fluctuating temperature (at r/d = 0) are clearly affected by the oncoming crossflow. Thermal mixing between the downstream wall jet and the crossflow also increases considerably.

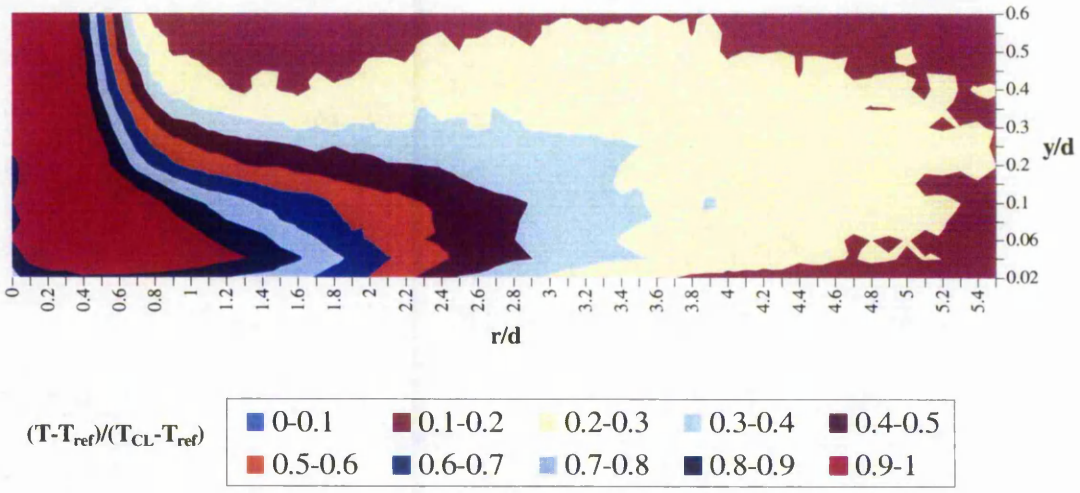

Figure 6.45: Temperature contour, z/d = 1.5, Re = 20 000,

$U_j / U_c = 3$, $0.02 \leq y/d \leq 0.6$.

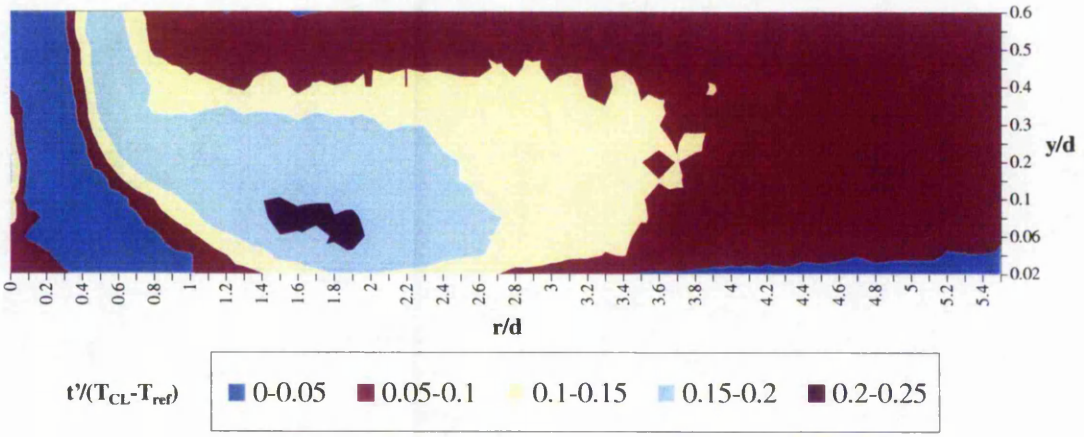

Figure 6.46: Fluctuating temperature contour, z/d = 1.5, Re = 20 000,

$U_j / U_c = 3$, $0.02 \leq y/d \leq 0.6$.

Figure 6.47 and 6.48 indicate that as the crossflow is strengthened to $U_j / U_c = 2$, the heated impinging jet is deflected downstream such that impingement only begins at r/d ≈ 0.5. The upstream crossflow dominates the near wall thermal characteristic at r/d ≤ 0.5, beyond which the temperature field of the impinging fluid builds up gradually. The fluid temperature in the vicinity of the wall (y/d ≤ 0.03) reaches a maximum normalised

value of only 0.6 - 0.7 (at r/d ≈ 2.1). This means that the heat transfer effectiveness of the impinging jet would be degraded appreciably for such a flow configuration.

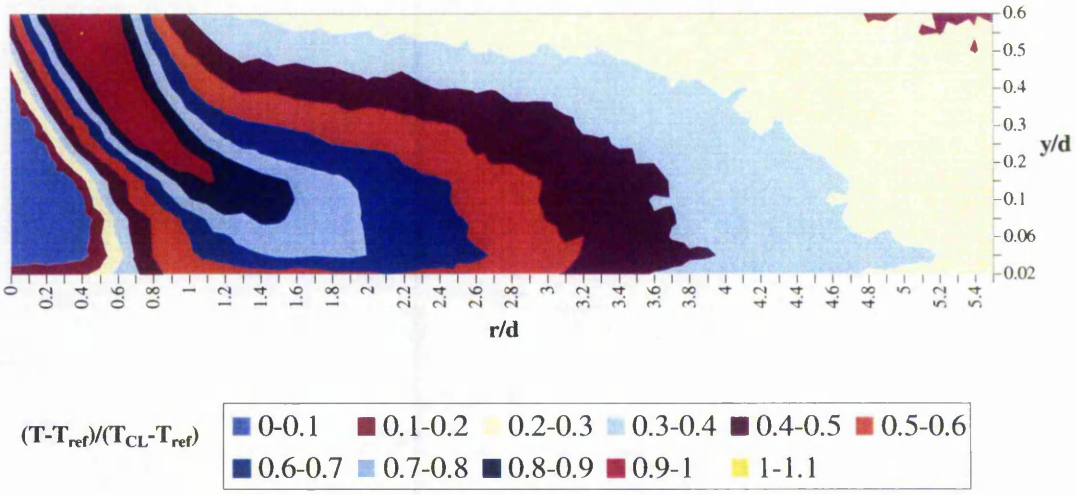

Figure 6.47: Temperature contour, z/d = 1.5, Re = 20 000,

$U_j / U_c = 2$, $0.02 \leq y/d \leq 0.6$.

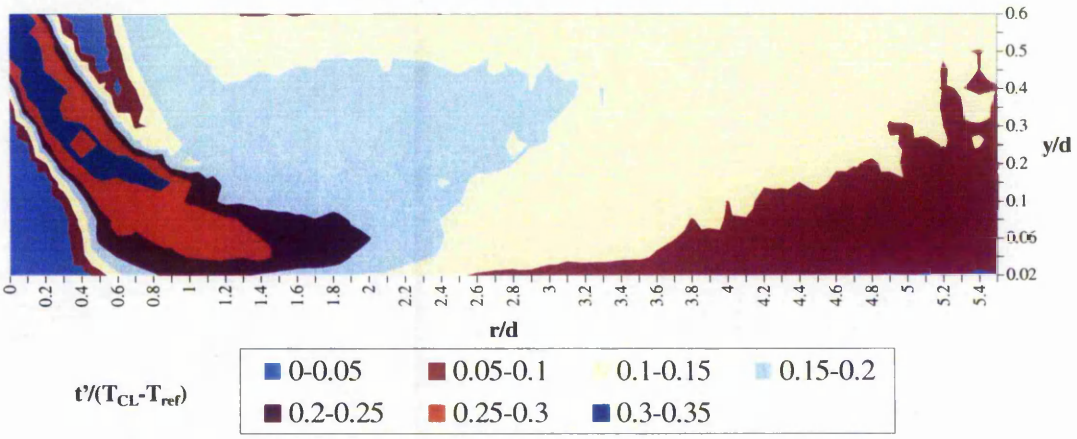

Figure 6.48: Fluctuating temperature contour, z/d = 1.5, Re = 20 000,

$U_j / U_c = 2$, $0.02 \leq y/d \leq 0.6$.

The near wall temperature and fluctuating temperature characteristics of the heated axisymmetric impinging jet for z/d = 3 and Re = 20 000 are presented in Figure 6.49 and 6.50 respectively. The fluid temperature within jet core remains at around 1 until y/d ≤ 0.04, where it starts to fall sharply. The temperature field changes more rapidly

(compared to the case for z/d = 1.5) due to increased mixing with the surrounding ambient fluid at the larger nozzle-to-plate spacing. This is demonstrated by the higher temperature fluctuations around the jet core and the wall jet region. Upon impingement, the temperature field diminishes as the bulk fluid moves radially outwards.

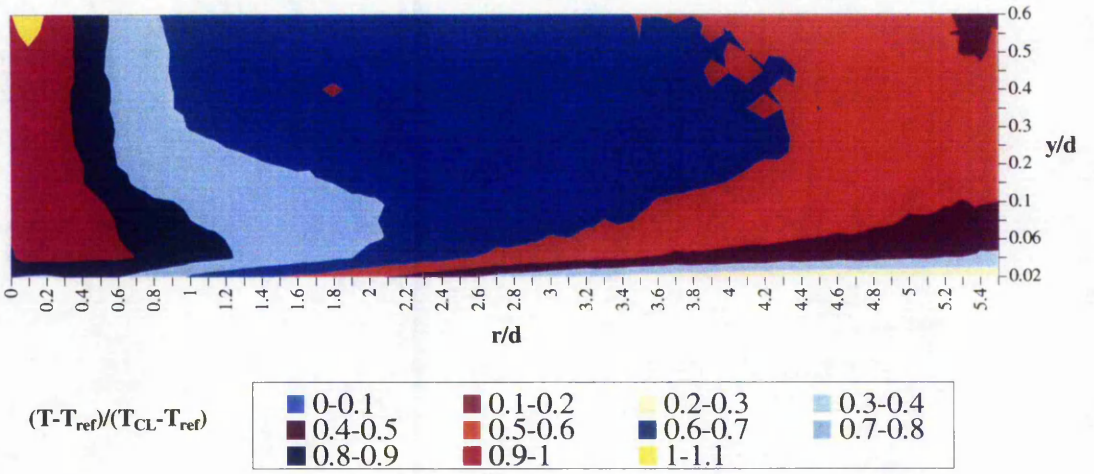

Figure 6.49: Temperature contour, z/d = 3, Re = 20 000,
no crossflow, $0.02 \leq y/d \leq 0.6$.

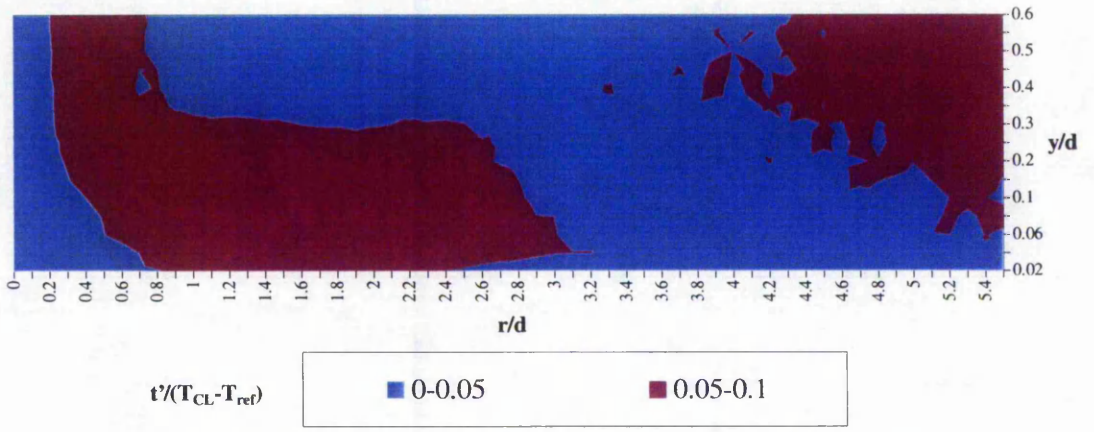

Figure 6.50: Fluctuating temperature contour, z/d = 3, Re = 20 000,
no crossflow, $0.02 \leq y/d \leq 0.6$.

Figure 6.51 and 6.52 demonstrate that when a crossflow is imposed at $U_j / U_c = 5$, the entire thermal field of the impinging jet is affected. The high temperature

fluctuations in the interval $0 \leq r/d \leq 0.4$ and $0.25 \leq y/d \leq 0.6$ indicate high level of thermal mixing in the core of the jet. The impinging jet is clearly less effective as the temperature at $y/d \leq 0.04$ attains a maximum normalised value of only 0.6 – 0.7, compared to 0.9 – 1.0 in the case for $z/d = 1.5$.

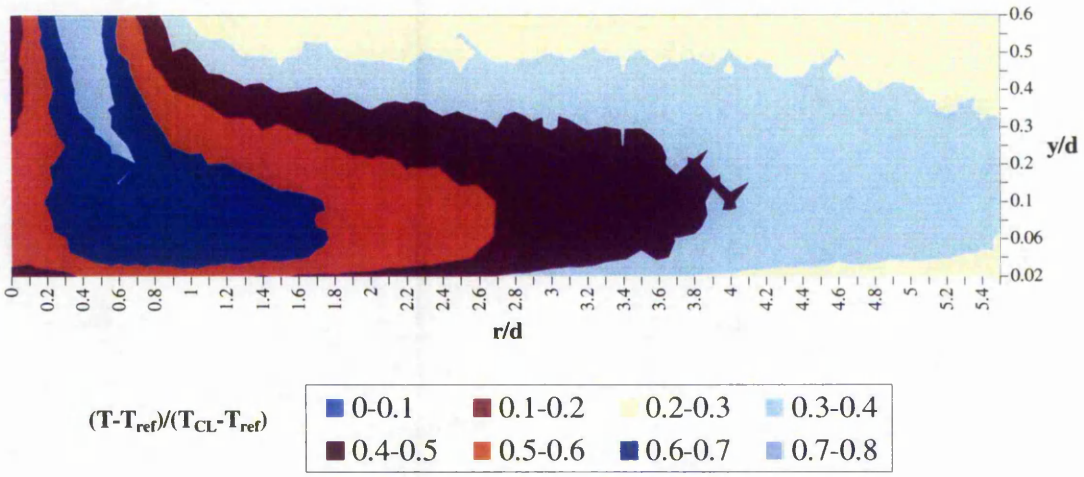

Figure 6.51: Temperature contour, z/d = 3, Re = 20 000, $U_j / U_c = 5$, $0.02 \leq y/d \leq 0.6$.

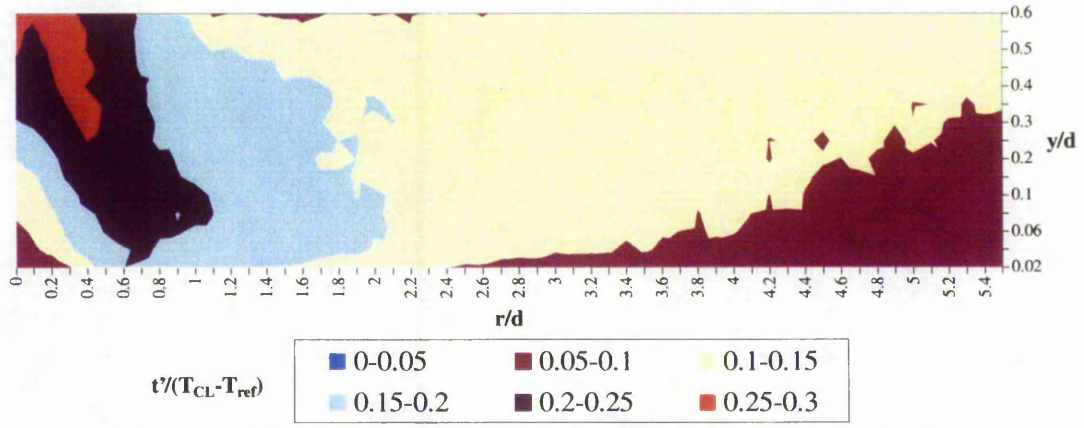

Figure 6.52: Fluctuating temperature contour, z/d = 3, Re = 20 000, $U_j / U_c = 5$, $0.02 \leq y/d \leq 0.6$.

At $U_j / U_c = 4$, the thermal mixing between the impinging bulk fluid and the upstream crossflow rises significantly. Figure 6.53 and 6.54 show that the thermal

disruption in the core of the jet intensifies as a result of the increased crossflow. Evidently, the thermal field at r/d ≤ 0.5 and y/d ≥ 0.27 is made up predominantly by the crossflow.

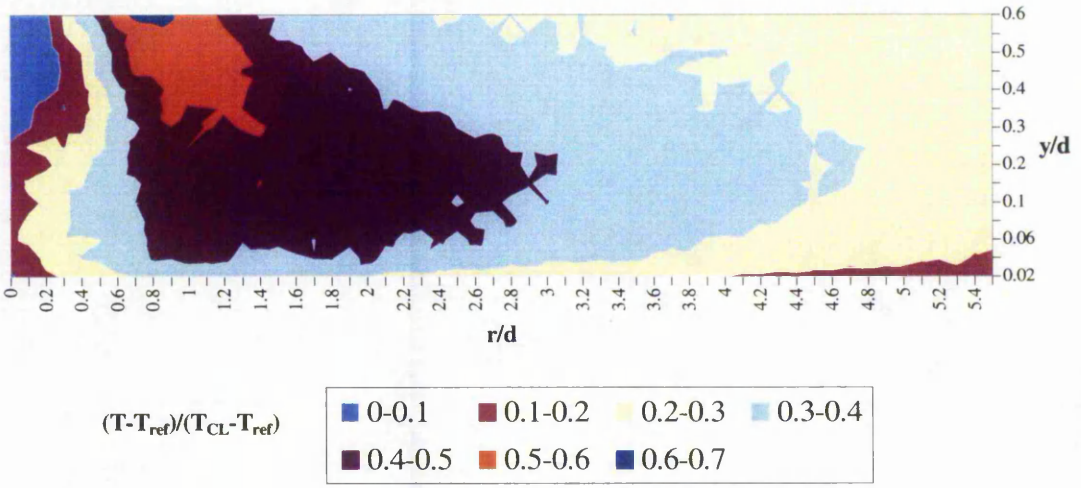

Figure 6.53: Temperature contour, z/d = 3, Re = 20 000,
$U_j / U_c = 4$, 0.02 ≤ y/d ≤ 0.6.

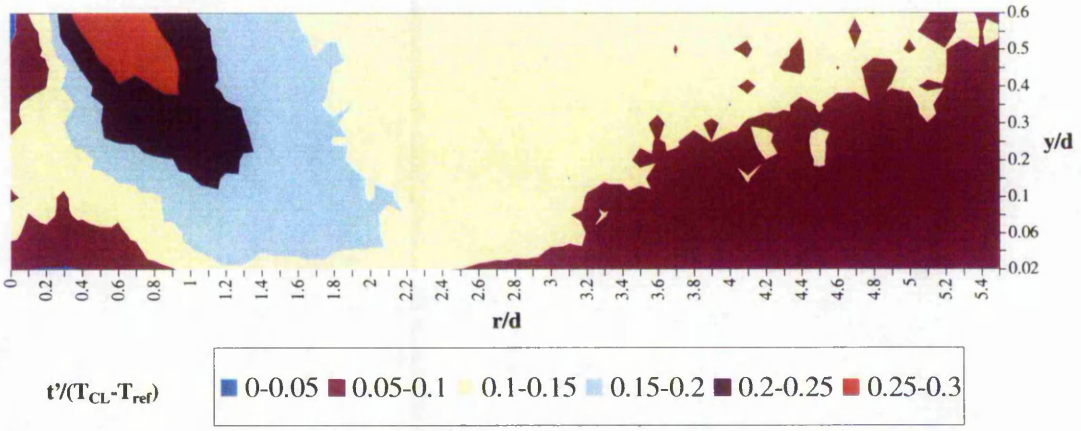

Figure 6.54: Fluctuating temperature contour, z/d = 3, Re = 20 000,
$U_j / U_c = 4$, 0.02 ≤ y/d ≤ 0.6.

Figure 6.55 and 6.56 illustrate that as the crossflow is strengthened to $U_j / U_c = 3$, the thermal field of the impinging jet is diverted from the geometrical centreline. Specifically, the crossflow dominates the near wall temperature (at y/d ≤ 0.04) up to r/d ≈

1.6, beyond which the thermal field of the impinging jet builds up slowly. The highest normalised temperature at y/d ≤ 0.04 is only 0.3 – 0.4, approximately 63 % lower than in the case for z/d = 1.5. Hence, the impinging jet is considered ineffective for such a flow configuration.

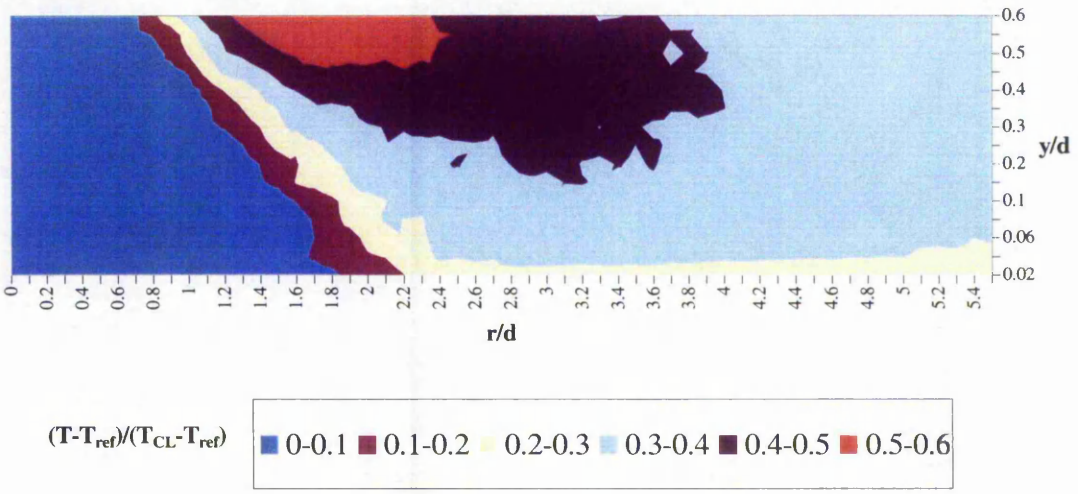

Figure 6.55: Temperature contour, z/d = 3, Re = 20 000,

$U_j / U_c = 3$, 0.02 ≤ y/d ≤ 0.6.

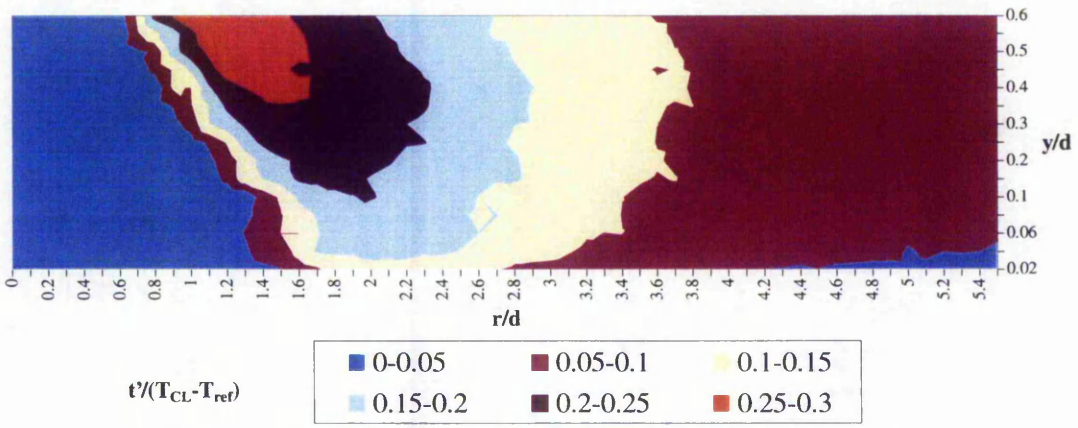

Figure 6.56: Fluctuating temperature contour, z/d = 3, Re = 20 000,

$U_j / U_c = 3$, 0.02 ≤ y/d ≤ 0.6.

6.3 Concluding Remarks

A detailed experimental study of confined single impinging jets with, and without, crossflow has been undertaken. Non-dimensional nozzle-to-plate spacings of 1.5d and 3d were investigated. For the near wall hydrodynamic investigation, the ambient temperature jet discharged with a uniform exit velocity profile at Reynolds numbers of 20 000 and 40 000, and was subjected to a crossflow at jet-to-crossflow velocity ratios of 2, 3, 4 and 5. For the near wall thermal investigation, the heated jet discharged with a uniform exit temperature profile at a constant Reynolds number of 20 000, and was also subjected to a crossflow at jet-to-crossflow velocity ratios of 2, 3, 4 and 5. The distributions of near wall velocity, turbulence, temperature and fluctuating temperature were determined using hot-wire anemometry and cold-wire thermometry techniques. The data have been fully analysed, interpreted and compared, wherever possible, with previously published work. Specifically, the data for the confined single axisymmetric impinging jets compare favourably with that obtained by Ball (1998) for the similar flow condition.

With the z/d = 1.5 configuration, the axisymmetric impinging jet for Re = 20 000 spreads slightly before striking onto the target surface covering $0.6 \leq r/d \leq 0.6$. The bulk fluid then diverts and accelerates radially outwards to develop into a wall jet. The core of the impinging jet is surrounded by large-scale turbulent structures which are transported onto the wall (at $r/d \approx 0.7$), thereby prompting a local thinning and transition of the wall jet from laminar to turbulent flow. A region of high turbulence is created in the interval $1.1 \leq r/d \leq 1.9$ and $0.02 \leq y/d \leq 0.15$, presumably due to an unsteady flow separation from the wall jet. At $r/d \geq 2$, the bulk fluid rolls-back upon itself and recirculates towards the upper confining plate. When the impinging jet is imposed with a crossflow at a jet-to-crossflow velocity ratio, U_j / U_c, of 5, the stagnation point is swayed downstream (by ≈ 0.1d). The primary impinging jet remains dominant over the crossflow. The crossflow tends to suppress flow separation (and hence the turbulence level) in the downstream wall jet region by forcing the bulk fluid to re-attach to the wall. At $U_j / U_c = 4$, the core of the impinging jet is deflected by ≈ 0.16d. The turbulence level in the downstream wall jet

rises due to intensified mixing with the crossflow. At $U_j/U_c = 3$, the crossflow drives the upstream impinging fluid towards the core of the jet, and deflects the stagnation point downstream by ≈ 0.32d. The turbulence level in the wall jet region continues to rise as a result of increased flow mixing. By $U_j/U_c = 2$, a large part of the jet core is destroyed and the impingement begins only at r/d ≈ 0.5.

The velocity and turbulence characteristics of the axisymmetric impinging jet for Re = 40 000 resemble that described for Re = 20 000. For the jet in crossflow at $U_j/U_c = 5$, the stagnation point is swayed slightly downstream by ≈ 0.12d. Interestingly, the crossflow again helps to suppress the turbulence in the downstream wall jet region, thereby suggesting that unsteady separation of the wall jet could be minimised by a moderate strength crossflow. At $U_j/U_c = 4$, the core of the jet is deflected downstream by ≈ 0.18d and the turbulence level of the developing wall jet continues to grow. The crossflow forces the upstream impinging fluid towards the core of the jet at $U_j/U_c = 3$, thereby resulting in a higher local turbulence level. The resulting deflection of the stagnation point increases to 0.35d. By $U_j/U_c = 2$, the crossflow completely penetrates into the core of the jet.

With the z/d = 3 configuration, the axisymmetric impinging jet for Re = 20 000 also, upon impingement, accelerates radially outwards to develop into a typical wall jet. The core of the jet is more turbulent (compared to the case for z/d = 1.5) as the surrounding toroidal vortices grow in size and strength at the larger nozzle-to-plate spacing. A drastic deceleration of the wall jet (at r/d ≈ 1.4) also leads to an unsteady flow separation and a region of high turbulence. When the impinging jet is coupled with an upstream crossflow at $U_j/U_c = 5$, the stagnation point is deflected as much as ≈ 0.4d downstream. This is in line with the work of Sparrow et al. (1975) who reported that jet deflection is increased at a larger nozzle-to-plate spacing. The crossflow disrupts the entire flow field of the impinging jet and causes a flow separation in the wall jet region. By $U_j/U_c = 4$, the core of the impinging jet is destroyed by the crossflow. As the

crossflow is strengthened to $U_j / U_c = 3$, the jet fluid is diverted such that the near wall hydrodynamic characteristic at r/d ≤ 1.6 is dominated by the crossflow. The impinging jet becomes ineffective as the fluid velocity in the boundary layer (y/d ≤ 0.02) attains a maximum of merely 0.2 - 0.3U_{CL} (at r/d ≈ 2.4).

The near wall velocity and turbulence characteristics of the axisymmetric jet for Re = 40 000 resemble that described for Re = 20 000. A sudden deceleration of the wall jet (at r/d ≈ 1.55) leads to an unsteady flow separation and a high local turbulence level. When a crossflow is imposed at $U_j / U_c = 5$, the stagnation point is deflected downstream by ≈ 0.5d. The interaction and mixing between the impinging fluid and the crossflow also lead to higher turbulence level throughout the flow field. At $U_j / U_c = 4$, the entire core of the impinging jet is destroyed by crossflow and light impingement begins only at r/d ≥ 1.0. As the crossflow is strengthened to $U_j / U_c = 3$, the impinging bulk fluid is diverted such that it only reaches the target plate from r/d ≈ 1.8 onwards. Essentially, the near wall hydrodynamic characteristic at r/d ≤ 1.8 is dominated by the crossflow. The effectiveness of the impinging jet is also depleted as the fluid velocity in the boundary layer (y/d ≤ 0.02) reaches a maximum of merely 0.3 - 0.4U_{CL} (at r/d ≈ 2.6).

For the heated axisymmetric impinging jet at z/d = 1.5 and Re = 20 000, the temperature within the core of the jet (r/d ≤ 0.5) remains constant until y/d ≤ 0.03, where sharp temperature gradients are observed. A thinning of the thermal boundary layer at r/d ≈ 0.6, where a thinning of the hydrodynamic boundary layer is also seen, proves the physics behind the formation of the primary maximum in heat transfer coefficient, as reported by Ball (1998), amongst others. The entrainment of the ambient fluid results in a higher fluctuating temperature in the shear layer around the core of the jet. Upon impingement, the temperature field diminishes gradually in the lateral direction. When the heated impinging jet is coupled with an ambient temperature crossflow at $U_j / U_c = 5$, the temperature in the wall jet region falls rapidly as a result of mixing with the crossflow. Nonetheless, the potential core of the jet remains thermally undisrupted by the

crossflow. At $U_j / U_c = 4$, the temperature of the wall jet falls more rapidly and therefore leads to higher local temperature fluctuations. The influence of the crossflow becomes significant at $U_j / U_c = 3$ such that the core of the jet undergoes both thermal and hydrodynamic mixings. At $U_j / U_c = 2$, the crossflow dominates the near wall thermal characteristic up to r/d = 0.5, beyond which the temperature field of the impinging fluid develops gradually.

The temperature field for the heated axisymmetric impinging jet at z/d = 3 and Re = 20 000 changes more rapidly (compared to the case for z/d = 1.5) due to increased thermal mixing with the surrounding ambient fluid at the larger nozzle-to-plate spacing. Upon impingement, the temperature field also diminishes gradually as the bulk fluid accelerates radially outwards. When a crossflow is imposed at $U_j / U_c = 5$, the entire thermal field of the impinging jet is affected. The temperature at y/d $\leq$ 0.04 attains a maximum normalised value of only 0.6 – 0.7, as opposed to 0.9 – 1.0 in the case for z/d = 1.5. The thermal mixing between the impinging bulk fluid and the crossflow continues to rise at $U_j / U_c = 4$. By $U_j / U_c = 3$, the crossflow dominates the near wall temperature field up to r/d $\approx$ 1.6. The maximum normalised temperature at y/d $\leq$ 0.04 is only 0.3 – 0.4, approximately 63 % lower than that in the case for z/d = 1.5. Therefore, the heat transfer effectiveness of the impinging jet is expected to be low.

Two additional observations can be drawn from the present study. Firstly, the near wall hydrodynamic and thermal characteristics for impinging jets at Re = 20 000 and 40 000 match closely despite minor differences exist in the magnitude and location of flow transformations. Secondly, impinging jets (with, and without, crossflow) at z/d = 1.5 are consistently more effective, both hydrodynamically and thermally, than those at z/d = 3.

CHAPTER 7
PRESENTATION AND DISCUSSION OF EXPERIMENTAL SURFACE HEAT TRANSFER RESULTS

In this Chapter the experimental results obtained from an investigation into the surface heat transfer characteristics of confined single impinging jets with, and without, crossflow are presented and discussed. The heated jet discharged at Reynolds numbers of 20 000 and 40 000 with uniform exit velocity and temperature profiles, and was subjected to an ambient temperature crossflow at jet-to-crossflow velocity ratios of 2, 3, 4 and 5. Two non-dimensional nozzle-to-plate spacings of 1.5d and 3d have been studied in detail.

The full distributions of surface heat transfer coefficients and effectiveness, defined using adiabatic wall temperature as the reference temperature, were determined using liquid crystal thermography technique and an intensity-based image processing system. The use of adiabatic wall temperature helps to separate the effects of fluid mechanics of the jets from the thermal boundary conditions. Hence, the surface heat transfer characteristic reflects only the influence of fluid mechanics. The heat transfer and effectiveness results are related directly to the near wall hydrodynamic and thermal characteristics of the impinging jets (described in Chapter 6). The Chapter closes with a summary of the main conclusions drawn from the experimental study.

7.1 Surface Heat Transfer Measurements

7.1.1 Heat Transfer Coefficient and Jet Effectiveness

The heat transfer results are normalised and presented in terms of full distributions of Nusselt number and jet effectiveness to facilitate understanding of the complex behaviour under varying flow conditions. The data are shown as a function of non-dimensional radial distance, r/d, and spanwise distance, x/d, where the liquid crystal colour plays appeared. Irrelevant data in areas where no liquid crystal colour play was discernible (e.g. on surface covered by the thermocouples) are filtered and represented by

white patches. Erroneous data resulted from curve-fitting in areas where only one of the crystals appeared (see Appendix C), particularly in the outermost region of a colour mapping, should be discarded.

Figure 7.1 shows the full Nusselt number distribution for the axisymmetric impinging jet at a non-dimensional nozzle-to-plate spacing of 1.5d and exit Reynolds number of 20 000. The Nusselt number rises from approximately 102 at the stagnation point ($x/d = 0$ and $r/d = 0$) to reach a maximum of about 128 at $r/d \approx 0.65$. The resulting domain of inner peak in heat transfer (at $0.5 \leq r/d \leq 0.8$) is attributed to the impingement of large-scale turbulence convected from the edge of the jet, as described by Gillespie et al. (1996). These impinging turbulent structures prompt a local thinning and transition of the wall jet from laminar to turbulent flow, thereby inciting the level of surface heat transfer. Figure 7.2 illustrates that the jet effectiveness (at $0.5 \leq r/d \leq 0.8$) decreases from approximately unity at the stagnation point to about 0.84 at $r/d \approx 0.65$. The decrease is linked to the fluid mixing between the large-scale impinging turbulent structures with the surrounding ambient fluid prior to the impact.

The Nusselt number declines at further downstream distances (to approximately 88 at $r/d \approx 1.2$) before rising again to a local peak of about 98 at $r/d \approx 1.6$. The formation of the secondary peak in heat transfer has been detailed by Ashforth-Frost et al. (2001), who ascribed it to the continuous increase in local turbulence level. The presence of well-mixed turbulence structures is also demonstrated by the marginally lower local effectiveness at $r/d \approx 1.6$ (Figure 7.2). At $r/d \geq 1.7$, the Nusselt number falls monotically due to the diffusion and recirculation of the wall jet fluid towards the upper confining plate.

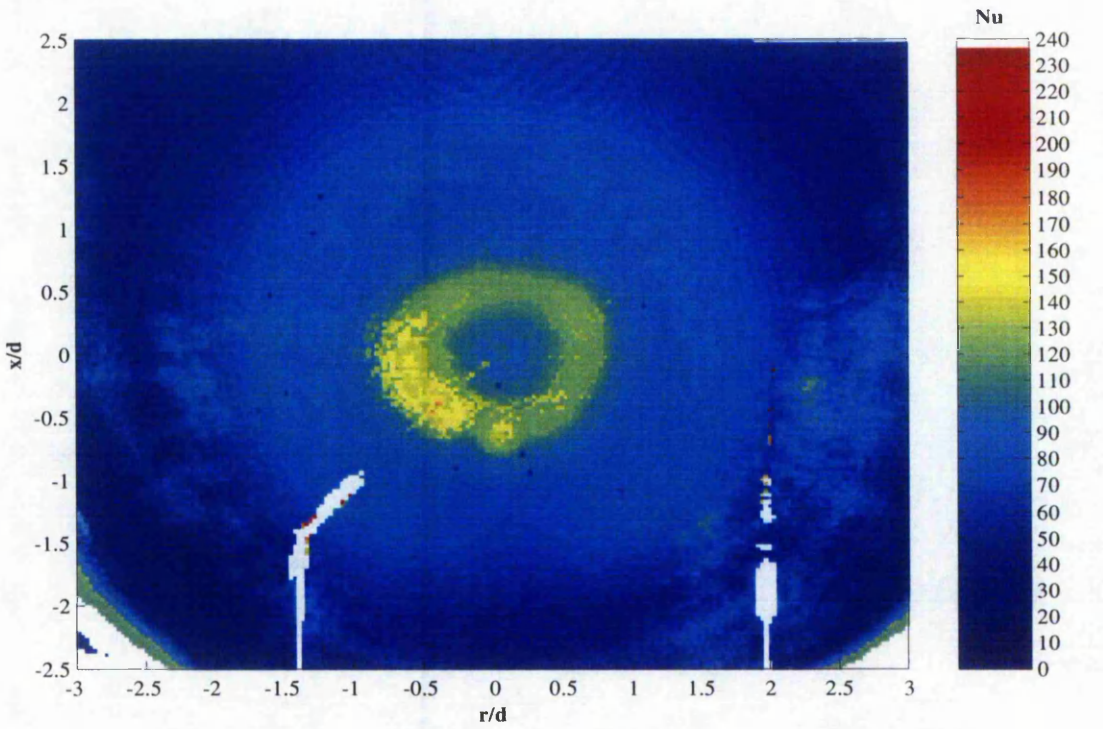

Figure 7.1: Nusselt number distribution, z/d = 1.5, Re = 20 000, no crossflow.

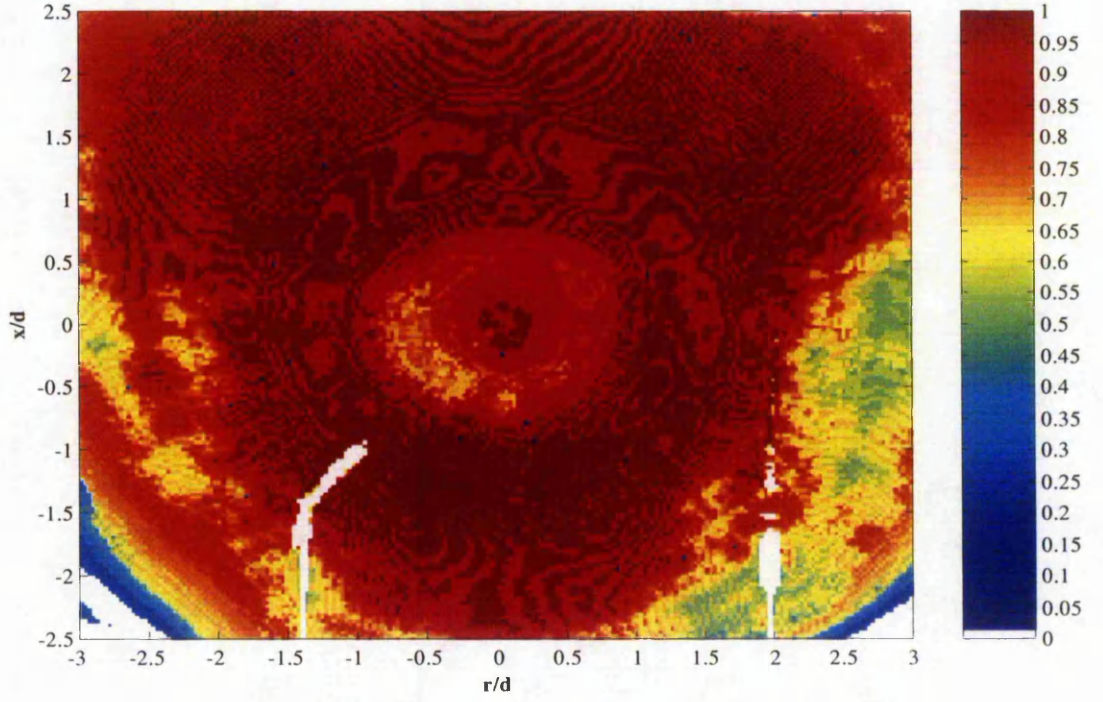

Figure 7.2: Jet effectiveness, z/d = 1.5, Re = 20 000, no crossflow.

Figure 7.3 and 7.4 show the respective distribution of Nusselt number and jet effectiveness when the impinging jet is coupled with an upstream crossflow at a jet-to-crossflow velocity ratio, U_j / U_c, of 5. The symmetry of the profiles is clearly disrupted by the crossflow. Typically, the stagnation point is swayed slightly downstream (by ≈ 0.1d) but the local Nusselt number remains at around 105. This indicates that the influence of the crossflow on the centre of the jet is negligible, which is consistent with the near wall results. The effect of the crossflow is pronounced around the core of the jet, particularly in the interval $-0.6 \leq r/d \leq -0.3$, where the Nusselt number surges to about 150. The increased heat transfer rate is due to the impingement of the upstream jet fluid that grows more turbulent as a result of direct collision and mixing with the crossflow. The intensity of the fluid mixing is exemplified by the reduction in the local jet effectiveness to about 0.7 (at $-0.6 \leq r/d \leq -0.3$). At $r/d \approx 0.65$, the downstream jet core does not interact directly with the crossflow. As described in Section 6.2.1, the crossflow flows pass the jet core and suppresses near wall separation and hence the turbulence level. This causes the inner peak in heat transfer (in the domain $0.5 \leq r/d \leq 0.8$) to diminish.

In the wall jet region ($r/d \geq 0.8$) the bulk fluid moves laterally outwards and the surface heat transfer decreases gradually. However, in the boundary of interaction between the wall jet and the crossflow (e.g. at $-2.1 \leq r/d \leq -1.8$ and $2.1 \leq r/d \leq 2.6$), the fluid becomes well-mixed and turbulent. Therefore, the local surface heat transfer rates are higher than those in the neighbouring areas. Note that the void data in the outermost region of the colour mappings (i.e. $-2.4 \leq r/d \leq -2.2$ and $3 \leq r/d \leq 3.4$) are due to bad curve fittings and should be ignored.

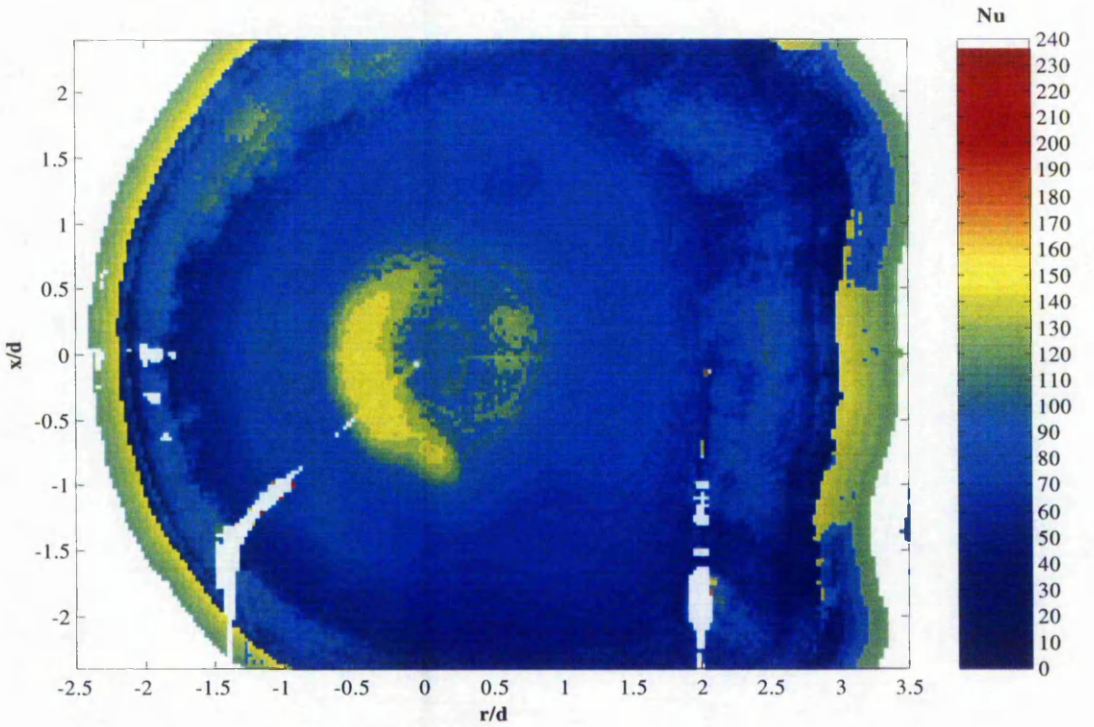

Figure 7.3: Nusselt number distribution, z/d = 1.5, Re = 20 000, $U_j / U_c = 5$.

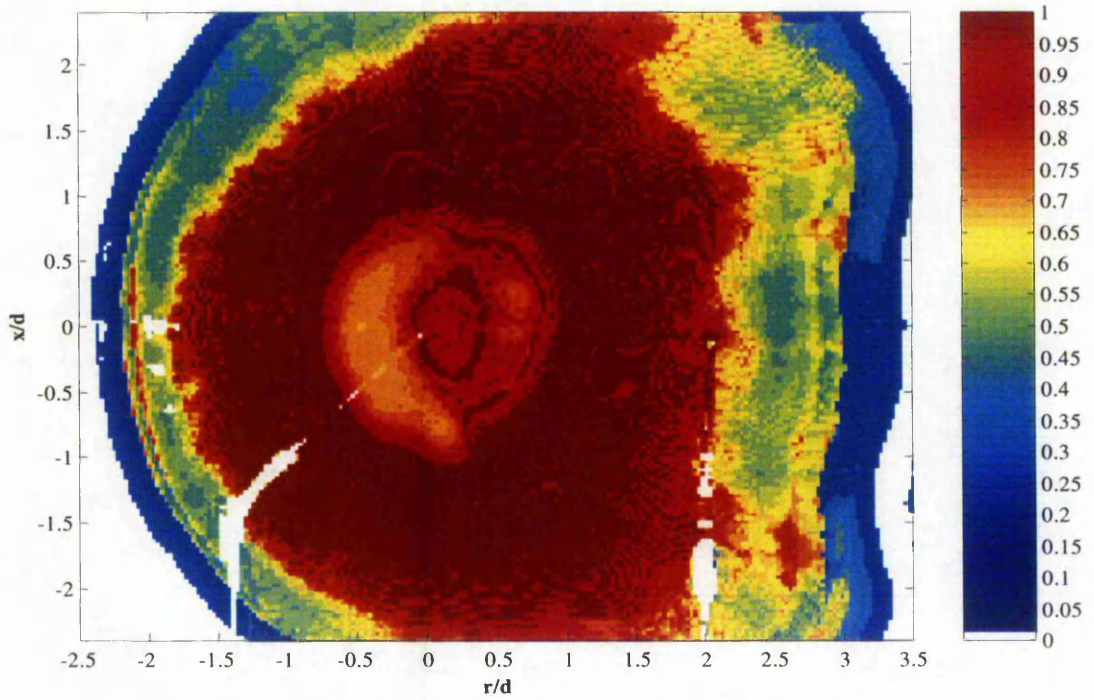

Figure 7.4: Jet effectiveness, z/d = 1.5, Re = 20 000, $U_j / U_c = 5$.

The distributions of Nusselt number and effectiveness for jet in crossflow at $U_j / U_c = 4$ are presented in Figure 7.5 and 7.6 respectively. The stronger crossflow sways the stagnation point further downstream by ≈ 0.18d. The Nusselt number at the stagnation point increases slightly to about 122.

The influence on surface heat transfer is more profound particularly in the domain where the crossflow interacts directly with the impinging fluid. Typically, the Nusselt number soars to about 198 in the interval -0.48 ≤ r/d ≤ -0.27. The intensity of the mixing can be demonstrated by the marked decrease in the local jet effectiveness. The Nusselt number around the downstream jet core (0.5 ≤ r/d ≤ 0.8) also increases significantly (to about 150) due to the higher mixing and turbulence levels induced by the bypassing crossflow, as shown in Figure 6.8. In the wall jet region the Nusselt number decreases gradually up to the boundary of interaction with the crossflow (e.g. at -1.6 ≤ r/d ≤ -1.4 and 2 ≤ r/d ≤ 2.8), where a minor increase in heat transfer is discernible.

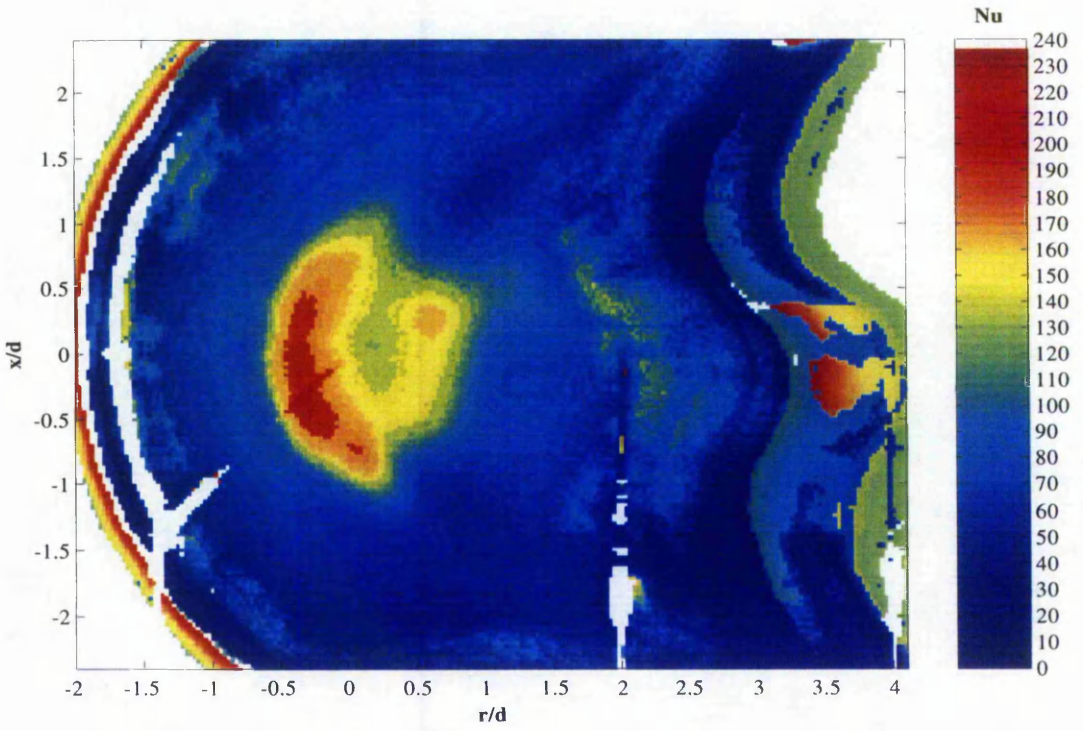

Figure 7.5: Nusselt number distribution, z/d = 1.5, Re = 20 000, $U_j / U_c = 4$.

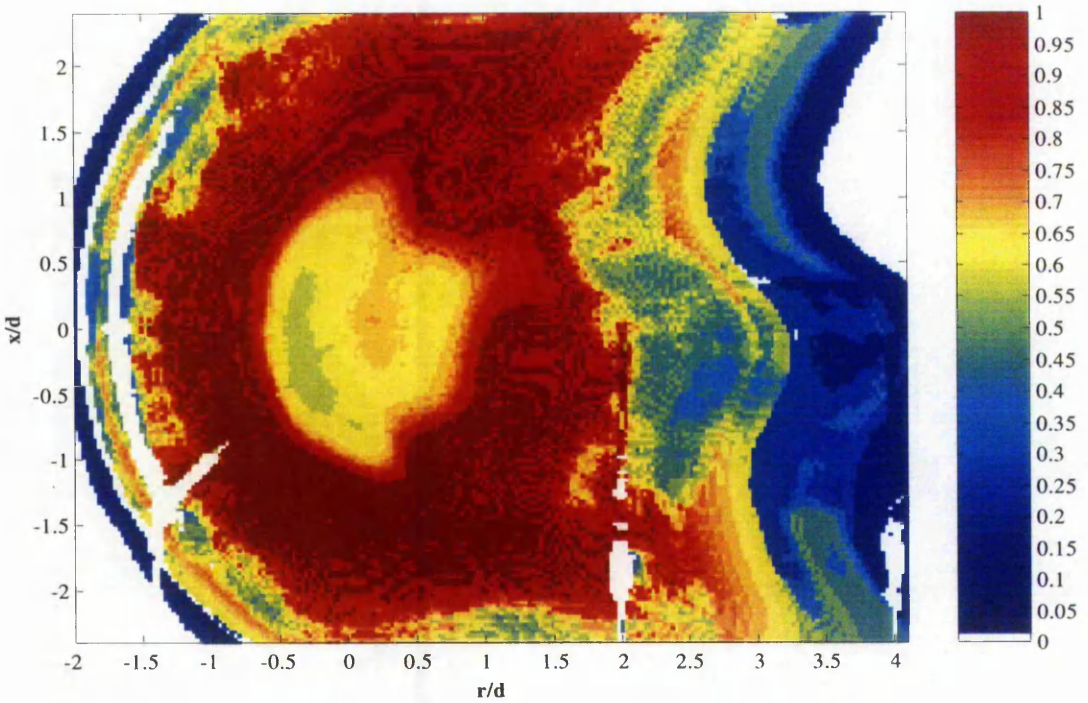

Figure 7.6: Jet effectiveness, z/d = 1.5, Re = 20 000, $U_j / U_c = 4$.

Figure 7.7 and 7.8 illustrate a typical horseshoe vortex profile formed beneath the impinging jet which interacts with the crossflow at $U_j / U_c = 3$. The stagnation point is deflected by approximately 0.32d downstream. The crossflow pushes the upstream jet core towards the centre and causes higher turbulence level through mixing, e.g. at r/d ≈ 0. As a result, the local Nusselt number escalates to about 205 and the heat transfer within the adjacent jet core also increases in magnitude. However, the heat transfer rates in the downstream wall jet region are generally lower (compared to at $U_j / U_c = 4$) due to reduced jet effectiveness under the increased influence of the crossflow. Further increase in the strength of the crossflow would only deteriorate the surface heat transfer performance.

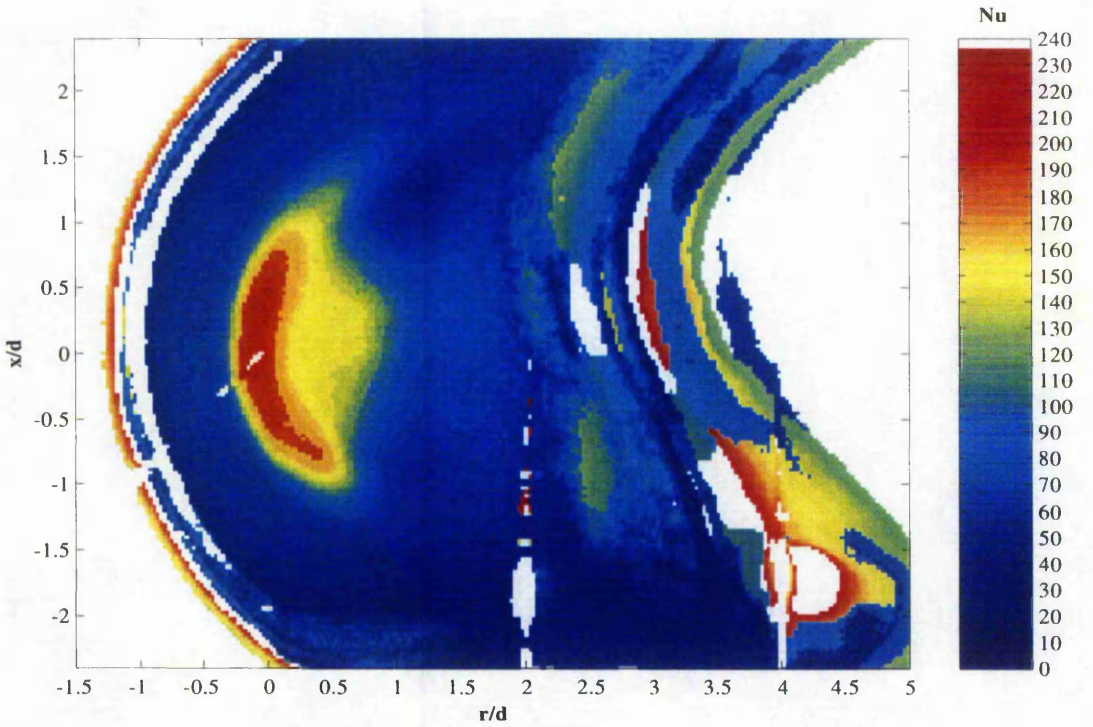

Figure 7.7: Nusselt number distribution, z/d = 1.5, Re = 20 000, $U_j / U_c = 3$.

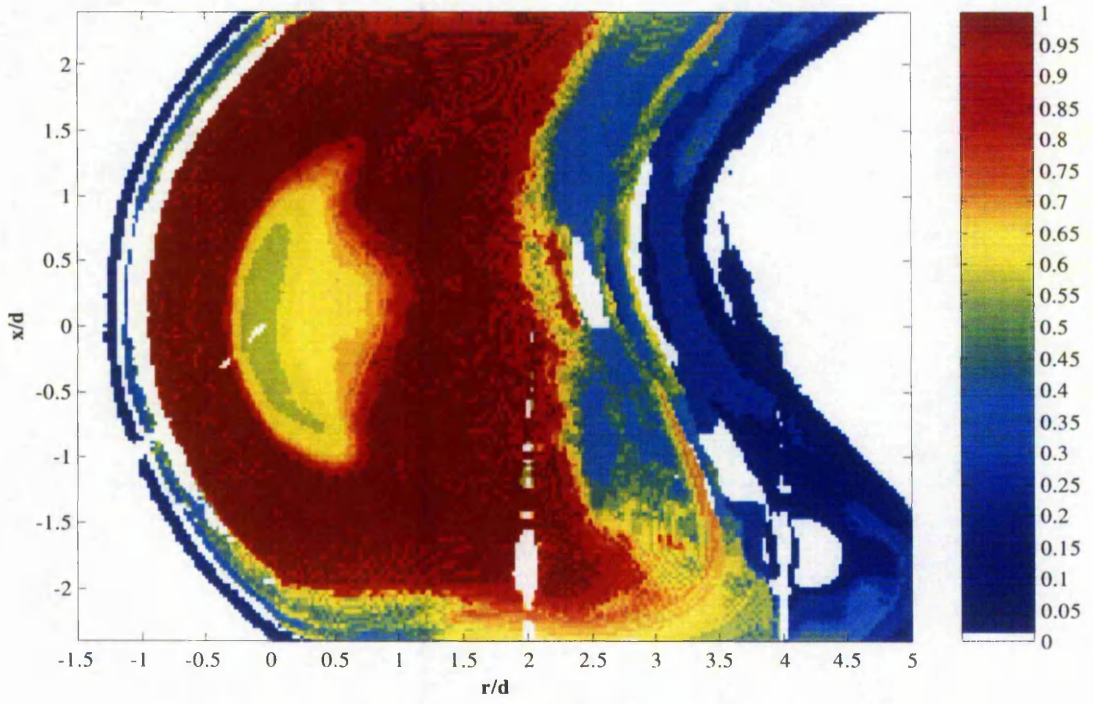

Figure 7.8: Jet effectiveness, z/d = 1.5, Re = 20 000, $U_j / U_c = 3$.

Figure 7.9 and 7.10 indicate that as the crossflow is strengthened to $U_j/U_c = 2$, the core of the jet is almost destroyed completely. The impinging jet becomes ineffective and spans over a much smaller area. The heat transfer is markedly lower (Nu ≤ 125) even though its distribution is more uniform. A stagnation point is no longer evident and the impingement heat transfer only begins at r/d ≈ 0.5. This corroborates with the near wall results which show that the upstream crossflow dominates the hydrodynamic and thermal characteristics up to r/d = 0.5.

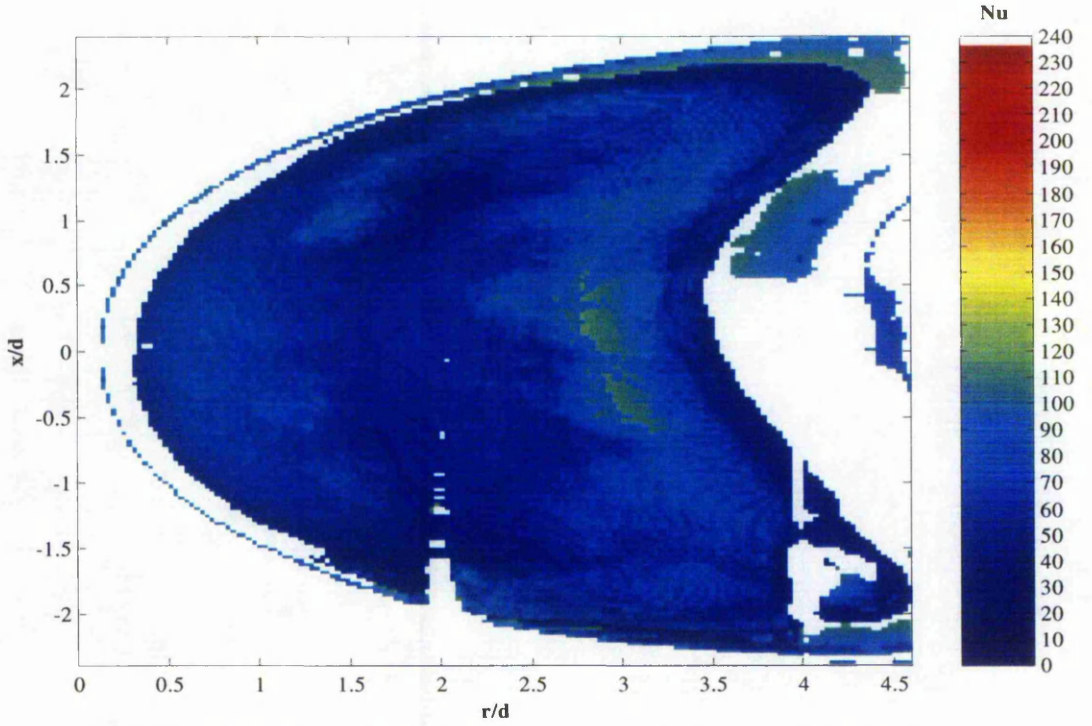

Figure 7.9: Nusselt number distribution, z/d = 1.5, Re = 20 000, $U_j/U_c = 2$.

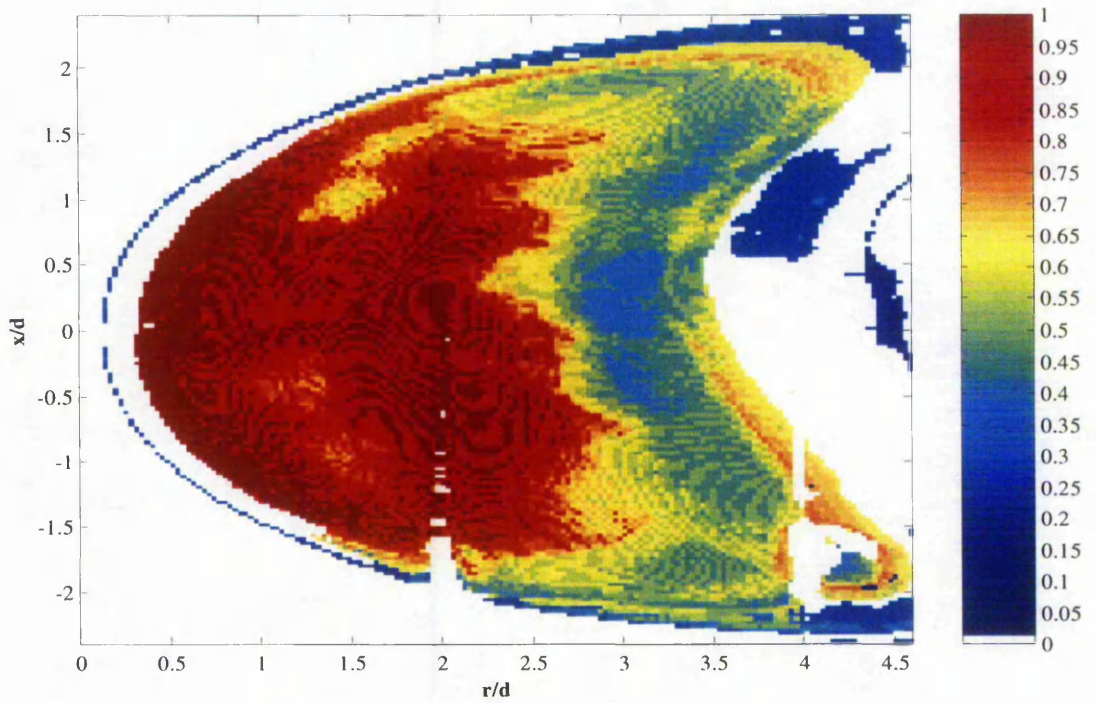

Figure 7.10: Jet effectiveness, z/d = 1.5, Re = 20 000, $U_j / U_c = 2$.

Figure 7.11 and 7.12 illustrate the respective distribution of Nusselt number and jet effectiveness for the axisymmetric impinging jet at a nozzle-to-plate spacing of 1.5d and exit Reynolds number of 40 000. The characteristic minima and maxima in heat transfer for axisymmetric jets at low nozzle-to-plate spacings are clearly exhibited by the two ring-shaped domains. The stagnation Nusselt number attains a value of 142, approximating a $Re^{0.5}$ increment (from Re = 20 000) expected for jets at low nozzle-to-plate spacings ($z/d \leq 4$). It then increases steeply to about 175 (at $r/d \approx 0.65$) before declining to around 132 (at $r/d \approx 1.2$). The resulting primary peak in heat transfer (at $r/d \approx 0.65$) is due to the impingement of large-scale turbulence convected from the edge of the jet. The impact of the turbulent fluid is indicated by the slight decrease in the local jet effectiveness. At $r/d \geq 1.3$, the Nusselt number increases again to form a secondary peak of about 160 at $r/d \approx 1.65$ due to the continuous growth of the local turbulence level, as shown in Figure 6.14. The well-mixed turbulent flow is also demonstrated by the minor reduction in local jet effectiveness. At $r/d \geq 1.8$, the Nusselt number declines gradually and monotically due to further flow diffusion and recirculation of the wall jet fluid.

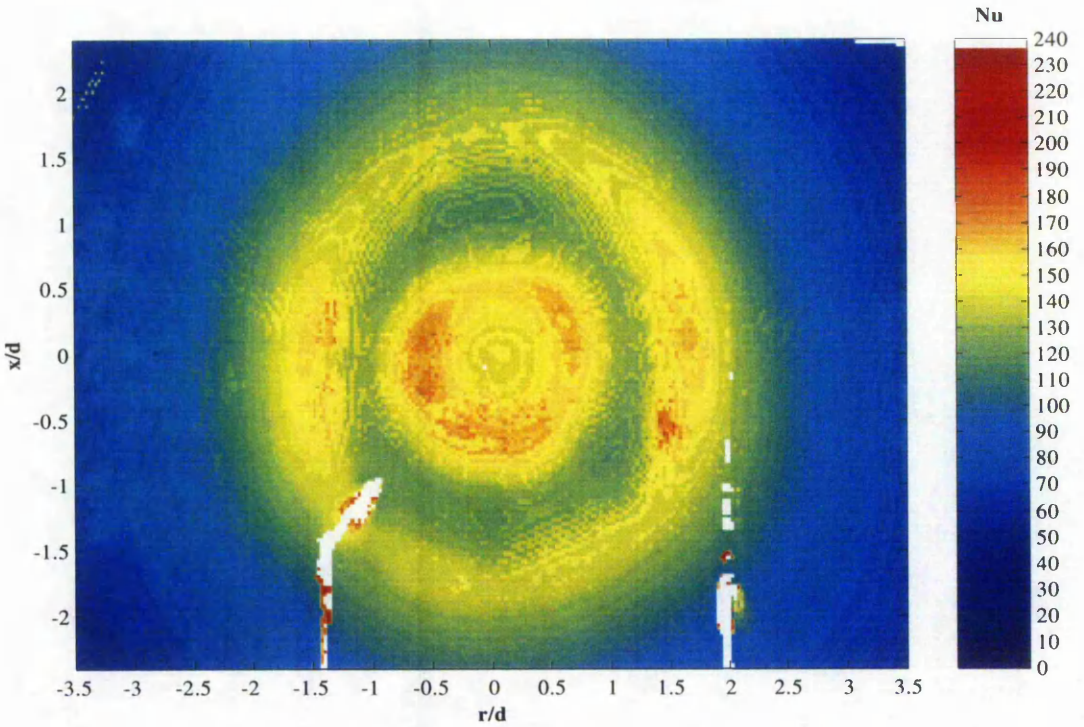

Figure 7.11: Nusselt number distribution, z/d = 1.5, Re = 40 000, no crossflow.

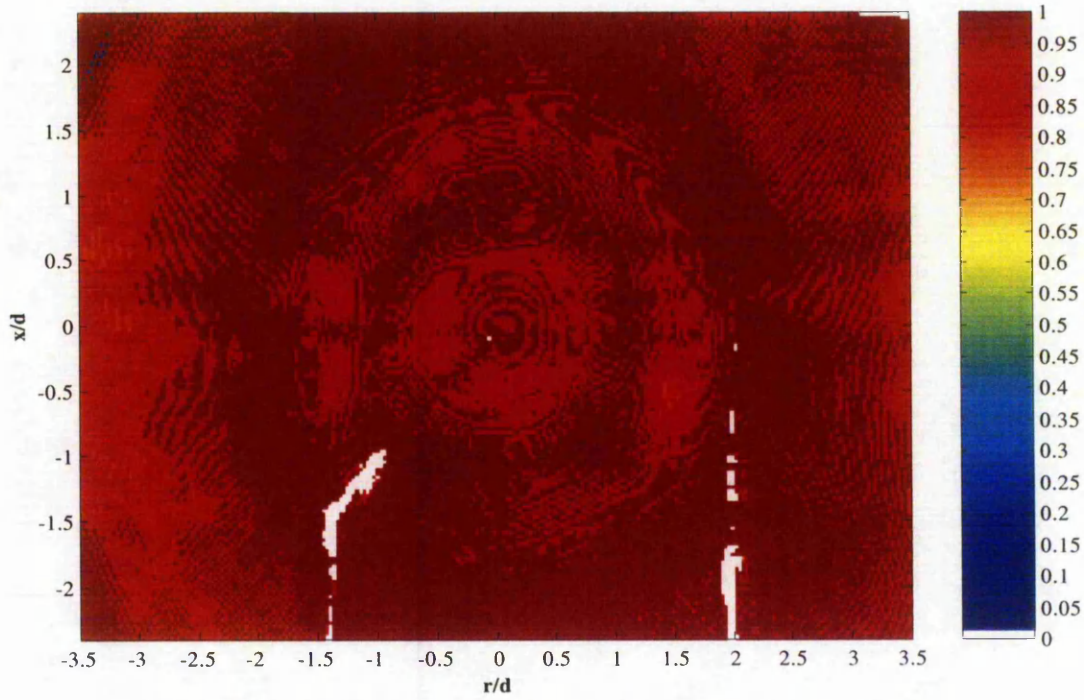

Figure 7.12: Jet effectiveness, z/d = 1.5, Re = 40 000, no crossflow.

Figure 7.13 and 7.14 show that when an upstream crossflow is imposed at $U_j / U_c = 5$, the stagnation point is deflected downstream (by ≈ 0.13d). The local Nusselt number remains around 143 as the flow field at the jet centre stays intact. Unlike the case for Re = 20 000, the crossflow seems to lead to a more uniform but marginally lower heat transfer distribution beneath the core of the jet. This is because the impinging bulk fluid (at Re = 40 000) is essentially very turbulent. Hence, the mixing with the crossflow no longer produces a boost in the local turbulence level but rather leads to a more influential decrease in the hydrodynamic energy.

At r/d $\geq$ 0.8, surface heat transfer decreases gradually as the wall jet develops and diffuses laterally outwards. The Nusselt number escalates to about 214 in the boundary of interaction between the wall jet and the crossflow (e.g. at -1.9 $\leq$ r/d $\leq$ -1.6 and 2.0 $\leq$ r/d $\leq$ 2.5), where the flow becomes highly turbulent. The superior convective heat transfer rates and uniformity achieved by the jet suggest that such a flow configuration is ideal for impingement cooling involving crossflow.

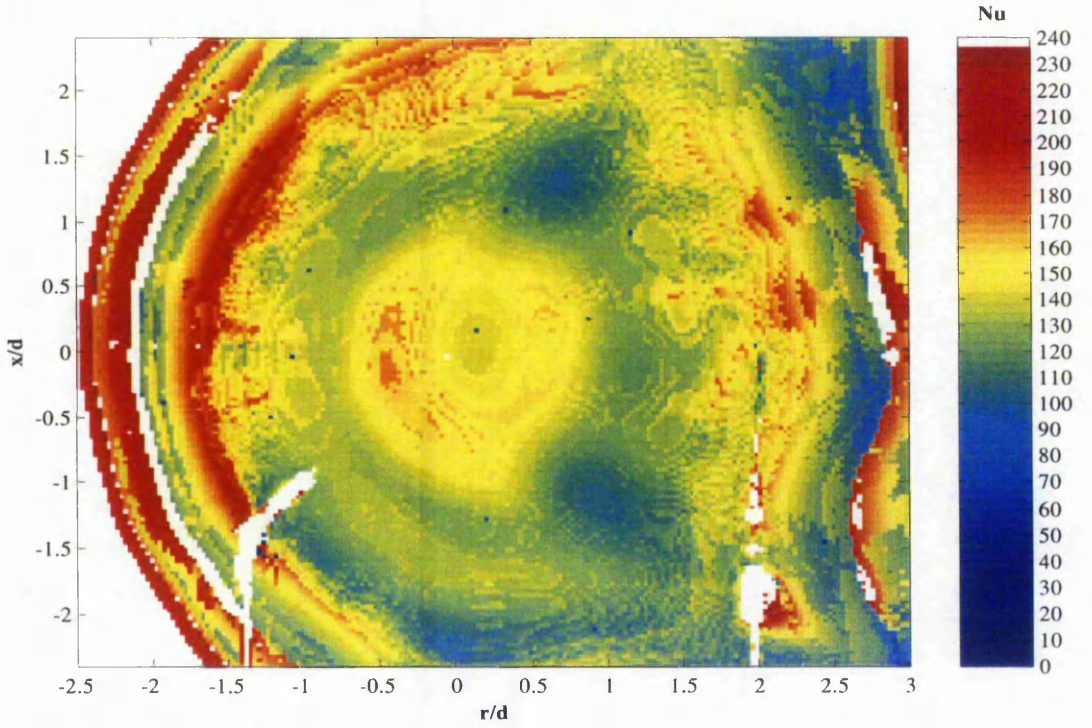

Figure 7.13: Nusselt number distribution, z/d = 1.5, Re = 40 000, $U_j / U_c = 5$.

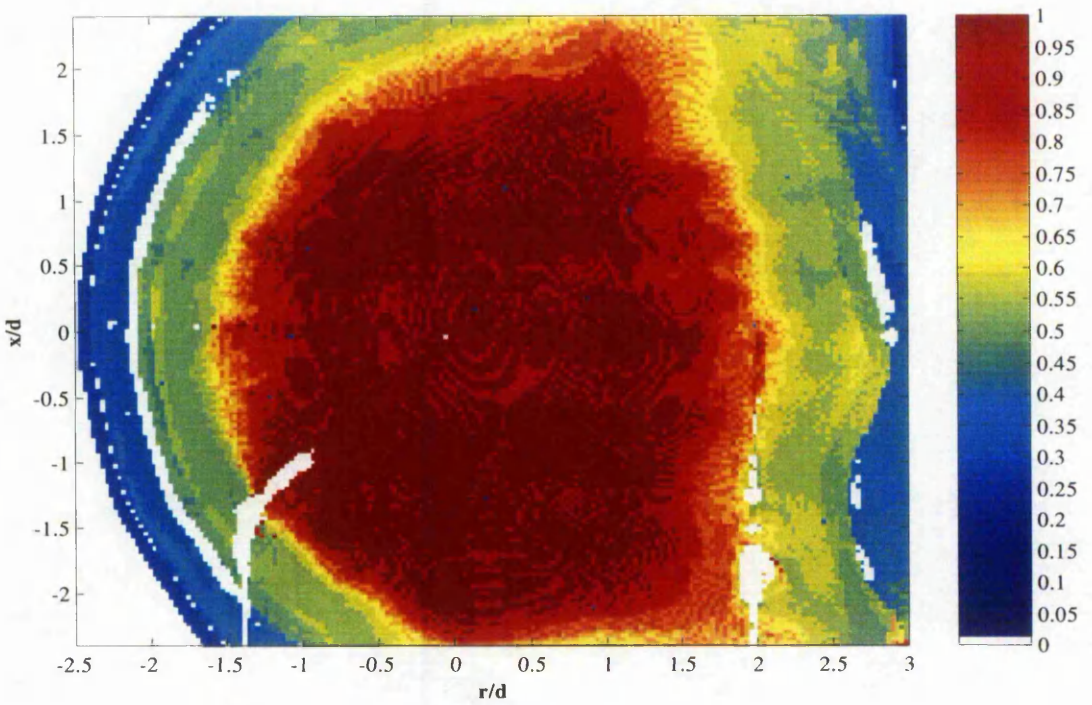

Figure 7.14: Jet effectiveness, z/d = 1.5, Re = 40 000, $U_j / U_c = 5$.

The distributions of Nusselt number and jet effectiveness at $U_j / U_c = 4$ are presented in Figure 7.15 and 7.16 respectively. Note that the isolated pixels are due to noise picked up during the experiment. The stronger crossflow sways the stagnation point downstream by ≈ 0.19d and causes a general decrease in the Nusselt number, despite the effect being insignificant at the centre of the jet core. The deterioration in heat transfer is due to the weakening of the intrinsically turbulent jet by the oncoming crossflow. The effect extends as far as to the boundary of interaction between the wall jet and the crossflow (e.g. -1.6 ≤ r/d ≤ -1.4), where the heat transfer rates are relatively higher than those in the neighbouring areas.

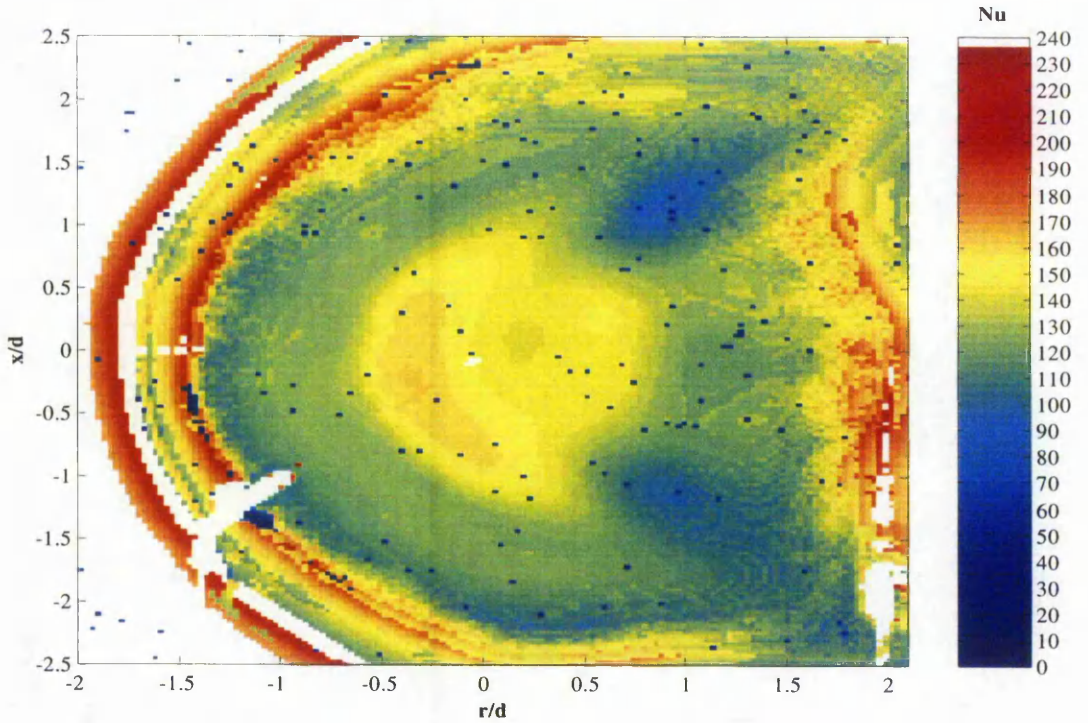

Figure 7.15: Nusselt number distribution, z/d = 1.5, Re = 40 000, $U_j / U_c = 4$.

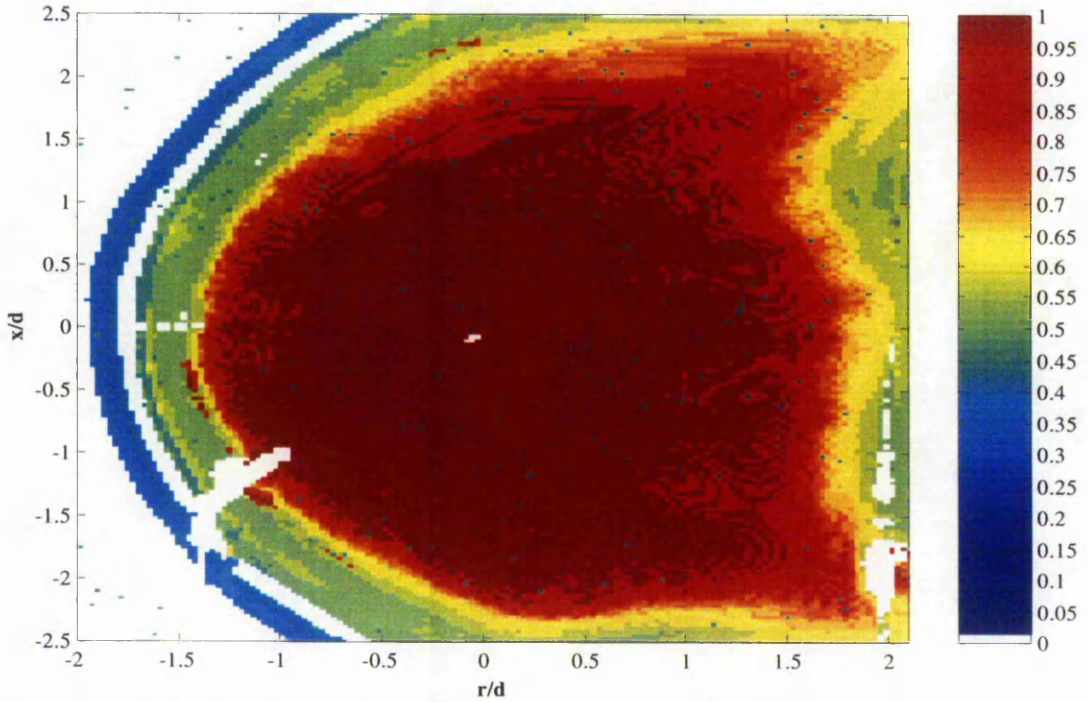

Figure 7.16: Jet effectiveness, z/d = 1.5, Re = 40 000, $U_j / U_c = 4$.

At $U_j / U_c = 3$, the upstream impinging fluid is driven towards the centre of the jet core and the stagnation point is shifted downstream by approximately 0.4d. Figure 7.17 and 7.18 indicate that the surface heat transfer rates continue to decline as the effectiveness of the jet degrades under the increased influence of the crossflow.

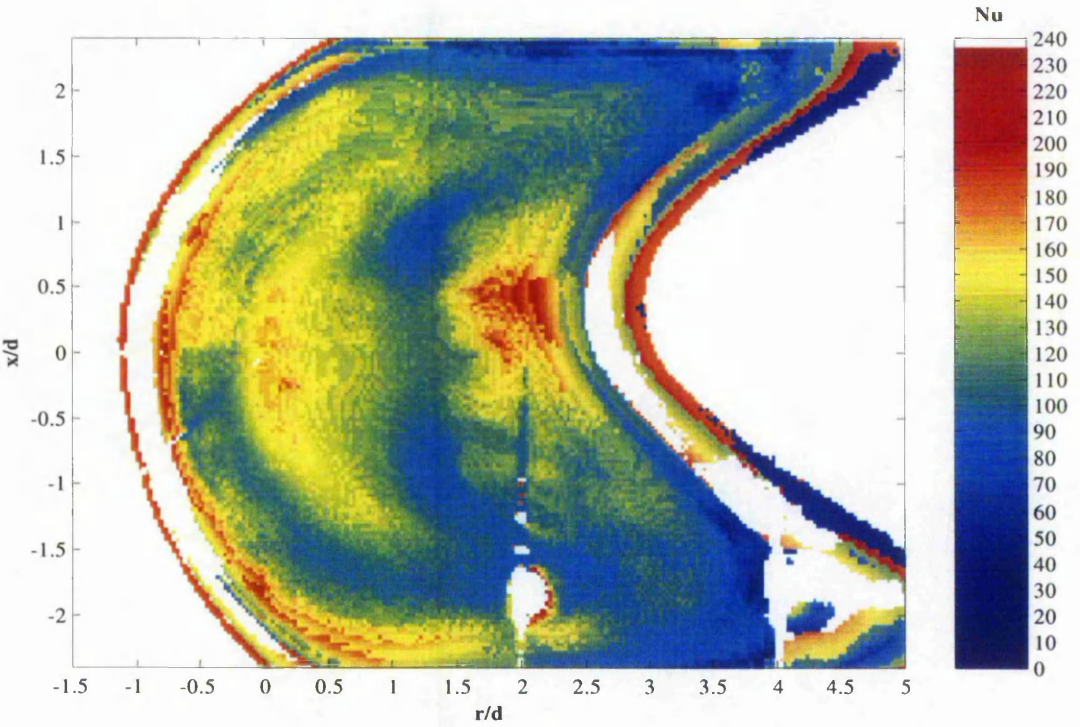

Figure 7.17: Nusselt number distribution, z/d = 1.5, Re = 40 000, $U_j / U_c = 3$.

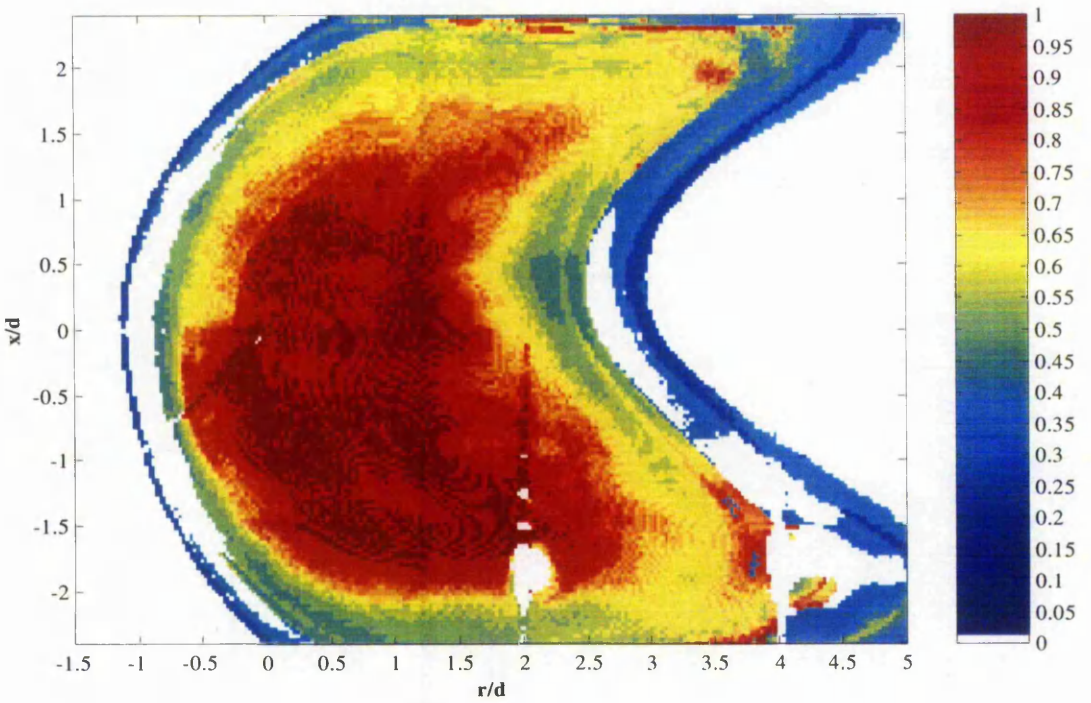

Figure 7.18: Jet effectiveness, z/d = 1.5, Re = 40 000, $U_j / U_c = 3$.

Figure 7.19 and 7.20 indicate that as the crossflow is strengthened to $U_j / U_c = 2$, the core of the jet is destroyed completely. In line with the near wall results, the impingement only begins at r/d ≥ 0.6. The surface heat transfer disperses irregularly and is particularly higher on the top half of the plate (x/d ≥ 0), presumably due to large-scale turbulent fluctuations triggered by the mixing process. Nonetheless, the jet is considered ineffective due to the low overall levels of heat transfer and uniformity, especially in the bottom half of the plate.

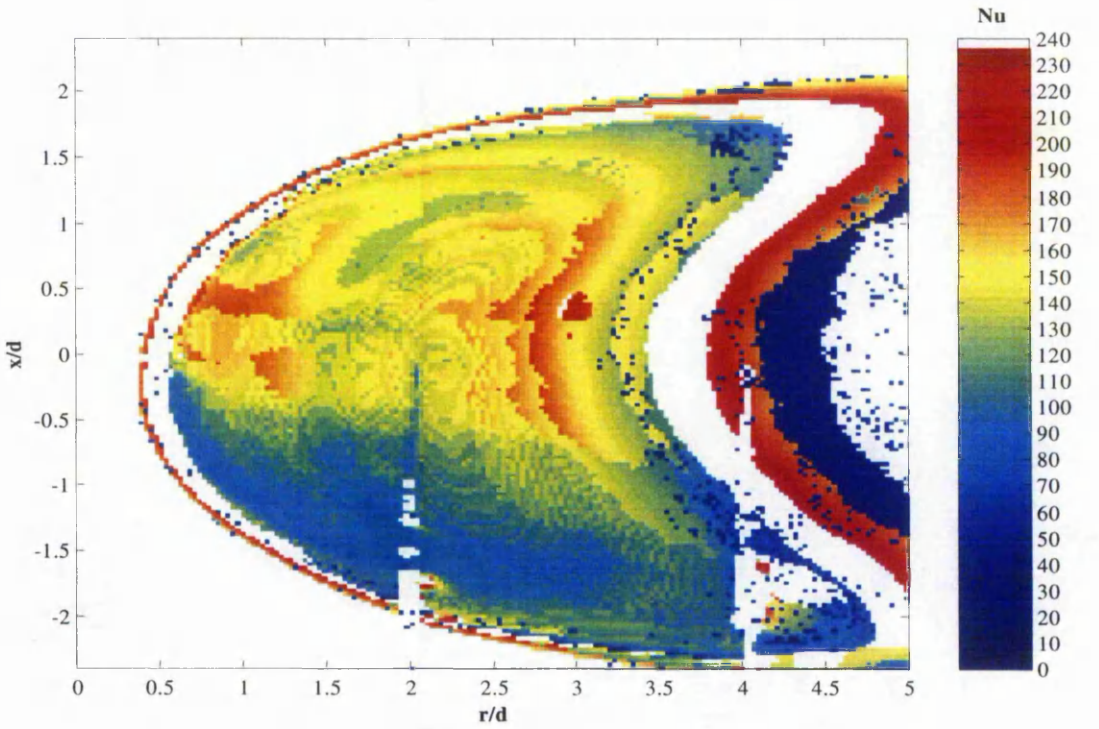

Figure 7.19: Nusselt number distribution, z/d = 1.5, Re = 40 000, $U_j / U_c = 2$.

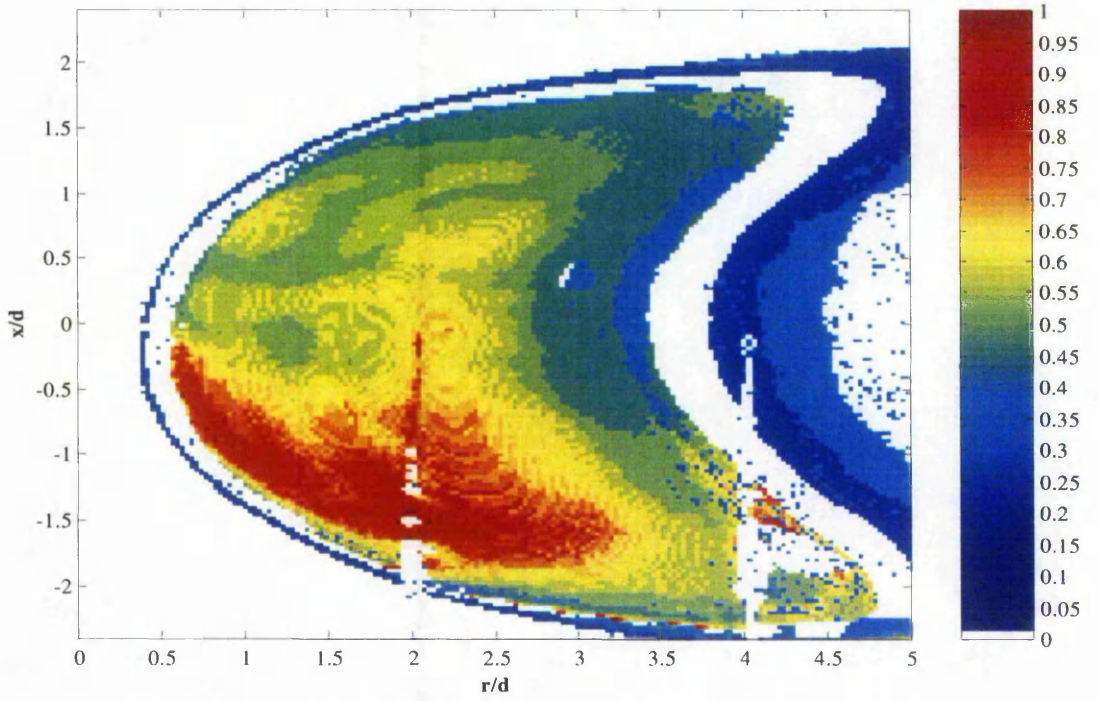

Figure 7.20: Jet effectiveness, z/d = 1.5, Re = 40 000, $U_j / U_c = 2$.

Figure 7.21 and 7.22 show the respective distribution of Nusselt number and jet effectiveness for the axisymmetric impinging jet at a non-dimensional nozzle-to-plate spacing of 3d and exit Reynolds number of 20 000. The Nusselt number rises from approximately 105 at the stagnation point to form a peak of about 130 at r/d ≈ 0.55. Again, the domain of high heat transfer (at 0.5 ≤ r/d ≤ 0.7) is attributed to the impingement of large-scale turbulence. The effectiveness in and around the jet core is lower (compared to at z/d = 1.5) due to increased mixing with the surrounding fluid at the larger nozzle-to-plate spacing, as described in Section 6.2.2. At r/d ≥ 0.8, the Nusselt number declines slowly as the wall jet moves laterally outwards.

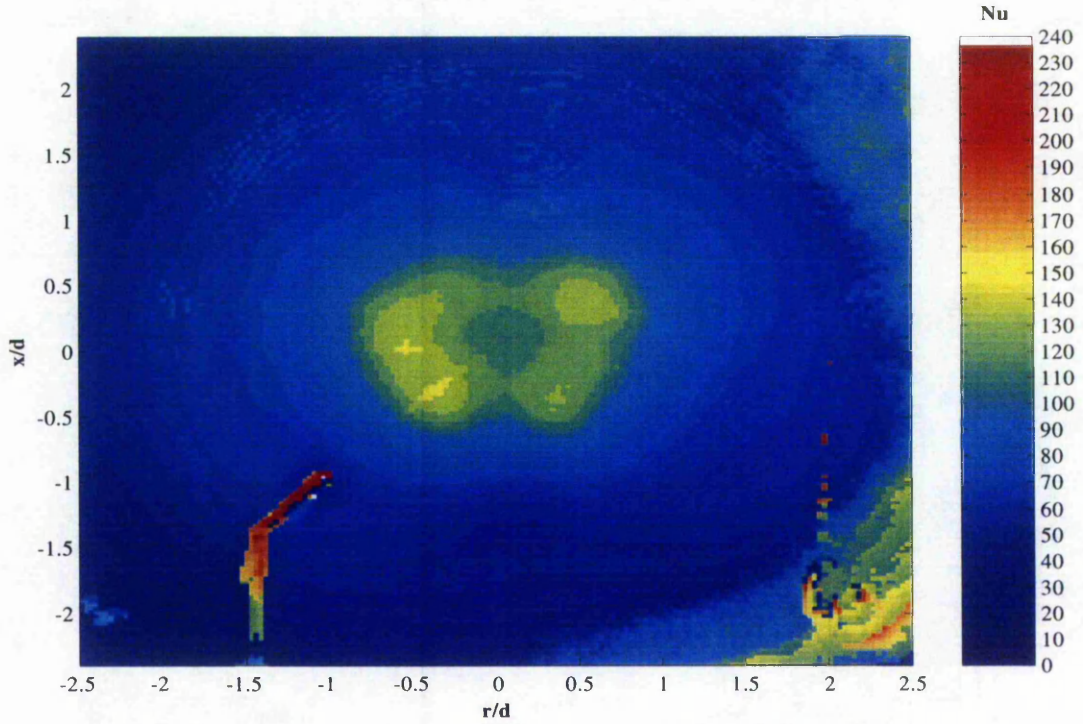

Figure 7.21: Nusselt number distribution, z/d = 3, Re = 20 000, no crossflow.

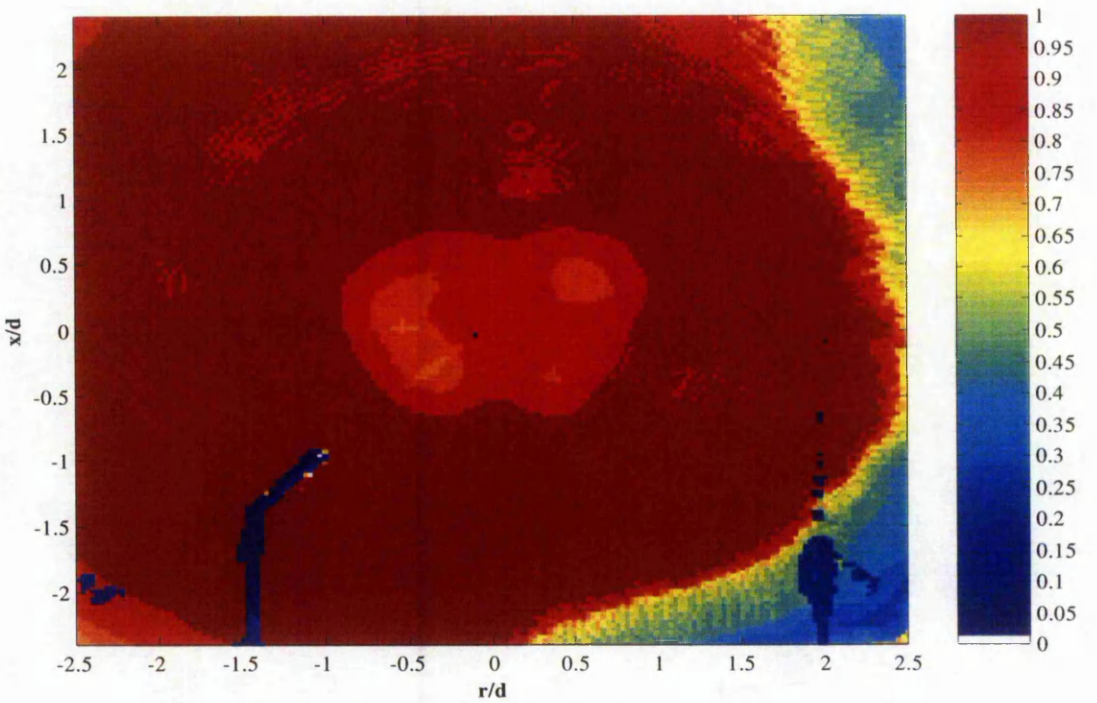

Figure 7.22: Jet effectiveness, z/d = 3, Re = 20 000, no crossflow.

When an upstream crossflow is imposed at a jet-to-crossflow velocity ratio, U_j / U_c, of 5, the entire flow and heat transfer phenomena are distorted. Figure 7.23 and 7.24 indicate that the stagnation point is deflected downstream by as much as 0.4d. This is consistent with the near wall results and the work of Sparrow et al. (1975) in which the extent of the jet deflection was accentuated at a larger nozzle-to-plate spacing. The Nusselt number at the stagnation point drops to approximately 75 as the influence of the crossflow extends to the centre of the jet core. The considerable loss in the hydrodynamic energy of the jet results in collectively lower surface heat transfer rates, which are distributed unevenly. A slight increase in Nusselt number is also seen in the boundary of interaction between the wall jet and the crossflow (e.g. $-1.1 \leq r/d \leq -0.6$ and $2.9 \leq r/d \leq 3.3$).

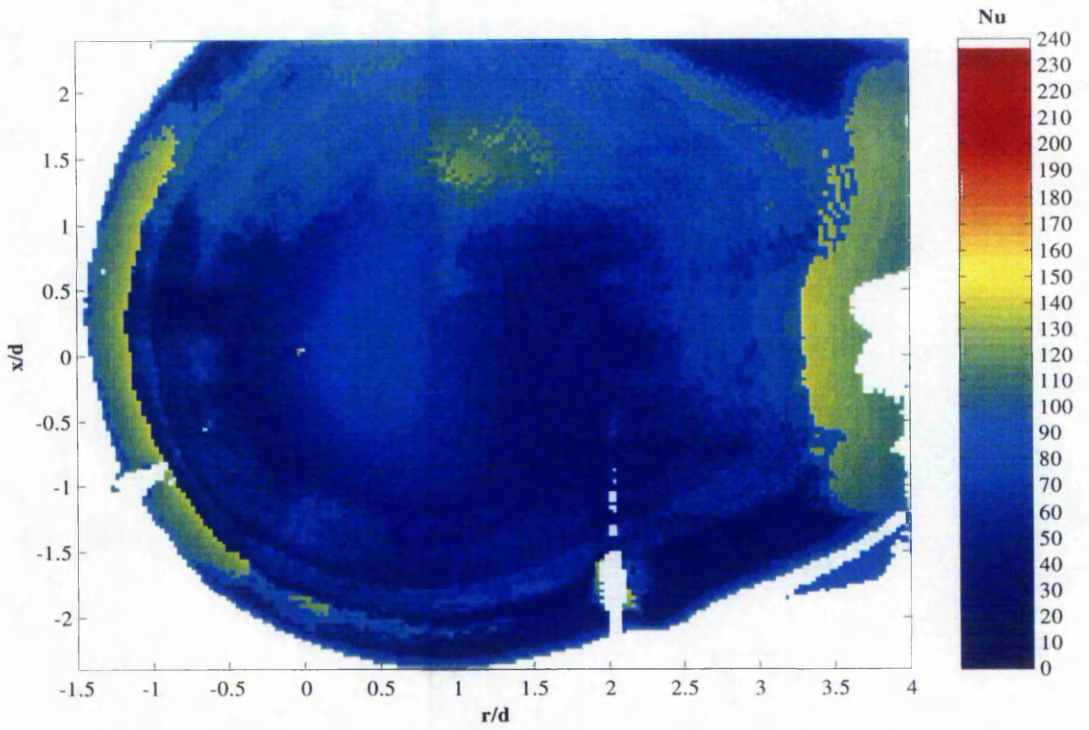

Figure 7.23: Nusselt number distribution, z/d = 3, Re = 20 000, $U_j / U_c = 5$.

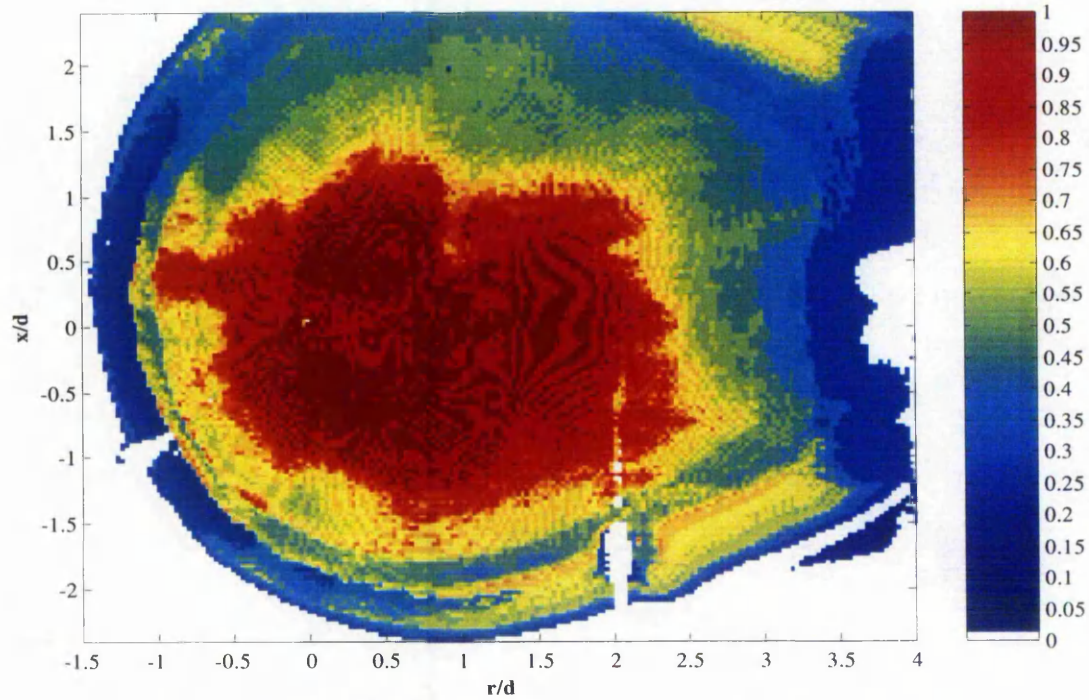

Figure 7.24: Jet effectiveness, z/d = 3, Re = 20 000, $U_j / U_c = 5$.

The distributions of Nusselt number and jet effectiveness beneath the impinging jet in crossflow at $U_j / U_c = 4$ are illustrated in Figure 7.25 and 7.26 respectively. The core of the jet is destroyed by the crossflow. Most of the turbulent bulk fluid impinges at r/d ≥ 0.8, resulting in a region of higher heat transfer (Nu ≈ 120-140) in the interval 0.9 ≤ r/d ≤ 1.4. Interestingly, a unique region of heat transfer is created at 0 ≤ r/d ≤ 0.3 due to the presence of a secondary vortex, as shown in Figure 6.27 and 6.28. The heat transfer rates in the boundary of interaction between the wall jet and the crossflow are also marginally higher.

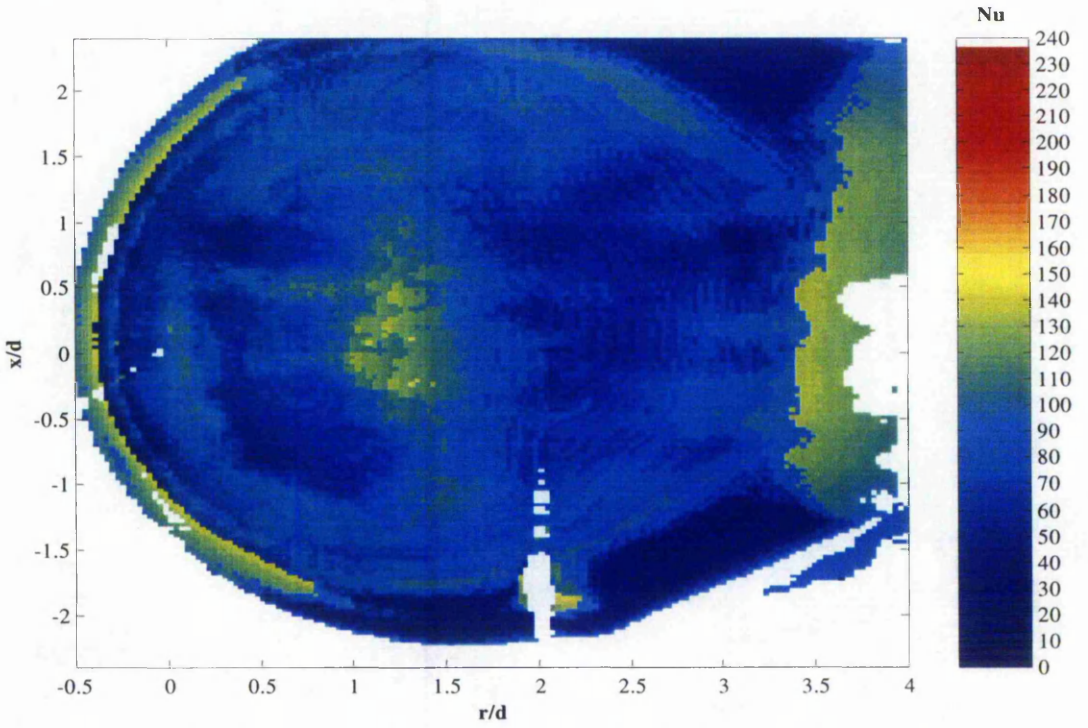

Figure 7.25: Nusselt number distribution, z/d = 3, Re = 20 000, $U_j / U_c = 4$.

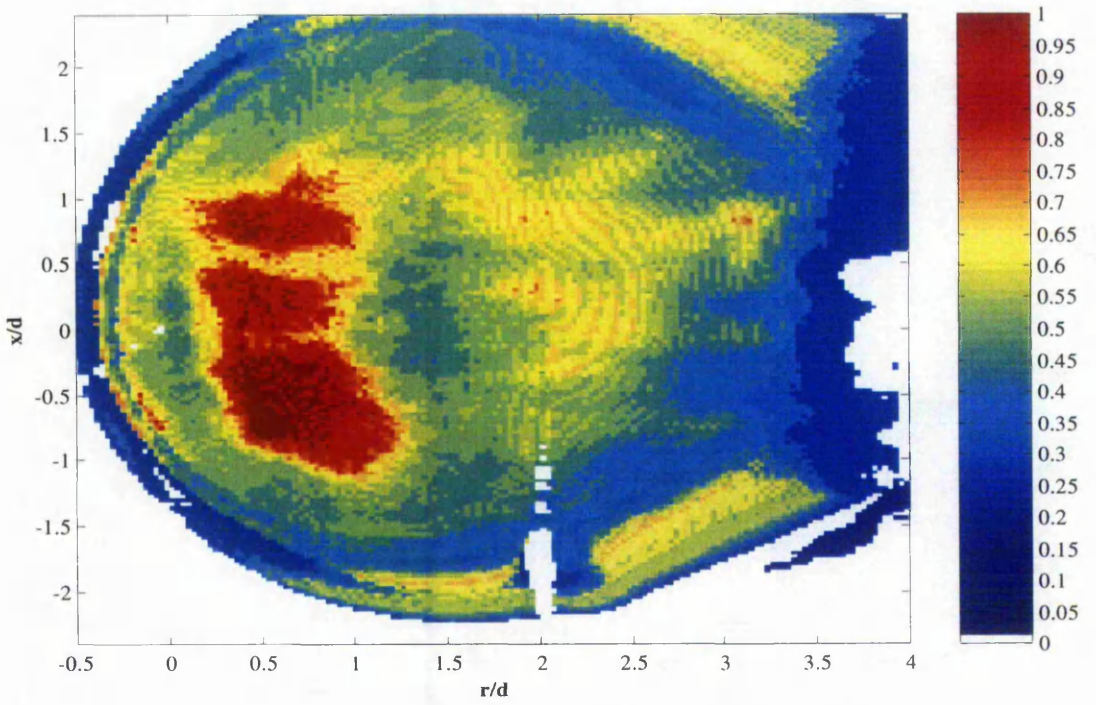

Figure 7.26: Jet effectiveness, z/d = 3, Re = 20 000, $U_j / U_c = 4$.

Figure 7.27 and 7.28 show the respective distribution of Nusselt number and jet effectiveness for the impinging jet in crossflow at $U_j / U_c = 3$. Consistent with the near wall results (in Sections 6.2.1 and 6.2.2), the crossflow dominates the surface heat transfer characteristic up to r/d ≈ 1.6, beyond which the influence of the impinging jet grows slowly. The convective heat transfer performance is severely degraded by the crossflow, which causes massive drops in the hydrodynamic and thermal energies of the impinging jet. The effective area of heat transfer is also reduced significantly, thus proving that the impinging jet is ineffective for such a flow configuration.

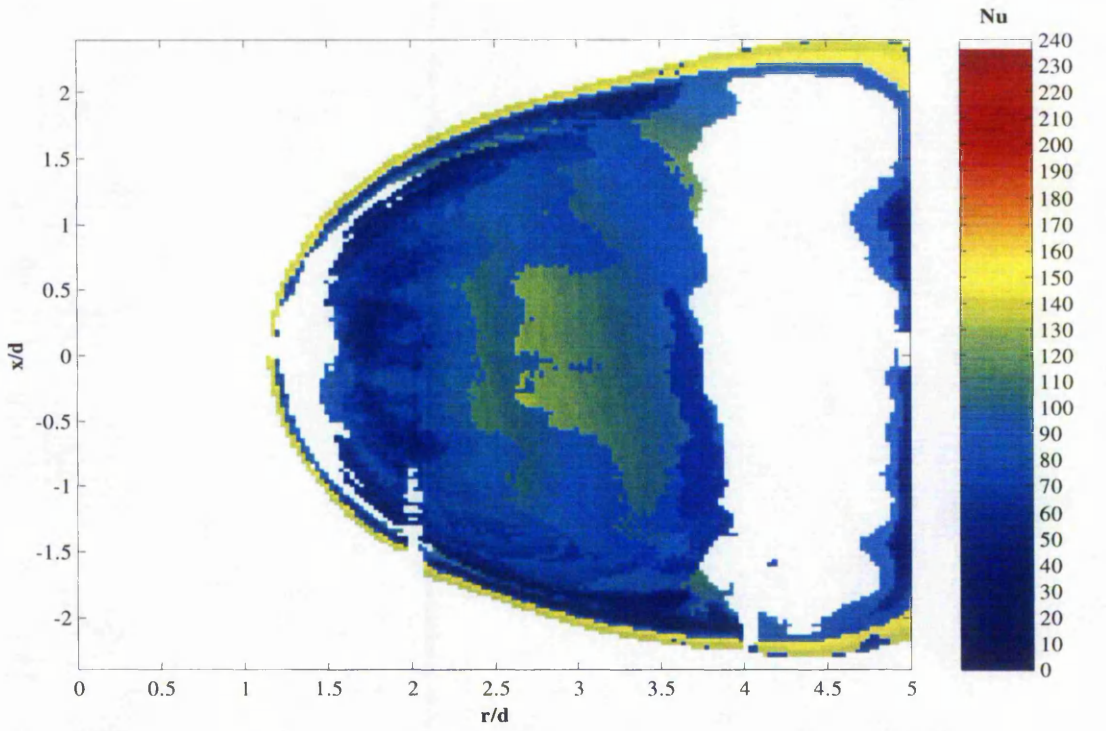

Figure 7.27: Nusselt number distribution, z/d = 3, Re = 20 000, $U_j / U_c = 3$.

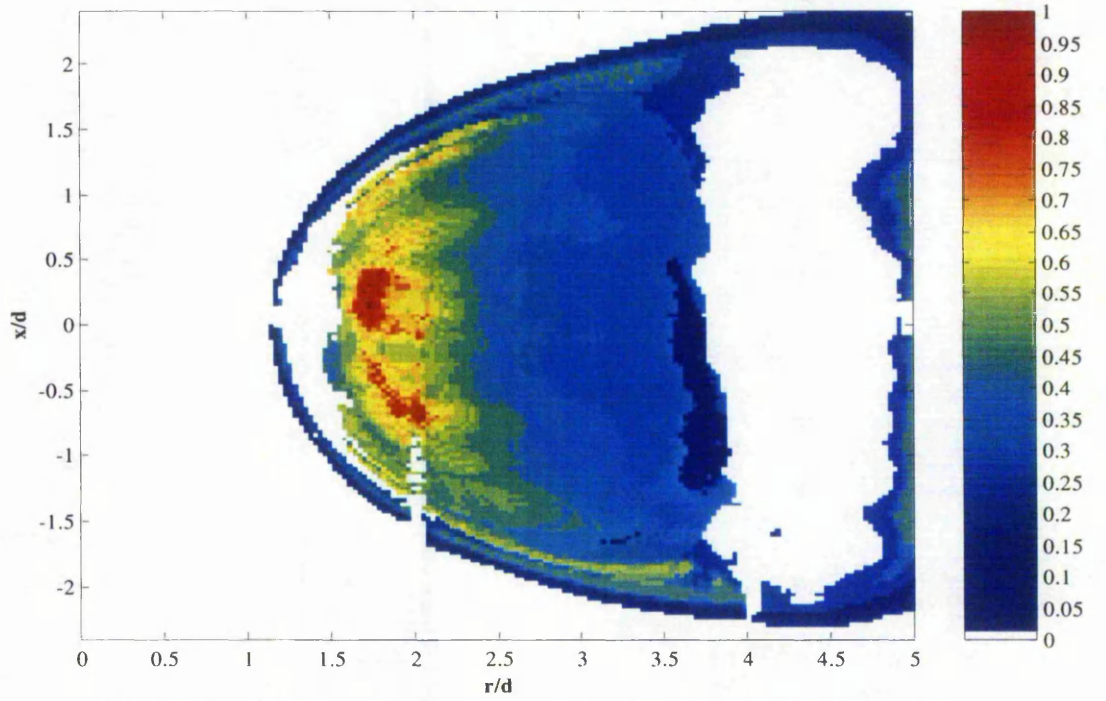

Figure 7.28: Jet effectiveness, z/d = 3, Re = 20 000, $U_j / U_c = 3$.

Figure 7.29 and 7.30 illustrate the distributions of Nusselt number and jet effectiveness for the axisymmetric impinging jet at a nozzle-to-plate spacing of 3d and exit Reynolds number of 40 000. The characteristic minima and maxima in heat transfer are depicted by the two ring-shaped domains. The stagnation Nusselt number rises to 145, approximating a $Re^{0.5}$ increment (from Re = 20 000). It then increases sharply to about 178 (at r/d ≈ 0.6) before declining to around 110 (at r/d ≈ 1.3). Again, the primary peak in heat transfer (at r/d ≈ 0.6) is a result of the impingement of large-scale turbulent structures, which is demonstrated by the slightly lower local jet effectiveness. As the turbulence level continues to grow at r/d ≥ 1.3, the Nusselt number increases accordingly to form a secondary peak of about 122 at r/d ≈ 1.8. At further downstream distances, the Nusselt number declines monotically due to continual flow diffusion and recirculation of the wall jet fluid.

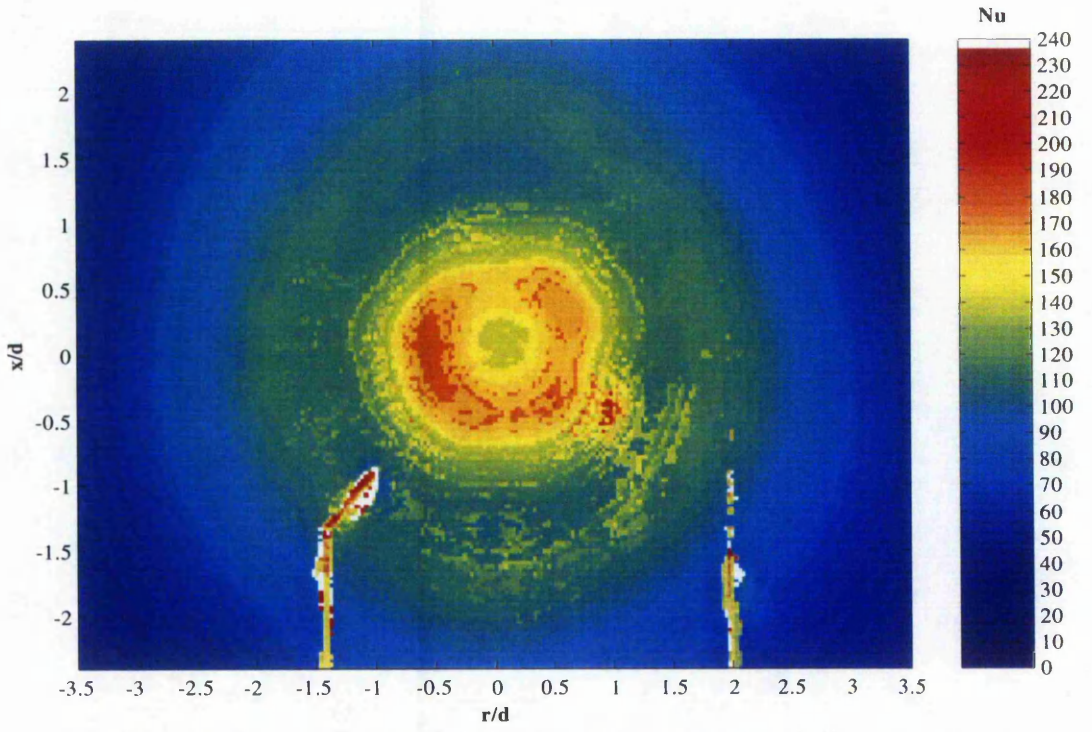

Figure 7.29: Nusselt number distribution, z/d = 3, Re = 40 000, no crossflow.

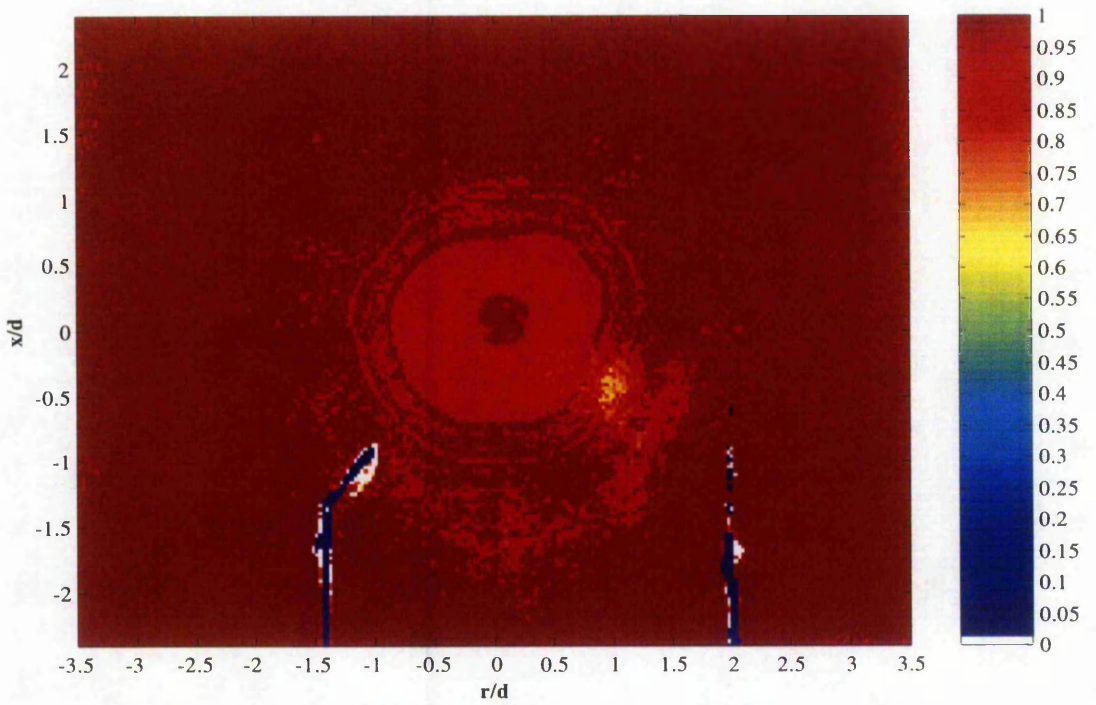

Figure 7.30: Jet effectiveness, z/d = 3, Re = 40 000, no crossflow.

The distributions of Nusselt number and jet effectiveness beneath the impinging jet in crossflow at $U_j / U_c = 5$ are illustrated in Figure 7.31 and 7.32 respectively. The stagnation point is shifted downstream to r/d ≈ 0.5, where the local heat transfer rates are marginally higher. The jet is generally ineffective in convecting heat, notably in the wall jet region. Nonetheless, in the boundary of interaction between the wall jet and the crossflow (e.g. -0.9 ≤ r/d ≤ -0.4 and 2.7 ≤ r/d ≤ 3.3), the surface heat transfer increases considerably due to the intense local turbulent mixing.

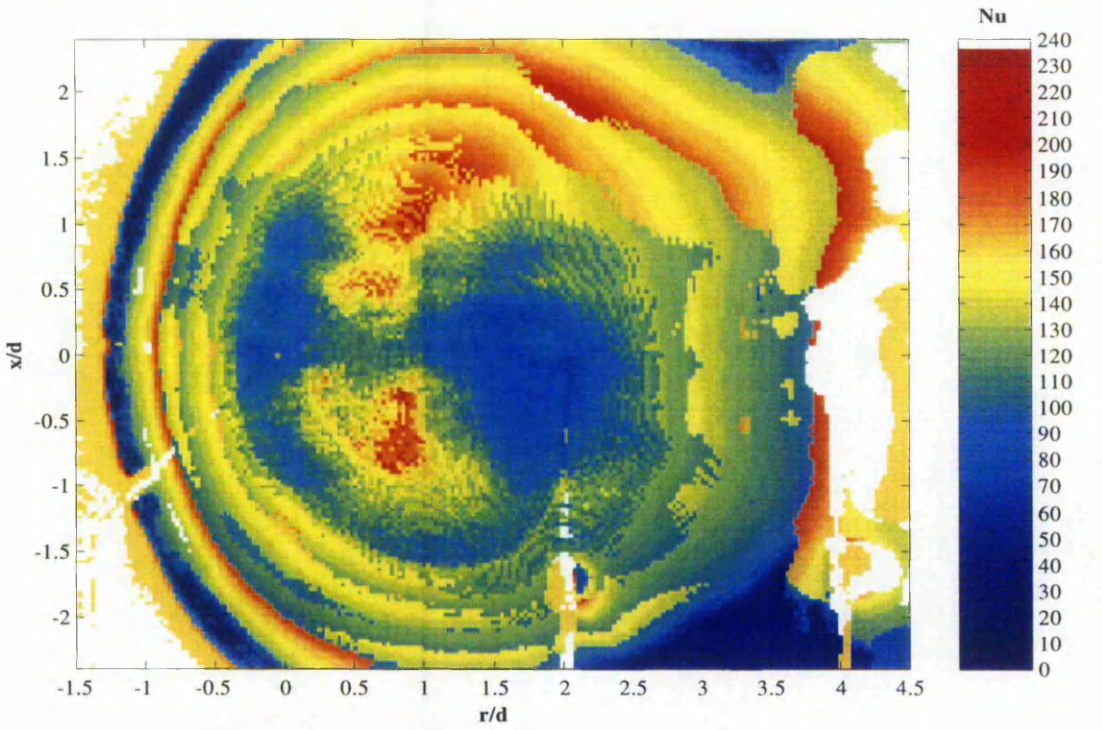

Figure 7.31: Nusselt number distribution, z/d = 3, Re = 40 000, $U_j / U_c = 5$.

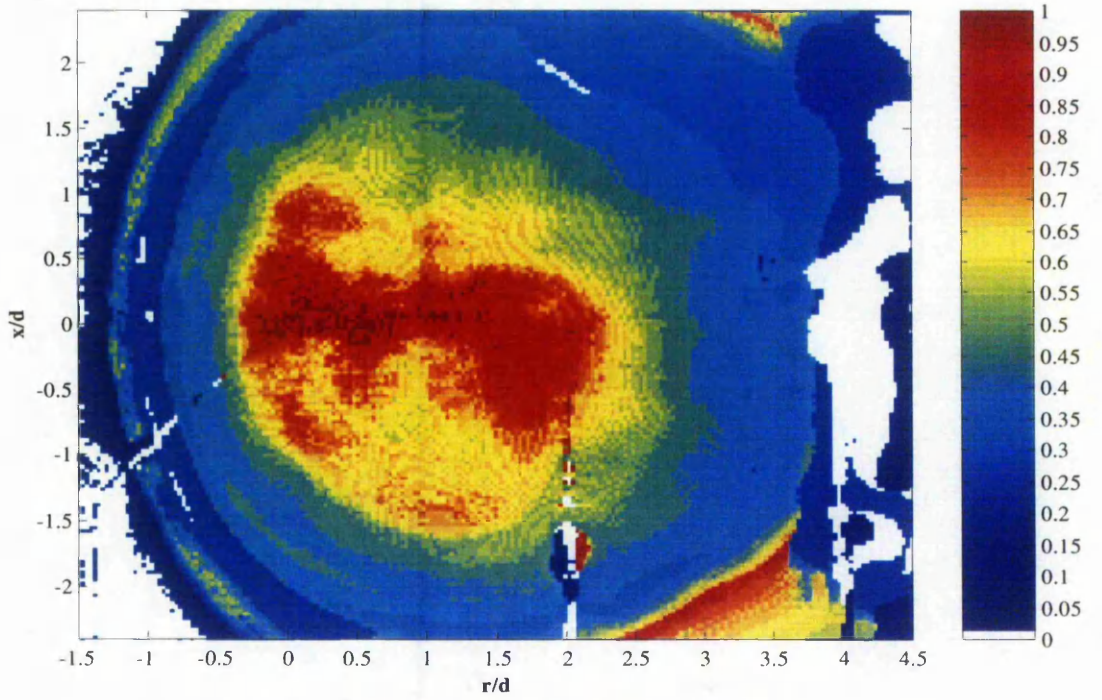

Figure 7.32: Jet effectiveness, z/d = 3, Re = 40 000, $U_j / U_c = 5$.

Figure 7.33 and 7.34 illustrate that at $U_j / U_c = 4$, the surface heat transfer is surprisingly high and distributed quite uniformly as the entire bulk fluid becomes extremely turbulent. This lends support to the work of Whidden et al. (1992), who postulated that the highest average heat transfer occurs when the impinging jet and the crossflow act with near equal intensity. The majority of the bulk fluid begins to impinge only at r/d ≈ 1.0, where the local Nusselt number varies from 160 to 190. Again, a unique region of heat transfer is created (at $0.3 \leq r/d \leq 0.6$) due to the presence of a secondary vortex, as demonstrated in Figure 6.35 and 6.36. Noticeably, the heat transfer in the boundary of interaction between the wall jet and the crossflow (e.g. $0.1 \leq r/d \leq 0.3$ and $2.9 \leq r/d \leq 3.7$) is also enhanced (i.e. $150 \leq Nu \leq 200$). This heat transfer condition is, arguably, the most efficient for a nozzle-to-plate spacing of 3d.

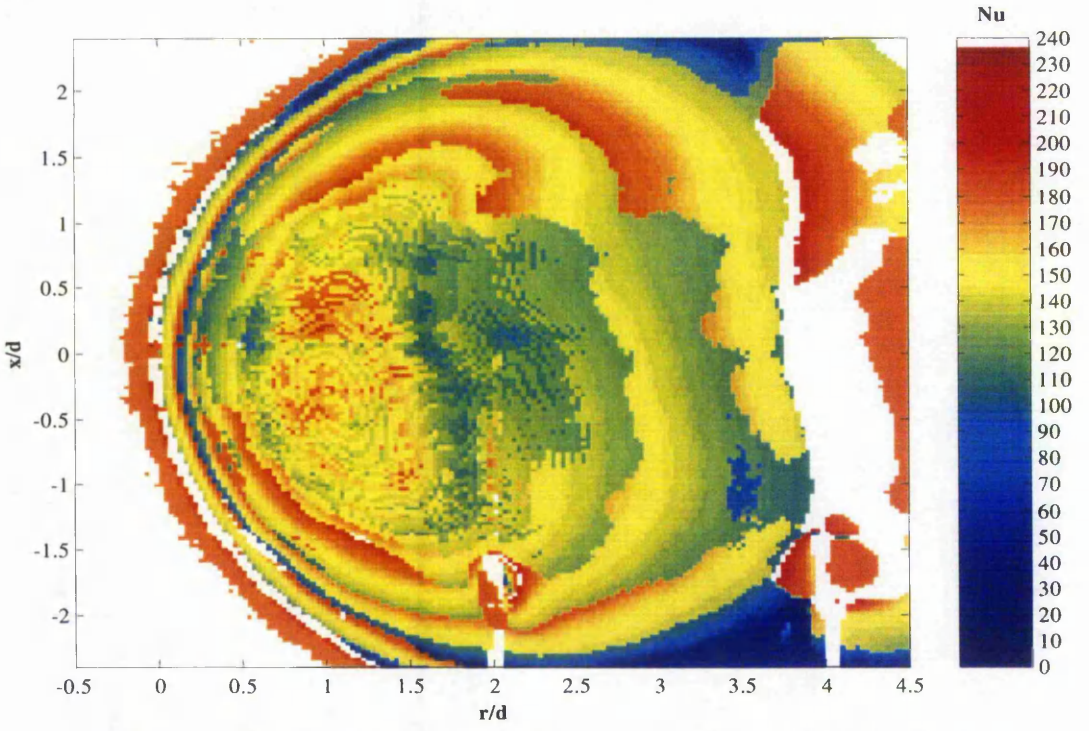

Figure 7.33: Nusselt number distribution, z/d = 3, Re = 40 000, $U_j / U_c = 4$.

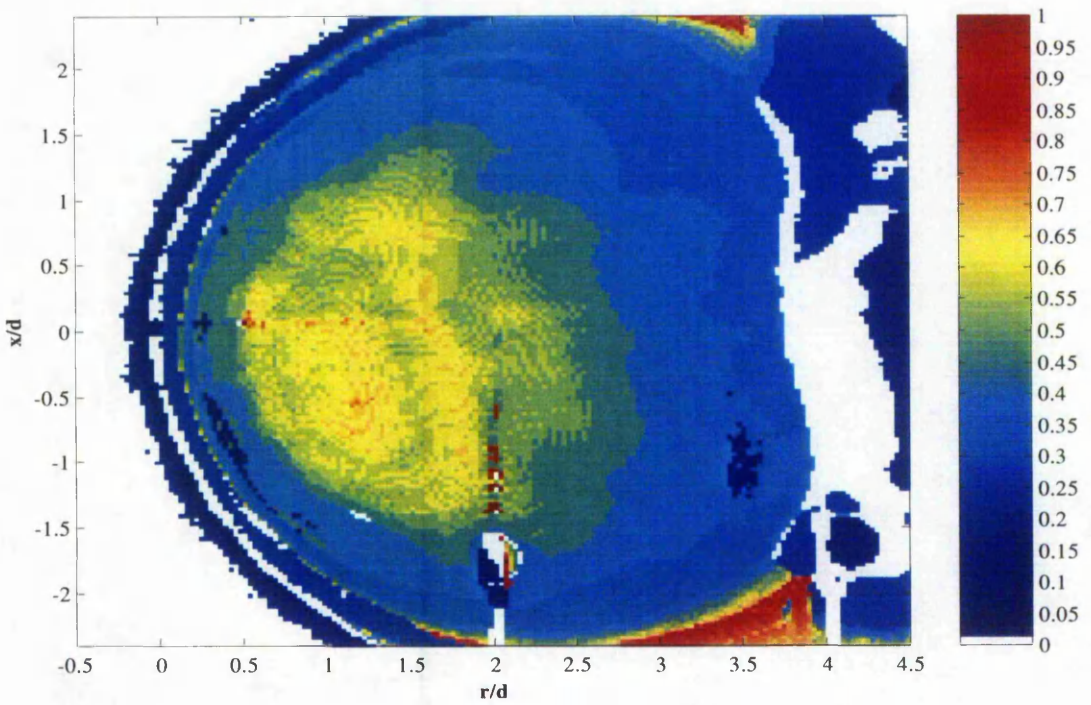

Figure 7.34: Jet effectiveness, z/d = 3, Re = 40 000, $U_j / U_c = 4$.

Figure 7.35 and 7.36 show that as the crossflow is strengthened to $U_j / U_c = 3$, the surface heat transfer distributes randomly within a smaller area and at a lower magnitude. The weakened impinging bulk fluid results in the heat transfer level to fluctuate largely within the interval $1.9 \leq r/d \leq 4.3$. The problems of uniformity and effectiveness associated with this jet means that it is inappropriate for practical heat transfer applications.

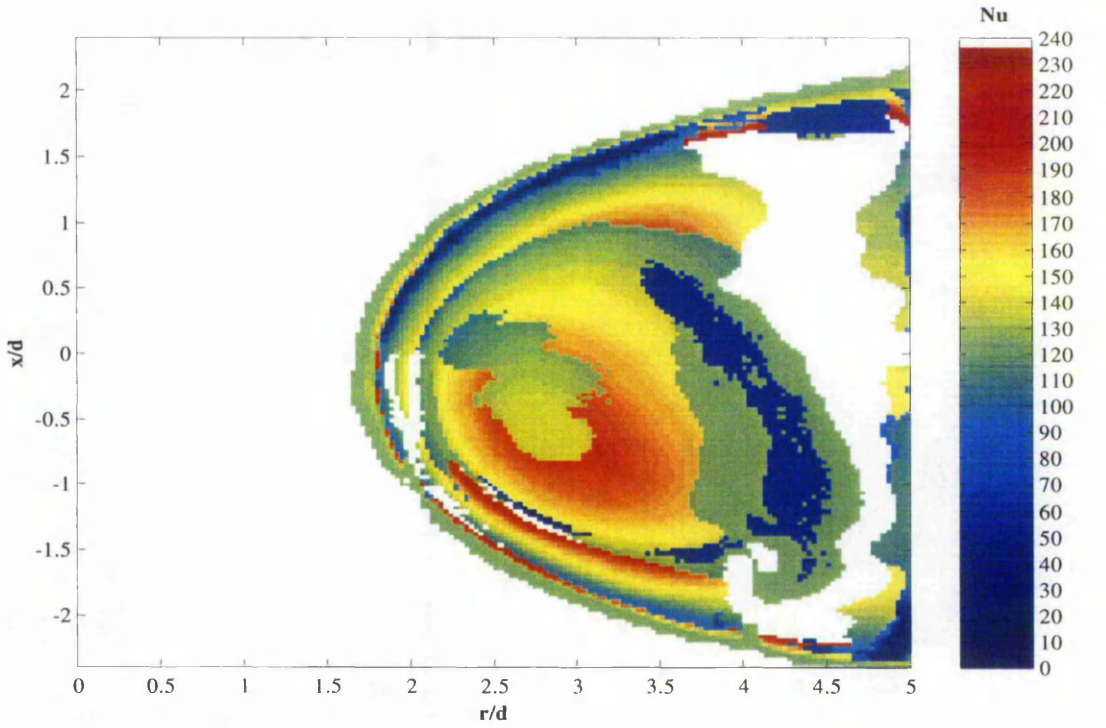

Figure 7.35: Nusselt number distribution, z/d = 3, Re = 40 000, $U_j / U_c = 3$.

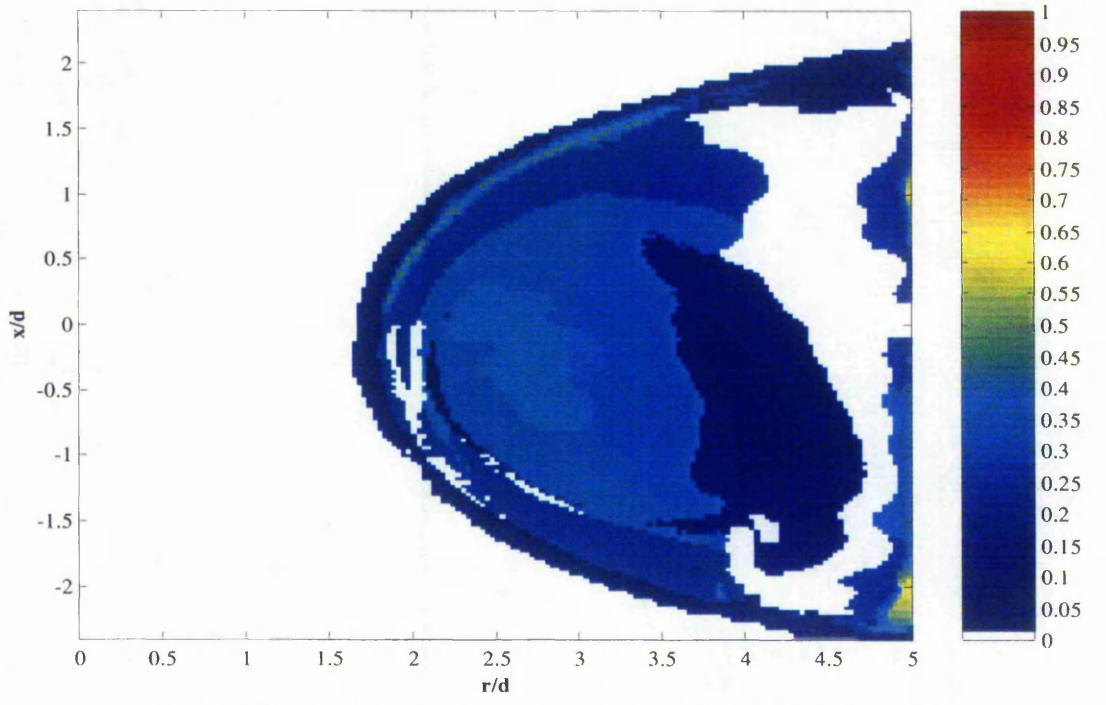

Figure 7.36: Jet effectiveness, z/d = 3, Re = 40 000, $U_j / U_c = 3$.

7.2 Concluding Remarks

An experimental study of surface heat transfer beneath confined single impinging jets with, and without, crossflow has been undertaken. The heated jet discharged with uniform exit velocity and temperature profiles at Reynolds numbers of 20 000 and 40 000, and was exposed to an ambient temperature crossflow at jet-to-crossflow velocity ratios of 2, 3, 4 and 5. Non-dimensional nozzle-to-plate spacings of 1.5d and 3d were considered. The techniques of liquid crystal thermography and an intensity-based image processing system have been used to determine the full distributions of Nusselt number and jet effectiveness. The Nusselt number data for the confined single axisymmetric impinging jets are consistent with previously published data for similar flow conditions, e.g. Baughn and Shimizu (1989), and Gillespie et al. (1996). All the heat transfer data have been fully analysed, interpreted and correlated, wherever possible, to the near wall hydrodynamic and thermal characteristics.

With the z/d = 1.5 configuration, the axisymmetric impinging jet for Re = 20 000 produces the characteristic minima and maxima in surface heat transfer. Specifically, the Nusselt number rises from approximately 102 at the stagnation point to reach a maximum of about 128 at r/d ≈ 0.65. The primary peak in heat transfer (at r/d ≈ 0.65) is incited by the impingement of large-scale turbulent structures convected from the edge of the jet. The secondary peak in heat transfer (Nu ≈ 98 at r/d ≈ 1.6) is attributed to the continuous increase in the local turbulence level. At further downstream distances (r/d ≥ 1.7), the Nusselt number attenuates due to the diffusion and recirculation of the wall jet fluid towards the upper confining plate.

When the impinging jet is coupled with an upstream crossflow at $U_j / U_c = 5$, the stagnation point is swayed downstream (by ≈ 0.1d) but the local Nusselt number remains unchanged (at ≈ 105). The heat transfer in the interval -0.6 ≤ r/d ≤ -0.3 is enhanced (Nu ≈ 150) as the upstream impinging fluid grows turbulent as a result of direct collision and mixing with the crossflow. At r/d ≈ 0.65, the crossflow flows pass the jet core and

suppresses the local turbulence level, hence causing the inner peak in heat transfer to diminish. In the downstream wall jet region ($r/d \geq 0.8$), surface heat transfer decreases gradually up to the boundary of interaction with the crossflow (e.g. at $-2.1 \leq r/d \leq -1.8$ and $2.1 \leq r/d \leq 2.6$), where intense fluid mixing promotes turbulence and heat transfer. At $U_j/U_c = 4$, the stronger crossflow deflects the stagnation point downstream by $\approx 0.18d$ and increases the local heat transfer (to ≈ 122) through the incitement of turbulence. Heat transfer in the domain where the crossflow collides directly with the impinging fluid also rises profoundly (to ≈ 198). In addition, the Nusselt number around the downstream jet core ($0.5 \leq r/d \leq 0.8$) increases (to ≈ 150) due to the higher turbulence level induced by the bypassing crossflow. At $U_j/U_c = 3$, the stagnation point is deflected downstream by $\approx 0.32d$. The crossflow pushes the upstream jet core towards its centre and causes a higher local turbulence level. As a result, the local Nusselt number escalates to about 205. Nonetheless, heat transfer in the downstream wall jet region deteriorates due to reduced jet effectiveness. As the crossflow is strengthened to $U_j/U_c = 2$, the jet becomes ineffective and spans over a much smaller area. The heat transfer is markedly lower ($Nu \leq 125$) and the impingement heat transfer only occurs at $r/d \geq 0.5$.

At Re = 40 000, the characteristic minima and maxima in heat transfer produced by the axisymmetric impinging jet become profound. The surface heat transfer characteristic resembles closely to that described for Re = 20 000. The stagnation Nusselt number approximates a $Re^{0.5}$ rise (from Re = 20 000) to 142, thus corroborating with Silbukin's laminar boundary layer theory. The Nusselt number attains a maximum of 175 (at $r/d \approx 0.65$) before declining to about 132 (at $r/d \approx 1.2$). From $r/d \geq 1.3$, the Nusselt number increases again to form a secondary peak of about 160 (at $r/d \approx 1.65$). At further downstream distances, heat transfer declines gradually due to the diffusion and recirculation of the wall jet fluid.

When an upstream crossflow is imposed at $U_j/U_c = 5$, the stagnation point is deflected downstream (by $\approx 0.13d$) but the local Nusselt number remains unchanged (at $\approx$

143). Heat transfer within the jet core is more uniform but marginally lower in magnitude (compared to without crossflow). In the wall jet region ($r/d \geq 0.8$), heat transfer decreases gradually up to the boundary of interaction with the crossflow (e.g. at $-1.9 \leq r/d \leq -1.6$ and $2.0 \leq r/d \leq 2.5$), where the Nusselt number escalates (to ≈ 214) due to the formation of highly intensified turbulence. The excellent heat transfer characteristic of this particular jet makes it ideal for impingement application involving crossflow. At $U_j/U_c = 4$, the crossflow sways the stagnation point further downstream by $\approx 0.19d$. Generally, the heat transfer performance is deteriorated as the intrinsically turbulent jet is weakened by the crossflow. Heat transfer continues to decline at $U_j/U_c = 3$. By $U_j/U_c = 2$, the jet becomes extremely ineffective with a low degree of heat transfer and uniformity.

With the $z/d = 3$ configuration, the axisymmetric impinging jet for $Re = 20\,000$ results in a stagnation Nusselt number of 105, which rises to a peak of about 130 at $r/d \approx 0.55$ where local impingement of large-scale turbulence also occurs. At $r/d \geq 0.8$, the Nusselt number declines slowly as the wall jet transports laterally outwards.

When an upstream crossflow is imposed at $U_j/U_c = 5$, the stagnation point is deflected downstream by as much as 0.4d. This is because the jet deflection is accentuated at the larger nozzle-to-plate spacing. The crossflow results in a considerable loss in the hydrodynamic energy of the jet, which extends to the centre of the jet core, and therefore lowers the convective heat transfer rates. Nonetheless, a slight increase in Nusselt number is still seen in the boundary of interaction between the wall jet and the crossflow (e.g. $-1.1 \leq r/d \leq -0.6$ and $2.9 \leq r/d \leq 3.3$). By $U_j/U_c = 4$, the core of the jet is destroyed completely by the crossflow. Most of the impingement heat transfer occurs at $r/d \geq 0.8$ but a unique region of heat transfer is created at $0 \leq r/d \leq 0.3$ due to the formation of a secondary vortex. Heat transfer in the boundary of interaction between the wall jet and the crossflow is also enhanced. At $U_j/U_c = 3$, the crossflow dominates the heat transfer characteristic up to $r/d \approx 1.6$, beyond which impingement heat transfer grows slowly over a much smaller area. The impinging jet is, therefore, considered ineffective.

At Re = 40 000, the characteristic minima and maxima in heat transfer for axisymmetric jets at low nozzle-to-plate spacings become apparent again. The stagnation Nusselt number increases to 145, a $Re^{0.5}$ increment from Re = 20 000. It then rises to about 178 (at r/d ≈ 0.6) before declining to approximately 110 (at r/d ≈ 1.3). The primary peak in heat transfer (at r/d ≈ 0.6) is again a result of the impingement of large-scale turbulent structures. At r/d ≥ 1.3, the Nusselt number increases to form a secondary peak of about 122 at r/d ≈ 1.8 before attenuating at further downstream distances due to the diffusion and recirculation of the wall jet fluid.

When a crossflow is imposed at $U_j / U_c = 5$, the stagnation point is deflected downstream to r/d ≈ 0.5. The jet becomes ineffective in convecting heat particularly in the wall jet region. Nonetheless, in the boundary of interaction between the wall jet and the crossflow (e.g. -0.9 ≤ r/d ≤ -0.4 and 2.7 ≤ r/d ≤ 3.3), surface heat transfer increases considerably due to the intense local turbulent mixing. At $U_j / U_c = 4$, heat transfer is surprisingly high and distributed quite uniformly as the impinging jet and the crossflow act with near equal intensity. The majority of the bulk fluid begins to impinge only at r/d ≈ 1.0, where the local Nusselt number varies from 160 to 190. Heat transfer in the boundary of interaction between the wall jet and the crossflow (e.g. 0.1 ≤ r/d ≤ 0.3 and 2.9 ≤ r/d ≤ 3.7) is also enhanced significantly (150 ≤ Nu ≤ 200). Arguably, this is the ideal impingement heat transfer condition for nozzle-to-plate spacing of 3d, despite it is difficult to establish in the real environment. Further strengthening the crossflow to $U_j / U_c = 3$ results in the surface heat transfer to distribute randomly within a smaller area and at a lower overall magnitude.

The major dilemma in the limited literature of impinging jets with crossflow is the considerable amount of contradictory conjectures. The present investigation has demonstrated that the surface heat transfer characteristic beneath a single impinging jet with crossflow, indeed, varies sensitively with the flow conditions. Nonetheless, several rules of thumb can be established for design purposes based on the following findings: -

1. The impinging jets at z/d = 1.5 (with, and without, crossflow) are evidently more effective in yielding greater magnitude and uniformity of surface heat transfer (than those at z/d = 3). Hence, it is a preferred spacing for impingement heat transfer involving crossflow.

2. The extent of jet deflection resulted from a crossflow is consistently greater at the higher nozzle-to-plate spacing (i.e. z/d = 3) and Reynolds number (i.e. 40 000), as illustrated in Figure 7.37. Therefore, a better control of impingement heat transfer process can be achieved at z/d = 1.5 and at a lower Reynolds number.

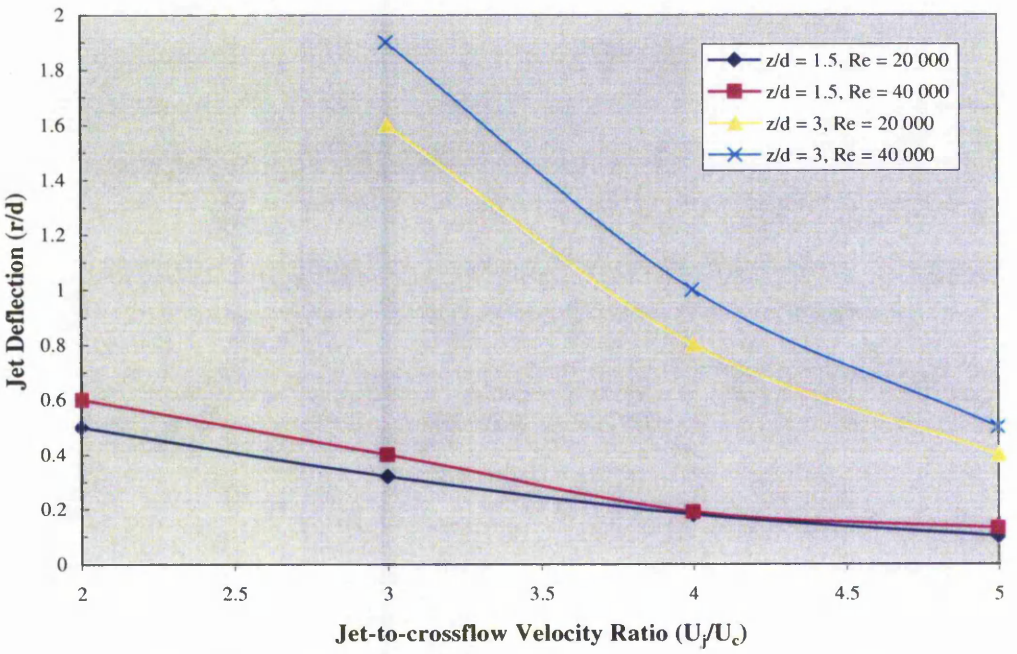

Figure 7.37: Jet deflection versus jet-to-crossflow velocity ratio.

Note: The location of the stagnation point is used to derive the jet deflection. In the case where the stagnation point becomes ambiguous, the point of the commencement of impingement is referred.

3. For z/d = 1.5, the highest overall convective heat transfer rate with reasonable uniformity is achieved when the impinging jet is coupled with a moderate strength crossflow, i.e. at $U_j/U_c = 5$ for Re = 40 000. The heat transfer performance becomes poor when strength of the crossflow is comparable to that of the primary impinging jet, i.e. at $U_j/U_c = 2$.

4. For z/d = 3, optimum heat transfer condition exists when the impinging jet and the crossflow act with near equal intensity, i.e. at $U_j/U_c = 4$ for Re = 40 000. Further strengthening of the crossflow would lead to a drastic deterioration of the heat transfer performance.

CHAPTER 8
CONCLUSIONS AND RECOMMENDATIONS

In this final chapter, a summary of the work undertaken and major findings from the research programme is provided with reference to the aims and objectives listed in Section 1.2. The conclusions drawn from the experimental and theoretical investigations are discussed in detail. The practical significance of the findings is then outlined and elaborated. Finally, recommendations for further work are given.

8.1 Summary of Work Undertaken and Major Findings

A versatile experimental wind tunnel facility and data acquisition system have been designed, built and commissioned to facilitate the measurement of velocity, turbulence, temperature and fluctuating temperature beneath confined single impinging jets with, and without, crossflow. The turbulent jet discharged from a contoured nozzle of 100 mm diameter with a uniform exit velocity profile at Reynolds numbers of 20 000 and 40 000, and subjected to a uniform crossflow at jet-to-crossflow velocity ratios of 2, 3, 4 and 5. Non-dimensional nozzle-to-plate spacings of 1.5d and 3d have been studied in depth. Hot-wire anemometry and cold-wire thermometry techniques have been applied to obtain near wall hydrodynamic and thermal flow fields respectively. A dual hot/cold-wire boundary layer probe was used to measure velocity, turbulence, temperature and fluctuating temperature adjacent to the impingement surface. The transient liquid crystal technique has been employed in conjunction with an intensity-based image processing system to determine the full heat transfer coefficients and effectiveness on the target impingement surface. A heater mesh has been developed for the initiation of the thermal transient experiments. Software has been written using Microsoft Visual C++ programming syntax to facilitate the control, collection and storage of experimental heat transfer data. Uncertainty analysis has been conducted during the initial design phase to identify and minimise factors that contributed to experimental error. This enabled the experimental facilities and measurement procedures to be optimised for accurate acquisition of data.

Measured near wall flow fields beneath a semi-confined single impinging jet were also compared with the theoretical solutions for stagnation three-dimensional flow (Homann's model) and viscous flow for an axisymmetric case (Froessling's theory). Smoke-flow visualisation has been used during the preliminary stages to provide a qualitative insight into the complex flow regimes of single impinging jets with, and without, crossflow. The experimental results have been fully analysed, interpreted and compared, wherever possible, to previously published work documented in a comprehensive literature review covering single impinging jets with, and without, crossflow.

As a direct result of this investigation new velocity, turbulence, temperature and fluctuating temperature data have been obtained for the case of confined single impinging jets with, and without, crossflow. Surface heat transfer results have been correlated with near wall hydrodynamic and thermal characteristics, thus extending the knowledge of jet impingement heat transfer involving crossflow. Ultimately, a set of guidelines has been proposed for the optimum design of impingement heat transfer devices. As far as the author is aware, prior to this study no direct correlation of surface heat transfer data with near wall characteristics had been established for the range of jet configurations considered. Finally, an application of liquid crystals for thermal field investigation across the streamwise horseshoe vortex has been furthered developed.

8.2 Theoretical Treatment of Experimental Results

Theoretical models for stagnation three-dimensional flow (Homann's model) and viscous flow for an axisymmetric case (Froessling's theory) have been used to predict near wall flow fields beneath a semi-confined impinging jet at z/d = 2 and 6.5. The results have been contrasted with experimental data obtained for the same geometry.

It has been demonstrated that the velocity profiles in the inviscid region of the near wall flow for z/d = 2 can be predicted accurately using Homann's stagnation three-dimensional flow model. As the core of the impinging jet (r/d = 0.5) is approached, the

flow regime becomes very complex and cannot be predicted using the model. Prediction of boundary layer profiles using the viscous flow solution for an axisymmetric case (Froessling's theory) is also reasonable providing the mean flow remains laminar and dominated by the radial wall jet. For z/d = 6.5, the near wall flow field is essentially turbulent on impact, and predictions using the stagnation three-dimensional model and the viscous flow for an axisymmetric case are both inappropriate.

8.3 Qualitative Flow Visualisation Results

Flow patterns created by single impinging jets with, and without, crossflow were silhouetted using smoke particles, produced by vaporising Propylene Glycol in a smoke generator. A non-dimensional nozzle-to-plate spacing of 3d has been studied. The experiments covered Reynolds number ranging from 5000 to 40 000, and jet-to-crossflow velocity ratios of 1, 2 and 5. Images were captured from the side of the test section using a CCD camera placed directly opposite to the exiting spent air.

For low Reynolds numbers (Re = 5000 and 10 000), the instability at the edge of axisymmetric jets incites flow disturbances, which grow into organised toroidal vortex structures that are convected downstream. These vortices promote entrainment of the ambient fluid and subsequently cause contractions and expansions of the potential core. In the wall jet region ($r/d \approx 0.6 - 0.7$), the impinging vortices consecutively induce ring-shaped wall eddies which are rolled up in the lateral direction and diminished over the interval $1 \leq x/d \leq 2$, an observation also made by Popiel and Trass (1991). At higher Reynolds number ($Re \geq 20\ 000$), toroidal vortex structures become less evident as turbulent structures dominate the edge of the jet core. These impinging large-scale turbulences instigate thinning and transition of the wall jet from laminar to turbulent flow, and subsequently result in the formation of the primary peak in heat transfer coefficient.

The jet diameter and turbulence level in the mixing region surrounding the potential core grow significantly under the influence of an imposed crossflow. The impinging jet is also distorted and deflected radially downstream by the crossflow. More

importantly, the effectiveness of the impinging jet is reduced drastically when the strength of the crossflow becomes comparable to that of the impinging jet ($U_j/U_c \leq 2$). This is in line with the conjecture of Obot and Trabold (1987), who reported that the average surface heat transfer for array jets is severely degraded under an intermediate crossflow condition. Typically at Re = 20 000 and $U_j/U_c = 1$, the impinging fluid is diverted to flow near the upper confinement wall, and the mainstream flow is essentially contributed by the crossflow. Single impinging jets (with, and without, crossflow) at Re = 20 000 and 40 000 resemble similar flow behaviours, despite the jets at higher Reynolds number are dominated by large-scale turbulent fluctuations with imposed fine-scale turbulence.

8.4 Quantitative Experimental Near Wall Results

The near wall hydrodynamic and thermal flow fields beneath confined single impinging jets with, and without, crossflow have been obtained experimentally to complement surface heat transfer data. Non-dimensional nozzle-to-plate spacings of 1.5d and 3d have been considered in depth. The jet discharged at Reynolds numbers of 20 000 and 40 000, and was subjected to a crossflow at jet-to-crossflow velocity ratios of 2, 3, 4 and 5.

At z/d = 1.5, the axisymmetric jet for Re = 20 000 impinges orthogonally onto the target surface before accelerating radially outwards to develop into a wall jet. Large-scale turbulent structures surrounding the jet core are transported onto the wall (at r/d ≈ 0.7), thereby prompting a local thinning and transition of the wall jet from laminar to turbulent flow. A region of high turbulence is created in the interval $1.1 \leq r/d \leq 1.9$ and $0.02 \leq y/d \leq 0.15$ due to flow separation. At $r/d \geq 2$, the bulk fluid diffuses and recirculates upward towards the upper confining plate. When a crossflow is imposed at a jet-to-crossflow velocity ratio, U_j/U_c, of 5, the stagnation point is deflected slightly downstream (by ≈ 0.1d). The moderate crossflow helps to suppress flow separation in the downstream wall jet region by forcing the bulk fluid to re-attach to the wall. At $U_j/U_c = 4$, the jet

deflection increases to ≈ 0.16d and the turbulence level in the wall jet rises due to increased mixing with the crossflow. At $U_j/U_c = 3$, the crossflow sways the stagnation point downstream by ≈ 0.32d. By $U_j/U_c = 2$, the core of the jet is almost destroyed and the impingement begins only at r/d ≈ 0.5.

The velocity and turbulence characteristics of the axisymmetric impinging jet for Re = 40 000 resemble that described for Re = 20 000. When a crossflow is imposed at $U_j/U_c = 5$, the stagnation point is deflected downstream by ≈ 0.12d and the turbulence level in the downstream wall jet region is suppressed. At $U_j/U_c = 4$, the core of the jet is deflected downstream by ≈ 0.18d but the turbulence level in the wall jet region rises due to intensified mixing with the crossflow. At $U_j/U_c = 3$, the crossflow starts to push the upstream impinging fluid towards the core of the jet. By $U_j/U_c = 2$, the crossflow becomes dominant over the flow within the jet core.

At z/d = 3, the core of the axisymmetric impinging jet for Re = 20 000 is marginally more turbulent (compared to the case for z/d = 1.5) as the jet develops further at the larger spacing. When an upstream crossflow is imposed at $U_j/U_c = 5$, the stagnation point is deflected downstream by as much as ≈ 0.4d, thereby corroborating with the work of Sparrow et al. (1975) who found that jet deflection is accentuated at a larger nozzle-to-plate spacing. The core of the impinging jet is destroyed by the crossflow at $U_j/U_c = 4$. By $U_j/U_c = 3$, the mainstream crossflow effectively dominates the near wall hydrodynamic characteristic up to r/d = 1.7. Typically, the fluid velocity in the boundary layer (y/d ≤ 0.02) attains a maximum of merely 0.2 - 0.3U_{CL}.

The near wall velocity and turbulence characteristics of the axisymmetric jet for Re = 40 000 are similar to that described for Re = 20 000. When a crossflow is introduced at $U_j/U_c = 5$, the stagnation point is deflected downstream by ≈ 0.5d. At $U_j/U_c = 4$, the entire jet core is destroyed by crossflow and a minor impingement begins only at r/d ≥

1.0. By $U_j/U_c = 3$, the impinging bulk fluid is virtually diverted such that it only reaches the target plate from r/d ≈ 1.8 onwards. The typical fluid velocity in the boundary layer (y/d ≤ 0.02) reaches a maximum of only 0.3 - $0.4U_{CL}$.

In the study of the near wall thermal characteristic for z/d = 1.5 and Re = 20 000, the temperature field within the core of the heated jet remains constant until y/d ≤ 0.03, whereby sharp temperature gradients are observed. A local thinning of the thermal boundary layer (at r/d ≈ 0.6) substantiates the physics behind the formation of the primary maximum in heat transfer coefficient, as described by Ball et al. (1998), amongst others. In the shear-driven layer the jet mixes with the ambient fluid and therefore resulting in a high local fluctuating temperature. Upon impingement, the temperature field diminishes gradually in the lateral direction. When coupled with an ambient temperature crossflow at $U_j/U_c = 5$, the potential core of the jet remains thermally undisrupted despite the temperature in the wall jet region drops rapidly. The temperature of the wall jet falls more sharply at $U_j/U_c = 4$ due to increased mixing with the crossflow. At $U_j/U_c = 3$, the influence of the crossflow extends to the centre of the jet core. By $U_j/U_c = 2$, the crossflow dominates the near wall thermal characteristic up to r/d = 0.5.

At z/d = 3, the temperature field of the heated axisymmetric impinging jet for Re = 20 000 declines faster (compared to at z/d = 1.5) due to increased mixing with the surrounding ambient fluid at the larger nozzle-to-plate spacing. The introduction of a crossflow at $U_j/U_c = 5$ affects the entire temperature field of the jet. Typically, the near wall temperature (at y/d ≤ 0.04) attains a maximum normalised value of only 0.6 – 0.7, as opposed to 0.9 – 1.0 in the case for z/d = 1.5. The thermal mixing between the jet and the oncoming crossflow continues to increase at $U_j/U_c = 4$. By $U_j/U_c = 3$, the crossflow dominates the near wall temperature field up to r/d ≈ 1.6. The highest normalised near wall temperature (at y/d ≤ 0.04) is only 0.3 – 0.4, approximately 63 % lower than in the case for z/d = 1.5.

8.5 Quantitative Experimental Surface Heat Transfer Results

Full surface heat transfer distribution beneath confined single impinging jets with, and without, crossflow has been obtained. The heated jet discharged with uniform exit velocity and temperature profiles at Reynolds numbers of 20 000 and 40 000, and was exposed to an ambient temperature crossflow at jet-to-crossflow velocity ratios of 2, 3, 4 and 5. Non-dimensional nozzle-to-plate spacings of 1.5d and 3d have been studied in detail.

At z/d = 1.5, the axisymmetric impinging jet for Re = 20 000 produces the characteristic minima and maxima in surface heat transfer. The primary peak in heat transfer (r/d ≈ 0.65) is triggered by the impingement of large-scale turbulent structures convected from the edge of the jet, as described by Gillespie et al. (1996). Whereas the secondary peak in heat transfer (at r/d ≈ 1.6) is attributed to the continuous increase in the local turbulence level, which has been detailed by Ashforth-Frost et al. (2001). Heat transfer attenuates at r/d ≥ 1.7 due to the diffusion and recirculation of the wall jet fluid towards the upper confining plate. When an upstream crossflow is imposed at $U_j / U_c = 5$, the stagnation point is deflected slightly downstream (by ≈ 0.1d) but the local heat transfer coefficient remains unchanged. Nonetheless, as the crossflow collides with the upstream impinging fluid (at -0.6 ≤ r/d ≤ -0.3), the resulting turbulence enhances the local heat transfer level. In the downstream wall jet region (r/d ≥ 0.8), heat transfer decreases gradually up to the boundary of interaction with the crossflow, where intense fluid mixing increases the local heat transfer. At $U_j / U_c = 4$, the stronger crossflow leads to increased deflection of the stagnation point (to ≈ 0.18d) and a marginally higher local heat transfer. Heat transfer in the jet core also rises profoundly due to the higher turbulence level induced by the oncoming crossflow. At $U_j / U_c = 3$, the stagnation point is shifted downstream by ≈ 0.32d. The crossflow pushes the upstream jet core towards its centre, causing the local Nusselt number to escalate. Nonetheless, the reduced jet effectiveness in the wall jet region results in a deterioration of the local heat transfer. At

$U_j/U_c = 2$, the jet spans over a much smaller area and impingement heat transfer occurs only at r/d ≥ 0.5.

At Re = 40 000, the stagnation Nusselt number approximates a $Re^{0.5}$ rise (from Re = 20 000), thereby lending support to Silbukin's laminar boundary layer theory. The characteristic minima and maxima in heat transfer produced by the axisymmetric impinging jet become more profound. Specifically, the Nusselt number attains a primary peak at r/d ≈ 0.65 and a secondary peak at r/d ≈ 1.65. At further downstream distances, heat transfer declines due to the diffusion and recirculation of the wall jet fluid. For the jet in crossflow at $U_j/U_c = 5$, the stagnation point is deflected downstream (by ≈ 0.13d). The crossflow causes heat transfer within the jet core to distribute more uniformly. Heat transfer in the wall jet region decreases slowly up to the boundary of interaction with the crossflow, where intense turbulent mixing enhances the local Nusselt number. Essentially, this jet configuration is ideal for impingement application involving crossflow due to its ability to yield a high magnitude and uniformity of the surface heat transfer. At $U_j/U_c = 4$, the deflection of the stagnation point increases to ≈ 0.19d and the convective heat transfer performance deteriorates as the turbulent jet is weakened markedly by the crossflow. Heat transfer declines further at $U_j/U_c = 3$, while the stagnation point is shifted downstream by ≈ 0.4d. By $U_j/U_c = 2$, the impinging jet is no longer effective in convecting heat.

At z/d = 3, the axisymmetric impinging jet for Re = 20 000 attains a peak in heat transfer at r/d ≈ 0.55 due to the impingement of large-scale turbulence. Heat transfer declines slowly at r/d ≥ 0.8 as the wall jet moves laterally outwards. When a crossflow is imposed at $U_j/U_c = 5$, the stagnation point is deflected appreciably (by 0.4d). The crossflow lowers collectively the surface heat transfer rates, despite a marginal increase in heat transfer is still discernible in the boundary of interaction with the wall jet. At $U_j/U_c = 4$, a unique region of heat transfer is created at 0 ≤ r/d ≤ 0.3 due to the formation of a secondary vortex from the collision between the impinging jet and the

crossflow. However, moderate impingement heat transfer occurs only at r/d ≥ 0.8. The jet becomes extremely ineffective at $U_j/U_c = 3$ as the crossflow dominates the surface heat transfer characteristic up to r/d ≈ 1.6, beyond which a minor impingement heat transfer occurs over a smaller area.

At Re = 40 000, the characteristic minima and maxima in heat transfer produced by the axisymmetric jet become pronounced again. The stagnation Nusselt number also assumes a $Re^{0.5}$ rise (from Re = 20 000). For the jet in crossflow at $U_j/U_c = 5$, the stagnation point is shifted downstream to r/d ≈ 0.5. Heat transfer is particularly low in the wall jet region despite a considerable increase is seen in the boundary of interaction with the crossflow due to an intense turbulent mixing. At $U_j/U_c = 4$, a significant impingement heat transfer occurs only at r/d ≥ 1.0. Nonetheless, the magnitude and uniformity of surface heat transfer are surprisingly high as the impinging jet and the crossflow act with near equal intensity. A substantial enhancement of surface heat transfer is also discernible in the boundary of interaction between the wall jet and the crossflow. Such a heat transfer condition is greatly desirable despite its difficulty to monitor in the practical environment. Further strengthening of the crossflow (to $U_j/U_c = 3$) would only deteriorate the convective heat transfer performance of the impinging jet.

8.6 Practical Application of the Work

The investigation has revealed that the surface heat transfer characteristic for a confined single impinging jet in crossflow varies sensitively with the near wall hydrodynamic and thermal phenomena. The maximum convective heat transfer with a fine uniformity is achieved at the nozzle-to-plate spacing of 1.5d under the influence of a moderate strength crossflow (i.e. at $U_j/U_c = 5$ for Re = 40 000). For design purposes entailing array jets such a flow configuration is recommended to achieve superior heat transfer performance.

For z/d = 1.5, high average values of Nusselt number are obtained when the crossflow leads to a uniform surface heat transfer distribution and a substantial increase in the turbulence level, with only a minor reduction in the strength of the jet. For z/d = 3, an ideal heat transfer condition exists when the impinging jet and the crossflow act with near equal intensity, that is, when the product of the hydrodynamic and turbulence energies attains a maximum value (i.e. at $U_j / U_c = 4$ for Re = 40 000).

The confined impinging turbulent jet in crossflow provides an ideal test case for the development and validation of turbulence and heat transfer models. The jet arrangement is geometrically simple to define from a numerical viewpoint. The complexity of the resulting flow and heat transfer phenomena, indeed, demands thorough assessment on the existing numerical models. The provision of near wall velocity, turbulence, temperature, fluctuating temperature and full surface Nusselt number data enables numerical modellers to assess the predictive performance and develop on the CFD codes. The experimental data are available in Microsoft Excel format upon request.

8.7 Recommendation for Further Work

The present work is novel such that it correlates the near wall hydrodynamic and thermal characteristics of confined single impinging jets with, and without, crossflow to the surface heat transfer results. Nonetheless, there are several other aspects of the jet flow that remain to be explored.

The quantification of the near wall characteristics should be extended to the upstream half of the jet where interaction with the crossflow often results in chaotic flow phenomena. The distribution of Reynolds shear stress and components of fluctuating velocity also need to be resolved and quantified. Such information can be acquired, for example, using a two-component Laser-doppler anemometer. In addition, the thermal field across the streamwise horseshoe vortex, created through the interaction between the jet and the crossflow, should be studied using the readily developed application of liquid

crystals. All these help to establish a further understanding of the flow and thermal fields for optimising the performance of jet impingement heat transfer.

The proposed design guidelines for single impinging jets in crossflow at low nozzle-to-plate spacings should be tested and implemented in a multiple-jet impingement heat transfer system. This would allow the design guidelines to be applied, with absolute confidence, for maximum heat exchange efficiency. The experimental data are also useful in the validation and further development of turbulence models. The easy-to-define jet impingement geometry means that the current work could be modelled numerically using a CFD package.

In due course, it may be possible to solve computationally, for all flow situations, the three-dimensional Navier-Stokes equations which are believed to give an adequate exact description of turbulence in simple fluids, Bradshaw (1997). Ultimately, the provision of a large amount of quality experimental test case data helps to edge closer to the successful solving of the complex governing equations.

REFERENCES

Abdel-Rahman, A., Tropea, C., Slawson, P. and Strong, A., 1987. On temperature compensation in hot-wire anemometry. J. Phys. E: Sci. Instrum., 20, 315 - 319.

Akino, N., Kunugi, T., Ichimiya, K., Mitsushiro, K. and Ueda, M., 1986. Improved liquid-crystal thermography excluding human color sensation - Part I. Concept and calibration, pressure and temperature measurements, ASME FED, 44, 57 – 62.

Akino, N., Kunugi, T., Shiina, Y., Ichimiya, K. and Kurosawa, A., 1989. Fundamental study on visualisation of temperature fields using thermosensitive liquid-crystals. Proc. 5th Int. Symp. on Flow Vis., Prague, August 21 – 25.

Ali Khan, M.M., Kasagi, N., Hirata. M. and Nishiwaki, N., 1982. Heat transfer augmentation in an axisymmetric impinging jet. Proc. 7th Int. Heat Transfer Conf., Munich, 6 - 10 Sept., 3, 363 - 368.

Allen, C., 1996. A computational and experimental examination of film cooling. PhD Thesis, University of Oxford, Oxford, U.K.

Andreopoulos, J., 1983. Heat transfer measurements in a heated jet-pipe flow issuing into a cold cross stream. J. Phys. Fluids, Vol. (26), 11, 3201 - 3210.

Andrews, G.E. and Hussain, C.I., 1986. Full coverage impingement heat transfer: the influence of channel height. Proc. 8th Int. Heat Transfer Conf., San Francisco, August, 1205 - 1211.

Ashforth-Frost, S., 1994. Flow visualisation of semi-confined jet impingement. PhD Thesis, The Nottingham Trent University, Nottingham, U.K.

References

Ashforth-Frost, S. and Jambunathan, K., 1994. Effect of nozzle geometry and semi-confinement on the potential core of a turbulent axisymmetric jet. Proc. 10th Int. Heat Transfer Conf., Brighton, 14 - 18 Aug., paper 63.

Ashforth-Frost, S., 1994. The use of liquid crystals in temperature visualisation. Biomechanics Conference proceedings, no. 75, 342 - 351.

Ashforth-Frost, S. and Jambunathan, K., 1996a. Effect of nozzle geometry and semi-confinement on the potential core of a turbulent axisymmetric free jet. Int. Commun. Heat Mass Transfer, 23(2), 155 - 162.

Ashforth-Frost, S., Jambunathan, K., Whitney, C.F. and Ball, S.J., 1996. Heat transfer from a flat plate to a turbulent axisymmetric impinging jet. Proc. IMechE Int. Symp. Optical Methods and Data Processing in Heat and Fluid Flow, London, 18-19 Apr., 71 - 79.

Ashforth-Frost, S., Jambunathan, K., Whitney, C.F. and Ball, S.J., 1997. Heat transfer from a flat plate to a turbulent axisymmetric impinging jet. J. Mechanical Engineering Science, Proc. Instn. Mech. Engrs. Part C, 211, 167 - 172.

Ashforth-Frost, S., Cheong, B.C.Y. and Ireland, P.T., 2001. Near wall flow characteristics beneath a turbulent impinging jet. Proc. 5th World Conf. on Exp. Heat Transfer, Fluid Mechanics, and Thermodynamics, Thessaloniki, 24 - 28 Sept., Vol. (2), 987 - 992.

Ball, S.J., 1998. Near wall flow characteristics in jet impingement heat transfer. PhD Thesis, The Nottingham Trent University, Nottingham, U.K.

Ball, S.J., Ashforth-Frost, S., and Jambunathan, K., 1998. Orthogonally impinging axisymmetric jet investigation – Heat transfer and near wall thermal flow field characteristics. Int. Heat Transfer Conference proceedings 11, Vol. (5), 457 - 462.

References

Ball, S.J., Ashforth-Frost, S., Jambunathan, K. and Whitney, C.F., 1999. Appraisal of a hot-wire temperature compensation technique for velocity measurements in non-isothermal flows. Int. J. Heat and Mass Transfer, 1 - 6.

Barata, J.M.M, Durão, D.F.G., Heitor, M.V. and McGuirk, J.J., 1991. Impingement of single and twin turbulent jets through a crossflow. AIAA J., 29(4), 595 – 602.

Baughn, J.W. and Shimizu, S., 1989. Heat transfer measurements from a surface with uniform heat flux and an impinging jet. ASME J. Heat Transfer, 111, 1096 - 1098.

Baughn, J.W. and Saniei, N., 1991. The effect of the thermal boundary condition on heat transfer from a cylinder in crossflow. ASME J. Heat Transfer, 113, 1020 - 1023.

Baughn, J.W., 1995. Liquid crystal methods for studying turbulent heat transfer. Int. J. Heat and Fluid Flow, 16, 365 - 375.

Bearman, P.W., 1971. Corrections for the effect of ambient temperature drift on hot-wire measurements in incompressible flows. DISA Info., No. 11, 25 - 30.

Beltaos, S. and Rajaratnam, N., 1977. Impingement of axisymmetric developing jets. J. Hydraulic Research, 15(4), 311 - 326.

Benedict, L.H. and Gould, R.D., 1996. Towards better uncertainty estimates for turbulence statistics. Experiments in Fluids, 22, 129 – 136.

Bradshaw, P., 1971. An Introduction to Turbulence and its Measurement. Pergamon Press, Oxford.

Bradshaw, P., 1997. Understanding and prediction of turbulent flow – 1996. Int. J. Heat and Fluid Flow, 18, 45 - 54.

References

BRITISH STANDARDS INSTITUTION, 1980. No 848. Fans for General Purpose. Section 24.5: Methods of Testing Performance.

BRITISH STANDARDS INSTITUTION, 1983. BS1042:1983. The Measurement of Fluid Flow in Closed Conduit. Section 2.1: Methods Using Pitot-static Tubes.

BRITISH STANDARDS INSTITUTION, 1992. BS1041-4:1992. Temperature Measurement – Part 4: Guide to the Selection and Use of Thermocouples.

Bruun, H.H., 1995. Hot-wire anemometry – Principles and signal analysis. Oxford University Press, Oxford.

Butler, R.J. and Baughn, J.W., 1996. The effect of the thermal boundary condition on transient method heat transfer measurements on a flat plate with a laminar boundary layer. J. Heat Transfer, Vol. (118), 831 - 837.

Button, B.L. and Wilcock, D., 1978. Impingement heat transfer – a bibliography 1890 – 1975. Previews Heat Mass Transfer, 4(3), 83 – 98.

Button, B.L. and Wilcock, D., 1982. Effect of nozzle geometry on single circular jet impingement heat transfer. Proc. 2nd Polytechnic Symp. on Thermodynamics and Heat Transfer, Leicester, 16 – 17 Nov., 86 – 99.

Button, B.L. and Tura, R.A., 1984. Design of a blower type low speed thermal wind tunnel. Coventry (Lanchester) Polytechnic, Report ME383.

Button, B.L. and Jambunathan, K., 1989. Jet impingement heat transfer: a bibliography 1976 - 1985. Previews Heat Mass Transfer, 15(2), 149 - 179.

Cadek, F.F., 1968. A fundamental investigation of jet impingement heat transfer. PhD Thesis, University of Cincinnati, Cincinnati, U.S.A.

Camci, C., Kim, K. and Hippensteele, S.A., 1991a. A new hue capturing technique for the quantitative interpretation of liquid crystal images used in convective heat transfer studies. ASME paper 91-GT-122.

Camci, C., Kim, K., Hippensteele, S.A. and Poinsatte, P.E., 1991b. Convective heat transfer at the curved bottom surface of a square to rectangular duct using a new hue capturing based liquid crystal technique. ASME Heat Transfer Division, 179, 7 – 22.

Catalano, G.D., Chang, K. and Mathis, J.A., 1989a. Calculation and measurement of turbulent jet impingement in a crossflow – Part I. Numer. Methods in Laminar and Turbulent Flow, 6th Int. Conf., Swansea, Wales, 11 – 15 July, 6(2), 1883 – 1894.

Catalano, G.D., Chang, K. and Mathis, J.A., 1989b. Calculation and measurement of turbulent jet impingement in a crossflow – Part II. Numer. Methods in Laminar and Turbulent Flow, 6th Int. Conf., Swansea, Wales, 11 – 15 July, 6(2), 1895 – 1906.

Chamberlin, G.J. and Chamberlin, D.G., 1980. Colour – its Measurement, Computation and Application. Heyden and Son Ltd., London.

Chan, T. L., Jambunathan, K. and Ashforth-Frost, S., 1999a. Jet Impingement Heat Transfer - A Bibliography: 1870-1977. Previews of Heat and Mass Transfer, 25(5), 464 - 473.

Chan, T. L., Jambunathan, K. and Ashforth-Frost, S., 1999b. Jet Impingement Heat Transfer - A Bibliography: 1978-1998. Previews of Heat and Mass Transfer, 25(6), 558 - 570.

Chevray, R. and Tutu, N.K., 1972. Simultaneous measurements of temperature and velocity in heated flows. Rev. Sci. Instrum., 43(10), 1417 – 1421.

Coleman, H.W. and Steele, W.G., 1999. Experimental and uncertainty analysis for engineers. Wiley, New York.

Collis, D.C. and Williams, M.J., 1959. Two-dimensional convection from heated wires at low Reynolds numbers. J. Fluid Mech., 6, 357 – 384.

Cooper, D., Jackson , D.C., Launder, B.E. and Liao, G.X., 1993. Impingement jet studies for turbulent model assessment – I. Flow-field experiments. Int. J. Heat Mass Transfer, 36(10), 2675 - 2684.

Cornaro, C., Fleischer, A.S. and Goldstein, R.J., 1999. Flow visualisation of a round jet impinging on cylindrical surfaces. Exp. Thermal and Fluid Science, 20(1999), 66 – 78.

Dantec Measurement Technology, 2000. StreamLine/StreamWare Installation & User's Guide. Dantec Measurement Technology, Skovlunde, Denmark.

den Ouden, C. and Hoogendoorn, C.J., 1974. Local convective heat transfer coefficients for jets impinging on a plate; experiments using a liquid crystal technique. Proc. 5th Int. Heat Transfer Conf., Tokyo, 3 – 7 Sept., 5, 293 – 297.

Donaldson, C. D. and Snedeker, R.S., 1971. A study of free jet impingement - Part 1. Mean properties of free and impinging jets. J. Fluid Mech., Vol. (45), 2, 281 – 319.

Downs, S.J. and James, E.H., 1987. Jet impingement heat transfer – a literature survey. ASME paper 87-HT-35.

Fergason, J.L., 1964. Liquid crystals. Scientific American, 210, 64 – 77.

Florschuetz, L.W., Truman, C.R. and Metzger, D.E., 1981. Streamwise flow and heat transfer distributions for jet array impingement with crossflow. J. Heat Transfer, 102, 337 – 342.

References

Florschuetz, L.W., Metzger, D.E. and Su, C.C., 1984. Heat transfer characteristics for jet array impingement with initial crossflow. J. Heat transfer, Vol. (106), 34 – 41.

Fondse, H., Leijdens, H. and Ooms, G., 1983. On the influence of the exit conditions on the entrainment rate in the development region of a free, round, turbulent jet. App. Sci. Research, 40, 355 – 375.

Gardon, R., and Cobonpue, J.C., 1962. Heat transfer between a flat plate and jets of air impinging on it. Int. Development in Heat Transfer, 2, 454 – 460.

Gardon, R., and Akfirat, J.C., 1965. The role of turbulence in determining heat transfer characteristics of impinging jets. Int. J. Heat Mass Transfer, 8, 1261 - 1272.

Gardon, R., and Akfirat, J.C., 1966. Heat transfer characteristics of impinging two-dimensional air jets. ASME J. Heat Transfer, February, 101 - 108.

Gauntner, J.W., Livingood, J.N.B. and Hrycak, P., 1970. Survey of literature on flow characteristics of a single turbulent jet impinging on a flat plate. NASA TM D-5652.

Gillespie, D.R.H., Wang, Z., and Ireland, P.T., 1995. Heating element. British Patent Application, PCT/GB96/2017.

Gillespie, D.R.H., Guo, S.M., Wang, Z., Ireland, P.T. and Kohler, S.T., 1996. A comparison of full surface local heat transfer coefficient and flow field studies beneath sharp-edge and radiused entry impinging jets. ASME J. Heat Transfer paper, 96-GT- 428.

Goldstein, R.J. and Behbahani, A.I., 1982. Impingement of a circular jet with and without crossflow. Int. J. Heat Mass Transfer, Vol. (25), 1377 – 1382.

References

Goldstein, R.J., Behbahni, A.I. and Heppelmann, K.K., 1986. Streamwise distribution of the recovery factor and the local heat transfer coefficient to an impinging circular air jet. Int. J. Heat Mass Transfer, Vol. (29), No. 8, 1227 – 1235.

Gundappa, M., Hudson, J.F. and Diller, T.E., 1989. Jet impingement heat transfer from jet tubes and orifices. National Heat Transfer Conf., Philadelphia, PA, 6 – 9 Aug., 107, 43 – 50.

Hishida, M. and Nagano, Y., 1978. Simultaneous measurements of velocity and temperature in nonisothermal flows. ASME J. Heat Transfer, 100, 340 – 345.

Hollingsworth, D.K., Boehman, A.L., Smith, E.G., and Moffat, R.J., 1990. Measurement of temperature and heat transfer coefficient distributions in a complex flow using liquid crystal thermography and true-color image processing, Proc. 9th Int. Heat Transfer Conf., Jerusalem.

Hollworth, B.R. and Berry, R.D., 1978. Heat transfer from arrays of impinging jets with large jet-to-jet spacing. J. Heat Transfer, 100, 352 – 357.

Hoogendoorn, C.J., 1977. The effect of turbulence on heat transfer at a stagnation point. Int. J. Heat Mass Transfer, 20, 1333 – 1338.

Hrycak, P., 1981. Heat transfer from a row of impinging jets to concave cylindrical surfaces. Int. J. Heat Mass Transfer, Vol. (24), 407 – 419.

Hrycak, P., 1983. Heat transfer from round impinging jets to a flat plate. Int. J. Heat Mass Transfer, 26(12), 1857 – 1865.

Huber, A.M. and Viskanta, R., 1994. Effect of jet-jet spacing on convective heat transfer to confined, impinging arrays of axisymmetric air jets. Int. J. Heat Mass Transfer, Vol. (37), 2859-2869.

Ireland, P.T. and Jones, T.V., 1985. The measurement of local heat transfer coefficients in blade cooling geometries. AGARD Conf. Proc., 390, paper 28.

Ireland, P.T. and Jones, T.V., 1986. Detailed measurements of heat transfer on and around a pedestal in fully developed passage flow. Proc. 8th Int. Heat Transfer Conf., San Francisco, CA, 17 – 22 Aug., 3, 975 – 980.

Ireland, P.T. and Jones, T.V., 1987. Note on the double crystal method of measuring heat transfer coefficient. Report no. 1710/87, University of Oxford, Oxford, U.K.

Ireland, P.T., Neely, A.J., Gillespie, D.R.H. and Robertson, A.J., 1999. Turbulent heat transfer measurements using liquid crystals. Int. J. Heat and Fluid Flow, 20, 355-367.

Ireland, P.T. and Jones, T.V., 2000. Liquid crystal measurements of heat transfer and surface shear stress. Meas. Sci. Tech., 11, 969 – 986.

Jambunathan, K., Kapasi, S., Button, B.L. and Bland, J.A., 1989. Numerical study of flow field for confined laminar jet impingement. 3rd Int. PHOENICS User Conf., Dubrovnik, Yugoslavia, 28 Aug – 1 Sept.

Jambunathan, K., Lai, E., Moss, M.A. and Button, B.L., 1992. A review of heat transfer data for single circular jet impingement. Int. J. Heat and Fluid Flow, 13(2), 106 - 115.

Jambunathan, K. and Button, B.L., 1994. Jet impingement heat transfer: a bibliography 1986 – 1991. Previews Heat Mass Transfer, 20(5), 385 – 413.

Jones, T.V. and Hippensteele, S.A., 1987. High-resolution heat transfer coefficient maps applicable to compound curve surfaces using liquid crystals in a transient wind tunnel. Development in Experimental Technique in Heat Transfer and Combustion, ASME HTD, 71 (Also NASA TM-89855, 1988).

Jones, T.V., 1991. The use of liquid crystals in aerodynamic and heat transfer testing. Proc. 4th Int. Symp. Transport Phenomena in Heat and Mass Transfer, Sydney, 14 – 19 July, 2, 1242 – 1273.
Jones, T.V., Wang, Z. and Ireland, P.T., 1992. Liquid crystal techniques. Int. Symp. on Heat Transfer in Turbomachinery, Athens, Greece.

Kanevce, G. and Oka, S., 1973. Correcting hot-wire readings for influence of fluid temperature variations. DISA Info., No. 15, 21 – 24.

Kataoka, K. and Mizushina, T., 1974. Local enhancement of the rate of heat transfer in an impinging round jet by free stream turbulence. Proc. 5th Int. Heat Transfer Conf., Tokyo, Japan, 3 – 7 Sept., 2, 305 – 309.

Kataoka, K., 1990. Impingement heat transfer augmentation due to large scale eddies. Heat Transfer 1990, 1, 255 – 273.

Kezios, S.P., 1956. Heat transfer in the flow of a cylindrical air jet normal to an infinite plane. PhD Thesis, Illinois Institute of Technology, Chicago, U.S.A.

Kim, Y.W. and Metzger, D.E., 1995. Heat transfer and effectiveness on film cooled turbine blade tip models. ASME J. Turbomachinery, 117, 12 – 21.

Kim, K.C. and Park, K.Y., 2000. The structure of counter-rotating vortex pair in a cross flow jet. 9th Int. Symp. on Flow Visualisation, paper 358.

Kline, S.J. and McClintock, F.A., 1953. Describing uncertainties in single-sample experiments. Mechanical Engineering, 75, 3 – 8.

Kreith, F. and Black, W.Z., 1980. Basic Heat Transfer. Harper and Row, New York.

References

LaRue, J.C., Deaton, T. and Gibson, C.H., 1975. Measurement of high-frequency turbulent temperature, Rev. Sci. Instrum., 46(6), 757 – 764.

Lemieux, G.P. and Oosthuizen, P.H., 1984. A simple approach to the compensation of constant temperature hot-wire anemometers for fluid temperature fluctuations. Proc. 30th Int. Instrum. Symp., Denver, AIAA, 277 – 282.

Ling, J.P., Ireland, P.T. and Turner, L., 2001. Film cooling research for DLE combustor discharge nozzles. Report no. 2244/01, University of Oxford, Oxford, U.K.

Livingood, J.N.B. and Hrycak, P., 1973. Impingement heat transfer from turbulent air jets to flat plates – a literature survey, NASA TM X-2778.

Lucas, M.G., Ireland, P.T., Wang, Z., Jones, T.V. and Pearce, W.J., 1992. Fundamental studies of impingement cooling thermal boundary conditions. AGARD Conf. Proc., 527, paper 14.

Lytle, D. and Webb, B. W., 1991. Secondary heat transfer maxima for air jet impingement at low nozzle-to-plate spacings. Experimental Teat Transfer, Fluid Mechanics and Thermodynamics 1991, Eds., 776 – 783, Elsevier, New York.

Martin, H., 1977. Heat and mass transfer between impinging gas jets and solid surfaces. Adv. Heat Transfer, 13, 1 – 60.

Martinez-Botas, R.F., Lock, G.D. and Jones, T.V., 1995. Heat transfer measurements in an annular cascade of transonic gas turbine blades using the transient liquid crystal technique. J. Turbomachinery, 117, 425 – 431.

Mehta, R.D., 1977. The aerodynamics design of blower tunnels with wide-angle diffusers. Prog. Aerospace Sci., 18, 59-120.

References

Meola, C., Cardone, G., Carmicino, C. and Carlomagno, G.M., 2000. Fluid dynamics and heat transfer in an impinging air jet, Int. Symp. on Flow Visualisation, paper 429.

Metzger, D.E., 1962. Spot cooling and heating of surfaces with high velocity jets. Technical Report No. 52, Dept. Mech. Eng., Stanford University.

Metzger, D.E. and Korstad, R.J., 1972. Effects of crossflow on impingement heat transfer. J. Eng. for Power, January, 35 – 41.

Metzger, D.E., Florschuetz, L.W., Takeuchi, D.I., Behee, R.D. and Berry, R.A., 1979. Heat transfer characteristics for inline and staggered arrays of circular jets with crossflow of spent air. J. Heat Transfer, Vol. (101), 526 – 531.

Moffat, R.J., 1985. Using uncertainty analysis in the planning of an experiment. ASME J. Fluids Eng., 107, 173-179.

Moffat, R.J., 1990. Experimental heat transfer. Proc. 9th Int. Heat Transfer Conf., Jerusalem, Israel, 19 – 24 Aug., 187 – 205.

Nishiyama, H., Ota, T., Hamada, M., Takahashi, Y. and Kamiyama, S., 1990. Temperature field of a slightly heated jet in a cross flow. Wärme- und Stoffübertragung 25, 369 – 375 (1990).

Obot, N.T., Mujumdar, A.S. and Douglas, W.J.M., 1979. The effect of nozzle geometry on impingement heat transfer under a round turbulent jet. ASME paper 79-WA/HT-53.

Obot, N.T., Douglas, W.J.M. and Mujumdar, A.S., 1982. Effect of semi-confinement on impingement heat transfer. Proc. 7th Int. Heat Transfer Conf., Munich, 6 – 10 Sept., 3, 395 – 400.

Obot, N.T. and Trabold, T.A., 1987. Impingement heat transfer within arrays of circular jets - Part I. Effects of minimum, intermediate, and complete crossflow for small and large spacings. J. Heat Transfer, Vol. (109), 872 – 879.

Perry, A.E., 1982. Hot-wire Anemometry. Clarendon Press, Oxford.

Polat, S., 1993. Heat and mass transfer in impingement drying. Drying Technology, 11(6), 1147 – 1176.

Polat, S., Huang, B., Mujumdar, A.S. and Douglas, W.J.M., 1989. Numerical flow and heat transfer under impinging jets: a review. Annual Review of Numerical Fluid Mechanics and Heat Transfer, (Ed. C.L. Tien and T.C. Chawla), 2, 157 – 197.

Popiel, C.O., van der Meer, T.H. and Hoogendoorn, C.J., 1980. Convective heat transfer on a plate in an impinging round hot gas jet of low Reynolds number. Int. J. Heat Mass Transfer, 23(8), 1055 – 1068.

Popiel, C.O. and Trass, O., 1982. The effect of ordered structure of turbulence on momentum, heat and mass transfer of impinging round jets. Proc. 7th Int. Heat Transfer Conf., Munich, 6 – 10 Sept., 6, 141 – 146.

Popiel, C.O. and Boguslawski, L., 1986. Mass or heat transfer in impinging single, round jets emitted by a bell-shaped nozzle and sharp-ended orifice. Proc. 8th Int. Heat Transfer Conf., San Francisco, CA, 17 – 22 Aug., 3, 1187 – 1192.

Popiel, C.O. and Boguslawski, L., 1988. Effect of flow structure on the heat and mass transfer on a flat plate in impinging round jet. Proc. 2nd UK National Conf. on Heat Transfer, University of Strathclyde, U.K., 14 – 16 Sept., 1, 663 – 685.

Popiel, C.O. and Trass, O., 1991. Visualisation of a free and impinging round jet. Experimental Thermal and Fluid Science, 4, 253 – 264.

Rao, V.V. and Trass, O., 1964. Mass transfer from a flat surface to an impinging turbulent jet. Can. J. Chem. Eng., 42, 95 – 99.

Saad, N.R., Douglas, W.J.M and Mujumdar, A.S., 1977. Prediction of heat transfer under an axisymmetric laminar impinging jet. Ind. Eng. Chem. Fundam., 16(1), 148 – 154.

Schlichting, H., 1968. Boundary layer theory. McGraw Hill, New York.

Schlichting, H., 1979. Boundary layer theory. McGraw Hill, New York.

Schlunder, E.U. and Gnielinski, V., 1967. Heat and mass transfer between surfaces and impinging jets. Chem. Ing. Tech., 39, 578 – 584.

Schultz, D.L. and Jones, T.V., 1973. Heat transfer measurements in short-duration hypersonic facilities. AGARD AG-165.

Sibulkin, M., 1952. Heat transfer near the forward stagnation point of a body of revolution. Journal of the Aeronautical Sciences, Aug., 570 – 571.

Sparrow, E.M., Goldstein, R.J. and Rouf, M.A., 1975. Effects of nozzle surface separation distance on impingement heat transfer for a jet in crossflow. J. Heat Transfer, 97, 528 – 533.

Sparrow, E.M. and Lee, L., 1975. Analysis of flow field and impingement heat/mass transfer due to a nonuniform slot jet. J. Heat Transfer, 97, 191 – 197.

Taylor, R.P., Coleman, H.W., Hosni, M.H. and Love, P.H., 1989. Thermal boundary condition effects on heat transfer in the turbulent incompressible flat plate boundary layer. Int. J. Heat Mass Transfer, 32(6), 1165 – 1174.

Viskanta, R., 1993. Heat transfer to impinging isothermal gas and flame jets. Experimental Thermal and Fluid Science, 6, 111 – 134.

Wang, Z., Ireland, P.T., Kohler, S.T. and Chew, J., 1998. Heat transfer measurements to a gas turbine cooling passage with inclined ribs. J. Turbomachinery, 120, 63 – 69.

Whidden, G.L., Stevens, J. and Webb, B.W., 1992. Heat transfer and flow characteristics of two-dimensional jets impinging on heated protrusions with crossflow of the spent air. J. Electronic Packaging, Vol. (114), 81-87.

Whitney, C.F., 1996. Heat transfer characteristics of slot jet impingement. PhD Thesis, The Nottingham Trent University, Nottingham, U.K.

Yan, X., Baughn, J.W. and Mesbah, M., 1992. The effect of Reynolds number on the heat transfer distribution from a flat plate to an impinging jet. ASME Heat Transfer Division, 226, 1 – 7.

Yokobori, S., Kasagi, N., Hirata, M., Nakamaru, M. and Haramura, Y., 1979. Characteristic behaviour of turbulence and transport phenomena at the stagnation region of an axi-symmetrical impinging jet. Proc. 2nd Symp. on Turbulent Shear Flow, London, 4, 4.12 – 4.17.

BIBLIOGRAPHY

Advanced Hot-wire Anemometry Course Notes, 1992. University of Manchester Institute of Science and Technology.

Bradshaw, P., 1971. An Introduction to Turbulence and its Measurement. Pergamon Press, Oxford.

References

Bruun, H.H., 1995. Hot-wire anemometry – Principles and signal analysis. Oxford University Press, Oxford.

Bryer, D.W. and Pankhurst, R.C., 1971. Pressure-probe methods for determining wind speed and flow direction. Her Majesty's Stationery Office, London.

Chamberlin, G.J. and Chamberlin, D.G., 1980. Colour – its Measurement, Computation and Application. Heyden and Son Ltd., London.

Coleman, H.W. and Steele, W.G., 1999. Experimental and uncertainty analysis for engineers. Wiley, New York.

Hinze, J.O., 1975. Turbulence. McGraw Hill, New York.

Kays, W.M. and Crawford, M.E., 1993. Convective Heat and mass transfer. McGraw Hill, New York.

Kreith, F. and Black, W.Z., 1980. Basic Heat Transfer. Harper and Row, New York.

Perry, A.E., 1982. Hot-wire Anemometry. Clarendon Press, Oxford.

Schetz, J.A., 1993. Boundary layer analysis. Prentice Hall, New Jersey.

Schlichting, H., 1979. Boundary layer theory. McGraw Hill, New York.

Appendix A - Structural Illustration of Uncertainty Elements for Velocity Measurement using a Hot-wire.

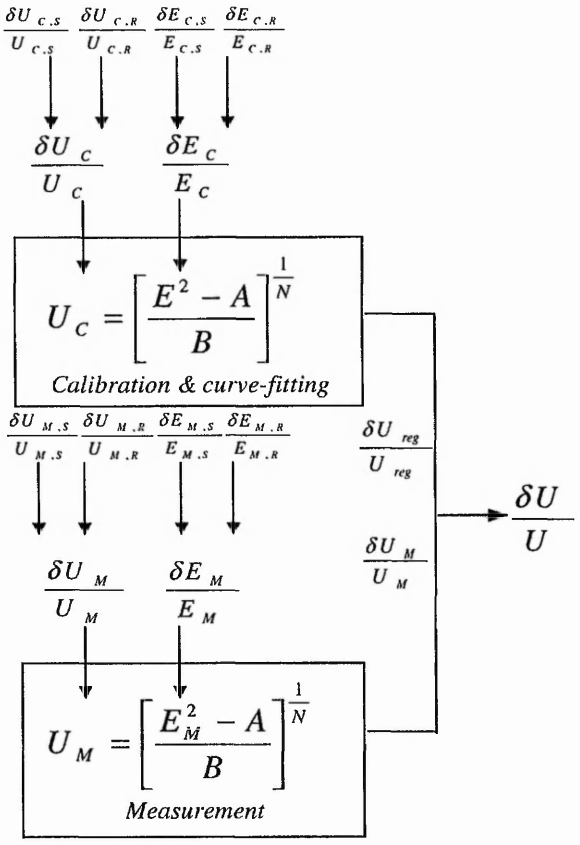

Where U and E represent velocity and voltage respectively and A, B, N are constants used in King's law. The subscripts c, M, R, S, denote calibration, measurement, random and systematic uncertainty elements respectively.

Appendix B - Visual C++ Software for Control, Collection and Storage of Heat Transfer Data

```
#include <stdio.h>
#include <stdlib.h>
#include <string.h>
#include <conio.h>
#include <time.h>
#include <malloc.h>
#include <windows.h>
#include <Windecl.h>

#define BufferSize 28000

int InitiateBoard(), DevMeasure();
unsigned char *Buffer;


main()

{
        InitiateBoard();

        DevMeasure();

        return 0;
}


/*********************InitiateBoard*****************************/


int InitiateBoard()

  {
        int Board;
        Board=ibfind("GPIB0");
        ibsic(Board);
        ibsre(Board,1);
        ibcac(Board,0);
        ibtmo(Board,T10us);
        ibclr(Board);
        return(0);
  }
```

```
/*********************DevMeasure*******************************/

int DevMeasure()

  {
        int Device;
        unsigned long BSize;
        char Command[100];

        Command1[]=":*RST",
        Command2[]=":SYST:PRES",
        Command3[]=":FUNC 'VOLT:DC'",
        Command4[]=":INIT:CONT OFF;:ABOR",
        Command5[]=":ARM:SEQ:LAY1:SOUR EXT",
        Command20[]=":ARM:SEQ:LAY2:SOUR TIM",
        Command10[]=":ROUT:SCAN (@2:5)",
        Command7[]=":ARM:SEQ:LAY1:COUN 1",
        Command21[]=":ARM:SEQ:LAY2:COUN 404",
        Command8[]=":TRIG:COUN 404",
        Command26[]=":ARM:SEQ:LAY2:DEL 0.25",
        Command6[]=":TRIG:DEL 0.25",
        Command19[]=":TRIG:TCON:DIR SOUR",
        Command9[]=":ROUT:OPEN ALL",
        Command11[]=":ROUT:SCAN:LSEL INT",
        Command12[]=":TRAC:POIN:404",
        Command13[]=":TRAC:FEED SENS",
        Command14[]=":TRAC:FEED:CONT NEXT",
        Command15[]=":FORM:ELEM READ, CHAN, UNIT",
        Command16[]=":INIT;*WAI",
        Command23[]=":ROUT:SCAN:LSEL NONE",
        Command17[]=":ROUT:OPEN:ALL",
        Command18[]=":TRAC:DATA?";


        unsigned char *Buffer;
        if ((Buffer=(unsigned char *)malloc(BufferSize*sizeof(char))) == NULL)
        exit(-1);

        Device=ibfind("K2001");
        strcpy(Command,"\x11\x2d\x40\x30");
        ibcmd(Device, Command, 4);

        BSize=sizeof(Command1);
        ibwrt(Device, Command1,BSize);
        printf("Multimeter has been reset \n");
```

```
BSize=sizeof(Command2);
ibwrt(Device, Command2,BSize);
printf("Multimeter has been reconfigured to exhibit original preset
characteristics\n");

BSize=sizeof(Command3);
ibwrt(Device, Command3,BSize);
printf("The Voltage function has now been set\n");

BSize=sizeof(Command4);
ibwrt(Device, Command4,BSize);
printf("Continuous scanning is turned off\n");

BSize=sizeof(Command5);
ibwrt(Device, Command5,BSize);

BSize=sizeof(Command20);
ibwrt(Device, Command20,BSize);

BSize=sizeof(Command10);
ibwrt(Device, Command10,BSize);
printf("The internal scanner directive is set\n");

BSize=sizeof(Command7);
ibwrt(Device, Command7,BSize);

BSize=sizeof(Command21);
ibwrt(Device, Command21,BSize);

BSize=sizeof(Command8);
ibwrt(Device, Command8,BSize);
printf("Trigger Timer set to 0.5 seconds\n");

BSize=sizeof(Command26);
ibwrt(Device, Command26,BSize);

BSize=sizeof(Command6);
ibwrt(Device, Command6,BSize);
printf("The trigger counter is set to (n) scans \n");

BSize=sizeof(Command19);
ibwrt(Device, Command19,BSize);

BSize=sizeof(Command9);
ibwrt(Device, Command9,BSize);
printf("2 channels will be scanned\n");
```

```
        BSize=sizeof(Command11);
        ibwrt(Device, Command11,BSize);

        BSize=sizeof(Command12);
        ibwrt(Device, Command12,BSize);

        BSize=sizeof(Command13);
        ibwrt(Device, Command13,BSize);

        BSize=sizeof(Command14);
        ibwrt(Device, Command14,BSize);

        BSize=sizeof(Command15);
        ibwrt(Device, Command15,BSize);

        BSize=sizeof(Command16);
        ibwrt(Device, Command16,BSize);
        ibtmo(Device, T100s);

        BSize=sizeof(Command17);
        ibwrt(Device, Command17,BSize);

        BSize=sizeof(Command18);
        ibwrt(Device, Command18,BSize);

        BSize=sizeof(Command23);
        ibwrt(Device, Command23,BSize);

        strcpy(Command,"\x5f\x50\x20\x3f");
        ibcmd(Device,Command, 4);
        ibrdf (Device, "a:Datafile.dat");

        return 0;
}
```

Appendix C - Typical Isotherm Contours from Heat Transfer Measurements.

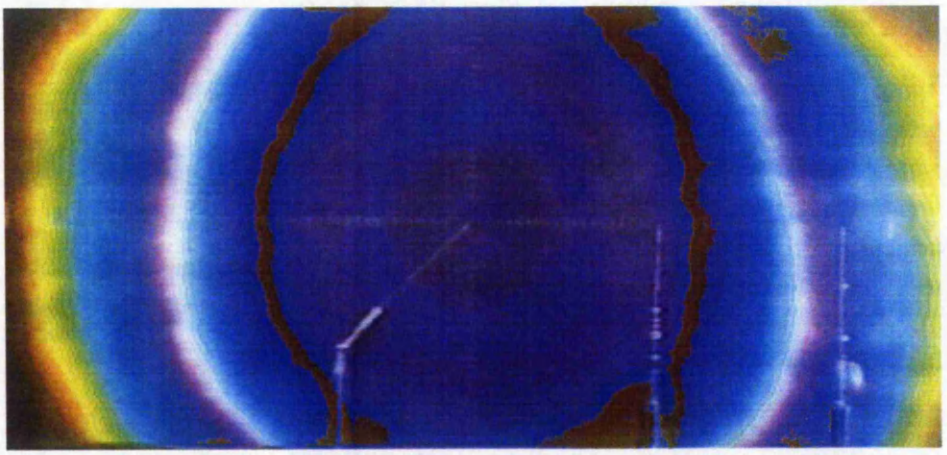

z/d = 1.5, Re = 40 000, no crossflow. (Elapsed time = 59.83s)

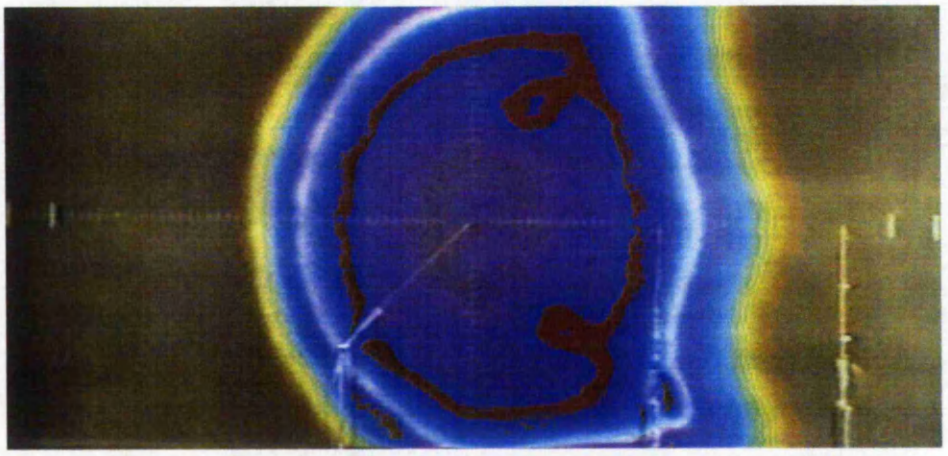

z/d = 1.5, Re = 40 000, $U_j / U_c = 5$. (Elapsed time = 59.63s)

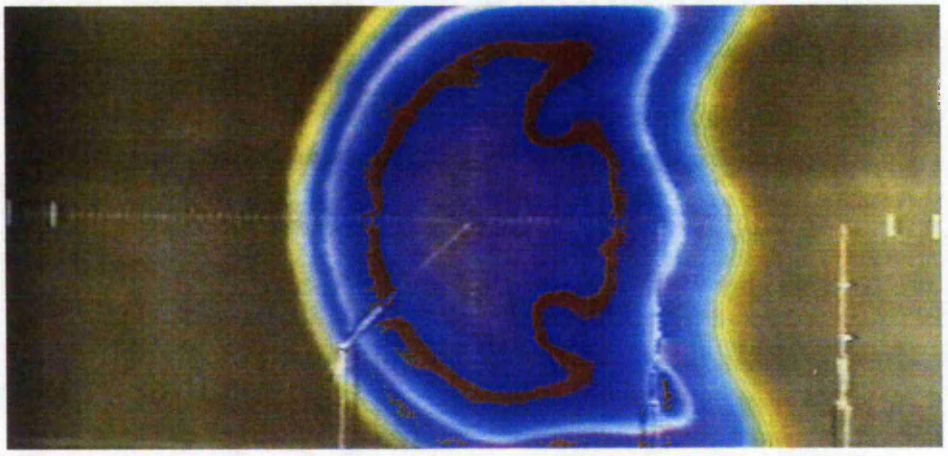

z/d = 1.5, Re = 40 000, $U_j / U_c = 4$. (Elapsed time = 58.75s)

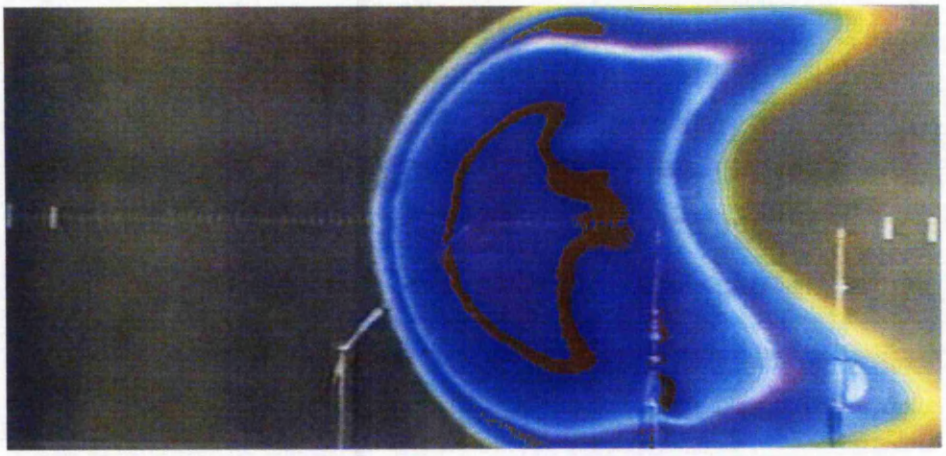

z/d = 1.5, Re = 40 000, $U_j / U_c = 3$. (Elapsed time = 59.73s)

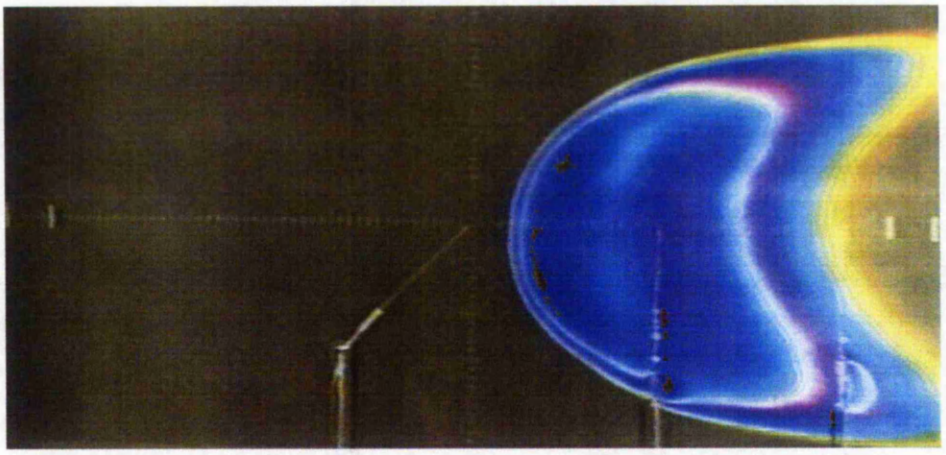

z/d = 1.5, Re = 40 000, $U_j / U_c = 2$. (Elapsed time = 59.58s)

PUBLICATION

Experimental Heat Transfer, Fluid Mechanics, and Thermodynamics 2001
G.P. Celata, P. Di Marco, A. Goulas and A. Mariani

NEAR WALL FLOW CHARACTERISTICS BENEATH A TURBULENT IMPINGING JET

S. Ashforth-Frost, B.C.Y. Cheong and P.T. Ireland

Dept of Mechanical and Manufacturing Engineering, The Nottingham Trent University, Burton Street, Nottingham NG1 4BU, U.K.; Corresponding E-mail: Brian.Cheong@ntu.ac.uk
Dept of Engineering Science, University of Oxford, Parks Road, Oxford OX1 3PJ, U.K.

ABSTRACT

Jet impingement is one of the most effective methods for cooling, heating or drying a target surface due to its excellent heat and mass transport characteristics. The current work investigates the near wall hydrodynamic flow field beneath a turbulent semi-confined impinging air jet and its effect on surface heat transfer. The jet issued from a convergent nozzle (which was integral to a flat plate parallel to the impingement surface) at Re = 20 000 and nozzle-to-plate spacings (z/d) of 2 and 6.5. For z/d = 2, the primary (nearest to the jet axis) maximum in heat transfer is associated with impingement of large-scale turbulence developed at the edge of the jet that leads to thinning and transition of the wall jet from laminar to turbulent. The secondary maximum in heat transfer is attributed to the continuous increase in turbulence at a constant flow velocity in the vicinity of the wall (y/d = 0.005). For z/d = 6.5, the heat transfer is maximum at the stagnation point due to the high level of local turbulent intensity.
Keywords: Jet Impingement, hot-wire, wall jet, turbulence, heat tranfer.

1. INTRODUCTION

Jet impingement is widely used throughout engineering and manufacturing industries to enhance engine performance and product quality, production capacity and energy savings. Typical applications of jet impingement include cooling of turbine blades and electronic components, heating of coated surfaces, drying of food and paper or tempering of glass.

Over the past three decades, a comprehensive literature has been published which addresses the hydrodynamic and heat transfer characteristics of impinging jets [1-2]. Cooper et al. [3] and Ashforth-Frost [4] identified the dominant role of near wall flow characteristics on impingement heat transfer. For many years, the distinctive formation of local maxima in heat transfer, particularly for jet low nozzle-to-plate spacings, has been associated with various flow mechanisms. However, the identification of the predominant heat transfer mechanisms is difficult as it varies according to Re, z/d, nozzle type, surface roughness, jet inclination angle and other parameters.

Local surface heat transfer on a flat plate underneath a confined turbulent impinging jet has been investigated [5]. For a jet discharging through a sharp edged hole at $z/d \leq 4$, local maxima in heat transfer were observed at $r/d \approx 0.5$ and $r/d \approx 1.5$ whilst local minima in heat transfer were reported at the stagnation point and $r/d \approx 1.25$. The primary maximum in heat transfer has been ascribed to thinning of the wall jet [6], and the convection of large-scale turbulence structure from the edge of the jet onto the laminar boundary layer [7]. The secondary maximum in heat transfer has been linked to wall jet transition from laminar to turbulent flow which occurs in the interval $1 \leq r/d \leq 2$ [8]. Popiel et al. [9] cited the contribution of wall eddies, induced by large-scale toroidal vortices impinging on the plate, to the enhancement of local momentum, mass and heat transfers. The ring-shaped wall eddies coalesced abruptly with the radially-diverging toroidal vortices (at $1 < r/d < 2$), while the flow developed into a turbulent radial wall jet. The wall eddies also cause an unsteady adverse pressure gradient and subsequent separation of the wall-jet [10]. More recently, Meola et al. [11] associated the primary maximum in heat transfer with thinning of the wall jet and to the growth in turbulence, and the secondary maximum to flow reattachment of the wall jet.

Despite extensive investigations, there has been no detailed evaluation of the predominant flow mechanism which leads to local maxima in heat transfer. A thorough description of the near wall flow characteristic, as to how the hydrodynamic structures interact with each other and influence the local heat transfer, has yet to be accomplished. Typically, the near wall phenomena that deserve further considerations are: -

a. The effect of the impingement of large-scale turbulence structures, convected from the edge of the jet, on the thickness and the turbulence level of the wall jet.
b. The influence of impinging toroidal vortices, originating around the circumference of the jet, on the flow and heat transfer characteristics of the viscous wall jet.
c. The predominant flow mechanism that is responsible for the secondary maximum in surface heat transfer (for jets at low nozzle-to-plate spacings).

Besides providing bench mark test case data for validation and development of CFD codes, this study reveals the near wall flow mechanisms which dominate the surface heat transfer, and the ultimate causes for the formation of local maxima in heat transfer. It is hoped that this will facilitate the design of jet impingement devices for greater heat transfer performance.

2. EXPERIMENTAL APPARATUS AND PROCEDURE

Figure 2.1 illustrates the hot-wire calibration facility. A *Dantec 55P15* near wall hot-wire probe with a 5 μm diameter sensor of 1.25 mm in length, was connected to the *TSI IFA*

100 Constant-Temperature Anemometer (CTA) [12]. The single-sensor probe allowed measurement close to the wall without disturbance from the probe body, which was beyond the boundary layer [13]. Since the single-wire probe only measured the mean flow vector, interpretation of the hot-wire signal was based on the expected dominant flow direction (e.g. axial components at the jet axis). The probe was first calibrated at the exit of the non-isothermal wind tunnel. A variable transformer powered the fan motor and enabled the jet speed to be altered from 0 - 6.5 m/s (i.e. Reynolds number of 0 - 40 000). Simultaneous exit dynamic pressure were recorded with an estimated error of 1% using a *Perflow PMM600* digital manometer connected to a *BS1042:1984* pitot-static tube placed in close proximity to the hot-wire. The dynamic pressures at different airflow speeds were later converted into velocities for a non-linear regression analysis against the corresponding hot-wire voltage readings.

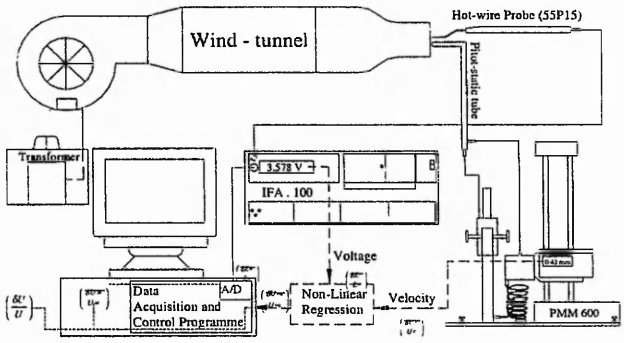

Figure 2.1: HW Calibration arrangement.

A schematic diagram of the hot-wire measurement arrangement is presented in Figure 2.2. The wind tunnel discharged a steady stream of ambient air from the 100 mm diameter nozzle to impinge onto the smooth perspex plate, measuring 700 x 400 mm, at a constant turbulence intensity of 1.5 - 1.7% across the jet exit. Near wall hot-wire data were obtained by traversing the probe parallel to the impingement plate using a computer controlled three-dimensional positioning system with a smallest step size of 2.5 μm. The reflective nature of the perspex plate was utilised for positioning and alignment of the probe accurate to ± 0.5°. Small measurement intervals (i.e. r/d = 0.1) were used to precisely locate local maxima in near wall velocity and turbulence. The vertical measurement interval was gradually increased from 0.5 - 5mm to obtain illustrative boundary layer profiles. Each set of measurements included a single point velocity taken at a fixed central position beneath the jet. The experiments were discarded and repeated if the 'before' and 'after' centreline velocity differed by more than 2%. The time varying hot-wire signal was output to an A/D converter card (i.e. *Advantech PCL-812*) which sampled at a specific rate of 360 Hz to accommodate medium to large-scale turbulent flow structures. The sampling rate represented the optimum speed to obtain statistically independent data in the shortest time-span. A sample size of 8000 (at which measured data converged) was selected for each measurement to obtain an ensemble average of airflow speed.

A detailed uncertainty analysis for the hot-wire system at a varying airflow speed was undertaken prior to the experiment. The approach was adopted from Coleman and Steele [14] to determine random and systematic uncertainties associated with hot-wire calibration, curve-fittings and measurement as illustrated in Figure 2.3. U and E represent velocity and voltage respectively and A, B, N are constants used in King's law. The subscripts c, M, R, S, denote calibration, measurement, random and systematic uncertainty elements respectively. Typical overall uncertainty of the measured mean velocity, V_m, at $Re \approx 20\,000$ (i.e. $U_{CL} = 3.04$ m/s) is 3.31%.

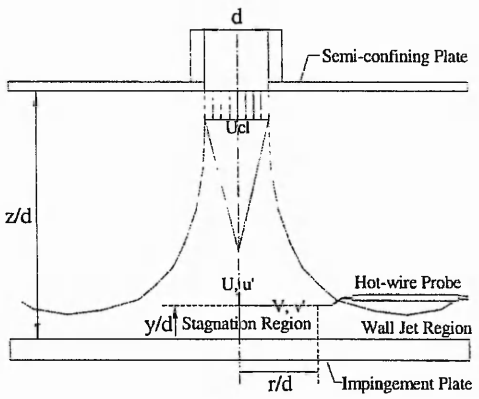

Figure 2.2: HW measurement arrangement.

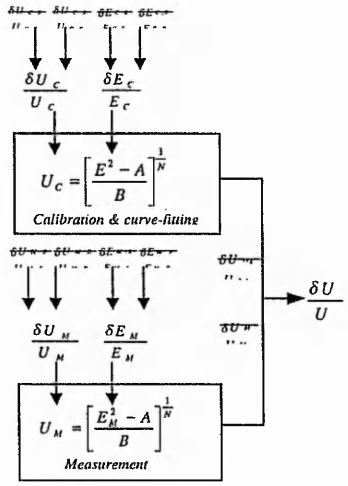

Figure 2.3: Structural illustration of uncertainty elements.

3. RESULTS AND DISCUSSIONS

This section evaluates the near wall hydrodynamic characteristic of the impinging axisymmetric jet and its impact on surface heat transfer. Most of the results are normalised by the centre jet exit velocity, U_{CL}. The mean velocity and turbulence contours for $z/d = 2$ are presented in Figure 3.1 and 3.2 respectively to aid understanding of the complex flow structures. The impinging jet spreads slightly upon striking orthogonally onto the wall surface covering $0.6 \leq r/d \leq 0.6$. The bulk fluid then diverts and accelerates radially outwards

to develop into a wall jet adjacent to the stagnation region. Figure 3.3 and 3.4 show that at the stagnation point (r/d = 0), the measured near wall ($y/d \leq 0.01$) velocity and turbulence approach the theoretical zero values. At increased radial distances, the near wall radial velocity and turbulence both rise steeply to form two peaks at r/d = 0.8 and $r/d \approx 1.7$, and at r/d = 1.1 and $r/d \approx 1.6$ respectively. In region beyond the wall jet, the influence of the axial velocity component, U, on the hot-wire signal increases significantly. Typically, the normalised mean velocity, V_m/U_{CL}, at r/d = 0 and y/d = 0.5 (Figure 3.8) reaches 0.82. Hence, the mean velocity vector, V_m, is considerably different from the radial velocity component, V, in the region beyond the vicinity of the wall ($y/d \geq 0.15$). However, at $y/d \leq 0.1$, the measured velocity is predominantly contributed by the radial wall jet.

Figure 3.5 illustrates the local Nussselt number profiles for z/d = 2 and 6.5 obtained by Ball [15] using the same wind tunnel facility and experimental settings. For z/d = 2, the impinging jet caused two local maxima in heat transfer at r/d = 0.6 and r/d = 1.7 respectively. The primary maximum in heat transfer is largely attributed to the radical increase in turbulent energy due to the onset of near wall ($y/d \leq 0.01$) jet transition from laminar to turbulent flow (Figure 3.6, r/d = 0.6). It is triggered by the large-scale turbulence structures convected from the edge of the jet (r/d = 0.6) onto the wall jet, as described by Gillespie et al. [7]. The large-scale structures penetrate into the vicinity of the wall (y/d = 0.005). Figure 3.8 illustrates the shear-driven mixing velocity at the edge of the jet which superimposes on the wall jet to form velocity peaks in the interval $0.3 \leq r/d \leq 0.6$ and $y/d \geq 0.15$. According to Cooper et al. [3], the turbulence (shown in Figure 3.8, $r/d \approx 0.5$) should strictly be interpreted as that in the direction of mean velocity vector. The joint action between the impinging shear turbulence and the diverted radial bulk flow prompts a local thinning and acceleration (Figure 3.1 and 3.10, $0.6 \leq r/d \leq 0.9$) of the wall jet. As a result, the near wall (y/d = 0.005) velocity peaks at r/d = 0.8 while the heat transfer (at r/d = 0.6) is also enhanced.

The influences of the impinging large-scale toroidal vortices and the induced wall eddies on surface heat transfer are rather insignificant (compared to wall turbulence) due to their intermittent nature. For instance, the impact of the impinging toroidal vortices (for z/d = 2, Re = 30 000 and at $r/d \approx 0.9$) becomes scarcely evident in an assemble-averaged velocity field [11]. Additionally, in most previous cases (including [15]), the primary maximum in heat transfer was seen at r/d = 0.6 with the toroidal vortices impinged slightly downstream at r/d = 0.7 - 0.9 where the convective coefficient started to decline. This effectively rules out the impinging toroidal vortices and the wall eddies as predominant mechanisms for surface heat transfer.

Furthermore, the toroidal vortices and the wall eddies, unlike the large-scale turbulence (which impinges at $r/d \approx 0.6$), do not penetrate through the viscous wall layer ($y/d \leq 0.15$). Figure 3.7, 3.8 and 3.9 indicate that the toroidal vortices and the induced small ring-shaped eddies accelerate radially outwards just over the edge of the wall jet ($y/d \geq 0.2$). The outer peak in local turbulence (at r/d = 1.7 - 2.6 and $y/d \geq 0.25$) is likely to be due to the flow reattachment of the ring-shaped eddies.

At $0.01 \leq y/d \leq 0.1$ (Figure 3.3), the radial velocity and turbulence form a single peak at $r/d \approx 1$ and $r/d \approx 1.4$ respectively. Typically, the mean velocity, V_m/U_{CL}, attains a maximum of 0.95 at y/d = 0.04 and r/d = 1. The fluid flows then decelerate monotonically at further radial distances. In close proximity to the wall (y/d = 0.005), the wall jet sustains at a plateau velocity level at $1.3 \leq r/d \leq 1.7$ amid continuous increase in the normalised turbulence and turbulent intensity. This leads to the formation of the secondary peak in heat transfer (Figure 3.5) at r/d = 1.7.

Figure 3.10 and 3.11 illustrate the development of the wall jet which is formed at r/d = 0.6 (note that the non-zero measured velocity at r/d = 0 is due to the contribution from axial velocity component). Typically, the wall jet thins from y/d = 0.1 at r/d = 0.6 to y/d = 0.04 at r/d = 0.9 due to the impingement of the large-scale turbulence and the rapid acceleration of the upstream radial bulk flow. The wall jet thickens radically from y/d = 0.04 at r/d = 1.8 to y/d = 0.08 at r/d = 3.0 and causes a drastic fall in the near wall bulk velocity. As a result, the heat transfer falls correspondingly at downstream distances.

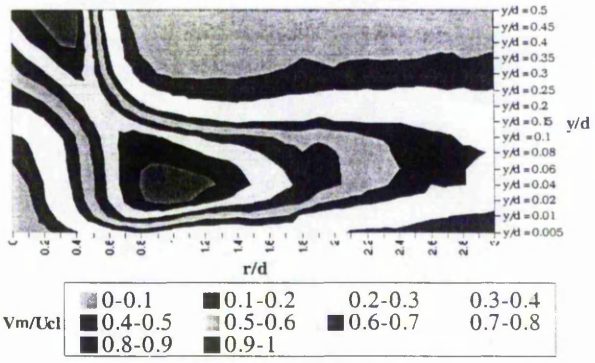

Figure 3.1: Mean velocity contour, z/d = 2, $0.005 \leq y/d \leq 0.5$.

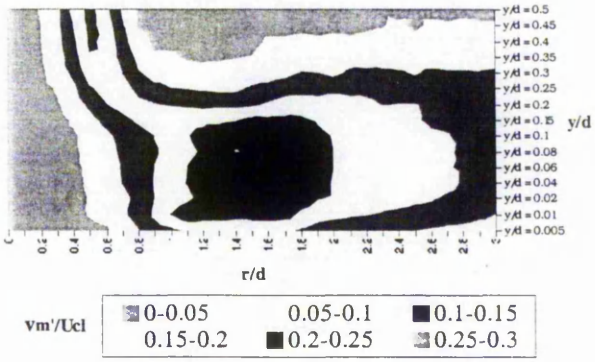

Figure 3.2: Mean turbulence contour, z/d = 2, $0.005 \leq y/d \leq 0.5$.

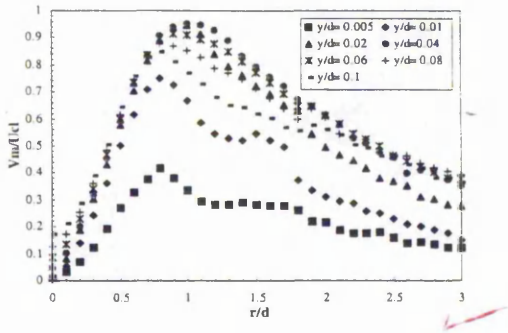

Figure 3.3: Radial variation in near wall velocity, z/d = 2, $0.005 \leq y/d \leq 0.1$.

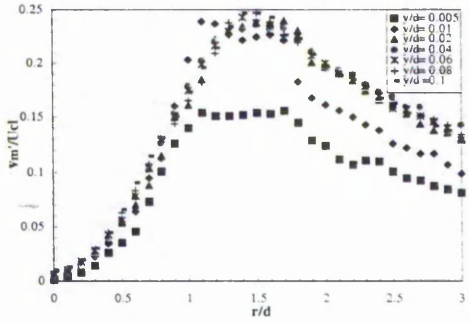

Figure 3.4: Radial variation in near wall turbulence, z/d = 2, 0.005 ≤ y/d ≤ 0.1.

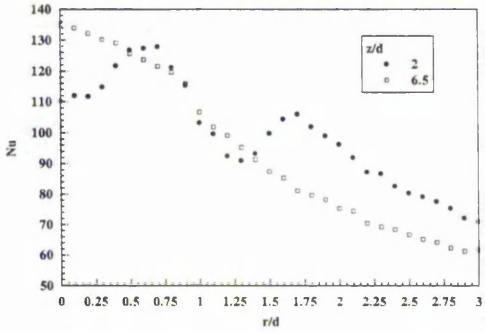

Figure 3.5: Radial variation of local Nussselt number, Ball (1998).

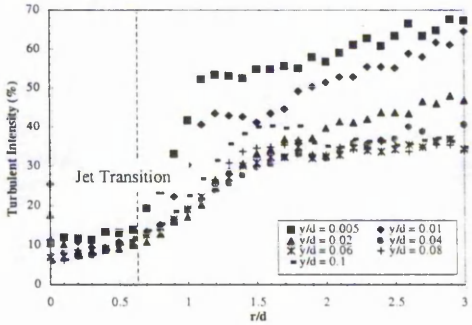

Figure 3.6: Radial variation in turbulence intensity, z/d = 2, 0.005 ≤ y/d ≤ 0.1.

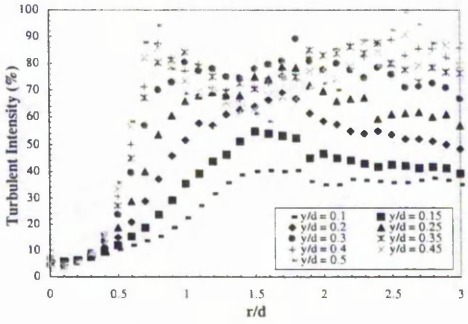

Figure 3.7: Radial variation in turbulence intensity, z/d = 2, 0.1 ≤ y/d ≤ 0.5.

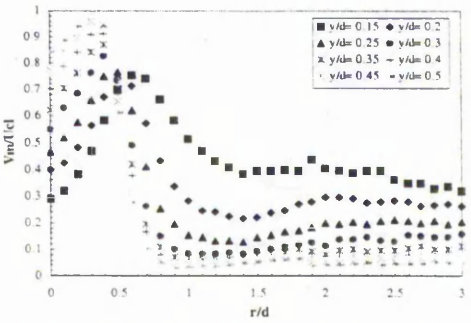

Figure 3.8: Radial variation in near wall velocity, z/d = 2, 0.15 ≤ y/d ≤ 0.5.

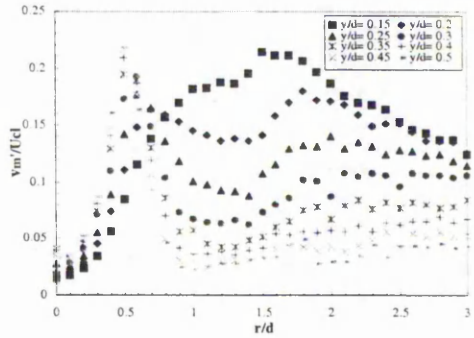

Figure 3.9 Radial variation in near wall turbulence, z/d = 2, 0.15 ≤ y/d ≤ 0.5.

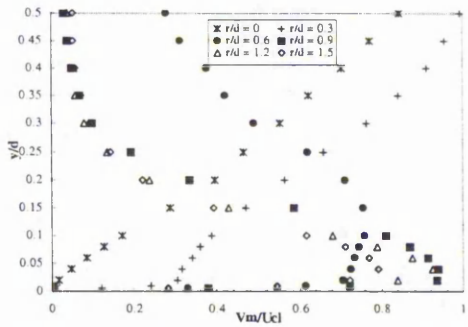

Figure 3.10: Mean velocity profile along the plate, z/d = 2, 0 ≤ r/d ≤ 1.5.

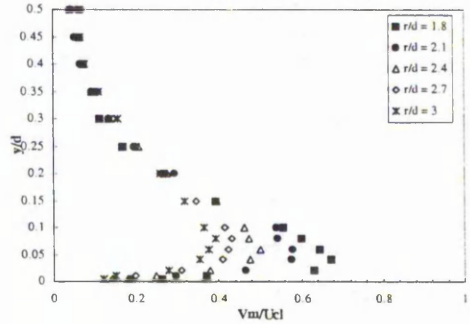

Figure 3.11: Mean velocity profile along the plate, z/d = 2, 1.8 ≤ r/d ≤ 3.

The mean velocity and turbulence contours for z/d = 6.5 are presented in Figure 3.12 and 3.13. Figure 3.14 and 3.15 show that the near wall velocity and turbulence at y/d = 0.005 also form two less pronounced peaks at r/d ≈ 0.6 and r/d ≈ 1.8, and at r/d ≈ 0.5 and r/d ≈ 1.8 respectively. The reduced hydrodynamic energy of the axial impinging jet (in the region beyond the potential core, z/d ≥ 5.5) has decreased the overall wall jet velocity. The wall jet attains a maximum velocity, V_m/U_{CL}, of 0.69 in the region 1.1 ≤ r/d ≤ 1.3 and y/d = 0.04, approximately 28% lower than the maximum for z/d = 2. Nonetheless, the flow in the stagnation region (r/d ≤ 0.4) becomes very chaotic as the axial impinging components effectively reach the immediate vicinity of the wall, resulting in non-zero velocity and turbulence readings (Figure 3.14 and 3.15, y/d = 0.005). The increased turbulence in the stagnation region and the reduced hydrodynamic energy of the wall jet result in higher stagnation and lower off-stagnation heat transfers respectively (Figure 3.5). The decrease in heat transfer from r/d = 0 to r/d = 0.5 is mainly caused by the fall in near wall turbulence intensity (Figure 3.16). At further downstream distances, the drastic fall in the absolute turbulence surpasses the slight increase in turbulence intensity, resulting in an overall decrease in heat transfer.

Figure 3.17 and 3.18 illustrate the development of the jet along the impingement surface. The flow accelerates from the stagnation region to form a typical wall jet at r/d ≥ 0.6 with no discernible thinning. The wall jet thickens gradually from r/d = 0.6 onwards and then decelerates due to loss of momentum caused by the wall friction.

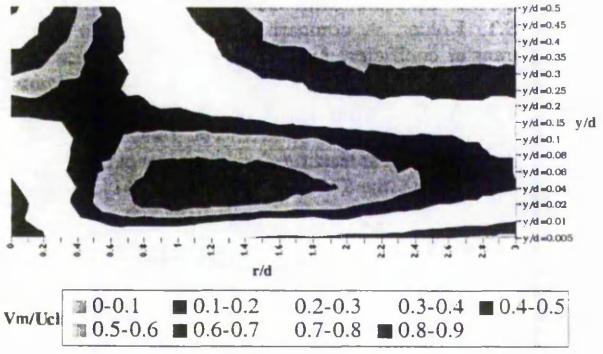

Figure 3.12: Mean velocity contour, z/d = 6.5, 0.005 ≤ y/d ≤ 0.5.

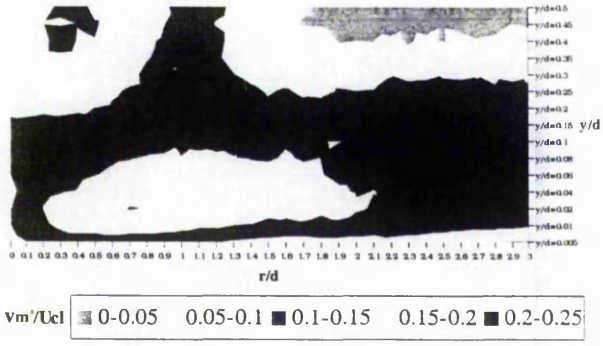

Figure 3.13: Mean turbulence contour, z/d = 6.5, 0.005 ≤ y/d ≤ 0.5.

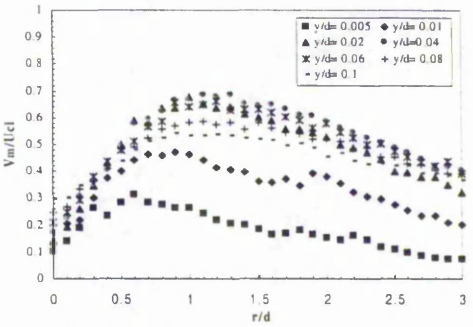

Figure 3.14: Radial variation in near wall velocity, z/d = 6.5, 0.005 ≤ y/d ≤ 0.1.

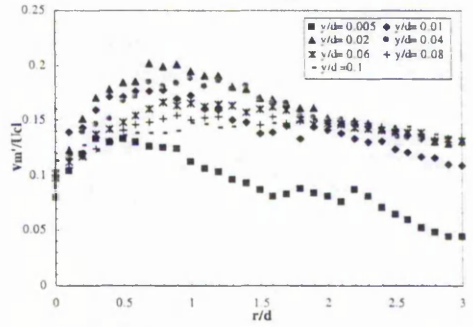

Figure 3.15: Radial variation in near wall turbulence, z/d = 6.5, 0.005 ≤ y/d ≤ 0.1.

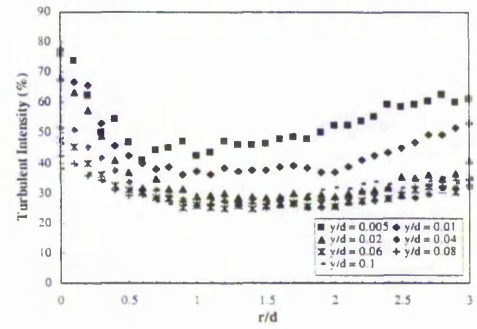

Figure 3.16: Radial variation in turbulence intensity, z/d = 6.5, 0.005 ≤ y/d ≤ 0.1.

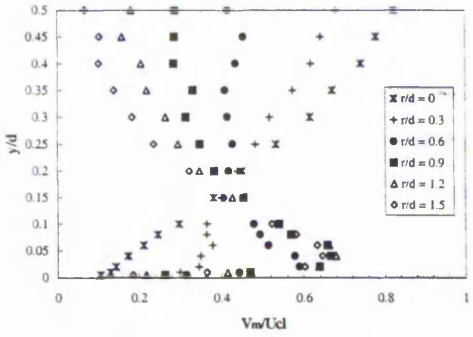

Figure 3.17: Mean velocity profile along the plate, z/d = 6.5, 0 ≤ r/d ≤ 1.5.

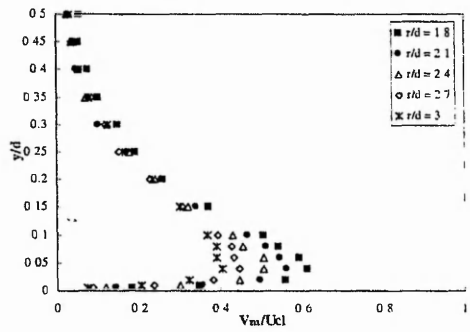

Figure 3.18: Mean velocity profile along the plate, $z/d = 6.5$, $1.8 \leq r/d \leq 3$.

4. CONCLUSIONS

The effects of near wall hydrodynamic characteristic beneath a semi-confined axisymmetric impinging jet on surface heat transfer have been closely investigated. The surface heat transfer is predominantly influenced by the turbulence levels (both absolute and normalised) in close proximity to the wall ($y/d = 0.005$), which in turn are manoeuvred by the local flow structures.

For $z/d = 2$, the convection of the large-scale turbulence from the edge of the jet prompts a local thinning and transition of the wall jet from laminar to turbulent flow. As a result, a primary maximum in heat transfer is formed at $r/d = 0.6$ and the near wall ($y/d = 0.005$) jet peaks at $r/d = 0.8$. The velocity then decays at further downstream distances ($0.8 \leq r/d \leq 1.2$) where the surface heat transfer falls correspondingly. At $1.3 \leq r/d \leq 1.7$, the near wall jet sustains at a plateau level while the absolute turbulence and the turbulent intensity continue to rise, invoking a secondary rise in heat transfer which peaks at $r/d = 1.7$.

At $z/d = 6.5$, the overall magnitude of the wall jet velocity is decreased as the axial impinging jet losses its hydrodynamic energy. The higher turbulent intensity at the stagnation point causes a local maximum in heat transfer. As the turbulent intensity declines from $r/d = 0$ to $r/d = 0.5$, the heat transfer decreases correspondingly. At $r/d \geq 0.5$, the effect of the drastic fall in the absolute turbulence exceeds the slight increase in the turbulent intensity, resulting in a continuous decrease in heat transfer.

ACKNOWLEDGEMENT

The authors would like to thank the Engineering and Physical Science Research Council (grant AF/97/0568 to Dr S Ashforth-Frost) for financial support towards this work.

NOMENCLATURE

d	Nozzle diameter, (m).
Nu	Nusselt number, [hd/k].
r	Radial distance from the stagnation point, (m).
u'	RMS axial velocity fluctuation, (m/s).
U	Axial velocity, (m/s).
U_{CL}	Jet exit centreline velocity, (m/s).
Tu	Turbulence Intensity, (%).
v'	RMS radial velocity fluctuation, (m/s).
vm'	RMS velocity fluctuation, (m/s).
V	Radial velocity, (m/s).
V_m	Mean velocity, (m/s).
y	Vertical distance from the impingement surface, (m).
z	Nozzle-to-plate spacing, (m).

REFERENCES

1. K. Jambunathan, E. Lai, M.A. Moss and B.L. Button. A review of heat transfer data for single circular jet impingement, *Int. J. Heat and Fluid Flow*, vol. 13(2), pp. 106 – 115, 1992.
2. R. Viskanta, Heat transfer to impinging isothermal gas and flame jets, *Experimental Thermal and Fluid Science*, 6, pp. 111 – 134, 1993.
3. D. Cooper, D.C. Jackson, B.E. Launder and G.X. Liao, Impingement jet studies for turbulent model assessment – I. Flow-field experiments, *Int. J. Heat Mass Transfer*, vol. 36(10), pp. 2675 - 2684, 1993.
4. S. Ashforth-Frost, Flow visualisation of semi-confined jet impingement. Ph.D. thesis, The Nottingham Trent University, Nottingham, UK, 1994.
5. M.G. Lucas, P.T. Ireland, Z. Wang, T.V. Jones and W.J. Pearce, Fundamental studies of impingement cooling thermal boundary conditions, *AGARD Conference proceedings*, 527, paper 14, 1992.
6. S.P. Kezios, Heat transfer in the flow of a cylindrical air jet normal to an infinite plane, Ph.D. thesis, Illinois Institute of Technology, Chicago, U.S.A, 1956.
7. D.R.H. Gillespie, S.M. Guo, Z. Wang, P.T. Ireland and S.T. Kohler, A comparison of full surface local heat transfer coefficient and flow field studies beneath sharp-edge and radiused entry impinging jets, *ASME Journal of Heat Transfer*, paper 96-GT- 428, 1996.
8. R. Gardon and J.C. Akfirat, The role of turbulence in determining heat transfer characteristics of impinging jets, *Int. J. Heat Mass Transfer*, vol. 8, pp. 1261 - 1272, 1965.
9. C.O. Popiel and O. Trass, Visualisation of a free and impinging round jet, *Experimental Thermal and Fluid Science*, 4, pp. 253 – 264, 1991.
10. N. Didden and C.-M. Ho, Unsteady separation in a boundary layer produced by an impinging jet, J. *Fluid Mech.*, vol. 160, 235-256, 1985.
11. C. Meola, G. Cardone, C. Carmicino and G.M. Carlomagno, Fluid dynamics and heat transfer in an impinging air jet, Int. *Symposium on Flow Visualisation*, paper 429, 2000.
12. IFA, IFA 100 System Instruction Manual, TSI Inc., U.S.A, 1983.
13. Dantec Measurement Technology, Probes for hot-wire anemometry, Dantec Measurement Technology, Denmark, 1996.
14. H.W. Coleman and W.G. Steele, *Experimental and uncertainty analysis for engineers*, Wiley, New York, 1999.
15. S.J. Ball, Near wall flow characteristics in jet impingement heat transfer, Ph.D. thesis, The Nottingham Trent University, Nottingham, UK, 1998.